

Experimental and numerical investigation of the hydrodynamics of mixed anaerobic digester

by

Daniel Asrat Balcha

A Thesis Submitted to the Graduate Studies of
The University of Manitoba
In Partial Fulfillment of the Requirements for the degree of

DOCTOR OF PHILOSOPHY

Department of Mechanical and Manufacturing Engineering
University of Manitoba
Winnipeg, MB
Canada

© Copyright 2014 by Daniel Asrat Balcha

ABSTRACT

A review of the literature indicates that the understanding of the mixing phenomena in anaerobic digesters is limited and the ability to measure digester mixing characteristics is lacking. Moreover, rheological characteristics of the sludge are largely ignored. The need for a more thorough understanding of fundamental mixing relationships and the ability to measure these relationships in the anaerobic digester is recognized. To this end, investigations using experimental and numerical methods to visualize flow patterns and quantify mixing that impact biogas yields is reported. Results from this research identifies optimum mixing regimes for digesters depending on their sludge rheology, operational regimes, digester dimensions and mixing systems, and also produces an industrial guide to improve digester design.

The study uses lab-scaled mixed anaerobic digester and a candidate transparent fluid with a minimum power law index, n , of 0.55 and the power law constant range 0.014 to 1.18 that is rheologically characterized and parameters affecting the viscosity are investigated at concentrations of 0.05–1.00% w/w HEC solution corresponding to 2–10% TS manure and temperatures of 5–45°C. The experimental tools used to analyze the systems under investigation are: particle image velocimetry for experimental determination of velocity profiles; a conductivity technique to quantify mixing time; a strain gage-based rotary torque transducer system to measure the power dissipated by the impeller; and an acid-base reaction coupled with image processing technique to understand the formation and degeneration of segregated flow regions that exist at low

Re and a visual observation method to determine the minimum agitation speed for complete solids suspension, N_{js} . A computational fluid dynamic model is developed to predict the behavior of the system in terms of its velocity profile, power number, pumping number, and mixing time. For a Re based on impeller diameter and blade rotational speed, the following flow regimes are identified and investigated in detail: laminar, $Re = 1, 6.9, \text{ and } 15.5$, transient, $Re \approx 3 \cdot 10^3$ and turbulent, $Re \approx 3 \cdot 10^4$. Numerical predictions are obtained using MRF/SM model coupled, when needed, with a volume of fluid model, in order to study systems in which a vortex could be expected to form over a range of Re covering laminar, transitional and turbulent flow regimes.

The results show variation of mixing intensities and duration eliminate dead zones in digester up to 28% faster and eliminate scum layer, maximize use of digester volume and efficiently mix incoming feed with digester contents. The results also indicated critical parameters that keep solids and heavier sediment in suspension for uniform liquid and temperature distribution and prevent sludge buildup leading to reduction and/or elimination of digester cleaning cost and digester downtime.

In addition, the experimental study on the effects of mixing intensity and mixing duration on the anaerobic digestion performance shows how biogas output is dependent upon, and can be influenced by flow patterns in an anaerobic digester. The mixing intensities studied had a significant effect on soluble chemical oxygen demand (SCOD) utilization rate. The Biogas yield showed an increase ranging from 2.5 to 14.6% for digesters operated under various intermittent mixing compared to biogas yield from

continuous mixing. Hence, it is possible to tailor mixing regimes to produce flow patterns that could potentially increase biogas production and/or reduce mixing energy input of an anaerobic digester.

ACKNOWLEDGMENT

This research was funded by the NSERC/Manitoba Hydro Industrial Research Chair and I wish to relate much appreciation for the opportunity for the creation of such a training program in renewable energy. Many thanks go to Mr. Tom Molinski for working on the Chair program.

I would like to thank my supervisor, Dr. Eric L. Bibeau, who has been of a great intellectual support. He shared with me a lot of his expertise and research insight and gave me complete academic freedom to explore and heighten my research interests in alternative energy field. That freedom was instrumental in helping me develop into an independent professional engineer.

I would also like to show my genuine appreciation to the other members of my PhD committee who monitored my work and took effort in reading and providing me with valuable comments on earlier versions of this thesis: Dr. Nazim Cicek, Dr. Robert Derksen (University of Manitoba) and Dr. Oladiran Fasina (Auburn University). I thank all of you to the bottom of my heart.

Many thanks to my wife Ribka Melesse, for her unconditional love, patience, assistance, support and faith in me. She has endured this long process with me, always offering me love and support. I deeply thank my Family: brothers, sisters, aunts and cousins for believing in me and for being proud of me. Most importantly, I would like to thank and

dedicate this work to my loving parents, Asrat Balcha and Aberash Dejene who are the angels that constantly watch over my head and whose simple voice gives me the necessary strength to hold on and persevere.

I am tempted to individually thank all of my friends but as the list might be long and for fear I might omit someone, I will simply and genuinely say: Thank you to you all for your love, care and trust. In particular, I would like to cite Kwadwo Owusu, Bafoor, Jonathan, Godwin (Ghana); Amir, Mohamed (Iran); Moftah Mohamed (Libya) and David Gaden and Jeremy Langner (Canada) for their constant presence, care, instant moral support and intellectual discussions.

I cannot finish without acknowledging how eternally grateful and thankful I am to The One, The Everlasting, The All Determiner, The Trustee, The Dependable and The Protecting Friend that guides me, teaches me to be patient and to never give up. Thank you Dear Lord!

የጥበብ መጀመሪያ እግዚአብሔርን መፍራት ነው፤ /ምሳ.1፡7/ አቤቱ አምላኬ እግዚሀብሔር ሆይ ለእኔ ያላደረከው ምን አለ? ወለታህና ቸርነትህ ፍቅርህና ምግባርህ ከአዕምሮዬ በላይ ነዉና ፈጣሪ ከፀሐይ መውጫ ጀምሮ እስከ መግቢያው ድረስ ስምህ ይመስገን።

አምላክ ቅዱሳን የኃይላን ኃይል የድንግል ማርያም ልጅ ጌታ መድኃኒዓለም ሀገራችንን ይጠብቅልን!!!

መታሰቢያ (Dedication)

ስንሰደድ የምናፈቅራቸውን ወላጆቻችንን የምንወዳቸውን እና የሚወዱንን ቤተሰቦቻችንን፣ ዘመድ አዝማዶቻችንን የኛ የምንለውን ማንነት የባለ ሃገርነትን ስሜታችንን ባህላችንን ፣ወጋችንን ስለራሳችን ያለንን ግምት ክብራችንን ተስማማህ/ሽ አማረብህ/ሽ የሚለንን፣የሚያስብልን የሚጨነቅልልን የሚያበረታታንን ብቸኝነት እንዳይሰማን እና ሙሉነት እንዲሰማን የሚያደረጉንን ነገሮች ትተን አዲስ ህልም ሰንቀን የተሻለ ህይወትን ፣ ብሩህ ነገን አስበን ወጥተናል። ሁላችንም በስደት ያለን በተለያየ ስራ ላይ ተሰማርተን ህልማችንን እና ግባችንን እውን ለማድረግ ደፋ ቀና በማለት ላይ እንገኛለን። አብዛኛዎቻችን ለኢትዮጵያ መስራት የምንችለውን እና መስራት የሚገባንን ሳይሆን ኑኖ ያስገደደን ስራ እየሰራን ሙሉ ችሎታችንን እውቀታችንን እና አቅማችንን ለኢትዮጵያ ሳንጠቀም እርካታም ሳይሰማን ቀን ይወጣል ቀን ይመጣል እያልን በተስፋ እንኖራለን ።

እያንዳንዱ ቀን ባለፈች ቁጥር ግን ኢትዮጵያ አስከፊና አማራሪ ቦታ አየሆነች ነው። አገር ሲቆረስ ድንበር ሲፈርስ ማንነት እና ታሪክ ሲሻር መሬት ሲገመስ አገር ያለ ባህር በር ስትቀር የዜጋ ማንነት በጎሳ ሲቀየር ድንበር ተቆርሶ ለባዕድ ሲለገስ ወገን ሲጨቁን መኖሪያ ቤቱ ሲፈርስ ሀብት ንብረቱ ተዘርፎ ከቀዬው ሲሰደድ የዜግነት ክብሩ ሲጣስ ሰብእናው ሲዋረድ በአረብ ምድር ሲገደል እንደ እንስሳ ሲታረድ ህይወቱ ሲቀጠፍ በገመድ ሲታነቅ ዜግነት ክብሩ ሲዋረድ ሰብእዊ መብቱ ሲናድ የመኖር ህልሙ ባዶ ሲሆን ፊቱ በእንባ ሲታጠብ በሀዘን ሲዋጥ ለስቃይ ችግር ሲዳረግ በረሀብ አለንጋ ሲገረፍ ጠኔ ሲመታው እና በከባድ ህመም ሕይወቱ ሲቀጠፍ ማየት የተለመደባት አገር ሆናለች።

ይህ መመረቂያ ፅሁፍ መታሰቢያነቱ ሰብእዊ መብቶች በሚደፈጠጡባት ስልጣኔ ወደኋላቀርነት በሚዘወርባት ፍትህ በሚጣሰባት፣ የዘር ማጥፋት በሚፈጸምባት፣ ህዝቦች በሚደከቡባት እና በሚረቡባት፣ ወጣቶች አፋቸው በሚሸበቡባት፣ በሚለገሙባት እና በሚታፈኑባት፣ የአካባቢ ተፈጥሮ ሀብት በሚወድምባት፣ ግድቦች ቋሚ ዝርያ ያላቸውን ህዝቦች መብት በሚገድቡባት እና ህዝቦች ወደ አስከፊ ሁኔታ እየወረዱ ባሉባት ሀገሪ ለሚኖሩ ኢትዮጵያዊ ወገኖቼ ይሁንልኝ። ኢትዮጵያ በልጆቿ የመንፈስ ጽናት ተመልሳ በእግሯ ትቆማለች።

ኢትዮጵያ በነጻነቷና በአንድነቷ ለዘላለም ኮርታ ትኑር።
ዳንኤል አሰራት ባልቻ

TABLE OF CONTENTS

ABSTRACT	ii
ACKNOWLEDGMENT	v
TABLE OF CONTENTS	viii
LIST OF TABLES.....	xii
LIST OF FIGURES	xiv
NOMENCLATURE AND ABBREVIATIONS	xxvi
1. Introduction.....	1
1.1 Feedstock for anaerobic digestion plants	4
1.2 Anaerobic digestion of livestock manure.....	5
1.3 Research motivation.....	7
1.4 Research objectives, procedures and outcomes	11
1.5 Outline of thesis	15
1.6 Publications	16
2. Summary of literature review	19
2.1 Anaerobic digestion process	20
2.2 Non-Newtonian fluids.....	22
2.3 Experimental and numerical studies in mixing.....	24
2.4 Anaerobic digestion modeling	27
3. Experiments on viscosity, mixing time, power and suspension using lab-scale AD	30
3.1 Laboratory scale experimental set up.....	31
3.2 Methodology	43
3.2.1 Viscosities measurement.....	43
3.2.2 Mixing time and power measurement.....	47
3.2.3 Experimental flow measurement	48
3.2.4 Determination of impeller pumping flow rate and pumping number ..	52
3.2.5 Determination of impeller discharge angle	53

3.2.6	Determination of the impeller power dissipation and power number ..	54
3.3	Data analysis and results	55
3.3.1	Non-Newtonian viscosities measurement	55
3.3.2	Mixing time and power measurement for Newtonian fluids	59
3.3.3	Mixing time and power measurement for non-Newtonian fluids	81
3.3.4	Suspension of high concentration non-Newtonian fluid in agitated AD	98
3.4	Conclusion	110
4.	Investigation of unmixed zone in mixed anaerobic digester	113
4.1	Scaled laboratory experimental set up	114
4.2	Methodology	116
4.3	Results and discussions	120
4.4	Effect of perturbation on segregated mixed regions	122
4.5	Effect of temperature change on segregated mixing regions	144
4.6	Conclusion	147
5.	Numerical modeling of hydrodynamics of mixed AD	149
5.1	Model geometry for lab scale digester	151
5.2	Governing equations	152
5.3	CFD modeling of mixing in a lab scale digester	157
5.3.1	Modeling viscosity	157
5.3.2	Volume of Fluid (VOF) method	158
5.3.3	Computational prediction of impeller pumping flow and pumping number	161
5.3.4	Computational prediction of impeller discharge angle	161
5.3.5	Computational prediction of impeller power dissipation and power number	162
5.3.6	Computational prediction of mixing time	163
5.4	Results and discussions	165

5.4.1	Laminar hydrodynamics.....	167
5.4.2	Transitional hydrodynamics.....	176
5.5	Conclusion	195
6.	Effect of geometrical and operating parameters on the performance of mixing in turbulent mixed AD.....	198
6.1	Methodology	199
6.2	Validation.....	200
6.3	Results and discussion (single phase)	202
6.3.1	Effect of impeller submergence ratio on flow pattern with $H/T < 1$..	202
6.3.2	Effect of off-bottom clearance (C_b/T).....	209
6.3.3	Effect of D/T and S_b/D Ratios	215
6.4	Results and discussion (two phase).....	217
6.4.1	Investigation of sedimentation in mixed AD	217
6.4.2	Investigation of suspension of solid in mixed AD.....	221
6.5	Conclusion	251
7.	Effect of mixing strategy on methane production on lab and pilot scaled AD.....	254
7.1	Experimental setup, materials and methods.....	254
7.1.1	Lab scale studies	254
7.1.2	Pilot-scale studies	257
7.2	Experimental results.....	259
7.2.1	Lab-scaled anaerobic digester	259
7.2.2	Effect of mixing on the performance of pilot-scale AD	275
7.3	Conclusions.....	280
8.	Conclusion, contributions and recommendations.....	282
8.1	Conclusions and contributions	282
8.1.1	Significance of experimental work	282
8.1.2	Significance of numerical work	285

8.2	Recommendations	287
	References.....	290
Appendix A.	Literature review on microbial aspects of anaerobic digestion process 309	
Appendix B.	Literature review on non-Newtonian fluid.....	318
Appendix C.	Literature review on experimental studies on mixing.....	329
Appendix D.	Literature review on CFD studies on mixing.....	348
Appendix E.	Literature review on AD modeling	361

LIST OF TABLES

Table 1.1: Possible feedstocks for waste-to-energy plants.....	5
Table 1.2: Potential biogas yield from various animals (Boe, 2006)	6
Table 2.1: Main steps and pathways of anaerobic digestion (modified from Batstone <i>et al.</i> , 2002a).....	21
Table 3.1: Test matrices for mixing time and power investigation with impeller dimensions.....	34
Table 3.2: Conductivity probe positions.....	37
Table 3.3: Power law constants and indices of pseudo-plastic fluids used for mixing time measurement experiment.....	41
Table 3.4: Consistency coefficients and flow behavior indices of HEC at various temperatures and concentrations.....	56
Table 3.5: Apparent viscosity at shear rate value of 100 s^{-1} as a function of concentration for HEC solution from 5 to 45°C for 0.25% HEC.....	57
Table 3.6: The activation energies, frequency factors and coefficients of determination while fitting data to Arrhenius model.....	58
Table 3.7: Newtonian mixing time results (T/3PBT) for individual probe mixing times, θ_1 , θ_2 and θ_3 corresponding to the 3 probe positions	66
Table 3.8: Newtonian mixing time results (T/2PBT)	67
Table 3.9: Newtonian mixing time results (T/3RT)	68
Table 3.10: Newtonian mixing time results (T/2A310).....	68
Table 3.11: $N\theta$ versus Re regression results.....	73
Table 3.12: Correlation regression results	74
Table 3.13: Comparison of constants	75
Table 3.14: Pseudoplastic mixing time results T/3 PBT	88
Table 3.15: Pseudoplastic mixing time results T/2 PBT	88
Table 3.16: Pseudoplastic mixing time results T/3 RT.....	89
Table 3.17: Pseudoplastic mixing time results T/2 A310 hydrofoil.....	89
Table 3.18: $N\theta$ versus Re regression results.....	93
Table 3.19: Correlation results	94

Table 3.20: Comparison of constants	95
Table 5.1: Constants of the turbulence model	156
Table 6.1: Pumping number for $D/T = 0.31$ and $C_b/T = 0.30$	201
Table 6.2: Power Number for $D/T=0.31$ and $C_b/T = 0.30$	201
Table 6.3: Critical fill ratios and impeller submergence ratios for different C_b/T	213
Table 6.4: Diameter of the impellers investigated.....	215
Table 6.5: Effect of impeller type on the quality of suspension, particle size of $350 \mu\text{m}$ with solid loading of 10 vol. %.....	225
Table 6.6: Experimental and predicted values of power number for digester equipped with RT, PBT and Hydrofoil impellers.	226
Table 6.7: Effects of off-centered shaft on N_{critical} and power consumption	229
Table 6.8: Effect of turbulence on floating particles at constant agitation speed of 9.8 s^{-1}	231
Table 7.1: Steady-state performance results	268
Table 7.2: Methane production during steady-state periods.....	271

LIST OF FIGURES

Figure 3.1: Experimental lab-scale digester arrangements (T = Digester diameter, D = Impeller of diameter, C _b = Off-bottom clearance, S _b = Impeller submergence)	33
Figure 3.2: Schematic diagram of a typical impeller with the dimension (a) and impellers under investigation with Rushton turbine (RT), Pitched blade turbine (PBT) and Lightnin A310 (A310) left to right.	35
Figure 3.3: Experimental set up and conductivity probe detail (T = Digester diameter, D = Impeller of diameter)	36
Figure 3.4: Positions of probes and injection position in the lab-scaled mechanically mixed digester (Injection T/10 from shaft axis, Probe 1 T/8.....	37
Figure 3.5: Sample comparison of manure with manure simulant HEC solutions	40
Figure 3.6: Experimental set up for the flow field measurement using PIV	42
Figure 3.7: Schematic of coaxial viscometer.....	44
Figure 3.8: Conductivity trace of added electrolyte to the bulk solution of HEC in a lab-scaled digester used to measure the mixing time.....	48
Figure 3.9: Schematic showing operation of PIV using two cameras	51
Figure 3.10: Effect of concentration on apparent viscosity at shear rate value of 100 s ⁻¹ at 25°C for HEC solutions tested form 0% to 1% concentration.....	57
Figure 3.11: Effect of temperature on apparent viscosity at shear rate value of 100 s ⁻¹ for water and HEC solutions tested.....	59
Figure 3.12: Plot of log variance, log σ _c ² , verses time where both C and σ _c ² are functions of root mean square concentration fluctuation over a time, Γ	61
Figure 3.13: Nθ versus Reynolds number for Newtonian data, T/3PBT.....	69
Figure 3.14: Nθ _i versus Reynolds number for Newtonian data, T/2PBT	69
Figure 3.15: Nθ versus Reynolds number for Newtonian data, T/3RT	70
Figure 3.16: Nθ versus Reynolds number for Newtonian data, T/2A310	70
Figure 3.17: Plot of mixing time correlation (Newtonian data - for all impellers) for the two regimes where the boundary between the two regimes occurring at 1/Fo ~ 10 ³	73

Figure 3.18: Vessel geometry used for the estimation of wall shear rate	84
Figure 3.19: Plot of individual probe $N\theta$ versus Reynolds number-pseudo-plastic data-T/3 PBT	90
Figure 3.20: Plot of individual probe $N\theta_i$ versus Reynolds number-pseudo-plastic data-T/2 PBT	91
Figure 3.21: Plot of individual probe $N\theta$ versus Reynolds number-pseudo-plastic data-T/3 RT	92
Figure 3.22: Plot of individual probe $N\theta$ versus Reynolds number-pseudo-plastic data-T/2 A310 hydrofoil	92
Figure 3.23: Effect of solids concentration of glass particles of $d = 12$ mm in non-Newtonian HEC solution on agitation power per unit slurry volume of a baffled digester equipped with a PBT impeller	99
Figure 3.24: Effect of solids concentration on specific power, ϵ_{js} , for a baffled AD using a PBT impeller and glass particles of $d = 12$ mm in HEC solution as obtained in this study.....	100
Figure 3.25: Effect of impeller type on specific power, ϵ_{js} , for glass particles of $d = 12$ mm baffled scaled digester investigated.....	102
Figure 3.26: Effect of impeller type on specific power, ϵ_{js} , for different concentration loadings obtained using scaled digester without baffles, non-Newtonian HEC solution and spherical glass particles of 12 mm diameter.	103
Figure 3.27: Specific power enhancement factor Re vs. solids concentration of glass particles of 12 mm diameter at just-off-bottom solids suspension condition.....	104
Figure 3.28: Effect of impeller diameter on specific power, ϵ_{js} , for two impeller dimension to tank diameter ratios, D/T , and for increasing concentration of 12 mm diameter spherical glass particles using the A310 impeller, baffled scaled AD, and non-Newtonian fluid.....	105
Figure 3.29: Effect of impeller diameter on specific power, ϵ_{js} , for two impeller dimension to tank diameter ratios, D/T , and for increasing concentration of 12 mm diameter spherical glass particles using the A310 impeller, unbaffled scaled AD, and non-Newtonian fluid.....	106

Figure 3.30: Effect of dual impellers on specific power, ϵ_{js} , in scaled AD without baffle equipped with A310 impeller, glass particles of diameter of A310 impeller and non-Newtonian HEC solution ($C_1 > 0.17T$ and $C_2 < 0.385T$)	107
Figure 3.31: Effect of particle size, d_p , on specific power consumption, ϵ_{js} , using an RT impeller, no baffles, and non-Newtonian fluid	108
Figure 3.32: Effect of particle size, d_p , on specific power consumption, ϵ_{js} , using an PBT impeller, no baffles, and non-Newtonian fluid	109
Figure 3.33: Effect of particle size, d_p , on specific power consumption, ϵ_{js} , using an A310 impeller, no baffles, and non-Newtonian fluid	109
Figure 3.34: Minimum power consumption, optimum solids concentration vs. particle size, at just-off-bottom solids suspension condition in lab-scaled digester equipped various impellers without baffle	110
Figure 4.1: Schematic of experimental set-up used to investigate unmixed zones in mixed anaerobic digesters using a scaled circular AD incased in a rectangular tank to prevent visual distortions (instrumentation not shown)	115
Figure 4.2: Dimensions of 6-blade Rushton Turbine RT impeller used to investigate unmixed zones in mixed anaerobic digesters	116
Figure 4.3: Flow visualization of acid–base reaction revealing the unmixed regions containing NaOH appear as dark pink structures whereas chaotic acidic regions that are well mixed appear as light areas. The round scaled digester is encased inside a rectangular tank filled with water to prevent distortion, as seen in the left and right side of the figure.	118
Figure 4.4: Three-dimensional structure of a torus volume and cross-sectional area of a torus showing the torus radius, R , and the cross-sectional radius of the torus, r	119
Figure 4.5: Cross-sectional view of stirred AD circular vessel without baffles using uniform RT impeller speed. Colour variations show the existence of unmixed region core structures in the upper, quadrants 1 and 2 and lower regions, quadrants 3 and 4 of the digester. All tests are for non-Newtonian flow unless otherwise specified.	121

Figure 4.6: Volume of unmixed region as percentage of initial digester volume as function of dimensionless time, Nt_m , which does not decrease with prolonged mixing time after 5,000.....	122
Figure 4.7: Visualization of unmixed mixed region tori locations at low and high impeller speed obtained by Re variations by changing shaft RPM. P_1 is the location of an unmixed region at low Re number and P_2 is the location of an unmixed region at high Re. Applications of a square wave to control shaft rotation improves mixing by movement of P_1 and P_2 , and creation of CW and CCW rotation.	123
Figure 4.8:-Effect on the four unmixed regions when applying square amplitude, A_1 , with $Re = 40$ and $Re = 60$ with a wave period of 20 s. Mixing effect shown at (a) high speed with $Re = 60$, and (b) low speed with $Re = 40$. The four pink unmixed regions with a magenta dot at the centre clearly are moving relative to white grid lines to show the enhanced mixing now occurring.....	124
Figure 4.9: Formation and destruction of the four “horseshoe” folds after a few period cycles applying a square amplitude, A_1 , with $Re = 40$ and $Re = 60$ with a wave period of 20 sec.....	125
Figure 4.10: Dimensionless time, Nt_m , to reach destruction of upper unmixed pockets using square-wave application, A_1 , with $Re = 40$ and $Re = 60$, for wave periods of 10, 20 and 40 sec	126
Figure 4.11: Dimensionless time, Nt_m , to reach destruction of upper unmixed pockets using square-wave application, $A_2 = 30$, with $Re = 30$ and $Re = 60$, for wave periods of 10, 20 and 40 sec	127
Figure 4.12: Dimensionless time, Nt_m , to reach destruction of lower unmixed pockets using square-wave application, $A_1 = 20$, with $Re = 30$ and $Re = 60$, for wave periods of 10, 20 and 40 sec	129
Figure 4.13: Dimensionless time, Nt_m , to reach destruction of lower unmixed pockets using square-wave application, $A_1 = 30$, with $Re = 30$ and $Re = 60$, for wave periods of 10, 20 and 40 sec	130
Figure 4.14: Chaotic mixing for upper and lower pockets using square-wave variation of mixing intensities with amplitude $A_2 = 30$ fluctuation with $Re = 30$ and $Re = 60$, for wave periods of 10, 20 and 40 sec.....	131

Figure 4.15: Chaotic mixing for upper and lower envelope using square-wave variation of mixing intensities with amplitude $A_1 = 20$ fluctuation with $Re = 40$ and $Re = 60$, for wave periods of 10, 20 and 40 sec	132
Figure 4.16: Reduction in volume of unmixed structure regions using 10, 20 and 40 sec periods with a sine wave applied at $Re = 30$ to $Re = 60$	133
Figure 4.17: Reduction of upper unmixed structure pocket to 20% volume using 10, 20 and 40 sec periods with a sine wave applied from $Re = 30$ to $Re = 60$	135
Figure 4.18: Evolution of total unmixed volume with dimensionless time, Nt_m using uniform impeller speed without baffles of $Re = 60$	136
Figure 4.19: Chaotic mixing of unmixed mixed regions for impellers RT, PBT and A310 using uniform impeller speed without baffles for $Re = 60$	137
Figure 4.20: Evolution of total unmixed volume with dimensionless time, Nt_m using square-wave variation of mixing intensities with amplitude $A = 10$ fluctuation with $R = 10$ and $Re = 20$, for wave period of 10 sec	138
Figure 4.21: Evolution of total volume of unmixed mixed zone with dimensionless time, Nt_m , using square-wave variation of mixing intensities with amplitude $A = 10$ fluctuation with $Re = 10$ and $Re = 20$, for wave period of 10 sec under unbaffled conditions using PBT (left) and RT (right).....	140
Figure 4.22: Variation of total percentage volume for unmixed core structures as function of dimensionless time, Nt_m for different impellers and normal baffles using uniform impeller speed without baffles for $Re = 60$	141
Figure 4.23: Unmixed core structures with 4-blade baffles normal to the digester wall using uniform impeller speed for $Re = 60$ uniform speed after several hours with impellers (a) RT, (b) PBT and (c) A310.....	142
Figure 4.25: Schematic of modification of baffles: (a) normal to the wall, and (b) baffles placed away from the wall.....	143
Figure 4.26: Evolution of segregated pockets with modified baffles placed away for the wall at uniform impeller speed using RT, PBT and A310 impellers and $Re = 60$	144
Figure 4.26: Cross sectional view showing the transition of unmixed flow structures in the vessel from $t = 15$ min to $t = 60$ min as result of temperature difference of $10^\circ C$, $Re = 30$	146

Figure 4.27: Cross sectional view showing the sequence of transition of upper chaotic flow structures in the vessel with schematic of evolution from $t = 15$ min to $t = 60$ min as result of temperature difference of 10°C , $\text{Re} = 30$	146
Figure 5.1: Geometry used for simulation dimensions of lab-scale digester: $T = 0.25$ m, six-blade RT impeller, $D = T/3$, $C_b = T/3$, $H_{BL} = 0.2D$, $L_{BL} = 0.25D$, $t_{BL} = 0.01T$, $L_B = T/10$ and $t_B = 0.01T$. $\text{Re} = 1, 6.9, 15.5$ for laminar, 3,000 for transitional, and 22,500 for turbulent cases.....	151
Figure 5.2: Geometric locations used to record normalized concentrations of tracer as a function of time. The square area marked red at the top of the digester is the location of tracer injection.....	164
Figure 5.3: Computational grid used to perform numerical simulation with local mesh refinement. In each simulation, the computational mesh is made up of two parts: an inner rotating cylindrical volume enclosing the impeller and an outer stationary volume containing the rest of the digester.....	166
Figure 5.4: Comparison of radial velocity components obtained from numerical simulation and experiment at various normalized distances r/T for $\text{Re} = 15.5$, near upper blade tip at $z/T = 1/30$	168
Figure 5.5: Comparison of radial velocity components obtained from numerical simulation and experiment at various normalized distances r/T for $\text{Re} = 6.9$, near upper blade tip at $z/T = 1/30$	168
Figure 5.6: Comparison of radial velocity components obtained from numerical simulation and experiment at various normalized distances r/T for $\text{Re} = 1$, near upper blade tip at $z/T = 1/30$	169
Figure 5.7: Three dimensional view of the fluid motion around the impeller for $\text{Re} = 1$ at $H_{BL}/2$	170
Figure 5.8: Radial velocity and pressure contours in units of Pa for $\text{Re} = 1$, in plane $z/T = 1/30$. The rotation of the blade is clockwise.	171
Figure 5.9: Variation of normalized acceleration, pressure and viscous forces in the radial direction for $\varphi = 0^{\circ}$, $z/T = 1/30$ (upper blade tip) and $\text{Re} = 15.5$	173
Figure 5.10: Radial force components at near upper tip location at normalized distance $r/T = 0.186$ and $z/T = 1/30$ for (a) $\text{Re} = 15.5$, (b) $\text{Re} = 6.9$ and (c) $\text{Re} = 1$	175

Figure 5.11: Experimental and computational results of radial and circumferential velocities normalized by the tip velocity denoted as V_r/V_{tip} and V_θ/V_{tip} at disk $x - y$ -plane for $z = 0$	178
Figure 5.12: Radial V_r/V_{tip} , circumferential V_θ/V_{tip} and axial V_z/V_{tip} normalized simulated and experimentally measured mean velocity in the x - y -plane at lower blade tip, $z/(H_{BL}/2) = -1$ as a function of normalized radial position r/R	180
Figure 5.13: Instantaneous flow unit-vectors and normalized velocity magnitude contours V/V_{tip} at (a) $x-z$, $y = 0$ and (b) disk-plane, $z = 0$	181
Figure 5.14: Instantaneous flow streamlines and normalized pressure contours $P/P_{dynamic}$ based on V_{tip} . Blade rotation is clockwise	182
Figure 5.15: Iso-surfaces of instantaneous swirl parameter at various locations in the digester indicating the presence of a turbulent wake associated with the impeller motion. The origin of the wake is the suction side of the blade whereupon the vortex detaches from the blade and convects outward due to the bulk motion of the fluid.....	183
Figure 5.16: Illustration of statistical sample regions: Impeller position associated with $\theta = 0^\circ$, $\phi = 45^\circ$	184
Figure 5.17: Mapped mean flow unit-vectors (unit length) and normalized velocity magnitude V/V_{tip} at various locations. The presence of the upper and lower bulk-flow recirculation zones above and below the disk-plane ($z = 0$) towards the outer digester wall are associated with the impeller jet.	185
Figure 5.18: Mapped mean flow streamlines and normalized pressure $P/P_{dynamic}$ based on V_{tip} with the upper and lower recirculation zones due to the impeller jet impinging on the outer digester wall, as well as the separation in the mean on the suction-side of the baffle.....	186
Figure 5.19: Iso-surfaces of swirl parameter for the mapped mean flow. There is a dual blade trailing on the suction-side where vortices are visible. Blade rotation is clockwise	187
Figure 5.20: Iso-surfaces for the mapped mean flow. Dual blade trailing vortices on the suction-side are visible. Blade rotation is clockwise	188

Figure 5.21: (a) Contour of normalized in-plane pressure force. (b) Near-blade contour and unit vector plot, (c) Contour of normalized pressure with pressure force unit vectors overlaid.....	190
Figure 5.22: (a) Iso-surface of normalized dissipation = 300, (b) normalized dissipation at disk-plane ($z = 0$), (c) normalized dissipation in $x - y$ -plane at $z/(H_{BL}/2) = -0.5$	192
Figure 5.23: Normalized mean-flow Kinetic energy iso-surface and contours. (a) Iso-surface of normalized k/k_{Vtip} of 0.75. (b) k/k_{Vtip} at disk-plane, $z = 0$ (c) k/k_{Vtip} in $x - y$ -plane at $z/H_{BL}/2 = -0.5$	194
Figure 5.24: Normalized mean-flow dissipation and kinetic energy in the $x - z$ plane at distance $2t_B$ downstream from blade suction surface.	195
Figure 6.1: PIV measurement and CFD prediction of velocity vectors for different H/T ratios, $C_b/T = 0.30$, $D/T = 0.31$ and $N = 300$ rpm.....	203
Figure 6.2: PIV measurement and CFD prediction of velocity contours for different S_b/D ratios, $C_b/T = 0.30$, $D/T = 0.31$ and $N = 300$ rpm.....	204
Figure 6.3: CFD simulations of radial and axial velocities for different S_b/D ratios on five different iso-surfaces, $C_b/T = 0.30$, $D/T = 0.31$ and $N = 300$ rpm	206
Figure 6.4: Effect of S_b/D on (a) Impeller discharge angle, (b) radial Pumping Number, N_{Qr} and (c) Power Number, Po for different S_b/D ratios, $C_b/T = 0.30$, $D/T = 0.31$ and $N = 300$ rpm calculated from both experimental and FS-CFD Simulation data	208
Figure 6.5: Velocity contour plots for different C_b/T , $H/T = 1$, $D/T = 0.31$, $N = 300$ rpm	209
Figure 6.6: (a) Impeller discharge angle, (b) N_{Qr} and (c) Po for different C_b/T , $H/T = 1$, $D/T = 0.31$ and $N = 300$ rpm	211
Figure 6.7: Power numbers obtained experimentally for different S_b/D at different C_b/T , $D/T=0.31$ and $N = 300$ rpm to show flow pattern transition a result of variation in C_b/T ratio	214
Figure 6.8: Power numbers obtained experimentally for different S_b/D at different D/T , $U_{tip}=1.2$ m/s and $C_b/T=0.30$ to show the effect of D/T variation on power number	216

Figure 6.9: Particle sedimentation pattern on the bottom for $0.0 < z < 0.3$ mm, $C_b = T/3$ with four baffles, b) distribution of $V_{f,z}$ just above the bottom for $z = 0.9$ mm, $C_b = T/3$ baffles	218
Figure 6.10: a) Horizontal fluid velocity vectors, $V_{f,r-\theta}$ just above the bottom, b) distribution of $V_{f,z}$ just above the bottom for $z = 0.9$ mm, $h = H/10$ with baffles	218
Figure 6.11: Particle sedimentation pattern on the bottom where $0.0 < z < 0.3$ mm for $C_b = T/10$ with baffles (left), and distribution of particles moving upward around the bottom where $0.3 < z < 4.0$ mm, for $C_b = T/10$ with baffles (right)	219
Figure 6.12: (a) Horizontal fluid velocity vectors, $V_{f,r-\theta}$ just above the bottom (b) distribution of $V_{f,z}$ just above the bottom at $z = 0.9$ mm for $C_b = T/3$ without baffles	220
Figure 6.13: (a) Particle sedimentation pattern on the bottom for $0.0 < z < 0.3$ mm, $C_b = T/3$ without baffles (b) distribution of particles moving upward around the bottom for $0.3 < z < 4.0$ mm, $C_b = T/3$ without baffles	221
Figure 6.14: Standard deviation values obtained from CFD with respect to impeller rotational speed for RT, PBT and A315 hydrofoil impeller, particle size of $350 \mu\text{m}$ with solids loading of 10 vol. %	223
Figure 6.15: Cloud height predicted by CFD simulation for PBT impeller at different rotational speeds, particle size of $350 \mu\text{m}$ with solid loading of 10 vol. %, particle size of $350 \mu\text{m}$	223
Figure 6.16: Cloud height predicted by CFD simulation for A310 hydrofoil impeller at different rotational speeds, particle size of $350 \mu\text{m}$ with solid loading of 10 vol. %	224
Figure 6.17: Schematic of experimental setup to examine the effect of impeller shaft position on mixing of floating particles in lab-scale digester.....	227
Figure 6.18: Axial profile of (a) mean axial velocity (b) radial velocity at different eccentricity, $r/T = 0.96$	228
Figure 6.19: Contour plot of radial profiles of the axial velocity component for cylindrical, curved and spherical digester equipped with PBT impeller showing the distribution of the mean velocity in the vertical plane containing the blade. The	

impeller generates a radial jet developed from the blade and propagates in the lower part of the digester.	232
Figure 6.20: Distribution of the turbulent kinetic energy in vertical plane containing the PBT blade for cylindrical, curved and spherical digester equipped with PBT impeller	233
Figure 6.21: Distribution of the dissipation rate of the turbulent kinetic energy in r-z plane for cylindrical, curved and spherical digester equipped with PBT impeller	234
Figure 6.22: Evolution of the power number as a function of Re for cylindrical, curved and spherical digester equipped with PBT impeller	234
Figure 6.23: Horizontal plane for surface integration to quantify the amount of axial flow passing through the impeller in a flat bottom digester equipped with PBT impeller	235
Figure 6.24: Mass flow rate vs. baffled width to digester diameter ratio for digester equipped with PBT impeller	237
Figure 6.25: Power consumption vs. baffle width to digester diameter ratio for digester equipped with PBT impeller	238
Figure 6.26: Mass flow rate vs. off bottom to reactor diameter ratio for digester equipped with PBT impeller.....	239
Figure 6.27: Power consumption vs baffled spacing to reactor diameter ratio for digester equipped with PBT impeller	240
Figure 6.28: Mass flow rate vs. number of baffle for digester equipped with PBT impeller	241
Figure 6.29: Power consumption vs. number of baffle for digester equipped with PBT impeller	242
Figure 6.30: Mass flow rate vs. N(rpm) for digester equipped with PBT impeller.....	243
Figure 6.31: Power consumed vs. N(rpm) for digester equipped with PBT impeller ...	244
Figure 6.32: Mass flow rate vs. number of blades for digester equipped with PBT impeller	245
Figure 6.33: Power consumed in Watts vs. N_{BL} for digester equipped with PBT impeller	246
Figure 6.34: Mass flow rate vs. D/T for digester equipped with PBT impeller	247

Figure 6.35: Power consumed in Watts vs. D/T for digester equipped with PBT impeller	248
Figure 6.36: Mass flow rate vs. N_I for digester equipped with PBT impeller	249
Figure 6.37: Power consumed vs. N_I for digester equipped with PBT impeller	250
Figure 6.38: Percentage increment in power consumption vs. increase in N_I for digester equipped with PBT impeller	250
Figure 6.39: For $H/T \leq 1.4$, $N_I = 2$, since beyond this number, the increase in the flow rate did not warrant the increase in the power consumption	251
Figure 7.1: Schematic of lab-scaled digester used for performance test of different mixing duration and intensities on gas production	256
Figure 7.2: Schematic of pilot-scaled anaerobic digester used to test the effect of mixing on the performance of anaerobic digestion process	259
Figure 7.3: Average loadings to the lab-scaled digesters as a function of time during T-1, mixing duration at 45 min/h is from day 41 to day 65; the steady-state period during T-2, mixing duration at 15 min/h is from day 125 to day 149 designated as steady-state periods of CASE-1 and CASE-2, respectively	260
Figure 7.4: TCOD and SCOD concentrations in the feed as a function of time during T-1, mixing duration at 45 min/h is from day 41 to day 65; the steady-state period during T-2, mixing duration at 15 min/h is from day 125 to day 149 designated as steady-state periods of CASE-1 and CASE-2, respectively	262
Figure 7.5: SS and VSS concentrations in the feed as a function of time during T-1, mixing duration at 45 min/h is from day 41 to day 65; the steady-state period during T-2, mixing duration at 15 min/h is from day 125 to day 149 designated as steady-state periods of CASE-1 and CASE-2, respectively	263
Figure 7.6: TCOD and SCOD concentrations in lab-scaled digester effluents as a function of time for mixing intensities corresponding to impeller speed of 20, 50, and 100 rpm for R_2 , R_3 , and R_4 respectively	264
Figure 7.7: SS and VSS concentrations in digester effluents as a function of mixing intensities corresponding to impeller speed of 20, 50, and 100 rpm for R_2 , R_3 , and R_4 respectively	266

Figure 7.8: Steady-state percent removals of organics and solids versus mixing intensities corresponding to impeller speed of 20, 50, and 100 rpm for R ₂ , R ₃ , and R ₄ respectively	269
Figure 7.9: Normalized steady-state digester performance versus mixing intensities corresponding to impeller speed of 20, 50, and 100 rpm for R ₂ , R ₃ , and R ₄ respectively	274
Figure 7.10: Effect of modes of mixing on biogas production. During continuous mixing, the mixer operates at 100 rpm while under alternating mixing strategy with square wave, the mixer operates at 100 rpm with interval of 2 hours every 3 hours of mixing.....	275
Figure 7.11: Performance of digester to different modes of mixing. During continuous mixing, the mixer operates at 100 rpm while under alternating mixing strategy with square wave, the mixer operates at 100 rpm with interval of 2 hours every 3 hours of mixing.....	276
Figure 7.12: Process performance during anaerobic digestion with steady state and square wave modes of mixing application where the mixer operates at 100 rpm with interval of 2 hours every 3 hours of mixing.	276
Figure 7.13: Effect of mixing mode on specific biogas yield during anaerobic digestion. During uniform mixing, the mixer operates at 100 rpm while under alternating mixing strategy with square wave, the mixer operates at 100 rpm for 3 hours with an interval of 2 hours stoppage time.....	278

NOMENCLATURE AND ABBREVIATIONS

		P_1	Torus position 1 at high speed (Re_{max})
2D	Two-dimensional	P_2	Torus position 2 at low speed (Re_{min})
3D	Three dimensional	p_d	Particle diameter (m)
A	wave amplitude	PT	Wave period (sec)
A310	Lingiunn hydrofoil	Q	Volumetric flow rate discharged from impeller tip (m^3/h)
c	Parameters in k- ϵ models	R	Major radius of the centre of torus core to axis of the rotation (mm)
C_b	Impeller clearance (m)	r	Minor radius of the torus being rotated (mm)
D	Impeller diameter (m)	r	Radial distance from center of impeller (m)
Fl	Flow number,	r^2	Correlation coefficient
Fr	Froude number	Re	Reynolds number
g	Acceleration due to gravity (m/sec^2)	T	Inner cylindrical tank diameter (m)
H	Height of liquid level (m)	T_1	Turbulent length scale
k	Turbulent kinetic energy (m^2/s^2)	(m)	
k_l	Kolmogoroff length scale (m)	t_m	Acid–base decolorization time (min)
L	Characteristic length scale (m)	U_r	Radial velocity (ms^{-1})
M	Mass flow rate (kg/h)	U_{tip}	Impeller tip velocity (ms^{-1})
N	Impeller rotational speed (revs/min)	U_z	Axial velocity (ms^{-1})
Ne	Newton number	U_θ	Tangential velocity(ms^{-1})
Nt_m	Dimensionless mixing time	V	Volume of inner cylindrical tank, (m^3)
P	Pressure, (bar, Pa)		

z	Vertical direction from center of impeller (m)	SM	Sliding Mesh
		SRT	Solids retention time
τ_{ij}	Shear stress ($\text{kgm}^{-1}\text{s}^{-2}$)	TS	Total solids
AD	Anaerobic digestion	TVS	Total volatile solids
AMR	Active mixing region (m)	UE	Upper envelope
BOD	Biological oxygen demand	VFA	Volatile fatty acids
CFD	Computational Fluid Dynamics	Greek symbols	
COD	Chemical oxygen demand	γ	Shear rate (s^{-1})
		θ	Mixing time
DNS	Direct Numerical Simulations	Λ	Torque (Nm)
		μ	Viscosity (Pa.s)
GC	Gas chromatography	μ	Viscosity (Pas)
GC	Gas chromatography	ν	Kinematic Viscosity (m^2/sec)
HCl	Hydrochloric acid		
HRT	Hydraulic retention time	ρ	Density (kg/m^3)
LE	Lower envelope	ρ	Density (kgm^{-3})
LES	Large Eddy Simulations	σ	Parameters in k- ϵ model
MRF	Multi Reference Frame	τ	Shear stress (Pa)
NaOH	Sodium hydroxide		
PIV	Particle Image Velocimetry		
RANS	Reynolds Averaged Navier-Stokes		
RPM	Revolution per minute		
RSM	Reynolds Stress Model		
RT	Rushton turbine		

1. Introduction

Global energy consumption has increased steadily for much of the twentieth century, particularly after 1950 (Bonhotal, 2001). In 2008, the world consumed 11,300 million tonnes (Mtoe) of oil equivalent in total energy, including hydroelectric and nuclear power (Pirog, 2009). Today, the world consumes approximately 320 billion kWh a day and the total energy consumption has increased 57% globally since 1980 (OMAF, 2000). The International Energy Agency has predicted world energy demand will rise 1.6% per year on average, between 2006 and 2030 (Bonhotal, 2001). A number of national and global issues have encouraged Canada and other countries to consider biomass resources for energy to address energy drivers. These drivers include greenhouse gases that lead to climate change, peak oil issues, sustainability, energy price increase, and a need for rural diversification and revitalization.

The growth of the livestock industry means a corresponding growth in animal wastes at dairy, swine, and poultry farms. While waste disposal can create significant environmental problems especially to water streams, their potential for conversion into sustainable and renewable bio energy offers substantial benefits. According to Environment Canada (2001) report, Canada generates 190 million tons (dry basis) of animal waste per year—over 6,000 kg per Canadian individual. The Alberta Research Council estimates production of 780 MW of electricity and 1,040 MW of thermal energy in Canada from the wastes of the livestock industry (ARC, 2003(1)). These biomass resources are often mishandled and underutilized, which results in environmental

impacts. Unsafe and improper disposal of decomposable livestock wastes can result in surface and groundwater contamination, odors, dust, and ammonia leaching. There is also the issue of methane emissions that has a greenhouse gas effect that is 22 times more than carbon dioxide (Sheffield, 2002). Here in Manitoba, eutrophication of Lake Winnipeg is a major issue due to phosphorus originating in part from hog farm operations (Cicek et al, 2006).

Anaerobic digestion of animal wastes is a promising waste management option. It is a waste treatment alternative for industrial and agricultural wastes and has several advantages over aerobic treatment, including higher organic removal rates, lower sludge production, and lower energy requirements. In addition, the production of biogas in anaerobic digestion process represents a source of renewable and sustainable bio-energy, which can be combusted directly in modified gas boilers, used to run an internal combustion engine, converted into methanol (Van Die, 1987), and cleaned and distributed using natural gas pipeline infrastructure. The caloric value of biogas varies from 17 to 25 MJ/m³ (Pirog, 2009). Typically, anaerobic digesters (AD) convert 40% to 60% of organic matter present in biomass to a biogas that is composed of mainly CH₄ and CO₂. The remainder is an odor-free residue rich in nutrients used as fertilizers and soil amendments.

Benefits of anaerobic digestion

Anaerobic digestion can provide a variety of benefits to the livestock industry, regulators and farming rural communities. Depending on the effectiveness of the treatment process and the contamination levels of the feedstock, can result in the destruction of most organic contaminants to a sufficient level to allow the resulting material to be safely applied to land

as a soil amendment material or used in agriculture as fertilizer. The outcomes include environmental, economic and energy benefits based on other factors need to be considered for each farm to determine if it is a viable system.

Environmental benefits include:

- elimination of malodorous compounds,
- reduction of pathogens,
- deactivation of weed seeds,
- production of sanitized compost,
- reduction in GHGs emission,
- reduced dependence on inorganic fertilizers by capture and reuse of nutrients,
- promotion of carbon sequestration,
- beneficial reuse of recycled water,
- protection of groundwater and surface water resources, and
- improved social acceptance.

Anaerobic digestion is advantageous in terms of energy in the following manner:

- anaerobic digestion is a net energy-producing process,
- a biogas facility generates high-quality renewable fuel,
- surplus energy as electricity and heat is produced during anaerobic digestion of biomass,
- anaerobic digestion reduces reliance on energy imports,
- such a facility contributes to decentralized, distributed power systems, and

- biogas is a rich source of electricity, heat, and transportation fuel.

The economic benefits associated with a biomass-to-biogas facility are:

- transformation of waste liabilities into new profit centers,
- minimization of the time devoted to moving, handling and processing manure
anaerobic digestion adds value to negative value feedstock,
- source of income from the processing of waste (tipping fees), sale of organic
fertilizer, carbon credits and sale of power,
- reduction of water consumption,
- reduces dependence on energy imports, and
- increase in self-sufficiency.

1.1 Feedstock for anaerobic digestion plants

A wide range of feedstock is available for AD. In addition to municipal sludge waste (MSW), the industry sector produces a large quantity of waste in solid and liquid forms. Industries that produce waste include breweries, sugar mills, distilleries, food-processing industries, tanneries, and paper and pulp industries (Chen et. al, 1990). The food industry alone contributes nearly 40% of the total pollution contributed by industrial sub-sector (Dauge et. al, 1970). Food products and agro-based industries together contribute 65% to 70% of the total industrial wastewater in terms of organic load (EPA, 2005). Livestock wastes have the highest calorific value per ton in the agricultural sector (Gujer and Zehnder, 1983).

Most small-scale units such as tanneries, textile bleaching and dyeing, dairy, slaughterhouses cannot afford effluent treatment plants of their own because of economies of scale in pollution abatement (Meynell, 1996) and lack of regulations. The application of suitable technology helps small-scale units to recycle, recover, or re-use products from waste. Generation of energy using anaerobic digestion process is potentially economically attractive in some cases. Proper treatment of urban municipal waste both solid and liquid, agro-waste and biomass in different forms has tremendous potential for energy (EPA, 2005). Table 1.1 populates possible feedstocks for waste-to-energy plants based on anaerobic digestion of biomass (IPCC, 2007a, IPCC, 2007b).

Table 1.1: Possible feedstocks for waste-to-energy plants

Agricultural Origin	Industrial Origin	Municipal Origin
Livestock manure	Wastewater	Sewage sludge
Agricultural residues	Industrial sludge	Municipal solid waste
Animal mortalities	Industrial by-products	Food residuals
Energy crops	Slaughterhouse waste	
	Spent beverages	
	Bio-solids	

1.2 Anaerobic digestion of livestock manure

The livestock industry is an important contributor to the economy of many countries. Animal manure is a valuable source of nutrients and renewable energy. However, in many cases manure collected in lagoons or left to decompose in the open poses a significant environmental hazard. Manure emits air pollutants such as methane, nitrous

oxide, ammonia, hydrogen sulfide, volatile organic compounds and particulate matter that cause serious environmental concerns and health problems (Chen *et al.*, 1990).

Anaerobic digestion can benefit the animal agriculture sector by addressing multiple issues, related to renewable energy, water pollution, and air emissions. Anaerobic digestion of animal manure is gaining popularity as a means to protect the environment and to recycle materials efficiently back into the farming systems. Waste-to-Energy (WTE) plants using anaerobic digestion of biomass are efficient in harnessing the untapped renewable energy potential of organic waste. These plants convert the biodegradable fraction of the waste into high calorific gases (Semmler, 2002). Table 1.2 shows potential biogas yield from various animals.

Table 1.2: Potential biogas yield from various animals (Boe, 2006)

Animal	Biogas yield per ton of manure	
	ft ³ /ton/day	m ³ /tonnes/day
Dairy	920	27.6
Beef	1,148	34.5
Swine	741	22.2
Poultry	2,266	68.0

The number of anaerobic digestion systems used for livestock manure stabilization and energy production has accelerated substantially in the past several years. In 2010, 162 anaerobic digesters generated 453 million kWh of energy in the United States in agricultural operations, enough to power 25,000 average-sized homes (U.S. EPA, 2011). In Europe, anaerobic digesters are used to convert agricultural, industrial, and municipal

wastes into biogases that can be upgraded to 97 percent pure methane as a natural gas substitute or to generate electricity. Germany leads the European nations with 6,800 large-scale anaerobic digesters, followed by Austria with 551 (IEA Bioenergy Task, 2011). In developing countries, small-scale anaerobic digesters are used to meet the heating and cooking needs of individual rural communities. China has an estimated 8 million anaerobic digesters while Nepal has 50,000 (IEA Bioenergy, 2011).

In the past, the agricultural sector recovered and marketed livestock waste as a fertilizer or spread it onto agricultural land. The introduction of tighter environmental controls on odor and water pollution means that some form of waste management is necessary and becomes incentives for biomass-to-energy conversion.

1.3 Research motivation

Anaerobic digestion (AD) has become an increasingly important industrial process. AD is a green technology involving the generation of methane-rich biogas via the biological degradation of regionally available biomass like agricultural and municipal solid wastes and wastewaters (Magnusson and Alvfors, 2012). Design of anaerobic facilities requires addressing of individual characteristics of each animal waste. However, most wastes with high TS content, such as waste active sludge, animal manure, and agricultural residue, are only slowly degradable as a result of the particulate characteristics of the waste (Lafitte-Trouqué and Forster, 2002). Therefore, the applications of AD to these high-solid wastes are often limited. Commercial and scaled digesters such as plug flow digesters, complete mixed digesters, slurry digesters, covered lagoon digesters, up-flow sludge blanket reactors, and sequence batch reactors employ various design and mixing

configurations (Lusk, 1998). Among the types of farm-based digesters in operation, the failure rates for complete-mix and plug-flow technologies are staggering, 70% and 63%, respectively (Wilkie, 1995). For covered lagoon digesters, the failure rate is 22% (Lusk, 1998). In general, poor design, insufficient mixing, and an insufficient understanding of hydrodynamics attribute to such high failure rates.

Good mixing can provide a good contact between the active biomass and feed sludge, maximise the biogas production, prevent solid deposition, and minimise sludge short-circuiting (Kaparaju, 2009). Uniformity of the temperature and solids concentration can also be achieved with adequate mixing. Temperature and concentration uniformity is essential for the bacterial activity in digesters. In contrary, poor design and improper mixing often lead to poor mixing and digester failures due to the presence of dead zones. Therefore, the operational efficiency of anaerobic digesters ultimately depends on the hydrodynamics produced by mixing. (Bello-Mendoza and Sharratt, 1998; Casey 1986; Meynell, 1976; Parkin and Owen). Additional concerns associated with inefficient mixing are foaming and scum formation, and excessive solids deposition. Mixing also helps in evolution of biogas bubbles. In short, adequate mixing provides a uniform environment, one of the keys to improve digester performance.

Process models are supposed to describe the qualitative and quantitative aspects of microbial reactions, ranging from hydrodynamics and mass transfer to population dynamics in different reactor configurations under different environmental and operational conditions (Yu *et al.*, 2013). A review of the information in the literature on

the actual role of mixing in AD is contradictory. Most of the literature on anaerobic digestion for low and high solids applications emphasizes the importance of adequate mixing to improve the distribution of microorganisms throughout the digester (Chapman 1989; Lema *et al.* 1991; Parkin *et al.* 1986; Strenstrom *et al.* 1983). Several studies on low solid digesters dealing with municipal waste indicate that the lack of sufficient mixing as the main cause to the formation of floating layer of solids (Diaz and Trezek 1977; James *et al.* 1980; Strenstrom *et al.* 1983). These literature sources report that an increase to the mixing level prevents the formation of the solids layer. Chen *et al.* (1990) observed the development of a floating layer of solids in a 4.5 m³ non-mixed digester treating a mixture of refuse derived fuel and primary sludge. They compared the performance of a non-mixed (downward flow) and a continuously impeller mixed digester at mesophilic conditions (30 to 40°C). The methane yield from the non-mixed digester is higher than the methane yield from continuously mixed digester.

In AD, it is possible to mix slurry continuously or intermittently. Dague *et al.* (1970) studied the effect of shifting from continuous mixing to intermittent mixing (2 min of mixing/h) during an anaerobic treatment of a liquid municipal waste. The shift in mode of mixing resulted in significantly higher gas production. Mills (1979) recommends intermittent mixing in an anaerobic digestion of livestock waste under mesophilic temperature conditions. Hashimoto (1982) found higher biogas production from beef cattle wastes under both continuous mixing and in vacuum pressure conditions rather than under intermittent mixing and normal pressure conditions. In contrast, Ben-Hasson *et al.* (1985) observed 75% lower methane production rates from a continuously mixed

reactor than from an unmixed reactor when treating dairy cattle manure anaerobically. Whitmore *et al.* (1987) suggested that rapid mixing disrupts the structure of flocs in completely mixed reactors, thereby disturbing the syntrophic cross-feeding relationships between organisms.

Dolfing (1992) provides a similar argument within the context of high-rate treatment systems. Biofilms and granules represent ideal conditions for close physical associations between electron-producing and electron-consuming microorganisms (Dolfing, 1992). Appropriate spatial distribution of syntrophic bacteria and their methanogenic partners allow high hydrogen fluxes at relatively low hydrogen concentrations by minimizing the development of electron gradients. In vigorously mixed systems, spatial associations are continuously disrupted leading to a state of instability in the system. The results observed by Stroot *et al.* (2001) suggest that vigorous and continuous mixing have a negative effect on the performance of high solids AD. Application of minimal mixing distributes feed adequately and allows the formation of new spatial associations. Therefore, minimal mixing improves high solids anaerobic digestion by providing a quiescent environment for bacteria.

The contradictory mixing findings reported in the literature indicate the need to conduct systematic performances and hydrodynamics investigation of mixed anaerobic digestion process using various parameters of digesters. Lack of proper quantification and characterization of how slurry mixes in AD is the main reason for the controversies and uncertainties about the effect of mixing. Quantification of the shear stresses produced

may be required. In addition, there is a lack of verified and calibrated mathematical models describing the mixing and anaerobic digestion process of animal manure in mixed AD. Development of such model contributes to an effective, efficient and economical method to design and control digestion systems.

Number of factors affect the performance and efficiency of AD, such as temperature, pH, feed characteristics, feed rate and feeding mode, toxicity, and mixing in the digester. Favourable conditions for the following factors maximize chances for achieving optimum design and efficient operation:

1. Optimum retention time
2. Adequate mixing (bacteria-substrate contact)
3. Proper pH
4. Proper temperature control
5. Adequate concentration of proper nutrients
6. Absence (or assimilation) of toxic materials
7. Proper feed characteristics.

Factors one to five directly relate to mixing in an AD.

1.4 Research objectives, procedures and outcomes

The main objective of this research is to better quantify mechanical mixing in AD system. In addition, it is the aim of this study to model the biological and physical

processes taking place in mixed AD using a mathematical model to investigate what if scenarios.

These objectives are achieved by employing experimental and numerical methods, which consists of:

- Understand and provide insight into flow mixing occurring in stirred AD by investigating the flow field generated by known impeller designs in scale-down transparent digesters filled with manure simulant solutions to model non-Newtonian behavior. Experimental techniques required for this application are conductivity, acid-base reaction flow visualization, and particle image velocimetry (PIV) flow measurement method.
- Develop, evaluate and validate the computational fluid dynamics (CFD) models and closures to model and simulate the hydrodynamics and mixing of the AD using a commercial modelling package Fluent[®].
- Predict flow variables and mixing characteristics using the computational fluid model that are unattainable with the experimental technique, investigate various designs and operating conditions, as well as configurations that can enhance mixing, phase distribution, and reduction or elimination of the inactive volume in mechanically mixed AD.
- Investigate the effect of mixing duration and intensity on the performance of anaerobic digestion process using both lab-scaled and pilot scaled digesters.

Implementation of results from the planned studies will improve the design and manufacturing of mixing system for AD to help avoid digester failures, improve the performance of anaerobic digestion systems and increase utilization of anaerobic technology on farms. The study provides a detailed and thorough analysis of manure flow physics, the biological and physical processes present within mechanically mixed AD, producing the following contributions:

Experimental:

1. Measurement of flow, mixing times in Newtonian and non-Newtonian fluids using manure simulant fluids at two scales using impellers common in the AD industry,
 - i) Correlation of data and formation of rules for mixing system design
 - ii) Determination of the characteristic shear rate to estimate viscosity, correlation of the mixing time data to explain the effect of non-Newtonian behaviour of manure on the mixing process in AD
 - iii) Determination of the velocity distribution, pumping rate, power, power number, and pumping number at different conditions
2. Characterization of unmixed regions that exist in an AD, the rate and means of destruction of unmixed regions in AD that provide knowledge for designing mechanically stirred digesters operating at low Reynolds numbers handling high concentration slurries
3. Investigation of effect of mixing duration and intensities on anaerobic digestion process using lab-scaled and pilot-scale anaerobic digester

Numerical:

1. Detailed investigation of laminar flow and the associated pumping breakdown within an AD operating with high TS manure:
 - i) Determination of physical mechanism responsible for the change in flow pattern from pumping to stall at very low Re
 - ii) Explicit investigation of the near impeller forces on the fluid particle
2. Detailed investigation of transitional flow within AD digesting low to medium TS manure:
 - i) Investigation of the near impeller mean flow forces on the fluid particle
 - ii) Investigation of near-impeller flow dynamics including initiation and propagation of the impeller-trailing vortex
 - iii) Formulation and utilization of a Reynolds stress parameter to quantify turbulence
3. Understand the detail hydrodynamic of turbulent flow in AD digesting low TS manure:
 - i) Effect of different geometrical conditions on mixing process in anaerobic digester (E.g. $H/T < 1$, free surface etc.) for single phase condition
 - ii) Determination of effects of digester height, impeller submergence, impeller off-bottom distances, impeller diameters and agitation speeds on achieving adequate mixing objectives in a two phase AD (solid and liquid)

1.5 Outline of thesis

Chapter 2 presents an overview of previous work on related topics that provide the necessary background for the purpose of this research. The literature review concentrates on experimental and numerical works that are related to mixing in anaerobic digester and anaerobic digester process as whole to define the research objectives.

Chapter 3 deals with the experimental set up, procedures and findings of the conductivity technique used to determine the macromixing characteristics of different impellers. This technique employs a probe that measures the conductance of salt solution as a function of time that can be converted to a concentration versus time scale using calibration of the conductivity device.

Chapter 4 deals with acid-base visualization method to investigate unmixed regions in mixed digesters and find ways of increasing the mixing efficiency of manure by modulating the impeller speed. Direct visualization of an acid-base neutralisation reaction coupled with image analysis is used to observe the flow patterns in scaled digester during various modes of mixing at low Re . Direct visualization of an acid-base neutralization reaction with fluorescent dye helps to measure the mixing time, the volume of unmixed flow elements and well-mixed flow elements by carrying out image analysis.

Chapter 5 concerns on development of a CFD model of mixed digester and evaluation using experimentally obtained data to see the model capabilities and limitations to

predict the effect of geometrical and rheological properties. From the computational model information on mixing variables including unmixed zones, three dimensional flow structures, dead zone size and shape are extracted.

Chapter 6 deals with turbulent flow with the focus in understanding the detail hydrodynamic changes that occur when H/T is decreased and effects of operational parameters that contribute to achieve adequate mixing both in a single liquid phase and in solid-liquid suspensions.

Chapter 7 reports the experimental set up, procedure and results concerning the investigation of effect of mixing with emphasis on mixing durations and intensities on anaerobic digester performance both on lab-scale and pilot scaled anaerobic digesters.

Chapter 8 summarizes the results obtained from this research, conclusions drawn from them and their significance and contributions to the community of anaerobic digester mixing system designers and operators.

1.6 Publications

Journal papers

Balcha D. and Bibeau E.L., “Formation and degeneration of segregated mixed regions in anaerobic digester”, Manuscript accepted by *Journal of Non-Newtonian Fluids Mechanics*.

Balcha D.A. and Bibeau E.L. “Effect of an off-centre shaft on mixing in a lab-scaled anaerobic digester,” Manuscript submitted to *The Int. Journal of Computational Multiphase Flows*.

Conference papers

Balcha D. A., Bibeau E.L., A. Kumar, “Parameters affecting viscosity of simulated manure power-law fluid,” CSME International Congress 2012, Winnipeg, MB, June 4-6, 2012.

Balcha D. and Bibeau E., “Modelling anaerobic digester to study the effect of organic loading rate change on apparent kinetic parameters,” ICABE 2013: International Conference on Agricultural and Biosystems Engineering, Toronto, Canada, June 20-21, 2013.

Balcha D.A., Bibeau E.L. and K. Anurag, “Response of lab-scale anaerobic digester to dynamic load, ICBEE 2013 5th International Conference on Chemical, Biological and Environmental Engineering, New Delhi, India, September 14-15, 2013.

Poster presentation

Balcha D. A. and Bibeau E.L., “Numerical modelling of flow in anaerobic digester,” Canadian Society for Biological Engineering, Winnipeg, Manitoba, Canada July 10-13, 2011.

Balcha D. A. Kumar A. and Bibeau E.L., “Mathematical modelling of an anaerobic digester to analyse a swine digestion process,” RENERGY 2013 Conference and Expo Chennai, India, May 9-11, 2013.

Technical Report

Kumar, A., Bibeau, E.L. and Balcha, D.A., “Effect of impeller type and mixing intensity on residence time distribution in anaerobic digester,” University of Manitoba, Report for MITACS GLOBALINK, 2011.

An additional 2 Journal papers are in preparation.

2. Summary of literature review

Proper understanding of the theory of AD is important to improve mixing of digesters. Of importance is to build upon the body of scientific knowledge summarized in Sections 2.1 to 2.4 to support the experimental and simulation work for the investigation of effect of mixing on AD. The details of the literature review for these sections are presented in Appendices A to D, respectively.

- 2.1 - *The microbial stages of AD*: It is important to review the 4 stages of how biomass is converted into methane and isolate where improper mixing contributes to a reduction of performance of AD (see Appendix A).
- 2.2 - *Non-Newtonian flow*: Rheological properties of manure are complex and dependent on numerous factors. Manure apart from mineral constituents also contains a substantial part of organic substances with majority of microorganisms. It has a range of properties that affect the flow behavior (see Appendix B).
- 2.3 - *CFD and experiments on mixing*: Decisions on mixing design phases of AD affect the performance of the process. In this sense, CFD technique is a promising tool for designers to optimize hydraulic behavior of digesters. Thus, to have a computational model that allows the internal analysis of the flow in AD is of imperative for the analysis of the behavior and detection of possible flow deficiencies. Design optimization based on calibrated mixing models using experimental data becomes an ideal tool to determine best solutions to understand mixing in AD. The CFD model development for

mixing and simulation methods are considered with experimental approaches of obtaining data to validate these models (see Appendix C).

2.4 - *AD models*: One of the major problems associated with mixed anaerobic digestion process is its poor record with respect to process stability. AD dynamic modeling and simulation are useful tools for investigating process stability and serves as an additional tool to quantify operation and improve design. Therefore, examination of important mathematical equations and the methods to construct the model are covered (see Appendix D).

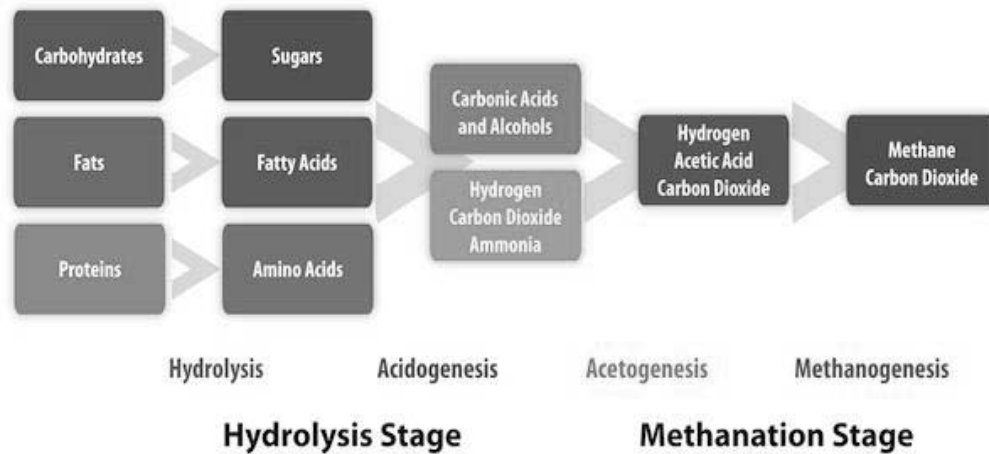
2.1 Anaerobic digestion process

Anaerobic digestion process technologies, intended initially for food wastes has been developed and applied over many centuries (Batstone *et al.*, 2002a). Application of AD for treatment of organic waste and biogas production is an environmentally attractive technology. The environmental benefits associated with the use of anaerobic digestion technology are waste treatment, pollution reduction, production of CO₂-neutral renewable energy and improvement of agricultural practices by recycling of plant nutrients (Boe, 2006).

The microbiology of anaerobic degradation of organic matter into methane and by-products is a complex multi-step process. These multi-step processes include the metabolic interactions performed by a well-organized community of microbial populations. Varieties of microorganisms coexist in AD even when utilizing a single substrate. The activity of these microorganisms is necessary for the complete bioconversion of organic materials to methane, carbon dioxide as well as trace gases

such as hydrogen sulphide and hydrogen (Lee *et al.*, 2009). Hence, microbial status and suitable operating conditions are crucial conditions in maintaining a healthy bacterial population (Björnsson, 2000).

Table 2.1: Main steps and pathways of anaerobic digestion (modified from Batstone *et al.*, 2002a)



Understanding each phase of digestion is required to elucidate the impact of improper mixing conditions on the performance of anaerobic digestion.

Anaerobic digestion depends on coordination of three trophic groups of microorganisms.

Areas where microbial process issues relate to mixing includes:

- The rate-determining step, which is often hydrolysis, depends on digester conditions: carbon substrates, temperature, pH, etc. and gradients in these parameters impacts digestion rates and pathways (Szalai *et al.* 2004; Stroot *et al.* 2001; Schink, 1997).
- The optimum pH of acidogenic bacteria is 5.2 to 6.5, and the specific growth rate is approximately 2 days. Acetogenic bacteria grow slowly, with a minimum

doubling time of 3.6 days. Methanogenic bacteria, the group of anaerobes most sensitive to environmental stresses, grow more slowly than acidogenic bacteria, at a rate similar to acetogens. The optimum pH environment for methanogens is 7.5-8.5. Proper mixing affects these steps (Rulkens *et al.*, 2005; Parkin and Owen 1986)

- AD operate in fed-batch or batch mode. If the added feed concentration is not kept uniform throughout the digester volume, then fast growing acidogenic bacteria will produce acids at a higher rate than the rate at which acids consumed by acetogenic or methanogenic bacteria. Increasing acids concentration lowers the pH, killing the methanogenic activity and pushing the digester towards failure. Thus, fast and uniform distribution of feed is required through proper mixing and help in exposing larger surface area of the substrate to biological attack as result of breaking of the substrate particles (Maingonnat *et al.*, 2005; Lusk, 1998).
- Spatial organization of populations is important, especially syntrophic acetogenic bacteria and archaea for interspecies metabolite transfer. Mixing impacts the spatial distributions of populations (Dolfing and Harrison, 1992; Lee *et al.*, 2009).

2.2 Non-Newtonian fluids

Rheology is a property of a fluid characterized by its flow curve that describes relationship between shear stress and shear rate and impacts digester mixing. The ratio of shear stress to shear rate is the fluid apparent viscosity. Linear flow curve that passes through the origin characterizes a Newtonian fluid as shown in Figure 2.3. The viscosity

of such a fluid is constant and independent of shear rate. Examples of Newtonian behaviour include water, milk, and sugar solutions (Holdsworth, 1993). A flow curve that is non-linear or/and does not pass through the origin represents non-Newtonian fluids. The apparent viscosity of such a fluid depends on the shear rate and is variable in shear flow. For some complex non-Newtonian fluids, the apparent viscosity depends also on the duration of shearing and the kinematic history of the fluid. Therefore, these more complex fluids are time dependent.

Non-Newtonian flow can impede mixing and requires proper understanding. Areas where mixing is affected by the rheology of manure in AD includes:

- During anaerobic digestion, processes occur in which organic matter yields mainly methane and carbon dioxide. Solids in the sludge decrease especially those of organic matter. Mixing changes the rheological properties of fermenting sludge.
- The retention time of the substrate in the digester and the degree of contact between the incoming substrate and the viable bacterial population affects performance of AD. These parameters are primarily a function of the hydraulic regime in the digesters. Mixing affects the hydraulic regime that is a function of the rheological behaviour of sludge and thus impacted by non-Newtonian flow effects.
- High viscosity prevents the development of unfavourable environments to methanogenic population (e.g. regions of low pH) and creates a non-uniform

temperature in the digester. The extent of variation of pH and temperature throughout the digester depends on mixing.

- Manure in AD has complex rheological properties, which can increase operating costs. Due to a close relation of the viscosity to torque on the impeller in the mixing digester, the variation in viscosity reflects in torque changes. If the viscosity increases too much, torque increases over the limit, which can lead to motor overloads.
- In mixed AD, the rheological properties of the fluid manure impact digester configuration. The viscosity influences the formation of the flow field inside the digester and, therefore, the mixing and power behavior. Thus, the viscosity is the most important characteristic value. While a constant viscosity characterizes Newtonian fluids, the processing of non-Newtonian materials demands the consideration of a changing viscosity through a viscosity function. For the configuration of agitators for the processing of non-Newtonian materials such as manure, the changing viscosity needs consideration where the Reynolds number is the decisive characteristic value. Of importance is the effect on the hydraulic retention time.

2.3 Experimental and numerical studies in mixing

The importance of mixing in achieving an efficient substrate conversion has been reported in the literature (Casey, 1986; Lee *et al.*, 1995; Smith *et al.*, 1996). However, there is no consistent information in the literature on the mixing intensity required to achieve efficient substrate conversion. Thus, more studies are required on digester

mixing to determine the optimum mixing intensity. Degree of mixing is closely related to the hydrodynamics inside digester. Therefore, it is important to understand the sludge mixing characteristics for each mixing mode used in digesters and thus improve digester efficiency.

The literature review indicates deficiencies in the form of detailed investigation of the near-impeller and outer-tank region in the case of turbulent flow (experimental or computational simulation) and comprehensive treatment of the TKE transport equation along with elucidation of the relevant transport mechanisms in the inner-impeller and outer impeller region, in particular investigation of the pressure diffusion/work mechanism. In addition, a detailed investigation of the impeller trailing vortex flow dynamics i.e. inception/formation and near impeller flow dynamics is also lacking.

Advances in laser technology, image capture, computer-aided image processing, and nuclear magnetic resonance spectroscopy (NMR) methods have increased the versatility and dynamic range of particle imaging and NMR imaging techniques. Hot Wire Anemometry (HWA), Laser Doppler Anemometry (LDA), and Particle Image Velocimetry (PIV) are currently the most commonly used and commercially available diagnostic techniques to measure fluid flow velocity. The great majority of the HWA systems in use employ the Constant Temperature Anemometry (CTA) implementation. The point measurement techniques of CTA and LDA can offer good spatial and temporal response. This makes them ideal for measurements of both time-independent flow statistics, such as moments of velocity (mean, rms, etc.) and time dependent flow

statistics such as flow spectra and correlation functions at a point. Although rakes of these sensors can be built, multi-point measurements are limited mainly due to cost.

LDV will provide highly spatial and temporal resolved point wise measurements of velocity, but is relatively expensive to implement. Homodyne light scattering spectroscopy can provide direct, point wise velocity gradient data provided the flow is repeatable, but requires independent information about the flow direction and is technically challenging to implement. PIV is a versatile tool for obtaining velocity fields in flows that uses seeding of small particles. This technique measures the displacement of tracer particles added to the fluid to obtain instantaneous velocity fields. On the other hand, a three dimensional representation of the steady-state flow is created using computational fluid dynamics. The primary strength of the PIV technique is its ability to measure flow velocity at many locations simultaneously, making it a unique diagnostic tool to measure three dimensional flow structures, and transient phenomenon. It is the choice of this study for the following advantages:

- Negligible distortion of the fluid flow
- Avoids the need for intrusive flow measurement probes
- Capable of measuring an entire two-dimensional cross section (geometry) of the flow field simultaneously
- Allows the generation of large numbers of image pairs that are analyzed in real or later time. Thus, it is possible to gain near continuous information.

- High degree of accuracy, since each vector is the statistical average for many particles within a particular tile, accuracy goes down to 10% of one pixel on the image plane.

The computational model solves the mass and momentum balance equations applied to the mixing domain to give information on pressures, velocities and related properties.

2.4 Anaerobic digestion modeling

In the past, there are several approaches used to model anaerobic digestion process. Each of these models has advantages and disadvantages. Their applicability is limited by time, expertise on the knowledge of the process structure, and available data. The models developed are generally applicable for specific cases. Black box type models do not explain the processes and lack the robustness to model the complex digestion process. The development of generic dynamic models based on the process dynamics and application as well as the extension of the models for different cases, such as different digester types, environmental conditions, and organic waste types for AD is important.

The ADM1 model (Batstone *et al.*, 2002) assumes all extracellular processes follow the first-order kinetics. The first-order kinetics equations that are dependent on the microbial concentration describe cellular decay processes. Monod type kinetics expresses the substrate utilization in terms of substrate consumption and not microbial growth, with the aim of simplifying the implementation of the inhibition functions. In addition to pH inhibition for all the bacterial groups, hydrogen inhibition for the acetogenic bacteria and free ammonia inhibition for the acetoclastic methanogens are also included in the model.

The chemical-physical processes are important in modeling the anaerobic systems as they express the inhibiting factors for the biological reactions and quantify some variable parameters such as gas flow rate, alkalinity, and pH. The gas phase in this model contains carbon dioxide, methane, and hydrogen. Henry's law describes the gas-liquid equilibrium for the diluted liquid phase. Carbon dioxide and ammonia are acids and bases present in the free form.

The information available for modeling of anaerobic microorganisms degrading complex substrates such as manure sludge has large gaps regarding reliable kinetic and stoichiometric parameters required for accurate modeling. None of the models available incorporates all of the important phenomena identified in anaerobic treatment. Within our own research group, there is an ongoing research to develop an Anaerobic Digestion Model with Multi-Dimensional Architecture (ADM-MDA), a spatially resolved numerical model for AD at any scale (Gaden, 2010) by extending ADM1. ADM-MDA is a general, spatially resolved AD model that incorporates both fluid flow and biochemistry. It uses ADM1 for the biochemistry and computational fluid dynamics for the flow. Available literature shows that exploration of the biological process assumes that the uniform distribution of physical parameters throughout the whole digester, even though it is well established that spatial variation in the physical environment affects the growth of anaerobic bacteria. On the other hand, there are limited attempts to link the internal flow behavior to the microbial kinetics. Therefore, developing a computational fluid dynamic (CFD) based simulation platform for solving the physical processes and

integrate them to ADM1 based model of the biological processes in AD is important and will be one of the contributions of this study.

3. Experiments on viscosity, mixing time, power and suspension using lab-scale AD

The literature review revealed that there is lack of detailed investigation carried out to measure manure (non-Newtonian) mixing times and no correlation exists which can be used to predict mixing times in mixed AD handling manure. In addition, there is lack of consistent method for determination of shear rate and viscosities in mixed digesters in which the mixing time prediction performed. For these reasons, this Chapter deals with the experimental investigation of mixing time and power in lab-scaled AD with the following contributions:

- Measure mixing times in Newtonian (low TS) and non-Newtonian fluids (high TS) for two scaled AD using three different types of impellers that are common in AD industry, correlate the data and provide rules for their design,
- determine the characteristic shear rate in a digester in which mixing takes place in order to estimate a viscosity which can be used to correlate the mixing time data,
- use the correlation to explain the effect of non-Newtonian behavior of manure on the mixing process in AD and, determine which impeller types are best suited to the mixing of manure in AD, and
- compare the energy efficiency in suspending solids for various designs and operational conditions.

In order to achieve these, as mentioned in Chapter 2, the method used for measurement of mixing times is the conductivity technique that relies on the detection of changes in conductivity in different parts of the digester after addition of electrolytic tracer on to the surface of the fluid. PIV technique allows determining the flow fields in lab-scale AD.

This Chapter starts with Section 3.1 that introduces and details the laboratory scale experimental set-up with the corresponding measurement techniques. Section 3.2 describes the methodology applied to conduct viscosity, mixing time and power measurements followed by Section 3.3 with reports of results with their corresponding discussions. Finally, Section 3.4 provides the conclusions drawn from the investigation performed.

3.1 Laboratory scale experimental set up

The laboratory scale digesters are reconfigurable where the following aspects can be varied depending on mixing experiments:

- Reactor geometry
- Free-surface versus open surface
- Mixing impeller
- Newtonian and non-Newtonian flow
- Baffles
- Flow rates and flow injection ports

The mixing time measurement uses two geometrically similar lab-scale digesters with diameters, T , where $T = 0.25$ and 0.50 m. The digesters have a flat base and four baffles that are equally spaced around the circumference of the digester. The baffles are $T/12$ wide and $T/60$ off the digesters wall. The construction of both lab-scale digesters uses Plexiglas to allow observation of the mixing process in the digester. In both cases, the fluid depth, H , is equal to the digester diameter, T . Figure 3.1 shows experimental arrangement of the lab-scale digester used for the experiment.

A centrally placed shaft of diameter: 1.27 cm coupled to an inline torque transducer that in turn connects to a variable-speed motor (Model CG-2033-1) serves to mount the impeller. The motor equipped with a controller and mounted on a separate framework allows the adjustment of the agitation speed in the range 0-1,000 rpm measuring the rotational speed within ± 1 rpm using an rpm-meter. A separate framework and carefully selected couplings provide means to mount the transducer on shaft with minimum wobbling of the impeller shaft and reduce the effect of vibration on the measurements of torque. This arrangement prevents the introduction of friction sources in the torque measurement, as reported in other systems (Chapple *et al.*, 2002). A traversing system supporting the motor allows changing the vertical position of the digester with respect to the impeller in order to vary the impeller clearance off the digester-bottom, C_b , measured from bottom of the impeller to the bottom of the digester.

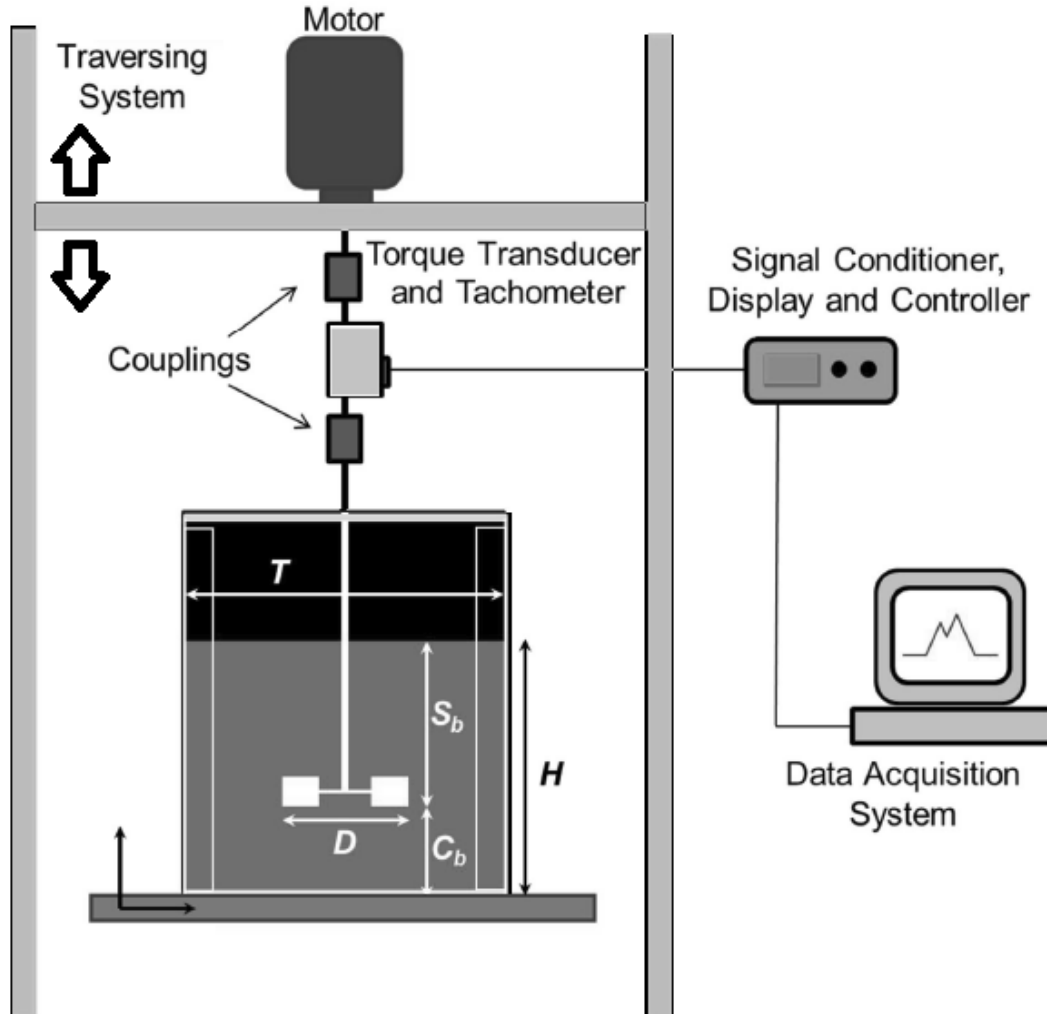


Figure 3.1: Experimental lab-scale digester arrangements (T = Digester diameter, D = Impeller of diameter, C_b = Off-bottom clearance, S_b = Impeller submergence)

Most of the literatures available on mixing of fluids concentrate on the performance of Rushton turbines and marine propellers. However, these two impellers are not the only ones widely used these days to perform mixing in AD. Therefore, this work uses the following impeller types to better represent commercial impellers:

- i) **PBT**: Pitched blade turbines of $T/2$ and $T/3$ diameter ($T/2$ PBT and $T/3$ PBT)
- ii) **RT**: Rushton turbine (i.e. with vertical blades) of $T/3$ diameter ($T/3$ RT)

iii) **A310:** Hydrofoil Lightnin A310 of T/2 diameter (A310)

The geometrical ratios are constant in scale-up. Table 3.1 shows the full dimensions of each impeller used in the experimental work, and Figure 3.2 shows pictures of these impellers.

Table 3.1: Test matrices for mixing time and power investigation with impeller dimensions

Impeller Type	Scale T(m)	Nominal Diameter	Impeller Diameter D (m)	Blade Angle to horizontal (deg)	Blade width w (m)	Fluids tested
PBT	0.25	T/3	0.083	45	0.020	Newtonian & Pseudoplastic
PBT	0.50	T/3	0.167	45	0.040	Newtonian & Pseudoplastic
PBT	0.25	T/2	0.115	45	0.020	Newtonian & Pseudoplastic
PBT	0.50	T/2	0.25	45	0.040	Newtonian & Pseudoplastic
PBT	0.25	T/3	0.083	90	0.020	Pseudoplastic
RT	0.50	T/3	0.167	90	0.040	Newtonian & Pseudoplastic
A310	0.50	T/2	0.250	-	-	Newtonian & Pseudoplastic

The positions of the center lines of impellers are T/2 and T/3 above the base of the digester. The rotation of all impellers is clockwise when viewed from the top of the digester. The pitched blade turbines and hydrofoil impellers pump fluid downwards.

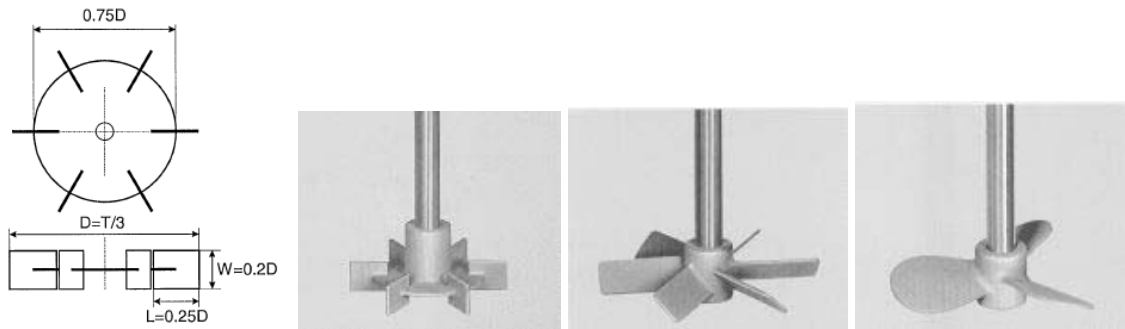


Figure 3.2: Schematic diagram of a typical impeller with the dimension (a) and impellers under investigation with Rushton turbine (RT), Pitched blade turbine (PBT) and Lingham A310 (A310) left to right.

The method used for measurement of mixing times is the conductivity technique presented in Chapter 2. Conductivity measurement method detects the changes in conductivity in different parts of the digesters after addition of electrolytic tracer on to the surface of the fluid. The conductivity changes in different regions of the digester. The conductivity probes measures changes of mixing intensities at different locations within the digester. An amplifier increases the analogue signal from the conductivity probe before analogue to digital conversion.

The design described by Khang and Fitzgerald (1975) forms the basis of the construction of the conductivity probe. The design requires embedding pieces of platinum wire soldered onto a screened signal lead in a bullet of epoxy resin 6 mm in diameter and 30 mm long, as shown in Figure 3.3. The outer electrode coils around the probe tip in the shape of a cone. It acts as an earth for the measuring electrode and as a screen to prevent interference from other electrodes or earthed objects in the digester. Coating the probes in platinum black makes their surfaces inert.

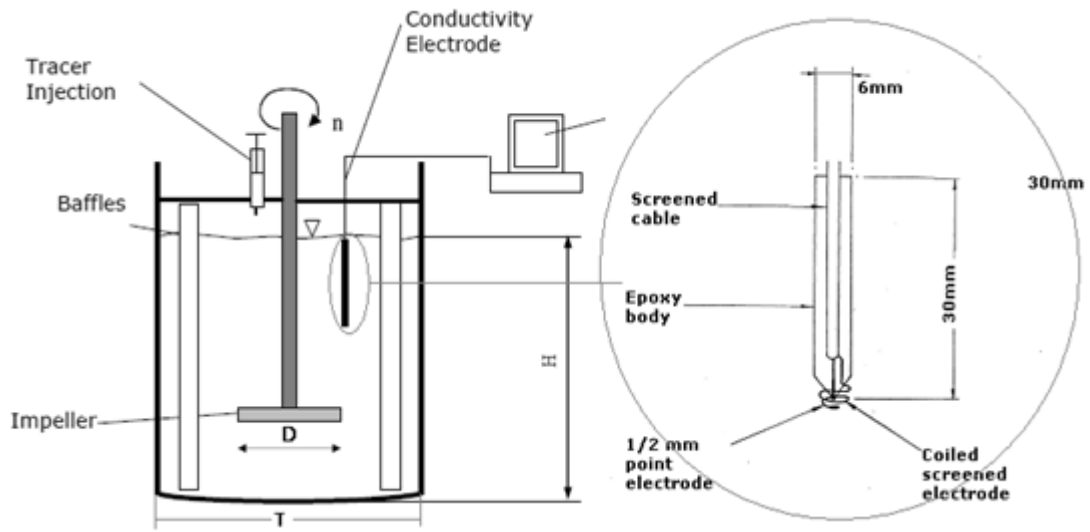


Figure 3.3: Experimental set up and conductivity probe detail (T = Digester diameter, D = Impeller of diameter)

It is important to keep the probes' measuring volume as small as practically possible to minimize its effect when measuring conductivity as their presence in the digester affects local mixing. Reducing the size of probes reduces probes interference. In addition, attaching the probe supports to the baffles reduces the interference of probe supports with the flow of fluid in the digester. The three positions of the conductivity probes in regions of differing mixing intensities shown in Figure 3.4 are:

- i) Probe 1: positioned beneath the impeller and near the blade tips in the region of highest mixing intensity
- ii) Probe 2: positioned halfway between the shaft and the digester wall
- iii) Probe 3: positioned behind a baffle in the region of lowest mixing intensity

Table 3.2 summarizes the specific positions of probes with respect to digester dimensions. Same positions used during scale-up.

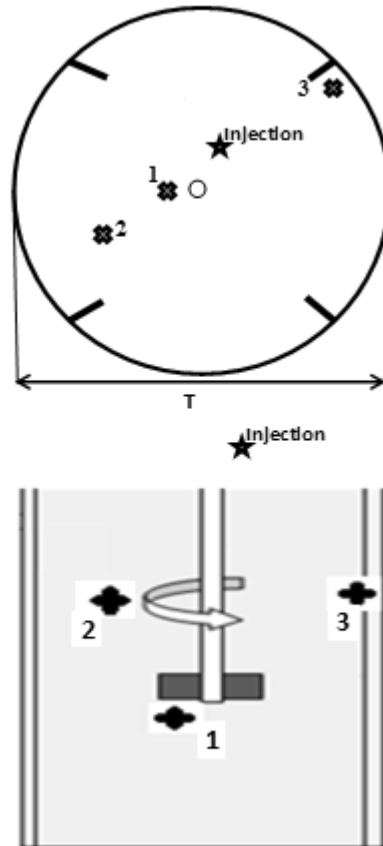


Figure 3.4: Positions of probes and injection position in the lab-scaled mechanically mixed digester (Injection $T/10$ from shaft axis, Probe 1 $T/8$)

Table 3.2: Conductivity probe positions

Injection	25 mm above fluid surface, $T/10$ from shaft axis
Probe 1	$T/50$ below bottom of impeller, $T/8$ from shaft axis
Probe 2	$T/4.5$ below fluid surface, $T/4.7$ from shaft axis
Probe 3	$T/3$ below fluid surface, $T/2.2$ from shaft axis, adjacent to baffle

AD is completely closed and therefore it is difficult to evaluate the intensity and type of movement induced by the impeller in a full-scale system. Due to the inherent opacity of sludge, it is not possible to visualize the mixing and flow patterns inside an AD. Therefore, choosing an appropriate transparent model fluid that can mimic the rheological behavior of manure is imperative for visualization of the hydrodynamic functioning of an AD. Hence, candidate transparent fluid model materials to mimic manure behavior are rheologically characterized. The parameters that affect the rheology of manure simulant fluid are investigated.

The study uses two types of test fluids representing a Newtonian rheology and a non-Newtonian (pseudo-plastic) rheology similar to manure in an AD. Selection of proper test fluids requires careful consideration. The evaluation process assesses potential fluids for the experimental investigation throughout this study based on the following factors:

- i) Transparency: Flow visualization is an important facet of the experimental investigation so it is important to find a clear fluid that allows observing all regions of the digester during experiments.
- ii) Foaming: The fluid surface draws air and forms small, stable bubbles reducing the mean density of the fluid and affecting the power consumption of the agitator. The presence of bubbles affects the performance of the conductivity probes causing large fluctuations in the signal as bubbles pass between the probe electrodes. A foam stabilizer may be required.
- iii) Salt solubility: Measurement of mixing times using conductivity technique involves the addition of a small volume of tracer with a high conductivity

tracer to measure the conductivity fluctuations in the digester. Therefore, it is important for the selected fluid to be able to dissolve an electrolyte without altering its rheology.

- iv) Cost: It is important to find a relatively low cost fluid.
- v) Disposal: Since the laboratory does not have facilities to handle large quantities of hazardous chemicals and means to dispose the used materials, this aspect needs considerations.

After careful assessment of several fluids, results show that Glycerol is the most appropriate fluid to represent Newtonian fluids for this study. In addition to satisfactorily meeting the above stated criteria, Glycerol has a quality of dissolving electrolytes readily.

For non-Newtonian fluid, many literature sources report the use of Xanthan gum and Carboxymethyl Cellulose (CMC) solutions to study the mixing of non-Newtonian, pseudo-plastic fluids. Among wide range of Cellulose-based polymers available on the market, we decided to use a grade of Hydroxyethyl Cellulose, Natrosol hydroxyethyl cellulose (HEC). HEC fulfills all criteria set out for assessing test fluids. This non-ionic, water-soluble polymer is a white, free-flowing granular powder. It is a product of reactions between ethylene oxide and alkali-cellulose under rigidly controlled conditions. HEC easily dissolves in cold or hot water to give clear solutions of varying viscosities. Solutions of HEC are pseudoplastic or shear thinning mimicking manure slurries. Randa (2001) used HEC previously for mixing tests.

A test is conducted to verify to what extent the assumption of HEC represents the characteristics of manure. For this purpose, sample of manure with different %TS from a hog operation at a 3,200 head grower/finisher farm located near Niverville, Manitoba is used to confirm the suitability of HEC solutions to mimic manure in AD. Figure 3.5 shows sample comparison of apparent viscosities of sampled manure with TS% 4, 6 and 8 against 0.15, 0.50 and 0.72 wt.% HEC solutions. The temperature for the HEC solution was kept at 20°C (room temperature) while the temperature for the manure is set to be 37°C to avoid the need to heat HEC solution for subsequent tests. Similar comparisons has been done by Langer (2009) to extensively examine the application of such solution to study manure rheology.

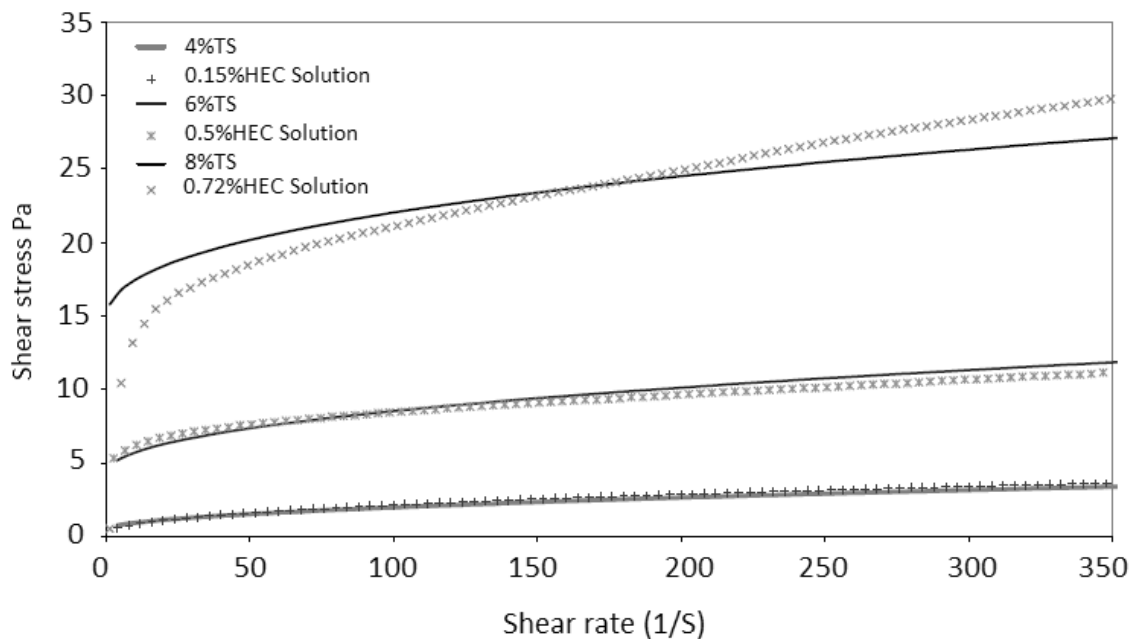


Figure 3.5: Sample comparison of manure with manure simulant HEC solutions

The tracer used for Newtonian mixing time measurements requires adding concentrated nitric acid to the HEC solution. It is important to make sure that the viscosity of the tracer is the same as the viscosity of the bulk fluid in the digester.

Table 3.3: Power law constants and indices of pseudo-plastic fluids used for mixing time measurement experiment

Concentration	Constant m [Pa.s ⁿ]	Index n (-)
0.25	0.014	0.88
0.50	0.068	0.86
0.75	0.258	0.79
0.25	0.092	0.80
0.50	1.180	0.55

The concentration of nitric acid in the tracer is 4.8 moles/liter. The viscosity is within ± 5 cP of the viscosity of the fluid in the digester. Addition of more glycerol or water adjusts the viscosity of the tracer used for the experiment. A regular verification of the viscosity ensures the viscosity is within the acceptable limits during the experiment.

The tracer used for the non-Newtonian mixing time measurements uses a saturated solution made of a small volume of fluid from the digester and sufficient salt of sodium chloride. After mixing, the undissolved salt settles at the bottom of the container and the clear fluid on the surface is returned to the digester. Viscosity tests use a coaxial cylinder viscometer. The measuring system conforms to the DIN 53019 standard. Table 3.3 shows the power law constants and indices of each of the HEC solutions used in the measurements of mixing times.

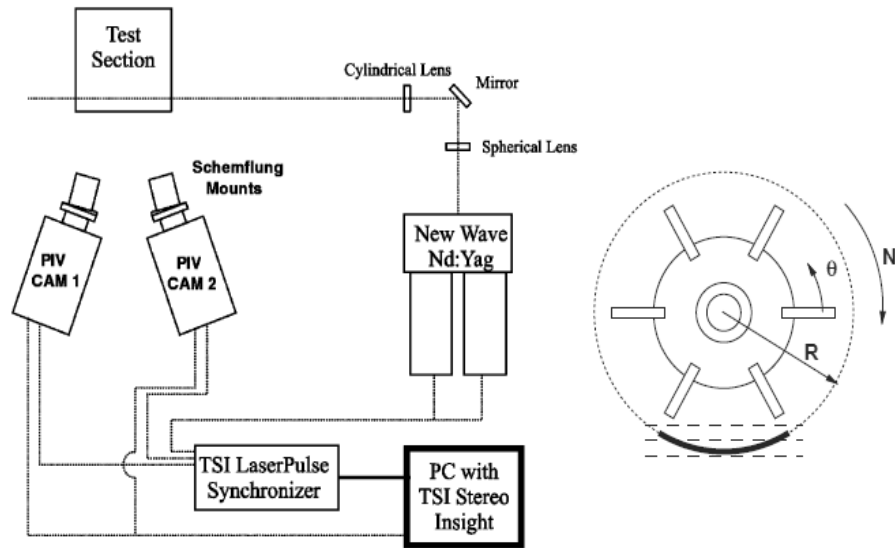
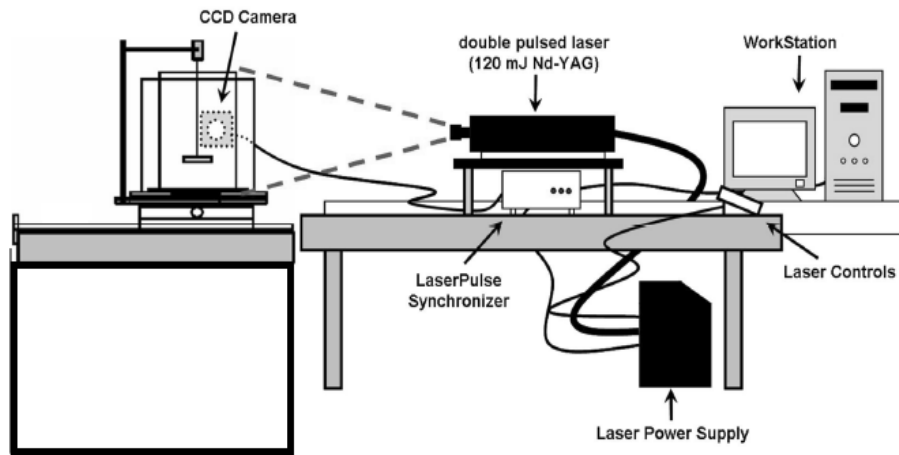


Figure 3.6: Experimental set up for the flow field measurement using PIV

The flow field measurement uses a 2D-PIV system from Dantec Dynamics Inc. and when there is a demand for a three-dimensional velocity measurement, single-PIV with only two-dimensional information is extended to stereo-PIV by introducing a second camera. The out-of-plane velocity component can be obtained by placing two cameras at different viewing angles, which causes a displacement in 2D images that can be interpreted into the third component velocity (Yianneskis, 2007). Figure 3.6 presents the

basic components of the experimental setup. The seeding in the transparent lab-scaled digester uses tracer particles PMMA-Rhodamine B particles with a size distribution of 20 to 50 μm and density of 1.19 g/cm³. The external cavity of the digester is filled with water and its purpose is to correct the optical distortion created by the curved surface of the cylindrical vessel.

3.2 Methodology

3.2.1 Viscosities measurement

Preparation of the test samples requires dissolving HEC powder into water. The testing samples of HEC solutions ranges from 0.15-1.00% (w/w) corresponding to 2-10 %TS manure. At first a high-speed blender disperses the HEC powder in to the water. At latter times, lowering the speed of the blender helps to avoid the formation of air bubbles and micro-gels.

Coaxial cylinder viscometer (Haake Visco tester model VT 550), with repeatability and accuracy: $\pm 1\%$, comparability: $\pm 2\%$ measures the viscosities of each test sample. The temperature of the samples are 5°C, 15°C, 25°C, 35°C, and 45°C with shear rates range from 0.5 to 3,000 s⁻¹. The fixture gap size, Δr is 1.0 mm, as shown in Figure 3.7. The loaded samples achieve thermal equilibrium with the surrounding water jacket. The shear rate of samples increased from 0 to 3,000 s⁻¹ within less than 6.7 minutes and then back to zero over a similar time interval. Shear rate, $\dot{\gamma}$, and shear stress, σ , are evaluated using (Haynes *et al.*, 1998):

$$\dot{\gamma} = 2\Omega \frac{R_c^2}{(R_c^2 - R_b^2)} \quad (3.1)$$

$$\gamma = 2\Omega \frac{R_c^2}{(R_c^2 - R_b^2)} \quad (3.2)$$

$$\sigma = \pi \frac{A.S}{2R_b h} \quad (3.3)$$

where Ω = angular velocity R_c = cup radius
 R_b = bob radius A = spring constant
 S = scale reading h = bob height

Computation of constants requires the calibration of the fixture and spring combination with viscosity standards. Silicone is used as standard fluid since it is less temperature sensitive. Three different rotational speeds (20, 30, 50 rpm) are used to verify how the instrument responds when sensing low, medium, and high % torques.

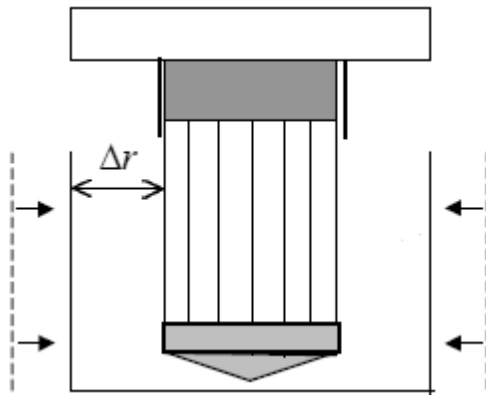


Figure 3.7: Schematic of coaxial viscometer

For each test condition, the flow behavior index, n , corresponds to the slope of the least squares regression of the logarithm of shear stress on the logarithm of shear rate data. Equation 3.4 uses the assumption that the fluid sheared in the coaxial cylinder gap is Newtonian to calculate the shear rate.

Application of the Kreiger-Maroon method (Harper and El Sahrighi, 1965) corrects the deviation from Newtonian flow to non-Newtonian:

$$\gamma = \frac{2\Omega}{n} \frac{R_c^{2/n}}{(R_c^{2/n} - R_b^{2/n})} \quad (3.4)$$

Apparent viscosity, η , calculation uses these corrected shear rates and the shear stress values as (Sherman, 1975):

$$\eta = m \gamma^{(n-1)} \quad (3.5)$$

Then, a power-law curve fitting allows the calculation of the flow behavior index, n , and the consistency coefficient, m , for each data set. In addition, the fluid's time dependence behavior is considered. Analysis of the covariance procedure (Agote *et al.*, 2001) on the linear forms of the up-curve and down-curve segments for $\log \eta$ vs. $\log \gamma$ at 1.00% (w/w) and at 5°C temperature tests the differences of slope n and intercept m values of each rheogram. The results show that there is no significant difference for $p > 0.05$.

A shear rate value of 100 s^{-1} is common in an AD (Sherman, 1975). In addition, selection of this shear rate allows comparing results with limited available literature. Hence, the study uses fluid at this shear rate to calculate the apparent viscosities based on the power-law constants. Derived apparent viscosities help to understand the relationship between viscosity, concentration and temperature.

At each of the five temperatures tested, fitting Equation 3.6 shows the effect of concentration, C, on the apparent viscosity at shear rate value of 100 s⁻¹:

$$\eta = a \cdot c^b \quad (3.6)$$

The slope and intercept of each of the five regressions of the logarithm of apparent viscosity vs. the logarithm of HEC concentration give parameters ‘a’ and ‘b’.

The Arrhenius model (Semg and Deng, 2000) allows examining the variation in apparent viscosity due to temperature at each HEC concentration:

$$\eta = A \cdot e^{(\Delta E/RT)} \quad (3.7)$$

where A is the frequency factor, e is the natural logarithm base, ΔE is the activation energy and R is the gas constant.

The slopes and intercepts of the regressions of the logarithm of apparent viscosity against the inverses of absolute temperatures give the frequency factors and activation energies at each of the five concentrations examined. Multiple linear regression techniques construct a combined relationship of apparent viscosity to shear rate, concentration and temperature. The logarithm of apparent viscosity is regressed on the logarithm of shear rate, the logarithm of HEC concentration, and the inverse of absolute temperature.

3.2.2 Mixing time and power measurement

A conductivity meter manufactured by BHR Group Ltd. and designed especially for mixing time measurement energizes the conductivity probes described in Section 3.1. The output from the meter is a 0 to 200 mV analogue signal that is directly proportional to the conductivity measured. An amplified signal of ± 5 V passes through an anti-aliasing filter and then input to the analogue-digital converter (ADC) board. The low-pass cut-off frequency to which the filters are set is dependent on the sampling frequency of the ADC. Irrespective of the sample time, the number of data points collected is 4096. The sampling frequency adjusts so that the sampling time is always between three and four times longer than the mixing time. For example, for a sampling frequency of 50 Hz, the sample time is 81.9 sec and the expected mixing time is between 20 and 30 sec.

The mixing time measurement method used in this work involves the addition of a small volume of electrolyte to the bulk fluid in the digester and recording the conductivity at three points in the digester, as shown in Figure 3.4. A solenoid valve activated by a Schmidt trigger adds the tracer to the digester. Figure 3.8 shows a typical conductivity trace.

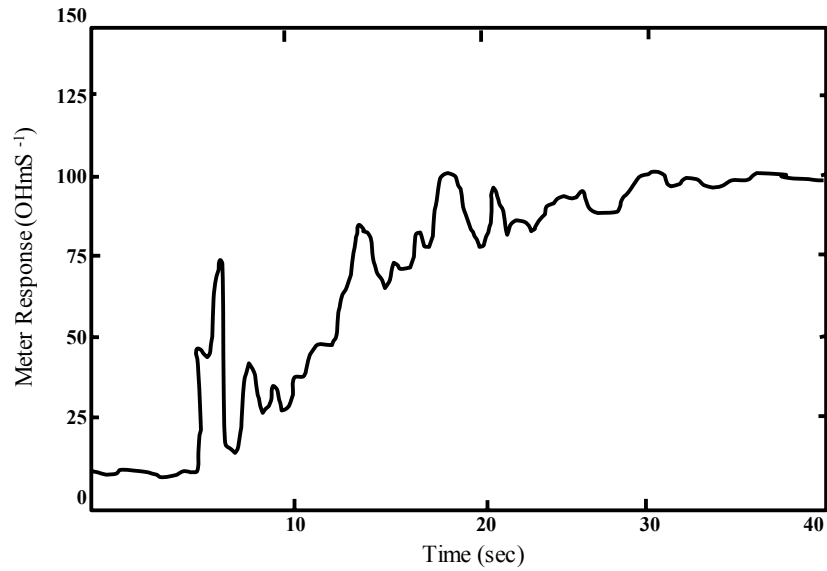


Figure 3.8: Conductivity trace of added electrolyte to the bulk solution of HEC in a lab-scaled digester used to measure the mixing time

3.2.3 Experimental flow measurement

A 2D and 3D Particle Image Velocimetry (PIV) are techniques used to obtain meaningful data about the flow field at specific positions inside the mixing domain as described in Chapter 2. Unlike other non-intrusive visualization techniques like Particle Tracking Velocimetry (PTV) and Laser Doppler Velocimetry (LDV), PIV provides high-density velocity fields in a defined grid, which may reveal circulation flow patterns and velocity gradients (Adrian, 1991). PIV extracts instantaneous local velocities and flow characteristics by measuring the displacement of small suspended tracer particles in a known time interval. The basis for the selection of the time between pulses, Δt , are the local velocities. As presented in Gomez *et al.*, (2010), an optimum Δt is the time a particle traveling perpendicular to the light sheet would need to travel 25% of the light sheet thickness. Researchers in the past report that the maximum velocity at only 2 mm

away from the impeller can only be a fraction of the U_{tip} usually between 30 to 50% (Zalc *et al.*, 2001; Bugay *et al.*, 2002; Gomez *et al.*, 2010). Thus, determination of Δt for each operating condition requires that:

$$\Delta t = \frac{0.8Z_l}{U_{tip}} \quad (3.8)$$

A synchronized camera allows capturing pictures at the same time the laser emits light. Thus, there are two frames acquired each time the impeller passes the trigger. These frames are processed in a computer using the software Flow Manager from Dantec Dynamics to obtain the velocity fields. The processing of the images requires a prior application of grid to each pair of pictures. Two different grids define the velocity field resolution i.e. 55×42 and 111×85 to create the velocity fields. The area of each element of the grid known as interrogation window is $4 \times 4 \text{ mm}^2$ and $3.85 \times 3.85 \text{ mm}^2$, respectively. The processing of each pair of images uses an adaptive correlation based on cross-correlation techniques (Keane and Adrian, 1992). This technique reduces the size of the interrogation window progressively to improve the dynamic range and increase the space resolution (Scarano and Riethmuller, 1999). This study uses a single refinement step and includes an overlap of 25% between interrogation areas in the correlation process. The averaging results of 800 instantaneous velocity fields give the steady-state flow fields at different conditions. The comparison of the velocity fields with a set of 1,600 instantaneous velocity fields shows no significant change in the velocity vectors. Therefore, 800 instantaneous velocity fields represent the steady-state flow. The light refracted by the plane is filtered using a 532 nm filter at the camera lens,

so that the light beams refracted by air bubbles is not recorded and only those from the particles are captured.

The 3D-PIV is based on the same fundamental principle as human eye-sight: stereo vision (Randal, 2001). Our two eyes see slightly different images of the world surrounding us, and comparing these images, the brain is able to make a 3-dimensional interpretation. As with 2D measurements, stereo-PIV measures displacements rather than actual velocities, and here cameras play the role of “eyes”. The most accurate determination of the out-of-plane displacement i.e. velocity is accomplished when there is 90° between the two cameras (Riethmuller, 2001). In case of restricted optical access, smaller angles can be used at reduced accuracy. For each vector, we extract 3 true displacements— ΔX , ΔY , ΔZ —from a pair of 2D displacements Δx and Δy as seen from left and right camera respectively. Data reduction then requires solving 4 equations with 3 unknowns in a least squares approach. Depending on the numerical model used, these equations may or may not be linear.

Parameters for the numerical model are determined through camera calibration. 3D evaluation requires a numerical model, describing how objects in space are mapped onto the CCD-chip of each camera. When viewing the light sheet at an angle, the camera must be tilted in order to properly focus the camera’s entire field of view. The image recorded using the lens onto the CCD-chip and object planes must cross each other along a common line in space for the images to be properly focused in the entire field of view.

This is referred to as the Scheimpflug condition (You, 2003), and a 45° is used in our system as illustrated in Figure 3.9.

3D evaluation is possible only within the area covered by both cameras. Due to perspective distortion each camera covers a trapezoidal region of the light sheet. Careful alignment is required to maximize the overlap area. Interrogation grid is chosen to match the spatial resolution. Left and right camera images are recorded simultaneously. Conventional PIV processing produce 2D vector maps representing the flow field as seen from left and right, as shown in Figure 3.9. The vector maps are re-sampled in points corresponding to the interrogation grid. Combining left/right results, 3D velocities are estimated.

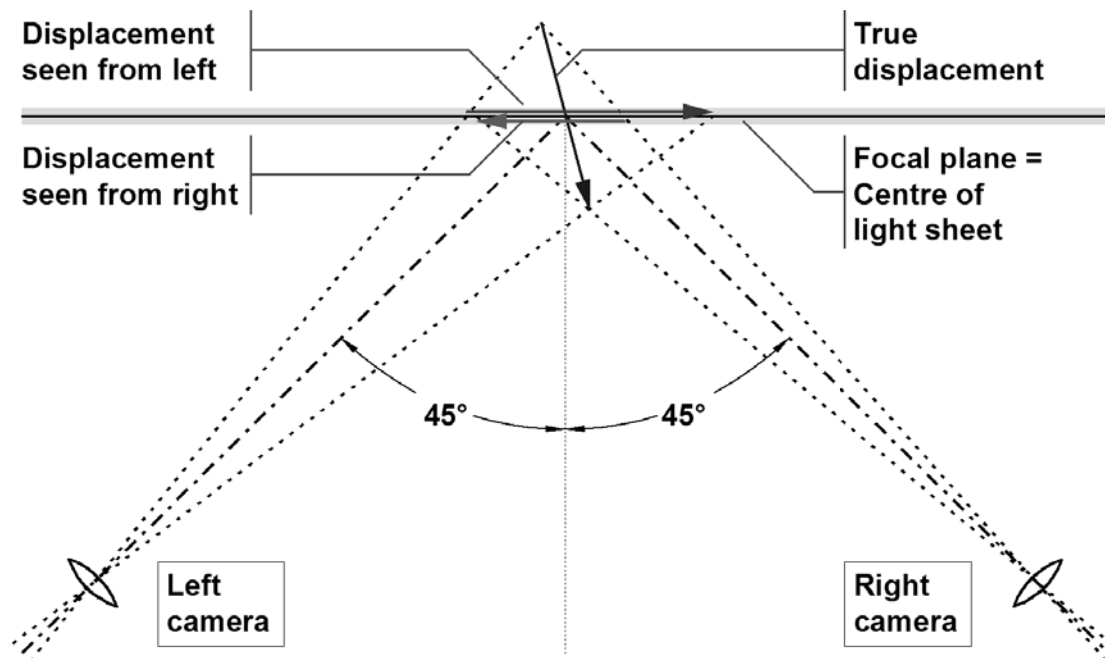


Figure 3.9: Schematic showing operation of PIV using two cameras

3.2.4 Determination of impeller pumping flow rate and pumping number

Both radial and axial impellers exert a pumping action within the digester. Different types of impellers produce different pumping actions that cause the establishment of fluid flow circulation patterns inside the digester. The pumping number, N_Q , is used to determine the impeller pumping capacity, which is defined as (Paul *et al.* 2004):

$$N_Q = \frac{Q}{N \cdot D^3} \quad (3.9)$$

In this equation, Q is the flow rate produced by the impeller, N is the agitation speed, and D is the impeller diameter.

The pumping action of the impeller results in a discharge flow rate around the impeller, Q_{out} , balanced by incoming flow toward the impeller, Q_{in} . In principle, the Pumping number can be calculated using either Q_{out} or Q_{in} since the conservation of mass for an incompressible liquid requires that Q_{out} and Q_{in} be equal (Randal, 2001). An appropriate control volume constructed around the impeller allows computing Q for an impeller. The common shape used to calculate Q around an impeller is a cylindrical volume. Radial pumping number, N_{Qr} , calculated based on radial discharge flow rate, Q_r , around the impeller will be reported in this work at different H/T ratio. The calculation of Q_r uses the radial velocities measured by PIV along a vertical segment (rake) close to the impeller blades. This rake contains 7 points and it is 0.38 cm away from impeller blades in radial direction. The rake begins 0.38 cm below the blades and ends 0.38 cm above the blades ($Z_1/T = 7.2$ cm and $Z_2 = 9.3$ cm). The following equation is used to calculate Q_r :

$$Q_r = \sum_{i=1}^{i=6} \overline{u_{ri}}(r, \overline{z_i}) \Delta z_i 2\pi r \quad (3.10)$$

where $\overline{u_{ri}}(r, \overline{z_i})$ is the average radial velocities measured by PIV at Z_i ($u_{ri}(r, Z_i)$) and Z_{i+1} ($u_{r(i+1)}(r, Z_{i+1})$) and we then define $U_{ri}(r, Z_i)$ as the average of the radial velocities of 800 PIV measurements at any given r and Z_i .

Since the PIV data are taken at any position of the impeller relative to the baffles, the average velocity obtained via PIV is the average of any point along a circle with a radius r and axial level of Z_i representing a circumferential average. After computing the appropriate average radial velocity, this value is multiplied by the elemental surface area $\Delta Z \cdot 2\pi \cdot r$ of the cylinder surrounding the impeller where the measurements are taken with ΔZ and r equal to 0.35 cm and 4.2 cm, respectively.

3.2.5 Determination of impeller discharge angle

The impeller discharge angle is the angle formed between the average vector of the discharge stream produced by the impeller and the horizontal plane. The impeller discharge stream angle is calculated by taking the average angle of the velocity vectors on the previously mentioned rake but only over the blade height. The radial and axial velocity components measured by PIV along a vertical rake close to the impeller blades are used to calculate impeller discharge angle. This rake contains 5 points and it is 0.38 cm away from impeller blades in the radial direction at $r/R = 0.34$. Its vertical length is equal to the impeller blade height with $Z_1 = 7.5$ cm and $Z_2 = 9.04$ cm. Positive angles indicate that the stream is flowing upward.

3.2.6 Determination of the impeller power dissipation and power number

The torque, applied to the impeller by the motor is experimentally measured with a strain gage-based rotary torque transducer (Model, T6-5-Dual Range, Interface, Inc. Scottsdale, AZ) connected to an external multi-channel signal conditioner, display and controller (Model 9850). The motor rests on a separate steel framework above the digester as shown in Figure 3.1 to minimize vibrations that could otherwise impact torque measurements. Carefully selected couplings are used to mount the transducer on the shaft between the motor and the impeller in order to minimize any wobbling of the impeller shaft. This arrangement prevented the introduction of friction sources in the torque measurement, as reported in other systems (Chapple *et al.*, 2002). The transducer operates by producing an output voltage, proportional to the applied torque and generated by the change in electric resistance within the strain gages. The strain gages bond (Model DCVA) to the torque sensor structure within the transducer. The magnitude of the resistance change is proportional to the deformation of the torque sensor and therefore the applied torque. In this apparatus, the controller feeds the torque transducer with a supply DC voltage, which converts to AC in the transducer stator, transferred inductively to the transducer rotor electronics, rectified, stabilized, and fed to the strain gage bridge also contained within the rotor. The output from the bridge is conditioned in an amplifier, converted to a digital signal, and transferred back to the stator by a rotating transformer. The transducer measures the torque applied to the rotating shaft in two different ranges, i.e., 0 to 0.5 Nm and 0 to 5 Nm. However, only the first range is used in this study. The torque measurement error is $\pm 0.1\%$ of full scale.

The experimental power dissipation is measured for different combinations of liquid level, impeller size, vessel size, impeller clearance, and agitation speed. All experiments are reproduced at least twice and each time the system is allowed to stabilize for 2 minutes before collecting power data in 20 sec time intervals. Equation 2.4 is used to obtain the experimental power number, P_o .

$$P_o = \frac{P}{\rho N^3 D^5} \quad (3.11)$$

where ρ is the liquid density.

3.3 Data analysis and results

3.3.1 Non-Newtonian viscosities measurement

For the range of shear rates used in this study, the power law properly describes flow behavior at each experimental concentration and temperature. Table 3.4 shows the consistency coefficients and flow behavior indices for each temperature along with coefficients of determination for each flow curve. At each concentration, there is a decrease in the consistency coefficient with temperature increase. However, no trend is evident in the flow behavior index. Increases in HEC concentration resulted in increased consistency coefficient and decreased flow behavior index, indicating that the solutions became more pseudo-plastic as the level of HEC increased. Figure 3.10 demonstrates this change in flow behavior with changes in HEC concentration at 25°C. Higher HEC concentration also results in increased apparent viscosity at shear rate of 100 s⁻¹ and corresponding test temperatures.

Application of Equation 3.12 developed by Cross (1982) to the data at each temperature gives good results. The regression of the logarithm of apparent viscosity on the logarithm of HEC concentration accurately fits with $p < 0.05$.

$$\frac{\eta_a - \eta_\infty}{\eta_o - \eta_\infty} = \frac{1}{1 + (\dot{\gamma} / \dot{\gamma}_m)^n} \quad (3.12)$$

where $\dot{\gamma}_m$ is the shear rate evaluated at the mean apparent viscosity $(\eta_o + \eta_\infty)/2$.

Table 3.4: Consistency coefficients and flow behavior indices of HEC at various temperatures and concentrations

Conc. (% w/w)	Temp (°C)	m (mPa·S ⁻¹)	n	r ²	No. of data points
0.05	5	47.2	0.631	0.979	30
	15	33.2	0.634	0.987	29
	25	28.4	0.654	0.984	28
	35	26.6	0.648	0.981	22
	45	24	0.635	0.984	25
0.10	5	228	0.445	0.933	28
	15	146	0.507	0.889	27
	25	126	0.487	0.995	28
	35	101	0.525	0.989	29
	45	77.4	0.546	0.982	29
0.25	5	1700	0.258	0.993	28
	15	1160	0.272	0.993	30
	25	971	0.294	0.994	29
	35	916	0.293	0.991	30
	45	783	0.315	0.997	30
0.50	5	2290	0.250	0.988	26
	15	2170	0.252	0.992	27
	25	2101	0.249	0.994	28
	35	2060	0.234	0.993	28
	45	1980	0.249	0.997	30
1.00	5	10100	0.232	0.993	27
	15	9540	0.178	0.994	29
	25	8220	0.141	0.995	30
	35	7930	0.149	0.996	30
	45	5750	0.164	0.998	30

Table 3.5 contains parameters ‘a’ and ‘b’ for Equation 3.6 and as well as the coefficient of determination for each regression.

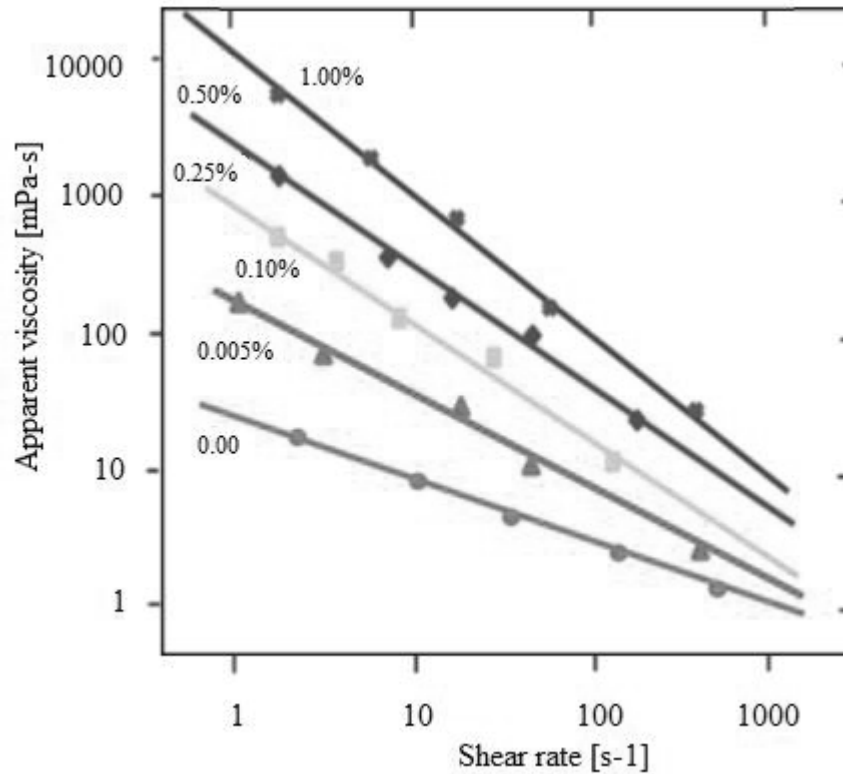


Figure 3.10: Effect of concentration on apparent viscosity at shear rate value of 100 s^{-1} at 25°C for HEC solutions tested from 0% to 1% concentration

Table 3.5: Apparent viscosity at shear rate value of 100 s^{-1} as a function of concentration for HEC solution from 5 to 45°C for 0.25% HEC

Temperature ($^\circ\text{C}$)	a	b	r^2
5	167	0.963	0.982
15	169	1.12	0.993
25	181	1.18	0.996
35	163	1.09	0.973
45	163	1.20	0.994

Examination of apparent viscosity at shear rate value of 100 s^{-1} shows the decrease in viscosity with temperature increase. Data fitted to Arrhenius model shows significant relationships ($p < 0.05$) for all but the 1.00% concentration level. Table 3.6 shows activation energies, frequency factors and coefficients of determinations. At the concentrations studied, the low values meant that their rheological behavior properties were less temperature-dependent. Higher activation energy means that the apparent viscosity is relatively more sensitive to temperature change.

Table 3.6: The activation energies, frequency factors and coefficients of determination while fitting data to Arrhenius model

Con (w/w)	ΔE (kcal/mole)	A (mPa-s)	r^2
0.05	1.87	0.263	0.881
0.10	2.40	0.211	0.791
0.25	2.04	1.28	0.851
0.50	0.523	27.6	0.530
1.00	0.264	283	0.116

Figure 3.11 contains rheograms for the five HEC concentrations studied including results for pure water for comparative purposes. Figure 3.8 shows small viscosity changes with increasing temperature. There is a decrease in the effect of temperature effect with the HEC concentration increase.

Finally, a relationship that allows calculating apparent viscosity as a function of shear rate, concentration and temperature combined is developed. Using multiple regressions, the following relationship is determined from the experimental data:

$$\eta = 396\gamma^{-0.642}c^{1.22}e^{668/T} \quad (3.13)$$

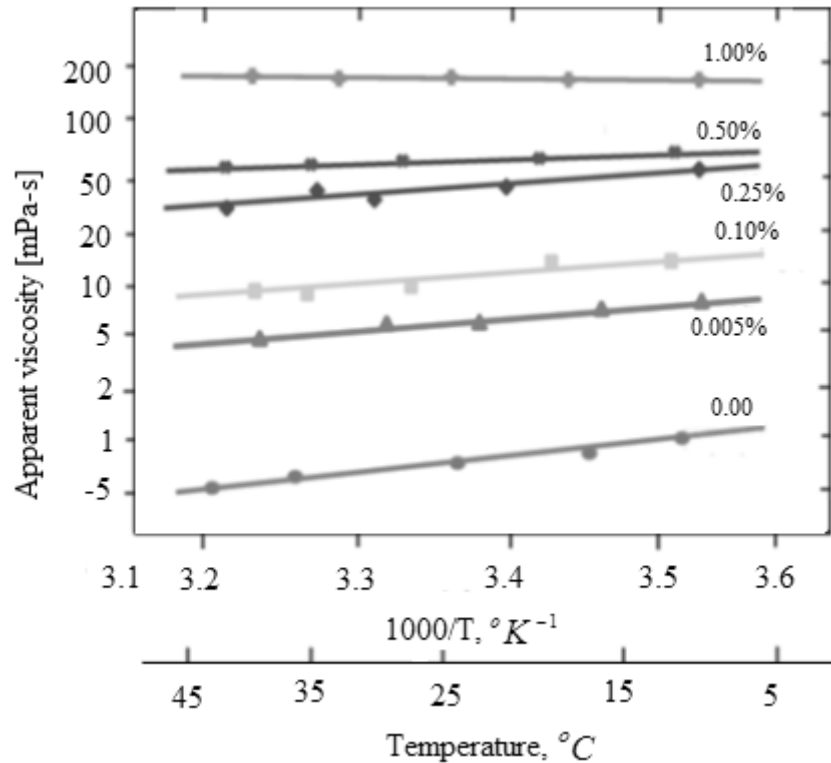


Figure 3.11: Effect of temperature on apparent viscosity at shear rate value of 100 s⁻¹ for water and HEC solutions tested

3.3.2 Mixing time and power measurement for Newtonian fluids

The mixing time measurement using Newtonian fluids includes performing tests eight times for each set of conditions and averaging the values. The relative standard deviation associated with each mean value is:

$$\text{RSD} = \frac{\sigma_{\theta}}{\bar{\theta}} \times 100\% \quad (3.14)$$

The technique used to analyze the viscous mixing time is similar to the method used by Ruszkowski (1985a). The quantity used to characterize the mixing in the scaled digester is the root mean square concentration. The mean concentration in the digester represents the time varying concentration in a digester at any point whereas time-varying components represent the time varying concentration in the digester:

$$C(t) = \bar{C} + C'(t) \quad (3.15)$$

where: $C(t)$ local concentration at time t

\bar{C} mean concentration

$C'(t)$ local fluctuating component of concentration at time t

The root mean square concentration fluctuation over a time Γ is:

$$\sigma_c^2 = \frac{1}{\Gamma} \int_0^{\Gamma} (C(t) - \bar{C})^2 dt = \frac{1}{\Gamma} \int_0^{\Gamma} (C'(t))^2 dt \quad (3.16)$$

Equation 3.17 deals with turbulent fluctuating quantities such as fluid velocities as measured by PIV. The situation in the digester is complicated since the concentration fluctuations are transient, whereas the magnitude of the root mean square velocity is constant with time. C and σ_c^2 are functions of Γ , the time over which the integration takes place. Addressing this problem requires the calculation of the root mean square

concentration for small sections along the conductivity-time. Figure 3.12 shows a typical plot of σ_c^2 versus time.

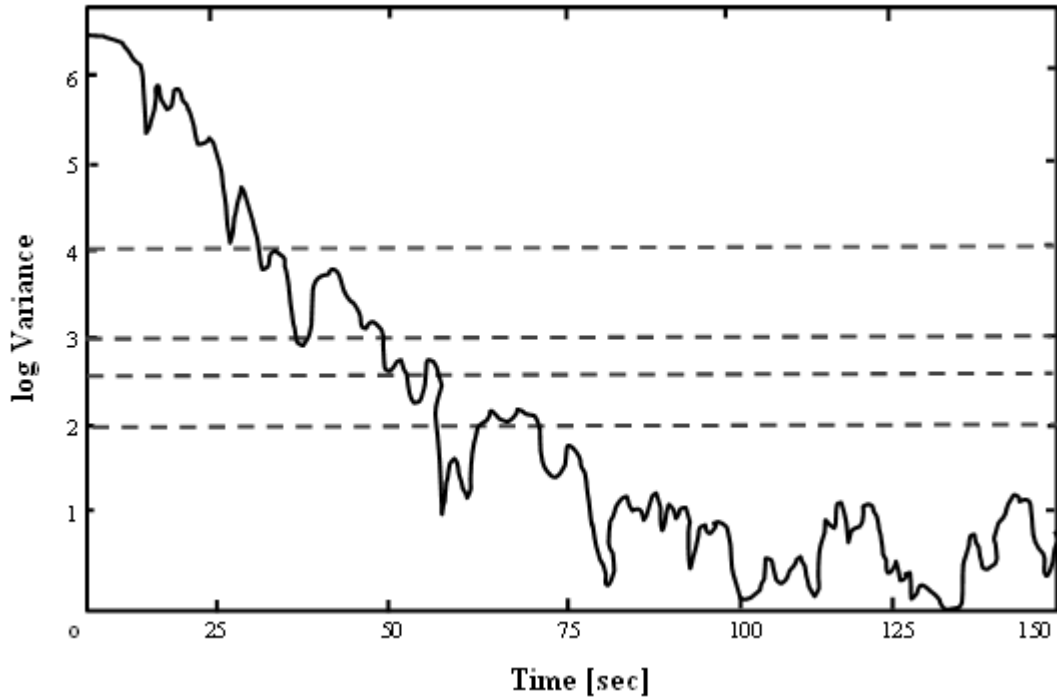


Figure 3.12: Plot of log variance, $\log \sigma_c^2$, versus time where both C and σ_c^2 are functions of root mean square concentration fluctuation over a time, Γ

The root mean square concentration fluctuation is:

$$\sigma_c^2(i) = \frac{1}{32} \sum_{4i}^{3i+31} (C_j - C(\infty))^2 \quad i = 1, 2, 3 \dots 1,016 \quad (3.17)$$

where: $\sigma_c^2(i)$ i^{th} estimate of the root mean square concentration fluctuation,
 C_j concentration of the j^{th} data point, and
 $C(\infty)$ concentration in the tank when mixing is complete.

The number of points required to calculate the root mean square is 32 since this covers a significant portion of the circulation time in the digester.

The mixing index, M , describes the degree of homogeneity using:

$$M = \frac{\Delta C - (\sigma_c^2)^{1/2}}{\Delta C} \quad (3.18)$$

where $\Delta C = C(\infty) - C(0)$.

M expresses the reduction in the root mean square concentration fluctuation as a fraction of the total change in concentration in the digester due to the injection of tracer. The value of M selected is 0.95, i.e. the mixing time defined as the time for the mixing process to be 95% complete.

The individual probe mixing times, θ_1 , θ_2 and θ_3 , are all calculated. A fourth mixing time, the root mean square mixing time θ_{RMS} , allows the estimation of the mixing time for the digester as a whole. The data taken at each individual probe by defining a root mean square concentration in the digester gives θ_{RMS} . The concentration of the j^{th} data point measured at each probe location is:

$$C_{j,RMS} = \left(\frac{1}{3} (C_{cj,1}^2 + C_{cj,2}^2 + C_{cj,3}^2) \right)^{1/2} \quad (3.19)$$

where $C_{j,1}$ is the concentration of the j^{th} data point measured at probe 1, etc.

Substituting $C_{j,RMS}$ for C_j in Equation 3.6 gives the value for $\sigma_{C,RMS}^2$ which in turn is substituted into Equation 3.18 to calculate M_{RMS} .

The analysis starts with the results of the mixing time measurements made using water as working fluid. The data fits to:

$$P_0^{1/3} N \theta \left(\frac{D}{T} \right)^{13/6} = k \quad (3.20)$$

This is developed by taking the dimensionless power per unit mass, as reported by Mersmann *et al.* (1976) and Havas *et al.* (1978b) and takes the following form:

$$P_0^{1/3} N \theta \left(\frac{D}{T} \right)^{5/3} = \left(\frac{\bar{\epsilon}}{T^2} \right)^{1/3} \theta = k \quad (3.21)$$

and introducing a scale factor:

$$P_0^{1/3} N \theta \left(\frac{D}{T} \right)^{5/3} \left(\frac{D}{T} \right)^a = k \quad (3.22)$$

Analysis of multiplicative regression of $N\theta$ on P_0 and D/T on data for water using the Statgraphics computer package gives:

$$N\theta \propto P_0^b \left(\frac{D}{T} \right)^c \quad (3.23)$$

The values of b and c are -0.319 and -2.062 respectively with a correlation coefficient, r^2 of 91.71% and F-ratio of 139, for 26 data points.

After rounding-up these values, the value of 'a' is 1/3, i.e.:

$$P_0^{1/3} N \theta \left(\frac{D}{T} \right)^2 = k'' \quad (3.24)$$

Carrying out regression, Equation 3.24 is re-arranged and both sides multiplied by ρ/μ to obtain:

$$P_0^{1/3} \frac{\rho N D^2}{\mu} = k'' \frac{\rho T^2}{\mu \theta} \quad (3.25)$$

where: $k'' = 5.20 \pm 10.0\%$

Re-writing Equation 3.26 gives:

$$P_0^{1/3} R_e = \frac{5.20}{F_0} \quad (3.26)$$

The terms on the left hand side of Equation 3.26 are the impeller power number and Reynolds number that are commonly used as dimensionless groups. The power number relates power input by an impeller to its speed and diameter. Reynolds number is a ratio between the inertial and viscous forces acting on the fluid. The term on the right hand side of Equation 3.26 is Fourier number used by other workers to correlate mixing time data (e.g. Hoogendoorn & Den Hartog (1967), Shiue & Wong (1984) in unsteady-state mass, heat or momentum transfer problems (Parkin, 1984). The general form is:

$$F_0 = \frac{\alpha \theta}{T^2} \quad (3.27)$$

where T is the characteristic length, θ is the characteristic time of the process in question, and α is the kinematic property of the fluid taking one of the following forms:

- i) the diffusion coefficient in mass transfer processes,
- ii) the thermal diffusivity (thermal conductivity divided by the volumetric heat capacity) in heat transfer processes, and
- iii) the kinematic viscosity in momentum transfer processes.

The viscosity of the fluid controls the mixing time in an AD so it is appropriate to use the third version of Fourier number for the analysis of the data. The parameter used to correlate and compare results with literature is θ_{RMS} since it defines mixing time for the whole digester. The analysis and reporting of the mixing time data uses the following three methods:

- i) individual probe mixing times which indicate how the mixing process proceeds in regions of different mixing intensities
- ii) root mean square mixing times which indicate how mixing proceeds for the digester as a whole
- iii) data fitting to correlation in the same form as the one developed for Equation 3.26

The investigation of the way in which the mixing process precedes in regions of high mixing and low mixing intensity requires measurement of individual probe mixing times. The three probe locations are beneath the impeller, half way between the shaft and digester wall and behind a baffle, as shown in Figure 3.4. Tables 3.7 to 3.10 show

viscous mixing experiment results. The tables show digester scale, nominal fluid viscosity, impeller speed, individual probe mixing times and root mean square mixing time for each set of experimental conditions. The mixing time reports the mean of eight repetitions of the measurement.

Table 3.7: Newtonian mixing time results (T/3PBT) for individual probe mixing times, θ_1 , θ_2 and θ_3 corresponding to the 3 probe positions

T (m)	μ (cp)	N (S^{-1})	θ_1 (S)	θ_2 (S)	θ_3 (S)	θ_{Rms} (S)
0.25	500.0	12.7	9.6	9.5	77.8	59.4
"	"	14.0	8.5	10.8	51.0	43.7
"	"	15.5	7.3	8.7	41.6	34.3
"	100.0	5.9	10.0	14.8	77.5	68.6
"	"	7.0	6.7	10.1	69.0	61.1
"	"	8.2	6.7	9.3	45.5	39.3
0.50	"	3.7	14.8	14.4	29.7	28.0
"	"	4.4	12.4	13.6	25.8	24.0
"	"	5.1	9.7	10.7	26.0	18.0
"	40.0	1.5	37.9	38.6	69.7	64.9
"	"	3.0	12.8	15.5	23.3	23.5
"	"	4.8	6.7	9.4	11.6	11.0

Table 3.8: Newtonian mixing time results (T/2PBT)

T (m)	μ (cp)	N (S^{-1})	θ_1 (S)	θ_2 (S)	θ_3 (S)	θ_{Rms} (S)
0.30	500.0	5.0	11.1	9.4	165.0	133.0
"	"	6.3	8.1	7.8	116.0	87.0
"	"	7.3	8.9	8.0	78.8	67.7
"	100.0	3.0	10.2	11.6	44.4	41.5
"	"	3.5	7.5	8.8	22.9	22.3
"	"	4.2	6.8	7.7	25.1	21.6
0.50	"	2.1	14.3	13.9	16.0	15.2
"	"	2.5	12.4	11.4	13.0	12.5
"	40.0	1.5	16.7	18.4	23.4	21.7
"	"	2.7	6.5	7.1	10.9	9.5
"	"	2.9	6.5	8.2	12.9	11.5
"	"	3.2	6.6	6.8	11.4	9.1

Figures 3.13 to 3.16 show individual probe measurements plotted as $N\theta$ versus Reynolds number. The plots show that a critical Reynolds number, Re_{crit} , exists for each impeller. When the viscosity of the fluid is low and $Re > Re_{crit}$, the mixing times are approximately equal. Increase in viscosity and $Re < Re_{crit}$ results in divergence of the mixing times such that:

$$N\theta_1 < N\theta_2 < N\theta_3 \quad (3.28)$$

The degree of divergence increases with decrease in Reynolds number for the two pitched blade turbines and Rushton turbine while the degree of divergence is constant for

the hydrofoil. This indicates that the way in which the tracer mixes into the bulk fluid differs for the various impellers.

Once $Re < Re_{crit}$, the mixing times throughout the digester are longer than the ones measured under turbulent conditions. Mixing times measured near the impeller are shorter than the ones measured in regions of low mixing intensity, i.e. near the digester wall, near the fluid surface or behind a baffle.

Table 3.9: Newtonian mixing time results (T/3RT)

T (m)	μ (cp)	N (S^{-1})	θ_1 (S)	θ_2 (S)	θ_3 (S)	θ_{Rms} (S)
0.50	100.0	1.7	28.4	32.2	202.0	168.0
"	"	2.6	21.6	20.5	88.7	71.1
"	"	3.3	11.0	11.8	39.7	30.5
"	40.0	1.8	20.9	21.7	22.9	21.8
"	"	3.8	8.8	10.3	8.7	10.4
"	10.0	1.7	16.3	21.0	25.5	23.6

Table 3.10: Newtonian mixing time results (T/2A310)

T (m)	μ (cp)	N (S^{-1})	θ_1 (S)	θ_2 (S)	θ_3 (S)	θ_{Rms} (S)
0.50	200.0	1.6	98.8	127.0	240.0	218.0
"	"	3.3	13.7	18.9	99.3	87.4
"	175.0	2.5	31.8	36.6	66.7	58.8
"	100.0	1.7	29.3	29.5	97.4	91.1
"	"	3.4	23.2	16.9	47.9	43.4
"	75.0	3.2	11.9	14.7	26.8	23.3

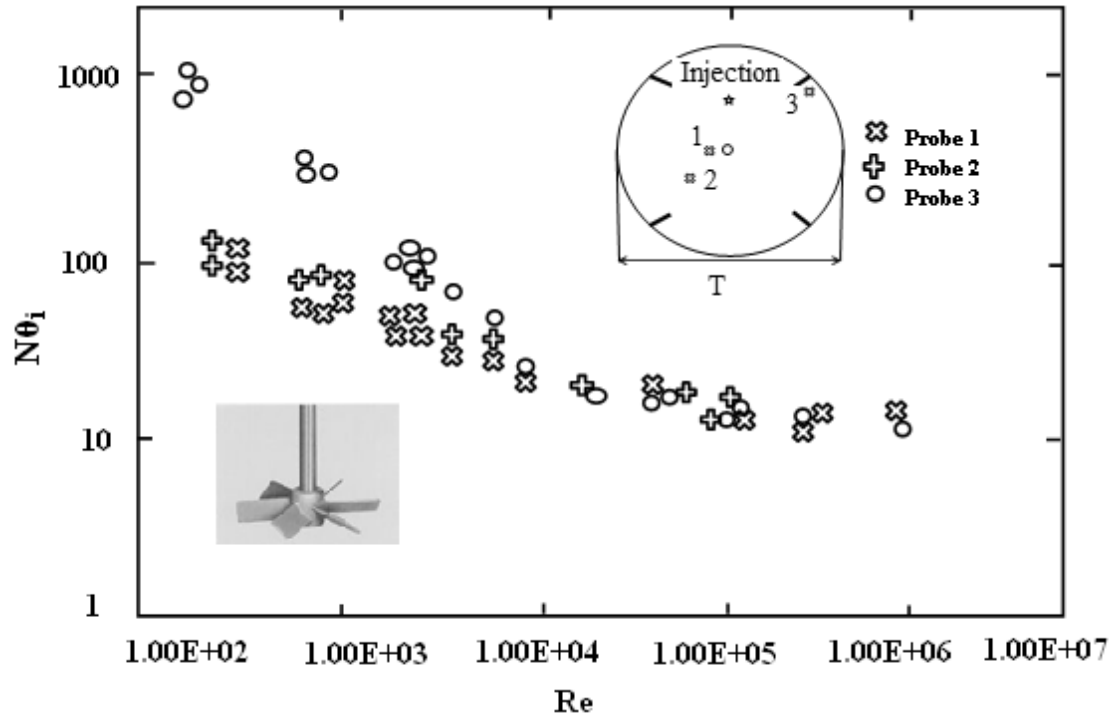


Figure 3.13: $N\theta_i$ versus Reynolds number for Newtonian data, T/3PBT

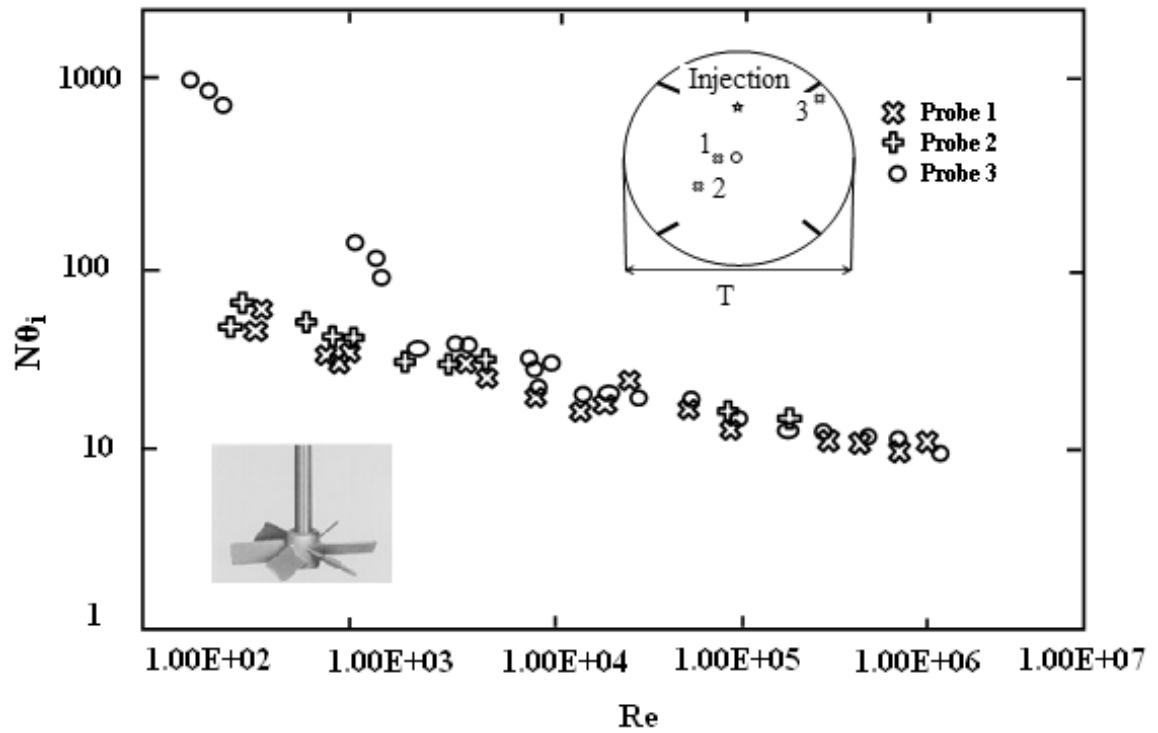


Figure 3.14: $N\theta_i$ versus Reynolds number for Newtonian data, T/2PBT

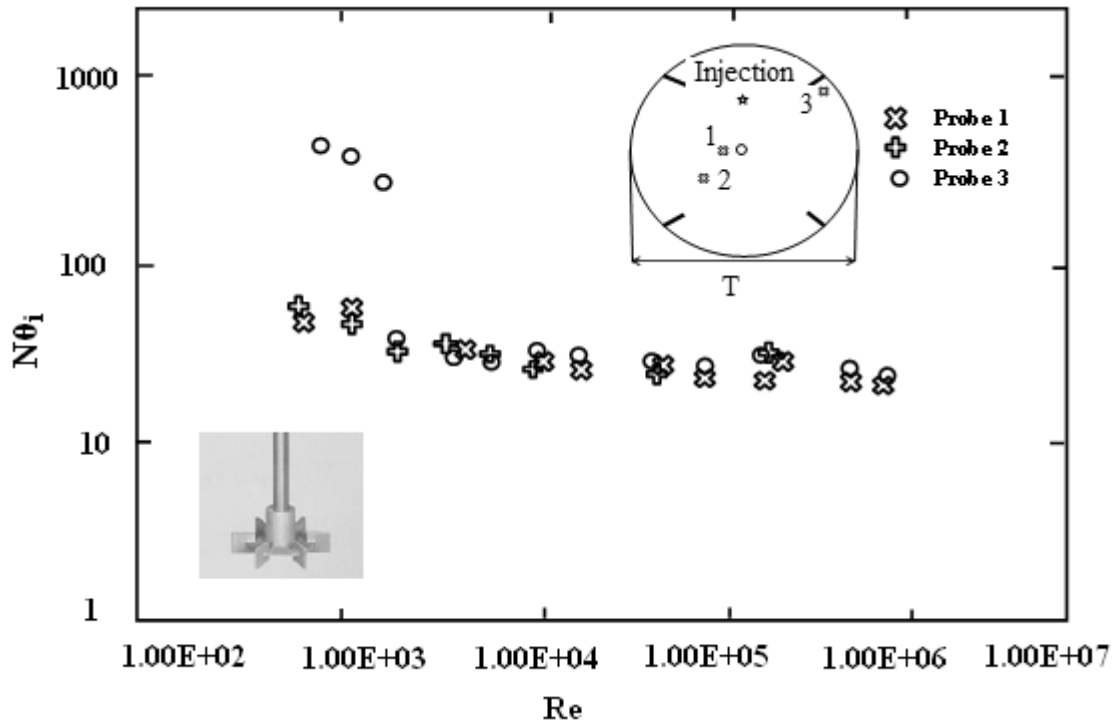


Figure 3.15: $N\theta$ versus Reynolds number for Newtonian data, $T/3RT$

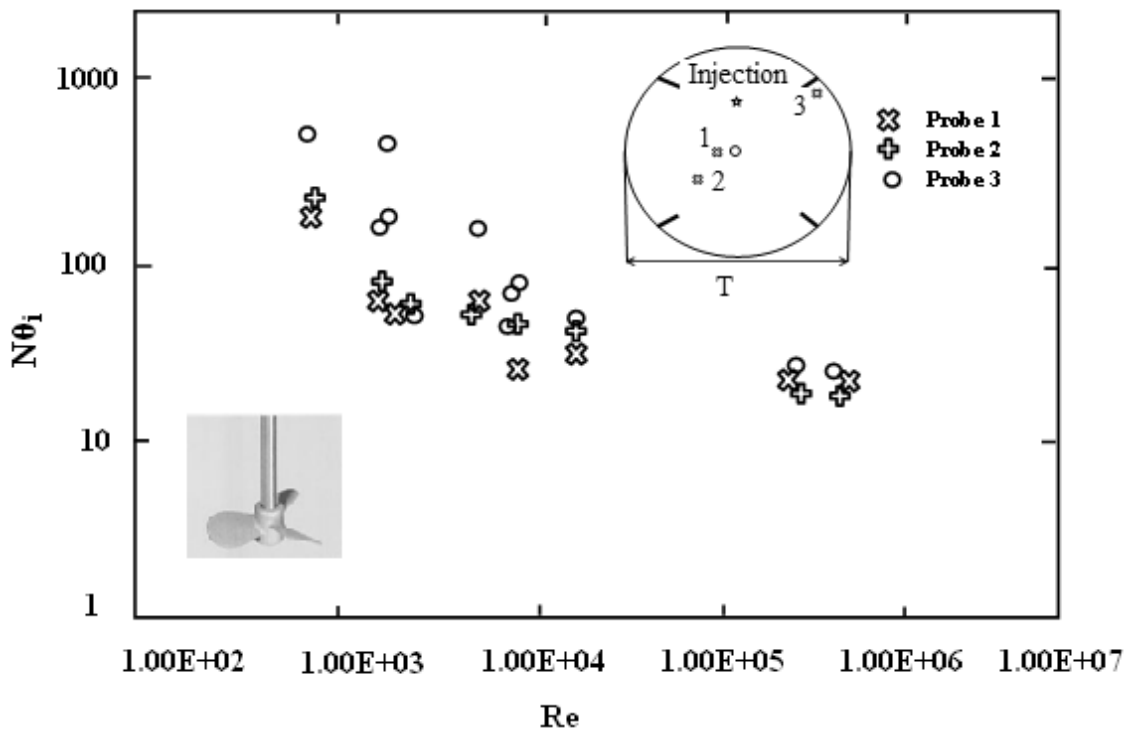


Figure 3.16: $N\theta$ versus Reynolds number for Newtonian data, $T/2A310$

Past workers assumed agitated tanks as a well-mixed region near the impeller in which the agitation intensity is high (Khang, 1975; Manamey, 1980). The assumption allows exchange of fluid between high and low regions of agitation intensities as the mixing process proceeds. In the turbulent regime, the pumping number of the impeller, F_l , is constant and flow between the well-mixed region and other parts of the digester uses the impeller speed since:

$$Q = F_l \cdot N \cdot D^3 \quad (3.29)$$

There is a critical Reynolds number where F_l is a function of Reynolds number and decreases as Reynolds number decreases. Wong and Huang (1988) indicates the boundary between these two regimes occur at $Re \approx 10^4$. The pumping capacity reduction explains the increase in mixing times measured near the wall and surface of the digester. Reduced pumping capacity implies less transfer of well-mixed fluid to these regions and unmixed fluid into the impeller. The critical Reynolds number determined from the $N\theta$ versus Re plots (Figures 3.13 to 3.16) occurs at about the same value supporting this explanation of the process. A point to note from these figures is that the degree of divergence between $N\theta_1$ and $N\theta_3$ varies with impeller type. The A310 hydrofoil impeller exhibits the most marked difference. The mixing times do not diverge but have a constant difference as Reynolds number decreases with $N\theta_3$ being 2-3 times greater than $N\theta_1$. This indicates that the proportion of the energy input to the digester devoted to flow and mixing vary according to impeller type. There is a small difference between the root

mean square mixing times comparing the impellers of the same diameter at equal power input.

The computed values of the root mean square mixing times show A310 hydrofoil is affected by viscosity at a higher Reynolds number than the other three impellers. Similar result reported by Zlokarnik (1967) and Khang (1975). Both measured mixing times for marine propellers and Rushton turbines. The value of Re_{crit} is approximately 2.0×10^4 and 2.0×10^3 for the marine propeller and the Rushton turbine respectively. The results of this study show the same trend with the highest $Re_{crit} \approx 1.0 \times 10^4$ for the hydrofoil and the lowest $Re_{crit} \approx 1.0 \times 10^3$ for Rushton turbine. The value of Re_{crit} for the two pitched blade turbines occurs at about 5.0×10^3 . The impeller with the highest power number (the Rushton turbine) has the lowest Re_{crit} and vice versa. This is because the power input to the fluid by the four impellers at a particular Reynolds number is different. For example, if a T/3 Rushton turbine with $P_o = 3.0$ is compared with a T/2 hydrofoil with $P_o = 0.3$ at equal Reynolds number, the Rushton turbine input approximately 15 times the power of the hydrofoil.

Generally, in the viscous mixing regime, the relationship between $N\theta$ and Re is:

$$N\theta \propto Re^{-x} \quad (3.30)$$

Regression of $N\theta$ is performed on Reynolds number for the data taken in the viscous regime (i.e. $Re < Re_{crit}$). Table 3.11 shows results tabulated. The values for both pitched blade turbines fit well this relationship given by Equation 3.31 with $x = 1$ while the Rushton turbine and hydrofoil slightly differ.

Table 3.11: N0 versus Re regression results

Impeller	x	r ² (%)	F-ratio	Data points
T/3 PBT	-0.989	93.09	163	13
T/2 PBT	-1.068	86.51	65	11
T/3 RT	-1.259	84.71	23	5
T/2 A310	-0.836	78.95	27	8

Zlokarnik (1967) found that the exponent, x, for a hydrofoil to be -0.8 which agrees quite well with the value of -0.84. Figure 3.17 shows plot of $Po^{1/3} Re$ versus $1/Fo$. The plot indicates the existence of two mixing regimes. The boundary between the two regimes occurs at:

$$\frac{1}{Fo} \approx 10^3 \quad (3.31)$$

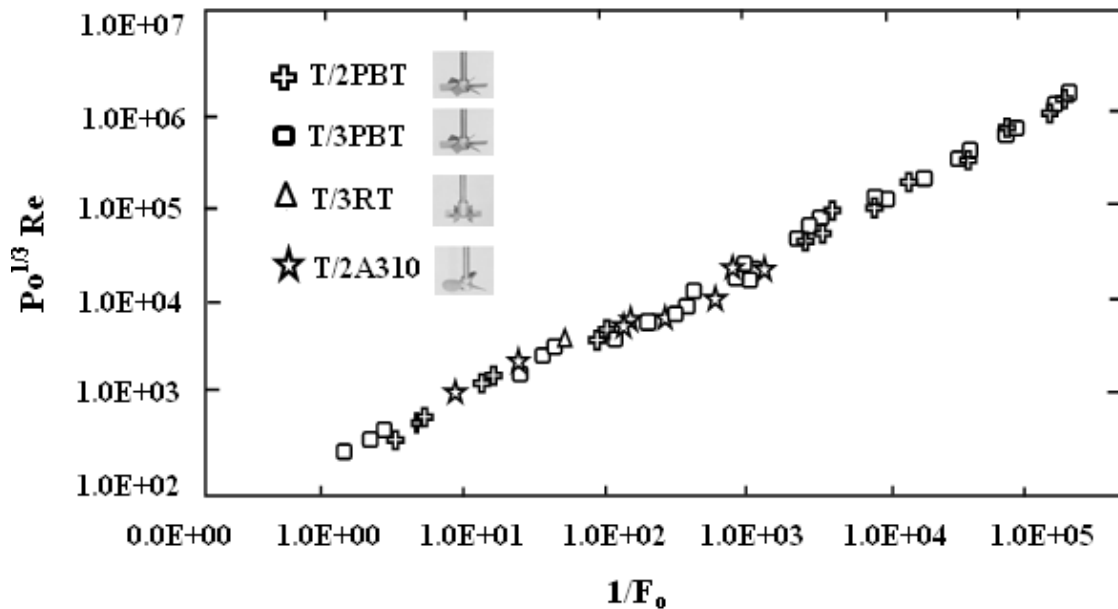


Figure 3.17: Plot of mixing time correlation (Newtonian data - for all impellers) for the two regimes where the boundary between the two regimes occurring at $1/Fo \sim 10^3$

Therefore, the data groups split at this value using the facility in the Statgraphics package. The correlation of the data in the groups defined by Equation 3.29 using regression is:

$$P_0^{1/3} R_e \propto F_0^y \quad (3.32)$$

Table 3.12 shows the correlation results tabulated. A very good fit of the data to the relationship obtained but the exponent, y , is different for each impeller. The correlation helps agitator design and impeller comparison in AD, if the exponents are equal.

Table 3.12: Correlation regression results

Impeller	y	r² (%)	F-ratio	Data Points
T/3 PBT	-0.497	98.46	769	13
T/2 PBT	-0.434	95.78	228	11
T/3 RT	-0.425	94.74	73	5
T/2 A310	-0.488	94.22	115	8
All	-0.464	96.49	990	37

Hence, value of y is rounded-up to -0.5 for each impeller and the constants and their standard deviations compared, i.e. the constants in the following two equations compared:

$$\frac{P_0^{1/3} R_e}{F_0^y} = k_y \quad (3.33)$$

$$\frac{P_0^{1/3} Re}{F_0^{-0.5}} = k_{0.5} \quad (3.34)$$

Table 3.13 shows the constants and their deviations. The table shows that rounding-up has very little effect on the scatter of the data. Thus, all the data taken at $Re < Re_{crit}$ fits to:

$$P_0^{1/3} Re = \frac{183}{\sqrt{F_0}} \quad (3.35)$$

Table 3.13: Comparison of constants

Impeller	k_y	RSD (%)	$k_{0.5}$	RSD (%)
T/3 PBT	179.5	10.98	177.7	10.99
T/2 PBT	238.8	21.8	186.1	25.22
T/3 RT	263.2	12.65	182	15.85
T/2 A310	199.9	14.98	190.2	15.18
All	222.5	16.26	183.5	17.4

Solving Equations 3.26 and 3.35 gives the critical values of the two correlating variables. This shows that:

$$P_0^{1/3} Re_{crit} = 6370 \quad (3.36)$$

$$\frac{1}{Fo_{crit}} = 1225 \quad (3.37)$$

$1/Fo_{crit}$ is close to the value taken to split the data ($1/F_o = 1000$) as expected. Rearranging Equation 3.37 provides the critical value of Reynolds number for a particular impeller showing:

$$\text{Re}_{\text{crit}} = \frac{6370}{\text{Po}^{1/3}} \quad (3.38)$$

This implies that an impeller with a high power number has a lower critical Reynolds number than an impeller with a low power number.

Comparison using power input

The information that will be of most interest to agitator designers is the type of impeller that gives the best performance in mixing fluids for the lowest power input. Re-arrangement of the data taken in the turbulent regime provides a relationship between mixing time, impeller diameter and digester scale:

$$\theta = \frac{5.20T^2}{\text{Po}^{1/3}ND^5} \quad (3.39)$$

this can be re-arranged to show:

$$\theta = 5.20 \left(\frac{T^3}{\text{Po}N^3D^5} \right)^{1/3} \left(\frac{T}{D} \right)^{1/3} T^{2/3} \quad (3.40)$$

where:

$$\theta \propto \left(\frac{1}{\bar{\epsilon}} \right)^{1/3} \left(\frac{T}{D} \right)^{1/3} T^{2/3} \quad (3.41)$$

Equation 3.41 shows comparison of impellers at equal power input and shows a large impeller with a smaller T/D ratio will give a shorter mixing time.

A similar analysis performed on the data taken in the viscous regime (Equation 3.35) shows:

$$\theta \propto \left(\frac{1}{\varepsilon}\right)^{2/3} \left(\frac{T}{D}\right)^{2/3} T^{-2/3} \quad (3.42)$$

Equation 3.39 shows that large impellers give a shorter mixing time when compared at the same power input and scale. Van de Vusse (1995) found that impellers should be as large as possible when $Re < 250$, but no information is presented on impellers greater than 50% of the digester diameter in the regime studied here, i.e. $200 < Re < 10^4$.

In the turbulent regime, at constant power input per unit mass and impeller/digester geometry, the mixing time increases with the ratio between the mixing times at large and small scale given by:

$$\frac{\theta_{\text{large}}}{\theta_{\text{small}}} = \left(\frac{T_{\text{large}}}{T_{\text{small}}}\right)^{2/3} \quad (3.43)$$

This relationship also shows that if a process is to be scaled-up at constant mixing time and geometry, the ratio in power inputs is:

$$\frac{P_{\text{large}}}{P_{\text{small}}} = \left(\frac{T_{\text{large}}}{T_{\text{small}}}\right)^5 \quad (3.44)$$

Re-arranging Equation 3.39 into the same form as Equation 3.40 shows that at constant power input per unit mass and impeller/digester geometry:

$$\frac{\theta_{\text{large}}}{\theta_{\text{small}}} = \left(\frac{T_{\text{small}}}{T_{\text{large}}} \right)^{2/3} \quad (3.45)$$

i.e. mixing time reduces as the process is scaled-up.

If a process is scaled-up at constant power input per unit mass and geometry, the ratio between the impeller speeds at large and small scale will be:

$$\frac{N_{\text{large}}}{N_{\text{small}}} = \left(\frac{D_{\text{small}}}{D_{\text{large}}} \right)^{2/3} \quad (3.46)$$

The ratio between Reynolds numbers will be:

$$\frac{Re_{\text{large}}}{Re_{\text{small}}} = \frac{N_{\text{large}} D_{\text{large}}^2}{D_{\text{small}} D_{\text{small}}^2} \quad (3.47)$$

Substituting Equation 3.43 into Equation 3.44:

$$\frac{Re_{\text{large}}}{Re_{\text{small}}} = \left(\frac{D_{\text{large}}}{D_{\text{small}}} \right)^{4/3} \quad (3.48)$$

Combining Equations 3.45 and 3.17 shows the relationship between $N\theta$ at different scales:

$$\frac{(N\theta)_{\text{large}}}{(N\theta)_{\text{small}}} = \left(\frac{D_{\text{small}}}{D_{\text{large}}} \right)^{4/3} \quad (3.49)$$

Cross multiplying the impeller speeds at the two scales and substituting Equation 3.43:

$$\frac{\theta_{\text{large}}}{\theta_{\text{small}}} = \left(\frac{D_{\text{small}}}{D_{\text{large}}} \right)^{2/3} \quad (3.50)$$

and since mixing time at constant geometry is being considered, the ratio between impeller and digester diameter is constant so Equation 3.47 can be re-written:

$$\frac{\theta_{\text{large}}}{\theta_{\text{small}}} = \left(\frac{T_{\text{small}}}{T_{\text{large}}} \right)^{2/3} \quad (3.51)$$

For a case where there is a need to design an agitator considering a constant mixing time, Equation 3.49 gives the ratio between the power requirements at the two scales:

$$\frac{P_{\text{large}}}{P_{\text{small}}} = \left(\frac{T_{\text{small}}}{T_{\text{large}}} \right)^2 \quad (3.52)$$

Use of the correlation for agitator design

Mixing times have been analyzed for $1 < 1/F_o < 10^6$ and two regimes have been identified with the boundary occurring at $1/F_o \approx 10^3$.

If $1/F_o < 10^3$, mixing time reduces with increasing scale and, if $1/F_o > 10^3$, mixing time increases with increasing scale provided power input per unit mass and impeller/digester geometry are constant. This result indicates that the optimum scale for operation of an agitator required to achieve a desired mixing time is the one that operates at the boundary between the two regimes. This is the point at which the mixing time corresponds to the minimum power input per unit mass calculated as:

$$t_m = \sqrt{\frac{10^3 \mu \theta}{\rho}} \quad (3.53)$$

The form of data correlation presented here is particularly useful because it allows comparison of various impeller types with one equation and it separates the variables determined by conditions at the impeller from those determined by the scale of operation and the desired mixing time results.

If mixing time is an appropriate design criterion for a particular mixing duty, the conditions determined by the scale of operation and process result will be known, i.e. the digester scale, T , fluid physical properties, ρ and μ , and desired mixing time, θ , are specified at the start of the design and Fourier number, F_o , can be calculated. Comparison of the calculated F_o with the $F_{o_{crit}}$ makes it possible to identify the mixing regime and find the value of $P_o^{1/3} Re$. This will allow the selection of impeller type, speed and diameter in order to satisfy the mixing time requirements for a given digestion process.

Similarly, if an existing agitator is to be rated for a mixing duty, the impeller type, P_o , speed, N , diameter, D , digester scale, T , and fluid properties ρ and μ , will be known. It is possible to calculate $P_o^{1/3} Re$, identify the mixing regime, calculate F_o and the mixing time.

The correlation shows that different impeller types will achieve the same mixing time at a given scale, provided the impellers have the same diameter and operate at the same

power input per unit mass. This is true in both the turbulent and viscous mixing regimes. Thus, there is no saving in agitator running costs by choosing one impeller type over another. The capital cost of an agitator relates to the shaft torque since the high torque requires a greater mechanical strength of gearbox, shaft and impeller. Hence, selection of an impeller that operates at low torque saves in capital cost. Equation 3.54 relates the torque, Λ , to the impeller power by:

$$P = 2\pi\Lambda N \quad (3.54)$$

When comparing two impellers at equal power input, the impeller with the higher rotational speed gives the lower torque. If a flat blade turbine, with $P_o = 3.0$, and hydrofoil, with $P_o = 0.3$ are compared at equal impeller diameter and power input, the difference in rotational speeds will be:

$$\frac{N_{A310}}{N_{FBT}} = \sqrt[3]{\frac{P_{O_{FBT}}}{P_{O_{A310}}}} = 2.154 \quad (3.55)$$

Therefore, a large diameter hydrofoil will give the most cost effective operation.

3.3.3 Mixing time and power measurement for non-Newtonian fluids

Estimation of the apparent viscosity at a particular point in a non-Newtonian fluid requires the shear rate in the fluid at that point known. One of the most important aspects of this study is to identify a method of characterizing the shear rates in mixed digester, and establish a mixing time correlation.

Examination of the Newtonian data shows the rate of mixing at probe 3, that is positioned behind a baffle controls the mixing in digester as a whole, as shown in Figure 3.4. Thus, the viscosity in this region of the digester controls the overall mixing process. A method for estimating the characteristic shear rate is therefore required in order to calculate this viscosity. Ideally, the viscosity estimation at probe 3 is required but this is very difficult. However, it is possible to relate the viscosity at the wall to baffle viscosity. The estimation of the shear rate depends on a torque balance, which equates the shear stress at the wall of the digester with the torque per unit volume.

Bird *et al.* (1990) provides an equation relating the shaft torque to the fluid viscosity, the velocity gradient (or shear rate) in the fluid at the wall and base of the digester and the pressure drop due to the fluid velocity changing as it impinges on the baffles:

$$\Lambda = \mu \iint_S R \left(\frac{\partial v_\theta}{\partial r} \right)_w dS + \iint_A RP_{baffle} dA \quad (3.56)$$

- where: v_θ tangential component of the fluid velocity
- S total surface area of the digester in contact with fluid
- A total surface area of the baffles
- R radial distance to any surface area element dS or dA from the impeller axis of rotation
- r distance measured into the fluid from any element of digester surface, dS or dA
- P pressure exerted on the baffles by the fluid

Once defined an average shear rate at the surfaces of the digester, this term can be re-written:

$$\mu \iint_S R \left(\frac{\partial v_\theta}{\partial r} \right)_w dS + \mu \dot{\gamma}_w \iint_A R dS = \tau_w \iint_S R dS \quad (3.57)$$

The definition of an average shear rate in Equation 3.57 requires the assumption of a constant shear stress at all points on the digester surface. Shamlou and Edwards (1985) measured the shear stress on the wall of an agitated tank using an electrochemical technique. The results show there is no variation of shear rate with position. Shear rate is also likely a function of impeller type. An axial flow impeller gives higher shear stresses on the base of the digester than a radial flow impeller that gives high shear stresses on the wall.

Describing Equation 3.56 in terms of three components balances with the shaft torque:

- i) the contribution of the cylindrical digester wall
- ii) the contribution of the digester base
- iii) the contribution of the pressure drop on the baffles

Therefore, the digester consists of three separate elements, each balancing a proportion of the shaft torque. If a term, G , represents the product of the area of a small element of the digester surface and its radial distance from the digester axis, then re-arranging Equation 3.56 and 3.57 gives:

$$\Lambda = \tau_w \left[\iint_{S_{cylinder}} dG_{cylinder} + \iint_{S_{base}} dG_{base} \right] + \iint_A P_{baffle} dG_{baffle} \quad (3.58)$$

In order to perform integration of Equation 3.58, the digester geometry needs simplification as shown in Figure 3.18 with the limits of each integral.

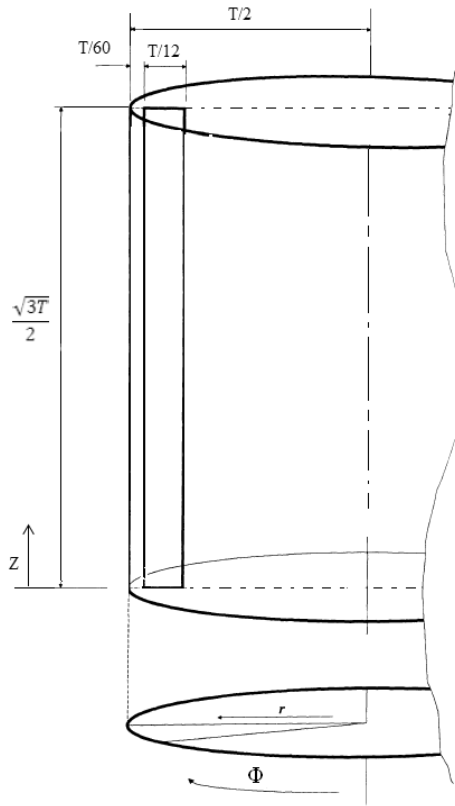


Figure 3.18: Vessel geometry used for the estimation of wall shear rate

The area of a small element of the digester wall is dS_{cy} . Therefore, the expression of the product of the surface area and radial distance for each element of the digester wall is:

$$RdS_{cylinder} = dG_{cylinder} = R((Rd\Phi)dz) \quad (3.59)$$

The limits of integration are the arc swept by the digester wall, Φ , which ranges from 0 to 2π radians, and the axial height of the digester wall, z , which ranges from 0 to $\sqrt{3T/2}$. The radial distance between the digester axis and the surface under consideration is constant for all elements and is equal to digester radius, $T/2$.

The integral equation becomes:

$$G_{\text{cylinder}} = \left(\frac{T}{2}\right)^2 \int_0^{2\pi} d\Phi \int_0^{\sqrt{3T/2}} dz \quad (3.60)$$

$$G_{\text{cylinder}} = \frac{T^2}{4} 2\pi \frac{\sqrt{3T}}{2} = 1.360T^3 \quad (3.61)$$

The area of a small element of the digester base is dS_b , and the radial distance r between the digester axis and each element varies (see Figure 3.15). Therefore, the product of the area and the radial distance for each element of the digester base is:

$$rdS_{\text{base}} = dG_{\text{base}} = r((rd\Phi)dr) \quad (3.62)$$

The radial position, r , varies from zero to $T/2$.

The integral gives:

$$G_{\text{base}} = \int_0^{2\pi} d\Phi \int_0^{T/2} r^2 dr \quad (3.63)$$

Integrating:

$$G_{\text{base}} = \frac{1}{3} 2\pi \frac{T^3}{8} = 0.262T^3 \quad (3.64)$$

Two quantities contribute to the effect of the baffles on the torque balance: the first is the area of the baffles and the second is the change in velocity of the fluid as it impinges on the baffles. The pressure drop due to the baffles presence is:

$$P_{\text{baff}} = \frac{1}{2} \rho (\Delta v)^2 \quad (3.65)$$

The area of a small element of the baffle is dA . The product of the area and the radial distance gives:

$$r dA = dG_{\text{baffle}} = r(dzdr) \quad (3.66)$$

The height of the baffles, z , ranges from zero to H and the baffles are $T/12$ wide and mounted $T/60$ off the digester wall, giving a total distance between the inner edge of the baffle and the digester wall of $T/10$. Considering one baffle, the integral is:

$$G_{\text{baffle}} = \int_0^{\sqrt{3T/2}} dz \int_{(T/2-T/10)}^{(T/2-T/60)} r dr \quad (3.67)$$

Integrating:

$$G_{baffle} = \frac{1\sqrt{3T}}{2} \left(\left(\frac{29T}{60} \right)^2 - \left(\frac{2T}{5} \right)^2 \right) = 0.03187T^3 \quad (3.68)$$

The three components of the equation combined are:

$$\Lambda = \tau_w (G_{cylinder} + G_{base}) + 4 \times P_{baffle} G_{baffle} \quad (3.69)$$

$$\Lambda = \tau_w (1.360 + 0.262)T^3 + \left(4 \times \left(\frac{\rho(\Delta v)^2}{2} \right) 0.03187T^3 \right) \quad (3.70)$$

Re-arranging Equation 3.71:

$$\tau_w = \frac{1}{1.622} \left(\frac{T}{T^3} - 0.0638\rho(\Delta v)^2 \right) \quad (3.71)$$

Application of Equation 3.71 to each data point computes the shear stress at the wall of the digester. The power-law in Equation 3.72 gives the shear rates and viscosities of the fluids:

$$\mu_w = m\dot{\gamma}_w^{(n-1)} \quad (3.72)$$

Using the wall viscosity it is possible to calculate Reynolds and Fourier numbers.

Tables 3.14 to 3.17 show the results of the pseudo-plastic mixing experiments. The tables show digester scale, the concentration used, individual probe mixing times and the root mean square mixing time for each set experimental conditions.

Table 3.14: Pseudoplastic mixing time results T/3 PBT

T(m)	HEC (%)	N (S⁻¹)	θ₁ (S)	θ₂ (S)	θ₃ (S)	θ_{Rms} (S)
0.25	0.50	8.33	81.40	89.20	768.00	740.00
"	"	10.00	17.50	18.90	670.00	601.00
"	0.25	3.33	18.00	21.10	265.00	240.00
"	"	5.00	10.20	18.20	91.60	83.80
0.50	0.50	4.17	38.80	37.90	193.00	170.00
"	"	5.50	28.50	28.70	66.00	58.50
"	0.25	3.00	17.90	18.30	39.10	29.70
"	0.75	3.33	34.70	30.30	135.00	115.00

Table 3.15: Pseudoplastic mixing time results T/2 PBT

T(m)	HEC (%)	N (S⁻¹)	θ₁ (S)	θ₂ (S)	θ₃ (S)	θ_{Rms} (S)
0.25	0.50	4.17	26.40	40.50	216.00	190.00
"	"	5.83	5.90	9.10	32.60	27.20
"	0.25	2.00	12.40	13.00	95.20	82.00
"	"	3.67	4.30	7.70	24.20	19.90
0.50	0.50	2.50	18.20	22.00	104.00	90.80
"	"	4.00	5.90	7.90	13.40	10.90
"	0.25	0.92	15.40	18.20	88.50	79.10
"	"	2.00	4.90	8.00	16.80	14.90

Table 3.16: Pseudoplastic mixing time results T/3 RT

T(m)	HEC (%)	N (S⁻¹)	θ₁ (S)	θ₂ (S)	θ₃ (S)	θ_{Rms} (S)
0.25	0.50	8.67	6.30	7.30	111.00	89.60
"	"	10.33	5.30	8.30	163.00	127.00
"	0.25	3.33	9.90	11.70	140.00	121.00
"	"	5.00	7.10	12.50	91.10	73.70
0.50	0.50	4.00	9.90	13.50	39.30	28.00
"	0.25	2.00	10.90	16.50	82.40	77.40
"	"	3.50	3.60	6.40	15.30	13.10
"	"	2.00	14.60	19.50	22.20	22.00

Table 3.17: Pseudoplastic mixing time results T/2 A310 hydrofoil

T(m)	HEC (%)	N (S⁻¹)	θ₁ (S)	θ₂ (S)	θ₃ (S)	θ_{Rms} (S)
0.25	0.50	7.50	53.10	51.50	292.00	283.00
"	"	9.17	16.50	14.30	205.00	160.00
"	0.27	3.67	18.10	28.80	117.00	111.00
"	"	5.33	11.10	14.70	93.50	84.10
0.50	0.50	3.33	23.80	25.80	71.70	61.00
"	"	5.00	39.90	28.80	47.90	44.30
"	0.25	2.00	22.60	21.50	82.00	61.00
"	"	3.00	14.50	13.50	17.70	16.80

The mixing time reported is the mean of eight repetitions. This is identical to the way in which the Newtonian data is reported. Figures 3.19-3.22 show the individual probe

results plotted as $N\theta$ versus Reynolds number. The plots include the data from water for comparison.

The plots are almost identical to Figures 3.13 – 3.16 that show $N\theta$, versus Reynolds number for the Newtonian fluids, i.e.:

- i) $Re > Re_{crit}$ $N\theta_1 \approx N\theta_2 \approx N\theta_3$
- ii) $Re < Re_{crit}$ $N\theta_1 < N\theta_2 < N\theta_3$

For this reason, the explanation given in Section 3.3.2 for the behavior of viscous Newtonian fluids applies to the behavior of pseudo-plastic fluids.

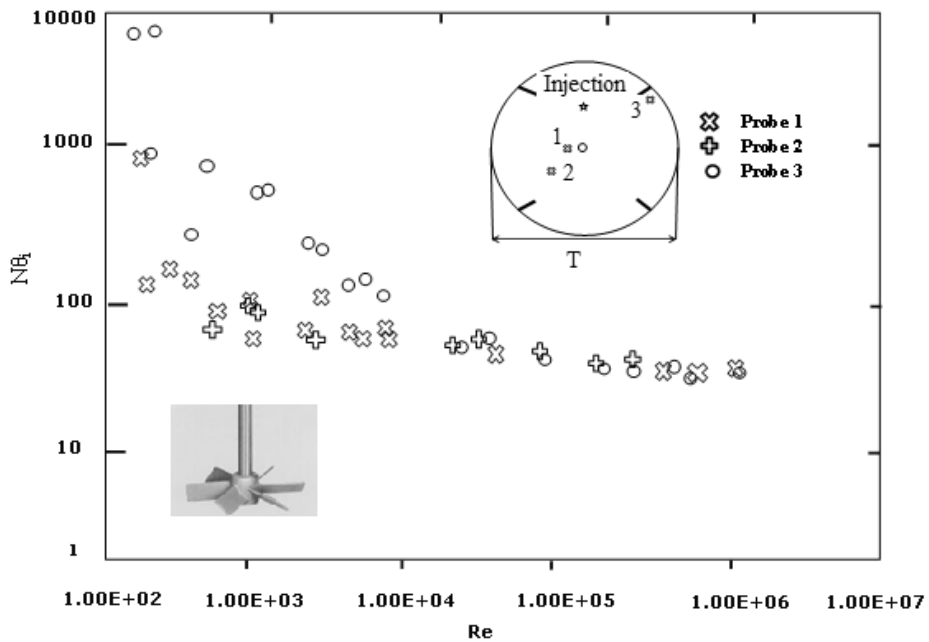


Figure 3.19: Plot of individual probe $N\theta$ versus Reynolds number-pseudo-plastic data- T/3 PBT

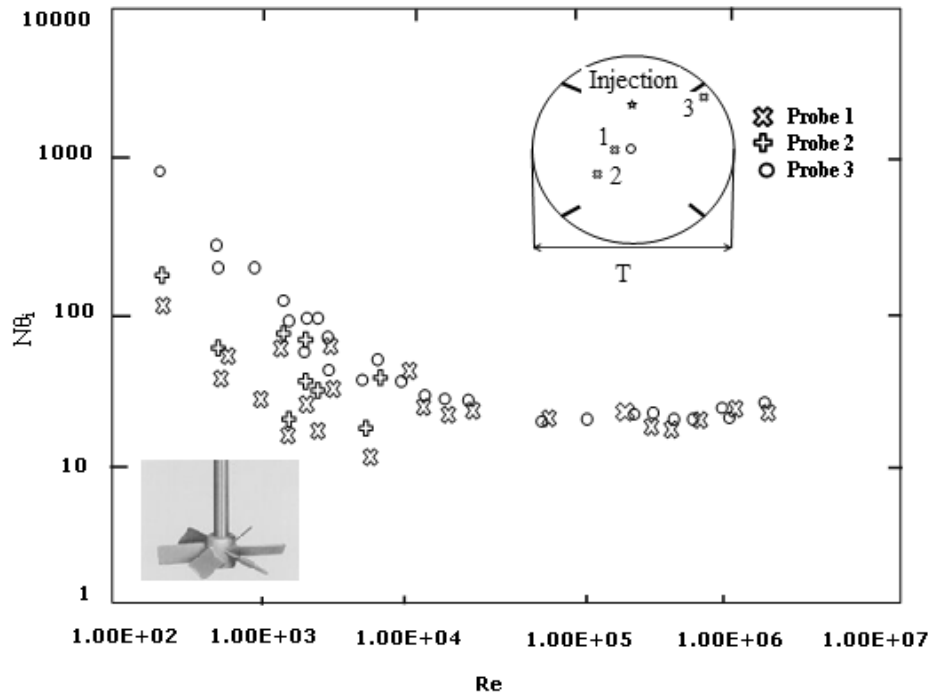


Figure 3.20: Plot of individual probe N_{0i} versus Reynolds number-pseudo-plastic data- T/2 PBT

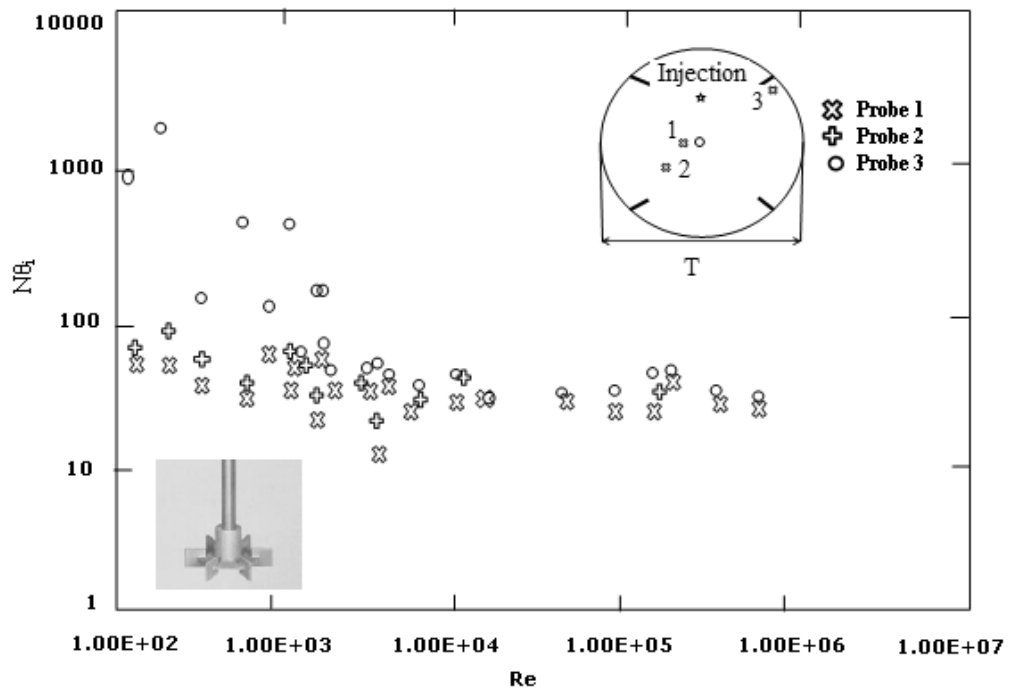


Figure 3.21: Plot of individual probe Nθ versus Reynolds number-pseudo-plastic data- T/3 RT

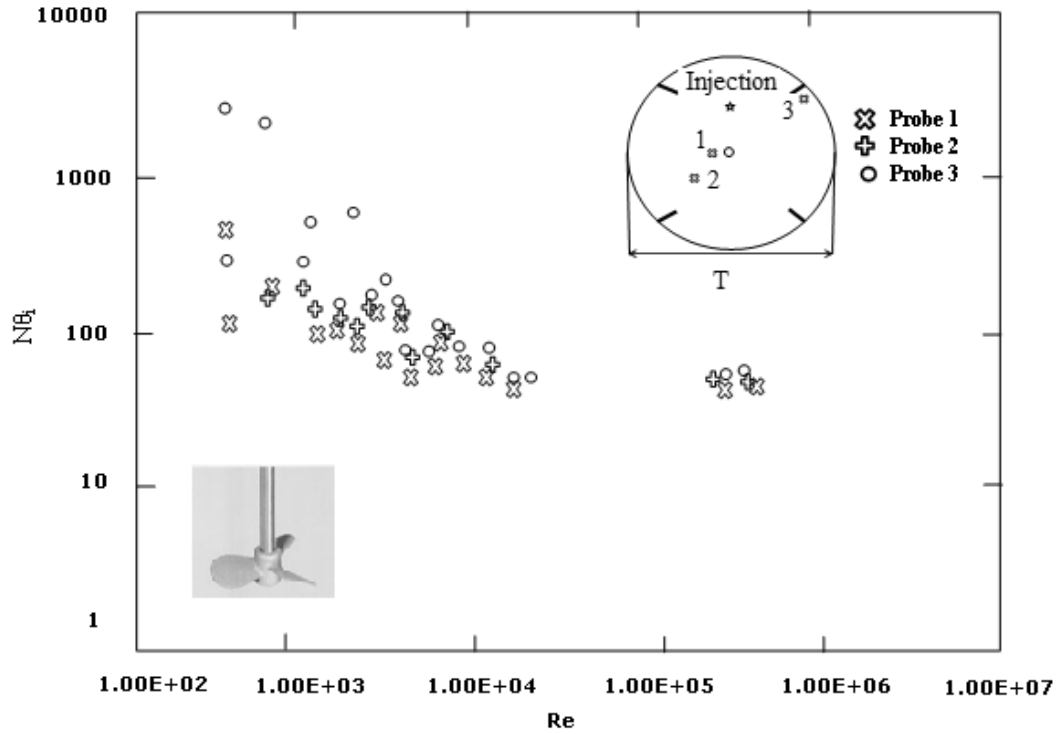


Figure 3.22: Plot of individual probe Nθ versus Reynolds number-pseudo-plastic data- T/2 A310 hydrofoil

The trends observed in the non-Newtonian root mean square mixing times are identical to Newtonian fluids, i.e.:

1. $Re > Re_{crit}$ $N\theta \approx \text{constant}$
2. $Re < Re_{crit}$ $N\theta \propto Re^{-x}$
3. the degree of divergence of the mixing times increases with decrease in Reynolds number

Table 3.18 lists the value of x for each impeller with relevant statistical information. The results are similar to Newtonian fluids with similar individual probe mixing times. The

explanation used to describe the mixing of Newtonian fluids applies to pseudo-plastic fluids.

Table 3.18: N θ versus Re regression results

Impeller	x	r² (%)	F-ratio	Data Points
T/3 PBT	-0.636	73.41	29	11
T/2 PBT	-0.842	84.94	74	14
T/3 RT	-0.894	67.23	26	13
T/2 A310	-0.96	64.21	24	14
All	-0.8	72.4	38.3	13.0

Determination of values of the two dimensionless groups, $P_o^{1/3}Re$ and $1/F_o$, requires first graphing the Newtonian and pseudo-plastic data points together. The boundary between the turbulent and viscous mixing regimes occurs at $1/F_o = 10^3$ as for the Newtonian fluids, so the data sets are also split at this value.

The turbulent data analysis uses a multiplicative regression of $N\theta$ on P_o and D/T in the same way as the Newtonian data. The result of the regression is:

$$N\theta \propto P_o^{-0.357} \left(\frac{D}{T} \right)^{1.933} \quad (3.73)$$

The correlation coefficient, r^2 , is 82.74% and F-ratio is 121 for 51 data points. After rounding-up, the constant of proportionality changed from 5.20 to 5.47 for the data described by Equation 3.26, therefore:

$$P_o^{1/3} \text{Re} = \frac{5.47}{F_o} \quad (3.74)$$

The relative standard deviation of the constant is $\pm 13.6\%$. Performing a regression of Equation 3.75 gives the correlation of the viscous data the same way as the Newtonian data:

$$P_o^{1/3} \text{Re} \approx 1/F_o^y \quad (3.75)$$

and Table 3.19 illustrates the results from regression.

Table 3.19: Correlation results

Impeller	y	r² (%)	F-ratio	Data Points
T/3 PBT	-0.58	94.76	182.00	11
T/2 PBT	-0.52	96.29	338.00	14
T/3 RT	-0.48	90.80	119.00	13
T/2 A310	-0.43	84.89	74.00	14
All	-0.45	89.71	463.00	52

Experimental data fit well, using an exponent of -0.5. Table 3.20 shows a comparison of constants obtained from exact y values and y = -0.5 correlations. Using -0.5 does not significantly worsen the standard deviation of the correlation allowing the presentation in this form. The correlation for all the viscous data (Newtonian and pseudoplastic) is:

$$P_o^{1/3} \text{Re} = \frac{193}{\sqrt{F_o}} \quad (3.76)$$

The relative standard deviation of the constant is $\pm 32.5\%$.

Table 3.20: Comparison of constants

Impeller	kx	r² (%)	F-ratio	RSD %
T/3 PBT	141.4	21.09	193.7	24.68
T/2 PBT	171.9	18.89	183.5	19.43
T/3 RT	188.6	30.4	175.8	31.17
T/2 A310	265.7	30.16	206.6	38.68
All	237.2	32.19	200	38.36

In addition, comparison of the Newtonian and pseudo-plastic data sets for each impeller using the "Student's t-test" shows no statistical difference at the 95% confidence level.

Analysis of the Newtonian data discussed in the previous chapter shows that the longest mixing time occurred behind the baffle and this region controls the mixing time of the digester. Mixing times measured in the bulk of the digester and near the impeller are much shorter than the limiting mixing time. For this reason, the analysis of the pseudo-plastic mixing time data started with finding a method of estimating the fluid viscosity in this longest mixing time region of the digester.

The method used to estimate the wall shear rate and viscosity applies torque balance between the shaft and the baffles and digester surfaces. Elson (1990) used the same method to correlate mixing data taken in yield stress fluids although there is no consideration of the baffles in the analysis. Ignoring the baffles resulted in the worse correlation between the Newtonian and pseudo-plastic data.

The definition of Fourier number, based on wall viscosity is sensible because it contains the controlling mixing time and the viscosity in the region of the digester where this mixing time occurs. Reynolds number determination considers the conditions at the impeller and therefore, includes the viscosity of the fluid in the impeller region. Defining Reynolds number with the wall viscosity gives a ratio of the inertial forces produced by the impeller and the viscous forces in the fluid in this region of the digester. This is sensible because, this approach accounts for the region of the digester where the controlling mixing time occurs.

Comparison using power input

As mentioned in the Section 3.3.2, the information of most interest to agitator designers is the type of impeller that gives the best performance in mixing fluids for the lowest power input. The conclusion drawn from the Newtonian mixing time data are:

- i) for a given process operated at constant geometry (D/T) and scale, there is no saving to be made in operating cost because mixing time is dependent on power input. A large diameter impeller will achieve a desired mixing time for less power than a small impeller.
- ii) for a given process, there are potential savings to be made if an impeller with a low power number is chosen because it must operate at a higher speed to input the same power as an impeller with a high power number.

These conclusions apply to the turbulent and viscous regimes.

Re-arranging Equation 3.76 indicates:

$$\theta \propto \left(\frac{1}{\varepsilon}\right)^{2/3} \left(\frac{T}{D}\right)^{2/3} \frac{\mu_w}{\rho} T^{-2/3} \quad (3.77)$$

This equation is identical to Equation 3.42 for Newtonian fluids. The fluid physical properties do not appear in Equation 3.42 because they are constant for a Newtonian fluid. They must be included during a pseudo-plastic fluid investigation because they will vary depending on the impeller type used to mixing the fluid. The derivation of the wall viscosity shows that its value is a function of the torque acting on the agitator shaft i.e. the higher the torque, the higher the wall shear rate and the lower the wall viscosity.

Considering mixing duty at constant power input per unit mass and geometry, (i.e. D/T is constant) and a given scale, the wall viscosity of the fluid will determine the mixing time. An impeller that minimizes the wall viscosity at a given power input will achieve a shorter mixing time. Comparing the three impellers tested at equal power input per unit mass, the $T/2$ pitched blade turbine produces the highest torque. The results of the mixing time measurements show that it is the best impeller to use for pseudo-plastic mixing duties. In fact, the results imply that an impeller with a higher power number would be even more efficient for mixing these fluids.

The results of the mixing time experiments show how important the measurement of fluid rheology is to agitator selection and design. Equation 3.76 shows how the mixing time varies with the viscosity of the fluid at constant power input per unit mass and impeller/digester geometry:

$$\theta \propto \mu_w \propto K \dot{\gamma}_w^{n-1} \quad (3.78)$$

Combination of Equation 3.72 and Equation 3.73 shows the relationship between the fluid's power law constant and index and the agitator shaft torque at constant scale:

$$\dot{\gamma}_w \propto \left(\frac{\Lambda}{K} \right)^{\frac{1}{n}} \quad (3.79)$$

3.3.4 Suspension of high concentration non-Newtonian fluid in agitated AD

Specific power consumption for a given power per solids mass, ε , given in units of W/kg is defined here to compare the energy efficiency in suspending solids for various designs and operational conditions, applicable to AD. A lower specific power input, implies less energy requirement for suspending a given unit mass of solids in a mixed digester. The specific power consumption at “just-suspended” condition is:

$$\varepsilon_{js} = \frac{2\pi N_{js}(T_m - T_r)}{M_s} \quad (3.80)$$

where M_s is the mass of solids in kg of suspended in the agitated digester system.

The reaction rate is controlled by specific solid surface area of solids in anaerobic digester and hence the result analysis uses the specific power input expressed on the basis of total mass of solids suspended, P_{js}/M_s . Therefore, the aim is to use the specific power expressed on the basis of mass of suspended solids to determine the optimum solids concentration to be used in baffled and unbaffled anaerobic digesters, investigate

the relationship between P_{js}/M_s , and investigate the effects of variables such as particle size, impeller type and number of impellers on P_{js}/M_s . The results are applicable to the overall goal of developing optimum agitator designs to minimize the power consumption for suspending unit mass of solid particles in mixed anaerobic digesters, where the off-bottom solids suspension is a limiting factor.

3.3.4.1 Effect of solids concentration on specific power

Figure 3.23 shows agitation power per unit slurry volume, P_{js}/Vol , required to just-suspend spherical glass particles of diameter 12 mm off the digester bottom, as a function of solids concentration. The impeller is a PBT. The power required to suspend solids increases with solids concentration. The value of P_{js}/V increases gradually with increase in concentration of up to 0.3 v/v, and thereafter it increases rapidly as the concentration approaches 0.50 v/v, approaching the packing coefficient of 0.58 v/v.

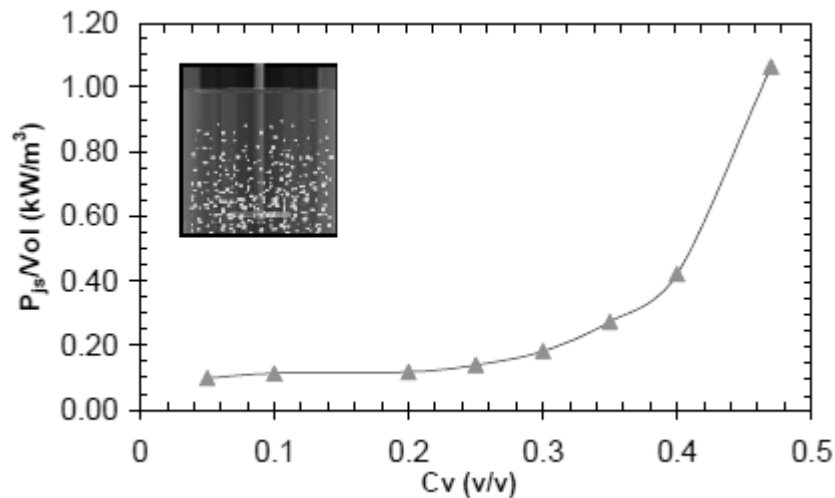


Figure 3.23: Effect of solids concentration of glass particles of $d = 12$ mm in non-Newtonian HEC solution on agitation power per unit slurry volume of a baffled digester equipped with a PBT impeller

The reason for the high power requirement at high C_v is the high energy loss due to particle-liquid friction, particle-particle collisions and particle-equipment collisions at high-solids concentration (Bubbico *et al.*, 1998). Figure 3.24 shows the plot of experimental specific power, ϵ_{js} , as a function of the solids concentration for a PBT impeller. It is interesting to note that the ϵ_{js} does not increase with solids concentration as is usually expected. Instead, ϵ_{js} decreases with increase in solids concentration until it reaches a critical value of 0.25 v/v and increases again beyond the critical value. The specific power ϵ_{js} at 0.05 v/v is three times greater than that at the critical solids concentration, 0.25 v/v. More solids are suspended per unit of impeller power input (kg solids/W) compared to those at lower C_v values. In other words, about 0.1 kg solids can be suspended per Watt of power at 0.25 v/v while only 0.02 kg solids can be suspended per Watt of power at a lower C_v of 0.02% (v/v). These results indicate that the energy efficiency of solid-liquid mixing vessels can be increased by operating the digester at higher solids concentrations than previously thought.

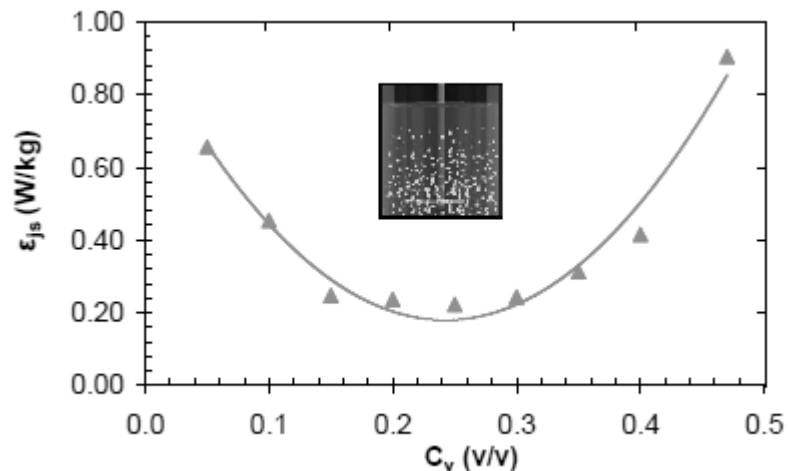


Figure 3.24: Effect of solids concentration on specific power, ϵ_{js} , for a baffled AD using a PBT impeller and glass particles of $d = 12\text{mm}$ in HEC solution as obtained in this study

3.3.4.2 Effect of impeller type on specific power

For the sake of simplicity, the solids concentration corresponding to the minimum specific power is defined as Optimum Solids Concentration (OSC). OSC represents a suitable solids loading for a given agitation system to achieve efficient power consumption. Kasat and Pandit (2005) suggested that the choice of a proper impeller to satisfy the requirement of solids suspension with minimum power requirement is the key to the economical operation of the process. Figure 3.25 shows ϵ_{js} values as a function of solids concentration for RT, PBT and A310 impellers, respectively in the presence of baffles. The results confirm the existence of OSC for all three types of impellers and the values are 0.35 for RT, 0.30 v/v for PBT and A310 impellers. The corresponding minimum ϵ_{js} values at OSC for RT, PBT and A310 impellers are 0.79, 0.23, and 0.21 W/kg, respectively. The effect of solids concentration on ϵ_{js} is more pronounced for RT as demonstrated by the U-shaped curve in Figure 3.25. For all solids concentration investigated, 0.05 to 0.4 v/v) ϵ_{js} values are highest for RT followed by PBT impellers, while the A310 impeller has the lowest ϵ_{js} values. A relatively flat curve observed for A310 suggests that the effect of solids concentration on ϵ_{js} is not as significant as on the other two impellers.

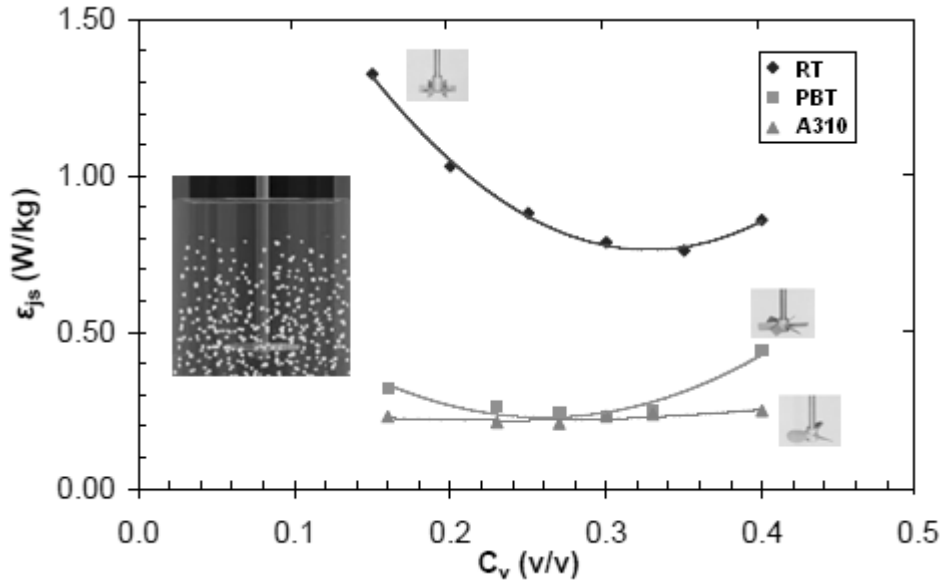


Figure 3.25: Effect of impeller type on specific power, ϵ_{js} , for glass particles of $d = 12$ mm baffled scaled digester investigated

Figure 3.26 shows ϵ_{js} values as a function of solids concentration for the three impellers on the absence of baffles. The figure shows that there is OSC for all three impellers. However, RT is more energy efficient than PBT ($N_p = 1.220$) and A310 ($N_p = 0.32$) irrespective of the solids concentration. While the difference in ϵ_{js} values for the impellers is obvious at low-solids concentrations of less than 0.2 v/v, the difference becomes marginal as C_v approaches a concentration of 0.4 v/v. At C_v of 0.4 v/v, the three impellers consume approximately the same amount of power.

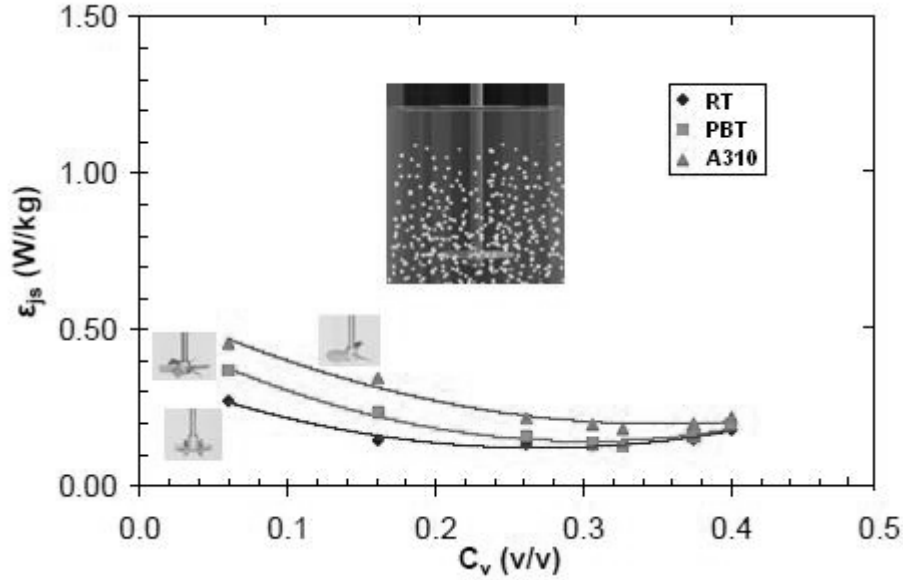


Figure 3.26: Effect of impeller type on specific power, ϵ_{js} , for different concentration loadings obtained using scaled digester without baffles, non-Newtonian HEC solution and spherical glass particles of 12 mm diameter.

3.3.4.3 Effect of baffle removal on specific power

While the significance of adequate baffling in solid-liquid agitated systems is frequently discussed in literature, little quantitative information has been published. To investigate the effect of baffle removal on specific power, a specific power enhancement factor R_ϵ is introduced and defined as follows:

$$R_\epsilon = \frac{\Delta\epsilon}{\epsilon_{js(baffle)}} = \frac{\epsilon_{js(baffle)} - \epsilon_{js(no\ baffle)}}{\epsilon_{js(baffle)}} \quad (3.81)$$

where $\epsilon_{js(baffle)}$ and $\epsilon_{js(no\ baffle)}$ are the specific power values with and without baffle, respectively.

The effect of removing baffles on specific power is illustrated in Figure 3.27 using a plot of R_ϵ versus solid concentration C_v (v/v). The figure shows that $R_\epsilon > 0$ for all the cases studied. These results suggest that the specific power required for suspending solids off the digester bottom generally decreases upon the removal of baffles over 0.15 to 0.4 v/v solids concentration investigated. The results further imply that improvement in energy efficiency for solids suspension can be accomplished by removing baffles for all types of impellers. The effect of removing baffles is more pronounced at low concentration for RT. An increase in solids concentration results in a reduction in R_ϵ for RT, which is opposite to the finding using the PBT impeller. For A310 impeller, an increase in solids concentration leads to an increase in R_ϵ between 0.15 and 0.3 v/v, and beyond that it leads to a decrease in R_ϵ . Of all the impellers used, RT is the most sensitive to baffles removal irrespective of solids concentration. The value of $R_\epsilon = 0.79$ at $C_v = 0.40$ v/v suggests that almost 80% energy saving can be achieved for the RT impeller by removing the baffles.

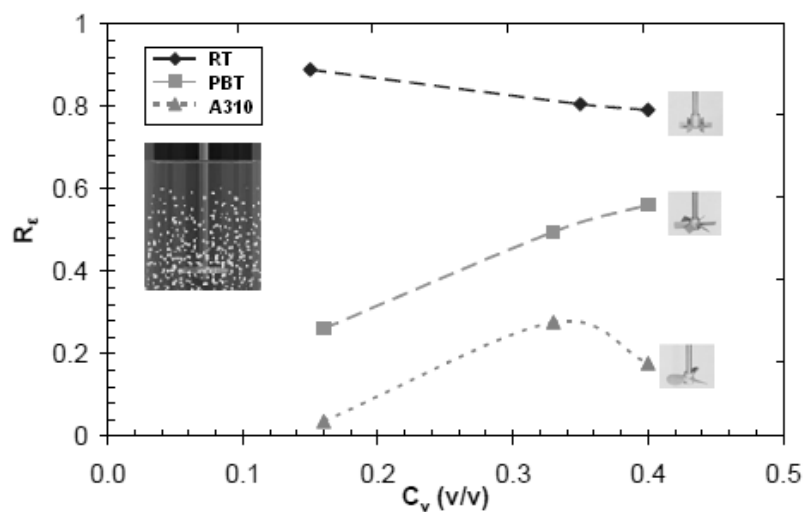


Figure 3.27: Specific power enhancement factor R_ϵ vs. solids concentration of glass particles of 12 mm diameter at just-off-bottom solids suspension condition.

3.3.4.4 Effect of impeller dimension (D/T) on specific power

The solids suspension in agitated vessels relies on both liquid flow and turbulence. It is expected that the turbulence intensity decays along the length of the flow path. An increase in the impeller diameter results in less decay in the turbulence owing to a reduction in path length. On the other hand, a decrease in impeller diameter will result in the reduction of liquid velocity. Figure 3.28 shows the effect of impeller diameter on ϵ_{js} in a digester equipped with baffle, A310 impellers with diameters of 0.16 and 0.18 m. The solids concentrations range from 0.1 to 0.4 v/v. In the digester equipped with baffle, the effect of impeller diameter is insignificant on ϵ_{js} at relatively high solids concentrations for $C_v > 0.30$. However, at lower solids concentration, the ϵ_{js} required for the smaller diameter impeller with $D/T = 0.41$ is lower.

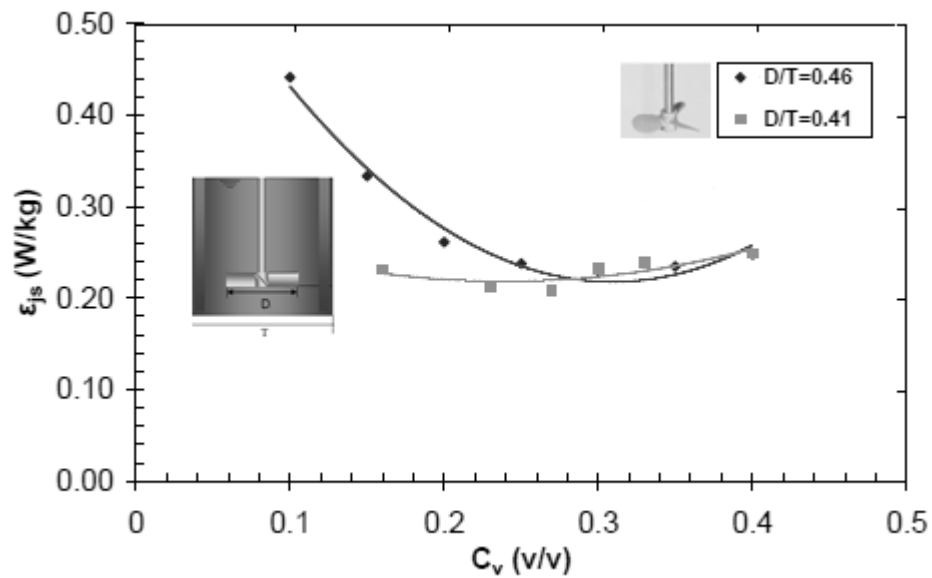


Figure 3.28: Effect of impeller diameter on specific power, ϵ_{js} , for two impeller dimension to tank diameter ratios, D/T , and for increasing concentration of 12 mm diameter spherical glass particles using the A310 impeller, baffled scaled AD, and non-Newtonian fluid

For the digester without baffle shown in Figure 3.29, an increase in impeller diameter leads to a reduction of $\approx 3\%$ in specific power ϵ_{js} over a wide range of solids concentrations investigated. The parallel curves indicate that the ratio of power consumption for two impellers with different diameters is fairly constant with increase in solids concentration in the absence of baffles.

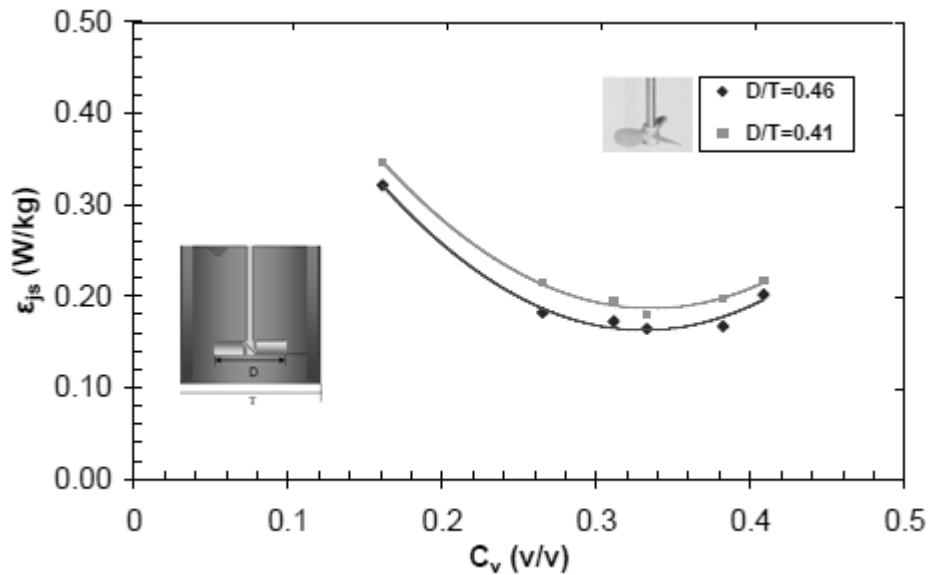


Figure 3.29: Effect of impeller diameter on specific power, ϵ_{js} , for two impeller dimension to tank diameter ratios, D/T , and for increasing concentration of 12 mm diameter spherical glass particles using the A310 impeller, unbaffled scaled AD, and non-Newtonian fluid

3.3.4.5 Effect of multiple impellers on specific power

In some anaerobic digestion systems, digesters are equipped with multiple impellers to ensure even distribution of shear and energy dissipation rates. Figure 3.30 shows the specific power data for a digester without baffle equipped with single and dual A310 impellers for D/T of 0.41 as a function of C_v (v/v). It is interesting to note that the optimum value for both cases is for a concentration of 0.33 (v/v) with the same diameter. The presence of an additional impeller at concentrations less than 0.3 v/v resulted in

more power input due to the interference of flow patterns generated by both impellers. However, it can be said that the increase in power due to the presence of an additional impeller is marginal (< 3%) at high solids concentration.

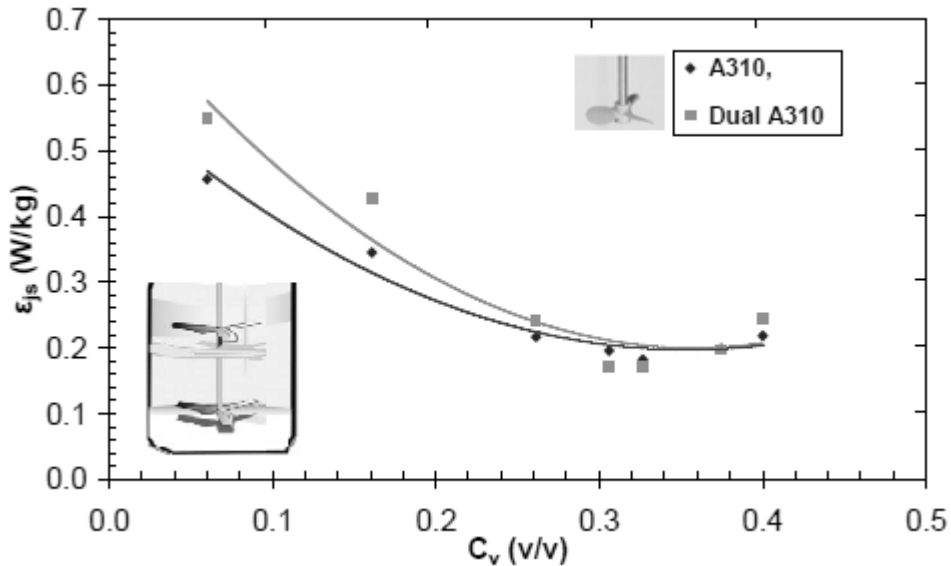


Figure 3.30: Effect of dual impellers on specific power, ϵ_{js} , in scaled AD without baffle equipped with A310 impeller, glass particles of diameter of A310 impeller and non-Newtonian HEC solution ($C_1 > 0.17T$ and $C_2 < 0.385T$)

Further simulations showed that the geometrical parameters C_1 (off-bottom clearance of the lower impeller), C_2 (separation between the two impellers) and C_3 (submergence of the upper impeller below the top surface) strongly affect the overall flow structure in the digester. The parallel flow pattern, with four ring vortices (impellers essentially not interacting) was obtained for $C_1 > 0.20T$ and $C_2 > 0.385T$. The merging flow pattern, with only two large ring vortices, was obtained for $C_1 > 0.17T$ and $C_2 < 0.385T$. Finally, the diverging flow pattern was obtained whenever $C_1 < 0.15T$ and $C_2 > 0.385T$. For intermediate configurations, unstable flow patterns were observed, alternating between any two or all three of the above regimes.

3.3.4.6 Effect of particle size on specific power

In a digester without baffle, the influence of particle size, d_p , on specific power, ϵ_{js} , for the three impellers investigated is shown in Figures 3.31 to 3.33. From these results, it can be concluded that an increase in particle size results in an increase in power consumption, irrespective of the impeller type and solids concentration. This is because larger particles settle faster and more power is required to create stronger upward fluid velocity to keep the particles circulating.

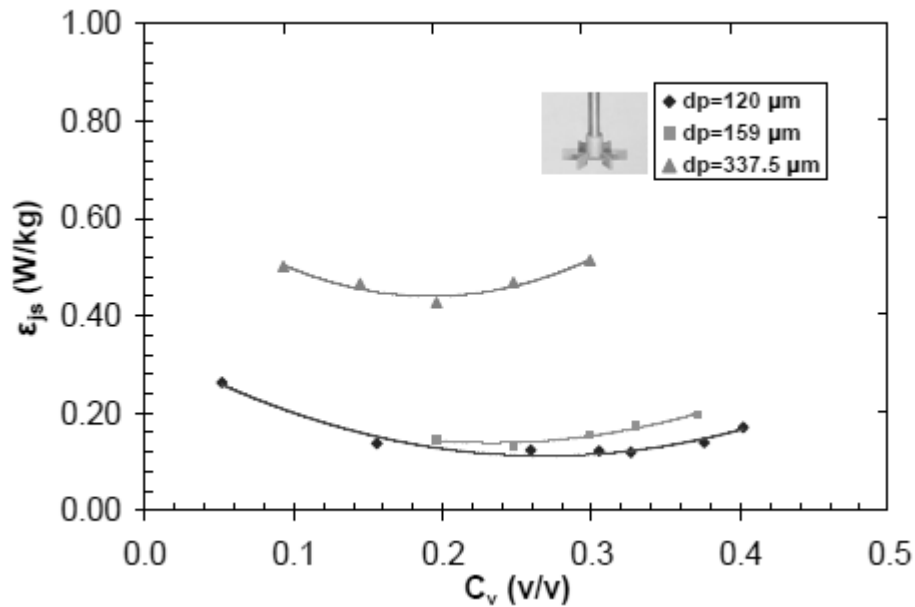


Figure 3.31: Effect of particle size, d_p , on specific power consumption, ϵ_{js} , using an RT impeller, no baffles, and non-Newtonian fluid

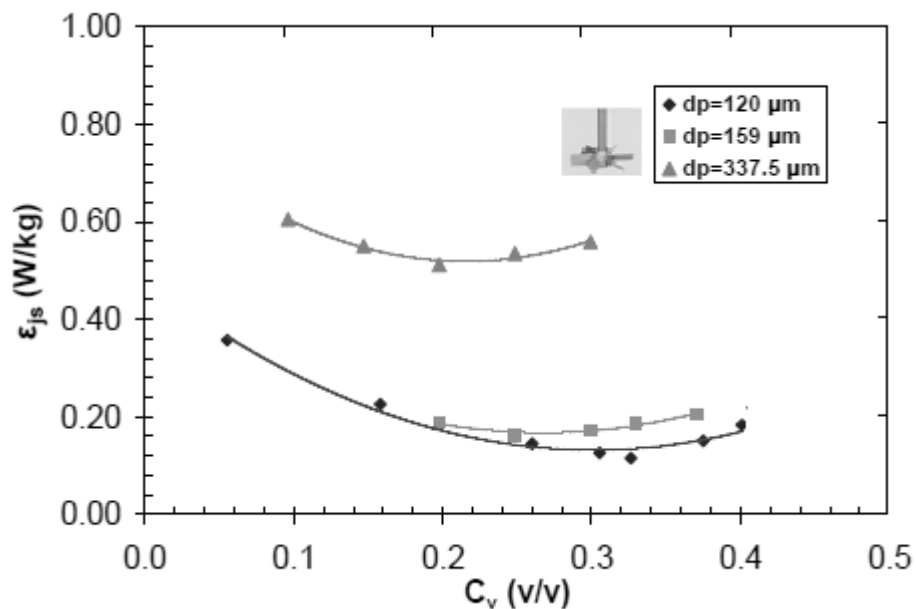


Figure 3.32: Effect of particle size, dp , on specific power consumption, ϵ_{js} , using an PBT impeller, no baffles, and non-Newtonian fluid

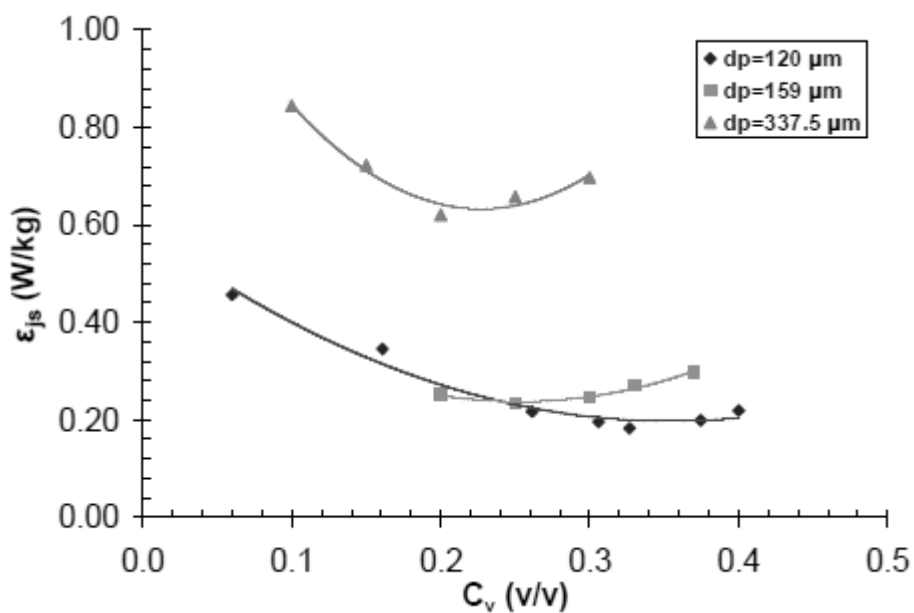


Figure 3.33: Effect of particle size, dp , on specific power consumption, ϵ_{js} , using an A310 impeller, no baffles, and non-Newtonian fluid

Figure 3.34 summarizes the influence of particle size on optimum solids concentration and the corresponding specific power. OSC is not affected by the impeller type for a given d_p in the absence of baffle and decreases with an increase in particle size, irrespective of the impeller used. In addition, the specific power increases dramatically with an increase in particle size.

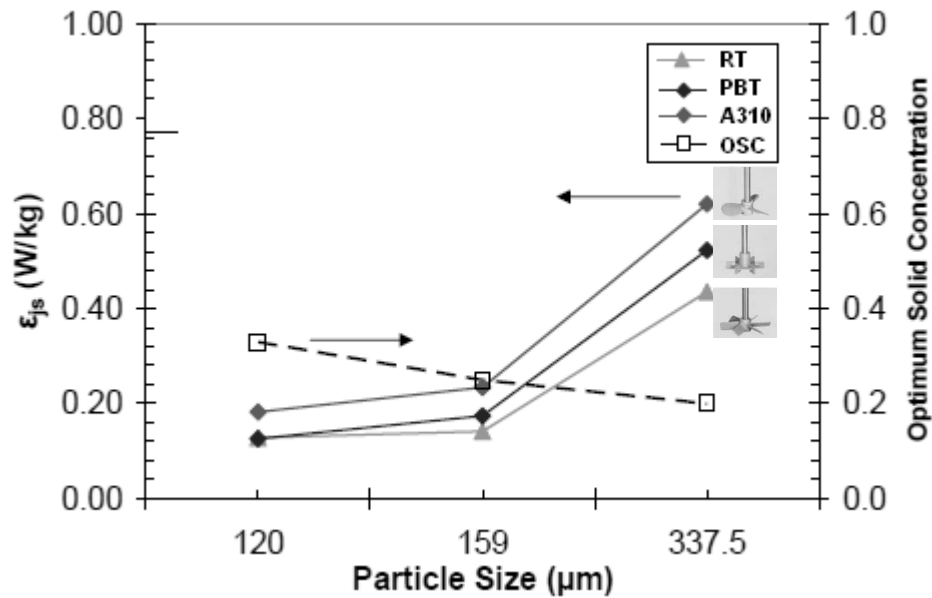


Figure 3.34: Minimum power consumption, optimum solids concentration vs. particle size, at just-off-bottom solids suspension condition in lab-scaled digester equipped various impellers without baffle

3.4 Conclusion

The contributions this chapter makes to the scientific literature and design practitioners are:

- The analysis of the effect of power input on mixing time shows that there are potential savings in the capital cost of an agitator by selecting an impeller with a low power number.

- The turbulent and viscous data are correlated and re-arranged to show that the mixing time is determined by the power input per unit mass, impeller to vessel diameter ratio and the scale of the vessel.
- In turbulent mixing, for a given power input and impeller geometry, mixing time increases with increasing scale. In viscous mixing, there is an effect of the fluid's viscosity at the wall of the digester.
- An impeller with a high power number, and shaft torque, produces a lower viscosity and therefore, a shorter mixing time for a given power input. Thus, there are savings in operating costs if a high power number impeller is used to mixing a pseudo-plastic fluid.
- The specific power required for the complete suspension of solids is studied over a range of solids concentration and particle size. The specific power required for just-off-bottom suspension increases rapidly with the solids concentration for $C_v > 0.3$ v/v when the power is determined on the basis of total volume of the suspension.
- When the power input is considered in terms of the mass of solids suspended in the mixed digester, the specific power decreases with solids concentration until a critical value is reached and increases thereafter. This observation is confirmed for radial, mixed and axial flow impellers under baffled and unbaffled conditions.
- Higher power number radial impellers are found to be more energy efficient than lower power number axial impellers for suspending fine particles for the unbaffled condition.

- The effect of removing baffles is more significant at low concentration for the radial flow impeller, RT, because it leads to significant reduction in its specific power.
- At higher solids concentration, there is a reduction in specific power of the RT impeller due to the removal of baffles, but the magnitude of reduction is not as significant as that at low solids concentration.
- Of all the impellers used, the radial flow impeller, RT, is the most sensitive to the removal of baffles irrespective of the solids concentration. These results imply that RT is the most energy efficient under unbaffled condition compared to axial and mixed flow impellers.

4. Investigation of unmixed zone in mixed anaerobic digester

Inadequate design and improper mixing in digesters often lead to poor mixing and digester failures due to the presence of dead zones formed. Tenney and Budzin (2002) found that about half of the primary digester volume can be stagnant using water as working fluid. Monteith and Stephenson (1981) reported that dead zones comprised 77% of the volume available for active mixing and 61% of the digester input is not treated properly due to short-circuiting. Concentrating the sludge could be one of the solutions but thicker sludge may upset the digesters more often. The problem of such inefficient mixing in mechanically mixed ADs is associated with the formation of segregated mixing regions in high viscous liquid (manure) and it usually occurs between low to moderate Reynolds numbers.

These segregated structures cause substantial material and financial losses to the digestion process industries. The knowledge on the phenomena of unmixed region in ADs working with manure characterized by non-Newtonian behaviour and the practical techniques required to destroy them is lacking. Therefore, this Chapter aims to investigate and contribute to the knowledge of:

- i. The formation and evolution of unmixed regions in ADs resulting dead zones,
- ii. effect of impeller speed modulation, influence of impeller type, baffle configuration and temperature variation on the behaviour of unmixed regions, and
- iii. strategies for the destruction or minimization of unmixed regions in ADs.

In order to achieve these objectives an acid-base reaction is used to observe the formation and degeneration of unmixed regions in lab-scaled ADs. A fluorescent green dye is used as a passive tracer to enable flow visualization of unmixed regions. Experiments are carried out using steady state impeller speed and different impeller speed modulation. Two waveforms, namely square and sine wave modules, are used for speed modulation. Both amplitudes, Re_{max} and Re_{min} , and the wave period in the speed modulation protocols are varied to investigate the effects of unsteady stirring on mixing performance. The size and the volume of segregated mixed regions are determined using digital video images captured during the mixing process. The dimensionless mixing time, N_{tm} , which corresponds to the disappearance of the isolated unmixed regions, is determined using the video images obtained at various time intervals.

Section 4.1 details the laboratory scale experimental set-up followed by the methodology described in Section 4.2. Section 4.3 describes the results with their corresponding discussions. Finally, Section 4.4 represents the conclusions drawn from the investigation performed. Table 1.3 in Chapter 1 shows how this section integrates into an overall research approach to quantify the effect of mixing and its impact on AD.

4.1 Scaled laboratory experimental set up

The flow visualization experiment uses the same lab-scale digester as the one used for measurement of mixing time and power in Chapter 3. The digester is located inside an acrylic square tank to reduce distortions. The same working fluid fills the square tank to

minimize the optical distortions due to the curvature of the inner cylindrical digester wall. Figure 4.1 shows the schematic diagram of 0.25 m digester.

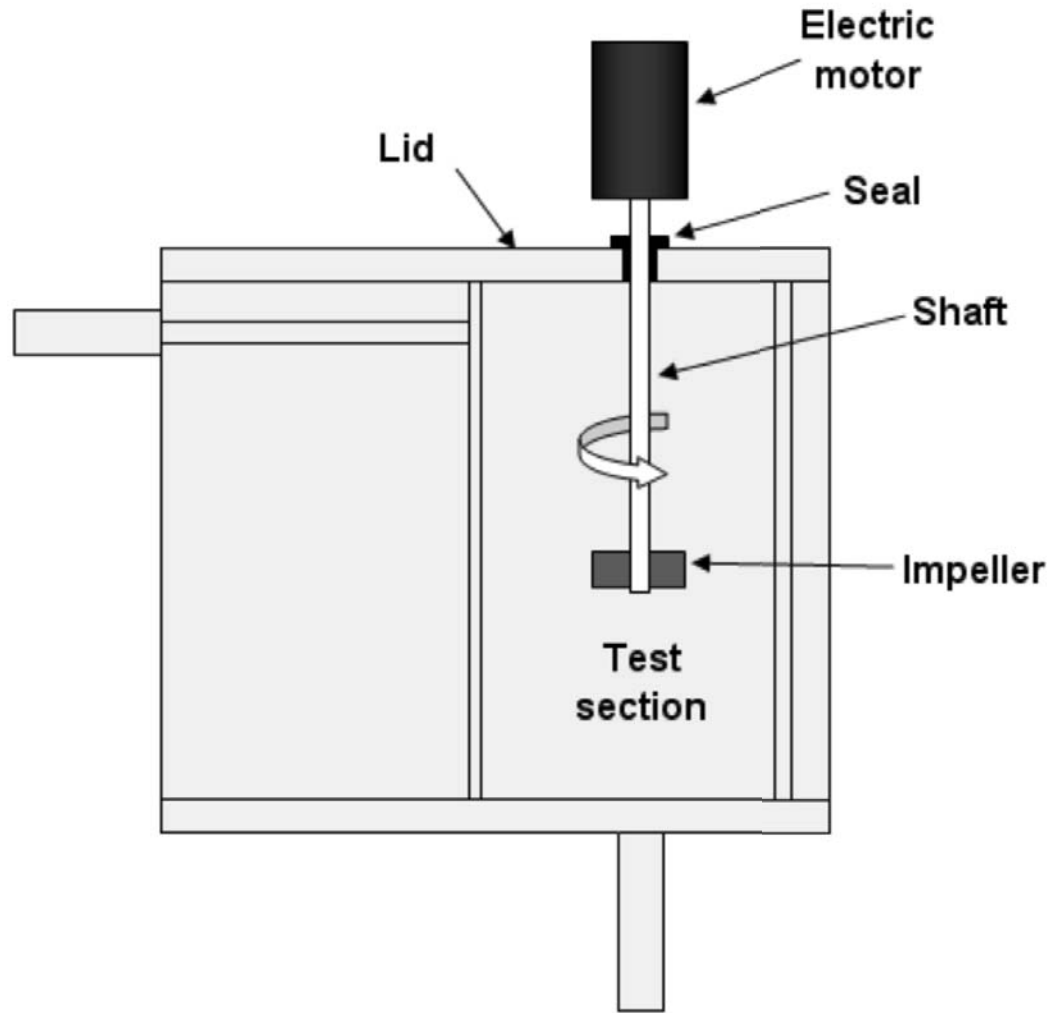


Figure 4.1: Schematic of experimental set-up used to investigate unmixed zones in mixed anaerobic digesters using a scaled circular AD incased in a rectangular tank to prevent visual distortions (instrumentation not shown)

The operating liquid height in the digester is equal to the digester diameter in all the experiments. The lab-scale digester uses a six-blade Rushton Turbine (RT) with diameter of 100 mm mounted on a central shaft driven by a motor (FREQROL-U100

Series). The rotational speed of the motor varies from zero to 500 rpm. Figure 4.2 shows the dimensions of the impeller used for this study.

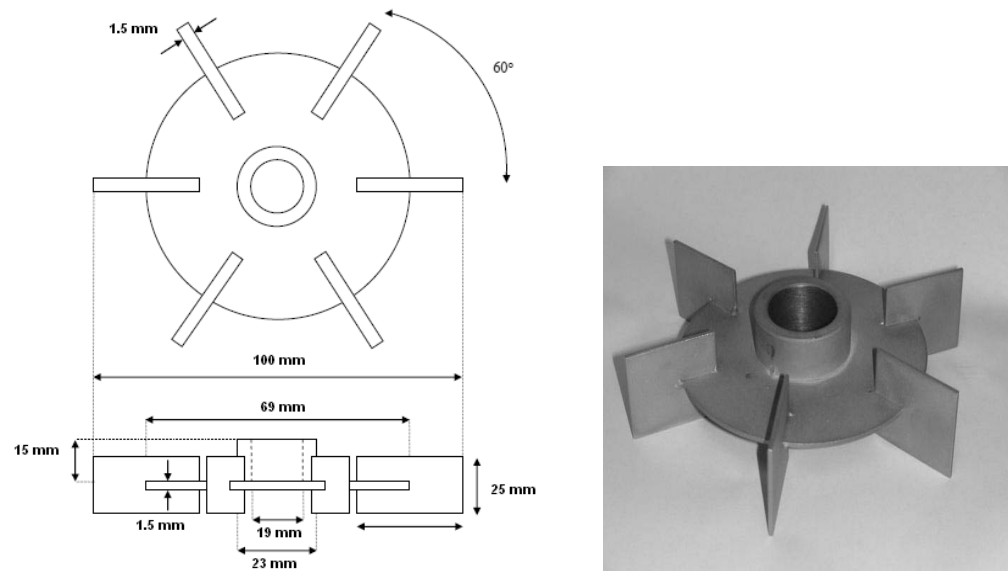


Figure 4.2: Dimensions of 6-blade Rushton Turbine RT impeller used to investigate unmixed zones in mixed anaerobic digesters

4.2 Methodology

To investigate unmixed zones and flow mixing patterns in mixed anaerobic digesters, a lab-scaled digester using a HEC-aqueous-manure-simulant that represent the non-Newtonian manure is used. Furthermore, the methodology employs a non-intrusive technique based on direct visualization of an acid-base reaction to measure mixing times for baffled and unbaffled lab-scale AD.

The lab-scale digester is 0.25 m in diameter equipped with a Rushton turbine, RT and Pitched Blade turbine (PBT), which provides the mixing. The passive tracer in all experiments is fluorescein, which is a fluorescent pH sensitive and neutrally buoyant

pink dye. Approximately 5 g of fluorescein powder is homogenously mixed with 500 mL of HEC solution. Filtering the solution removes solid particles before pouring it into the scaled digester. Then, the mixture solution remains in the digester for 24 hr. This helps the release of any air bubbles trapped during the filling process. Adjustment of the pH value of the solution to basic requires addition of 40 – 70 mL of 1M NaOH depending on the pH of the original solution. Application of a constant stirring for 30 min at 300 rpm results in a uniform fluorescent pink colour. The pH meter displays a steady value when the solution is homogenously mixed.

A pH-temperature probe placed at different locations in the digester allows the determination of the spatial variations of pH and temperature of the mixing fluid. Computation of average values of pH and temperature uses the respective measured values. Subsequently, a 10 mm tube placed next to the impeller shaft injects 40 – 70 mL of 1M HCl. The unmixed regions show up immediately following the injection of acid solution because of the diffusion limitation caused by the highly viscous HEC solution.

A black cardboard covers the entire surface of the square outer acrylic tank except the front side facing the video camera. The cardboards on both sides had 5-mm slits at the centre to allow the formation of a plane sheet of light across the lab-scale digester. Figure 4.3 illustrates the flow visualization achieved by illuminating both sides of the digester using 650W Arri IP23 lamps in an otherwise dark room. A Sony Digital HD video camera recorder (HDR-SR5E) captures the image of the flow. The position of the camera is the front side of the digester perpendicular to the plane sheet of light. It

records the evolution and dynamics of the unmixed mixed regions. The digitized periods obtained from the recorded digital video determines decolourization time of the acid-base reaction.

The test uses an impeller speed operating under steady state or dynamic conditions. A PC computer running LabView allows controlling the speed of the impeller. The control system involves operating the impeller consisted of a dual variable frequency drive controller (Model 001) connected to a three-phase electric motor. Using this arrangement, variation of both the amplitude and wave period of a speed modulation scheme is possible.

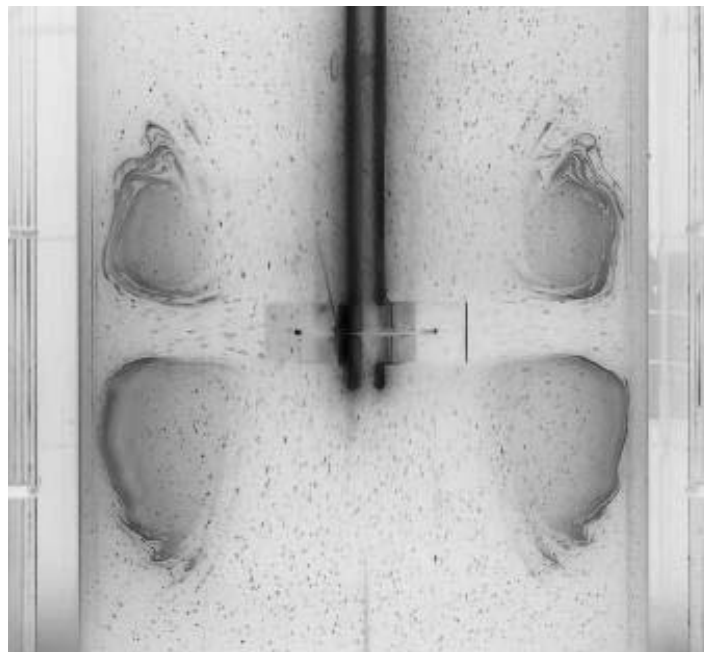


Figure 4.3: Flow visualization of acid–base reaction revealing the unmixed regions containing NaOH appear as dark pink structures whereas chaotic acidic regions that are well mixed appear as light areas. The round scaled digester is encased inside a rectangular tank filled with water to prevent distortion, as seen in the left and right side of the figure.

Analysis of the digital video images of unmixed regions allows the determination of the efficiency of the mixing process. It is also possible to obtain the boundary for the unmixed regions at defined time intervals for each experimental run.

The flow visualization technique allows the estimation of the volume of the unmixed regions. Image analysis traces out the elliptical cross-sectional area of unmixed regions in two-dimensional plane. Subsequently, the theorem of Pappus (Berky, 1984) applies to calculate the elliptical volume of each torus by multiplying the calculated cross-sectional area by the mean circumference of the torus as shown in Equation 4.1, where volume of torus = volume of cylinder = (cross-section area) x (length):

$$V = (\pi r^2)(2\pi R) = 2\pi^2 Rr^2 \quad (4.1)$$

In this Equation, r is the radius of the circular cross-sectional area measured in the two dimensional plane and R is the mean radius of torus measured from the center of torus to the axis of the impeller shaft, as seen in Figure 4.4.

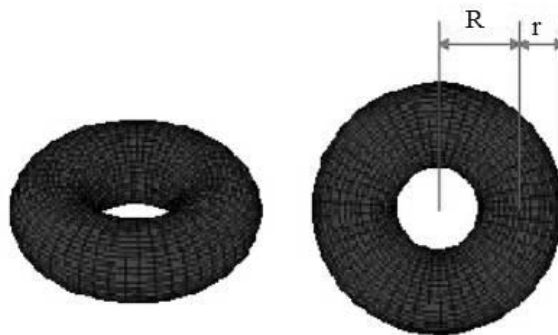


Figure 4.4: Three-dimensional structure of a torus volume and cross-sectional area of a torus showing the torus radius, R , and the cross-sectional radius of the torus, r

Repeating the flow visualization runs at least three times for each test serves to check the reproducibility of unmixed regions volume measurement. The variation in the unmixed region volume varies by $\pm 5\%$ in most cases.

4.3 Results and discussions

The investigation of mixing characteristics of the unmixed regions is a function of dimensionless mixing time, Nt_m , defined by:

$$Nt_m = N \times t_m \quad (4.2)$$

where N is the impeller speed in revolutions per minute and t_m is the acid–base decolourization time from the beginning of the formation of unmixed regions. Note that Nt_m also refers to the number of impeller rotations required, either to destroy the unmixed regions or to diminish their size.

Figure 4.5 shows that there are two unmixed regions inside the lab-scale digester under a steady-state impeller speed application corresponding to $Re = 60$: one above and the other below the rotating impeller. In order to determine Nt_m , the time at which both the upper and lower unmixed regions form is considered as the start of unmixed regions formation.

Each upper and lower region consists of two similar ‘zones’ which can be seen from the cross-sectional view of the digester in Figure 4.5.

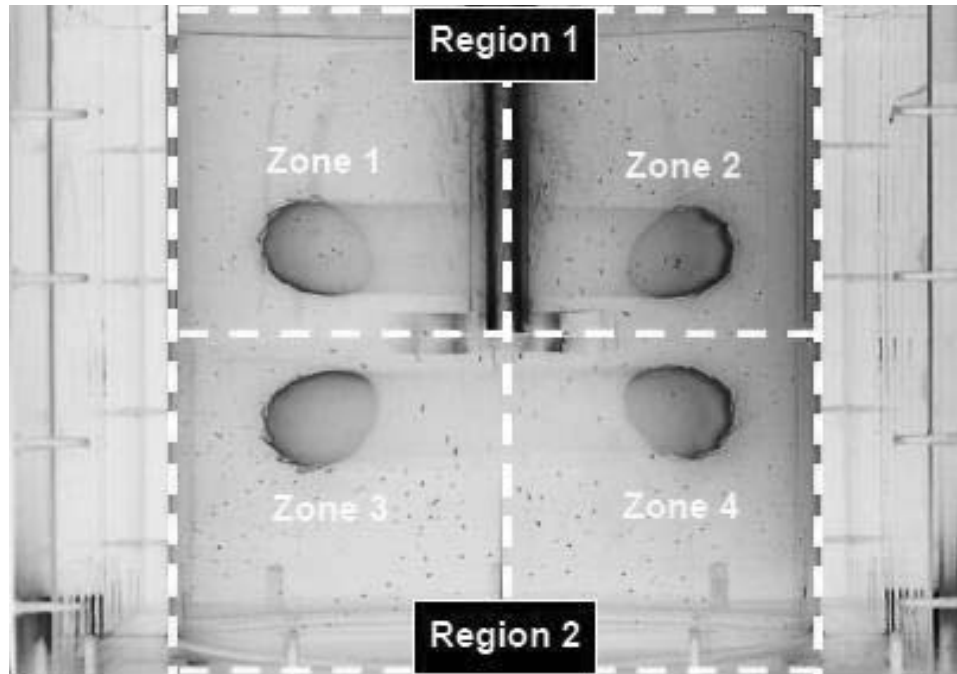


Figure 4.5: Cross-sectional view of stirred AD circular vessel without baffles using uniform RT impeller speed. Colour variations show the existence of unmixed region core structures in the upper, quadrants 1 and 2 and lower regions, quadrants 3 and 4 of the digester. All tests are for non-Newtonian flow unless otherwise specified.

The rotating blades of the impeller create a jet of fluid stream that leads fluid to circulate within each zone by pushing the fluid outwards along the digester wall and recirculating it back in the opposite direction towards the centre of the rotating shaft. In the upper region, fluid moves upward along the digester wall and in the lower region, it moves downward along the wall. This motion is due to the high-speed jet-like flow at the end of the turbine, observed in a vertical cross-section, as shown in Figure 4.5. The fluid recirculates in each zone in a direction towards the centre of the digester, which is opposite to the fluid direction along the wall in each region.

Figure 4.6 shows the total percentage volume of unmixed regions—sum of volume of upper and lower unmixed regions—as a function of dimensionless mixing time, Nt_m . Uniform application of stirring with variation in period decreases the unmixed region to $\sim 10\%$ within a dimensionless mixing time of 5,000. The volume of doughnut-shaped unmixed region does not decrease below this value even after extended period of mixing. The core rings of unmixed regions above and below the rotating impeller stabilize thus exhibiting no sign of total destruction for several hours (Figure 4.5).

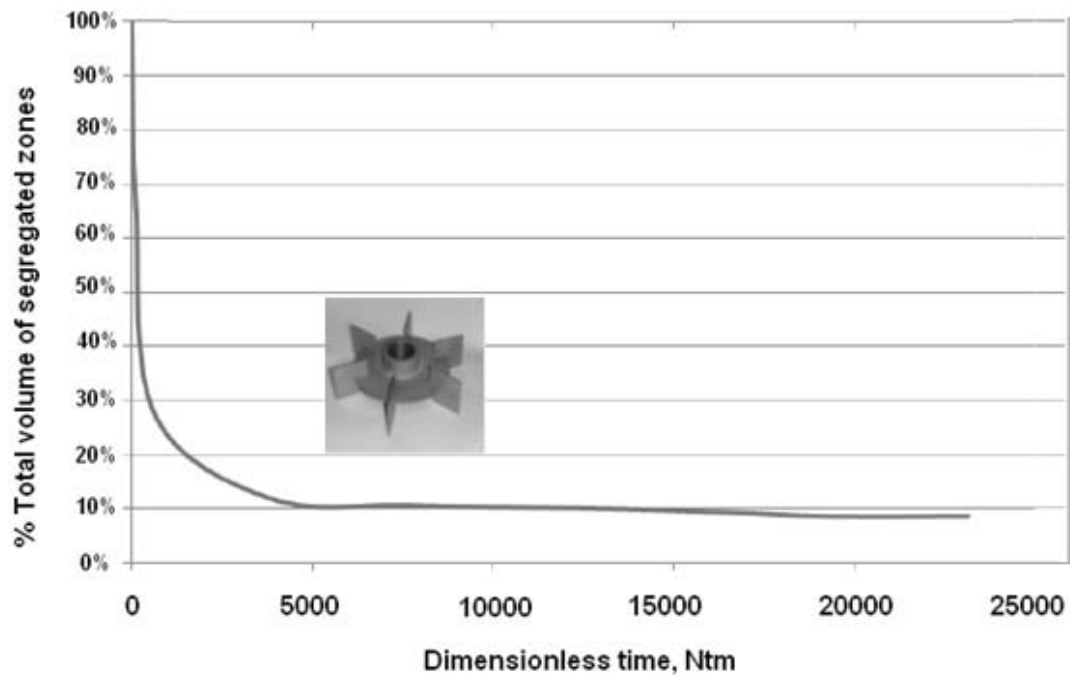


Figure 4.6: Volume of unmixed region as percentage of initial digester volume as function of dimensionless time, Nt_m , which does not decrease with prolonged mixing time after 5,000

4.4 Effect of perturbation on segregated mixed regions

We used two additional impeller mixing modes to examine the effects on the formation and destruction of unmixed regions in AD:

- Square-wave application with amplitude $A_1 = 20$ achieved using $Re_{max} = 60$ and $Re_{min} = 40$
- Square-wave application with amplitude $A_2 = 30$ achieved using $Re_{max} = 60$ and $Re_{min} = 30$

Variation of the wave periods to 10, 20 and 40 sec for each amplitudes, A_1 and A_2 allows examining the effects of different wave periods on the unmixed regions. Figure 4.7 shows a schematic diagram, which illustrates the cyclic motion of tori from one location to the other due to the continuous fluctuation of impeller speed. During the cyclic motion, results will show the volume of each torus decreasing, which eventually leads to their complete destruction using the proposed method.

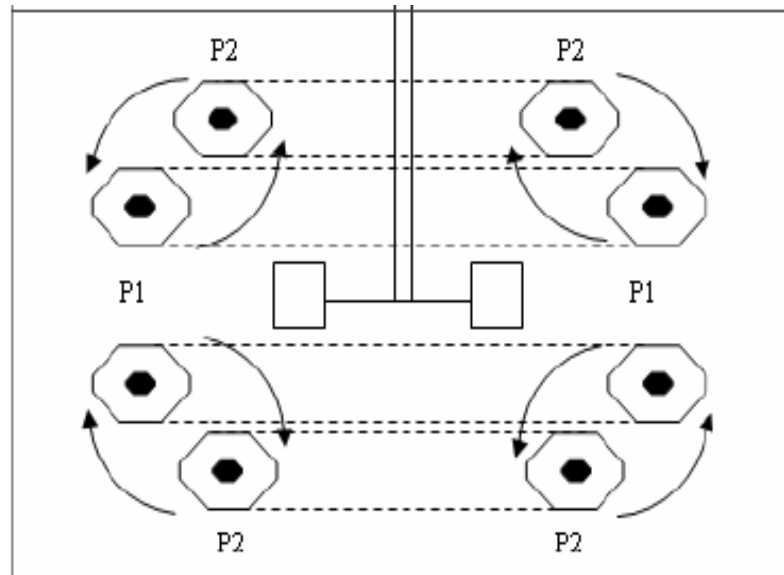


Figure 4.7: Visualization of unmixed mixed region tori locations at low and high impeller speed obtained by Re variations by changing shaft RPM. P_1 is the location of an unmixed region at low Re number and P_2 is the location of an unmixed region at high Re. Applications of a square wave to control shaft rotation improves mixing by movement of P_1 and P_2 , and creation of CW and CCW rotation.

Figure 4.8 illustrates the different tori locations at low and high impeller Re. As the impeller speed increases, the upper torus moves outwards and downwards, while the lower torus also moves outwards but upwards making them closer to each other. However, both tori move closer to the impeller shaft and further apart from each other in an elliptical manner as the impeller speed decreases to a low Re.

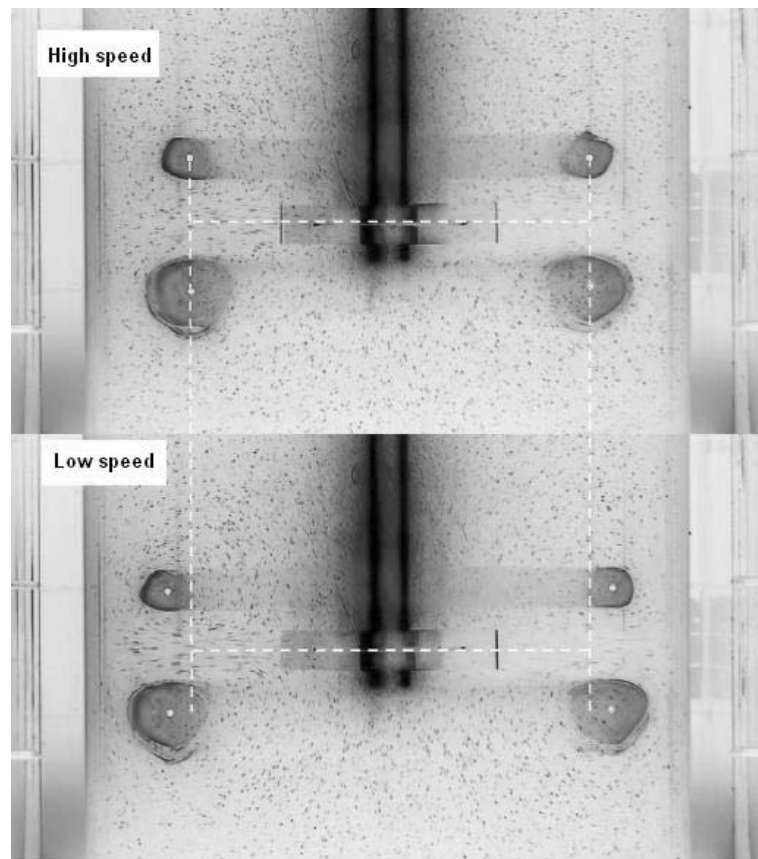


Figure 4.8:-Effect on the four unmixed regions when applying square amplitude, A_1 , with $Re = 40$ and $Re = 60$ with a wave period of 20 s. Mixing effect shown at (a) high speed with $Re = 60$, and (b) low speed with $Re = 40$. The four pink unmixed regions with a magenta dot at the centre clearly are moving relative to white grid lines to show the enhanced mixing now occurring

At low impeller speed, the periodic stretching and folding of the fluid motion is evident immediately after the injection of acidic solution into the alkaline solution. Figure 4.9

shows the formation and destruction of four ‘horseshoe’ folds after a few wave period cycles. These horseshoe-shaped tori are previously reported by others investigating two-dimensional chaotic mixing (Ottino et al., 1988; Liu et al., 1994). At a higher impeller speed, unmixed regions form immediately. The sudden fluctuation of impeller speed allows fresh HCl acidic solution, shown as light pink areas, from well-mixed region to spread towards the wall in a radial flow pattern, surrounding the unmixed regions containing NaOH alkaline solution, shown as dark pink areas. At low speed, existing unmixed regions deform at low speed and stretch outward, leaving strands of acid traces diffusing into the actively mixed regions. This type of stretching and folding mechanism forms an envelope-like structure consisting of pockets of acidic and alkaline strands showing non-uniform mixing within a single wave period.

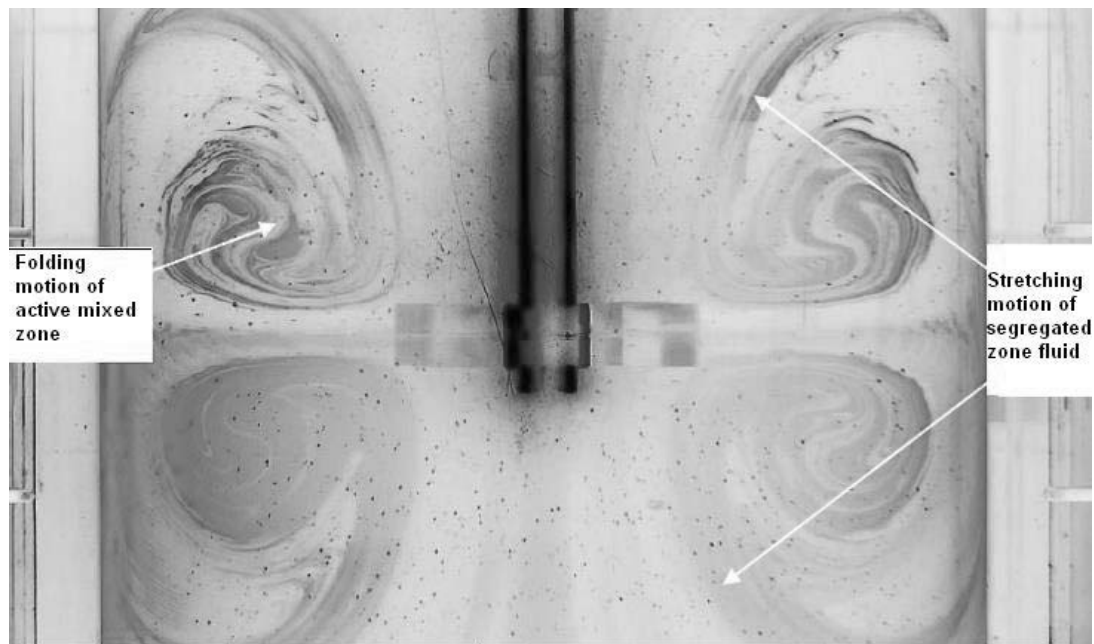


Figure 4.9: Formation and destruction of the four “horseshoe” folds after a few period cycles applying a square amplitude, A_1 , with $Re = 40$ and $Re = 60$ with a wave period of 20 sec

After a number of periodic cycles, the stretching and folding continue until the unmixed regions disappear, yielding a homogenous solution that will improve AD operations.

Figure 4.10 shows the evolution of the upper unmixed pocket volume with respect to dimensionless time, Nt_m . In this case, the test uses the square-wave application of mixing intensities for $A_1 = 20$ with different wave periods. There is no significant difference in the upper unmixed pocket volumes below $Nt_m = 150$ though for $Nt_m > 150$, wave-period of 20 and 40 sec applications significantly increased Nt_m values (52% and 61%, respectively). However, between these two variations in period, the 40 sec, which has the higher wave period, leads to a slower destruction rate of upper pocket volume. Therefore, it requires the longest destruction time of $Nt_m = 639$.

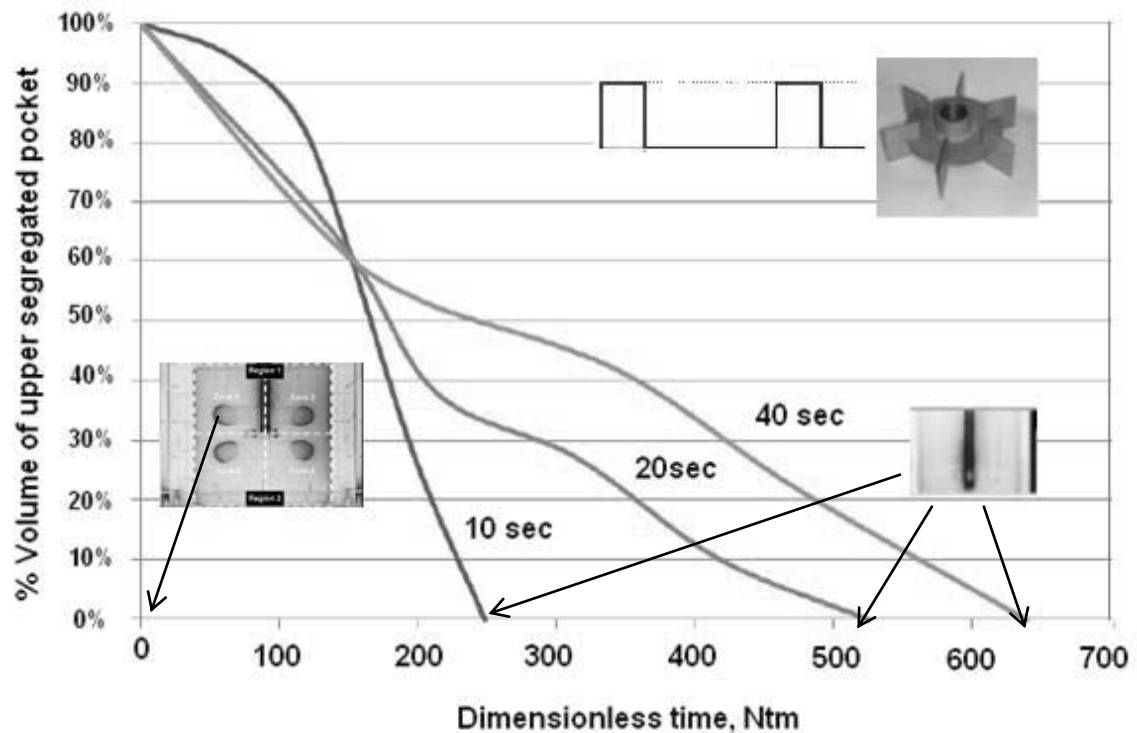


Figure 4.10: Dimensionless time, Nt_m , to reach destruction of upper unmixed pockets using square-wave application, A_1 , with $Re = 40$ and $Re = 60$, for wave periods of 10, 20 and 40 sec

Figure 4.11 shows the evolution of upper unmixed pocket volumes with respect to Nt_m for the square-wave mixing with amplitude $A_2 = 30$ and different wave periods. Upper unmixed pocket volume decreases linearly as Nt_m increases. The stretching and folding caused by the impeller blades allows the upper unmixed pocket to decrease gradually as the impeller speed fluctuates periodically. The 40 sec application requires $\sim 75\%$ more time for the upper unmixed pocket to vanish completely when compared with the 10 sec application. This is because the perturbation caused by the impeller rotation increases when wave period decreases and vice versa. Figure 4.7 shows the shift of the core of the upper unmixed pocket between two locations: position P_1 for Re_{max} and position P_2 for Re_{min} .

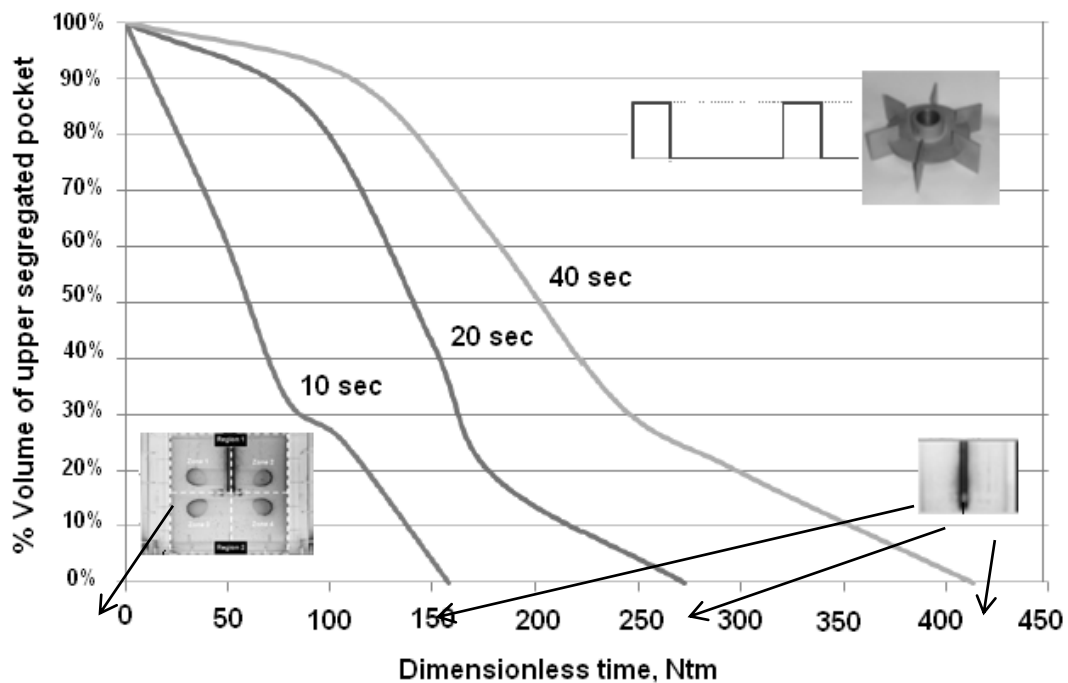


Figure 4.11: Dimensionless time, Nt_m , to reach destruction of upper unmixed pockets using square-wave application, $A_2 = 30$, with $Re = 30$ and $Re = 60$, for wave periods of 10, 20 and 40 sec

The cyclical action of the impeller speed with a shorter wave period allows the core of the upper unmixed pocket to change from P_1 to P_2 in a shorter time. In addition, it promotes more stretching and folding of the upper unmixed pocket. The core of the upper unmixed pocket shifts further away from the impeller shaft at the larger amplitude, while it moves closer to the axis of the digester at the smaller amplitude. These phenomena lead to an increase in the distance traveled by the upper unmixed pocket between P_1 and P_2 . It allows more interaction between the unmixed regions and the well-mixed regions thereby significantly reducing the volume of upper unmixed mixed pocket.

Overall, the destruction time of the upper unmixed pocket increases with larger amplitude fluctuations. However, the inclusion of a shorter wave period produces much better mixing than just amplitude fluctuation. Therefore, the wave period or frequency modulation yields more efficient mix than mere amplitude modulation in AD. Overall, the combination of large amplitude and a short wave period results in optimum mixing performance in an AD.

Figure 4.12 shows the changes in the volume of the lower unmixed pocket as a function of Nt_m for the variation with an amplitude $A_1 = 20$ with wave periods of 10, 20 and 40 sec.

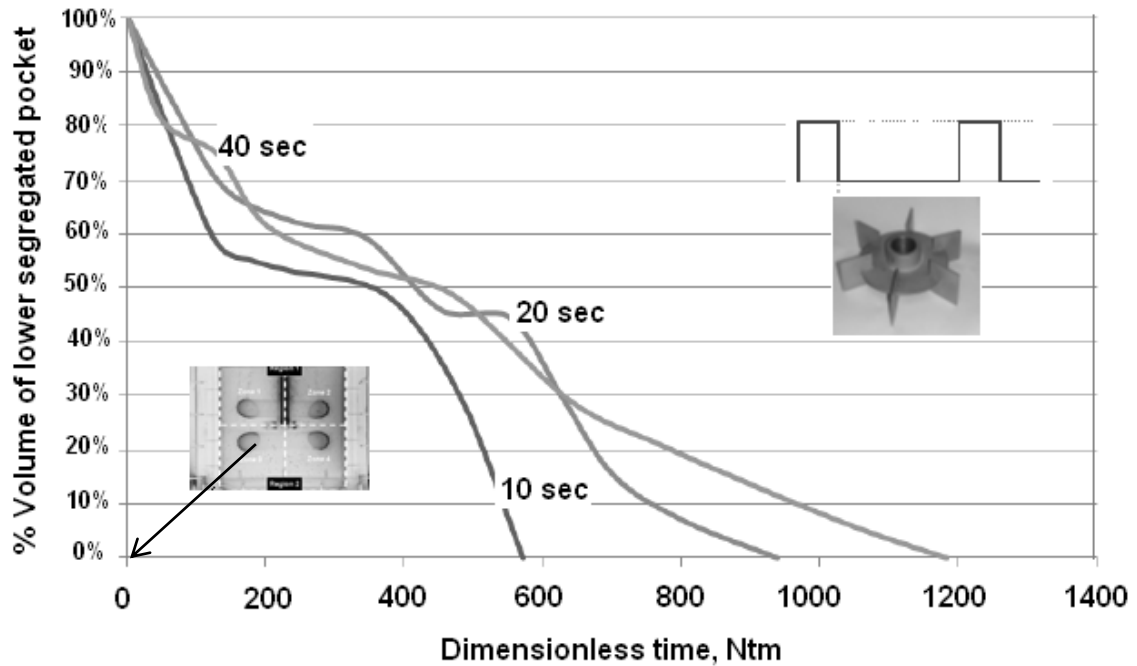


Figure 4.12: Dimensionless time, Nt_m , to reach destruction of lower unmixed pockets using square-wave application, $A_1 = 20$, with $Re = 30$ and $Re = 60$, for wave periods of 10, 20 and 40 sec

In this case, the smallest wave period produces the optimum mixing. There are differences in lower unmixed pocket mixing rates for the applications with the wave periods of 20 and 40 sec up to $Nt_m = 650$. However, for $Nt_m > 650$, the square wave application with a wave period of 20 sec exhibits better mixing. Figure 4.13 shows the changes in lower unmixed pocket volume as a function of Nt_m for the application using an amplitude $A_2 = 30$ and wave periods of 10, 20 and 40 sec. There is no significant difference in volume reduction rate for all three wave periods up to $Nt_m = 200$. Above $Nt_m = 200$, the mixing application with the shortest wave period of 10 sec exhibits the greater volume reduction rate. This observation is similar to the result discussed above where the variation in intensities with the longer wave period requires a longer mixing time. The results show the possibility of achieving significant improvement in mixing

efficiency in mixed ADs with different wave periods while keeping the amplitude the same.

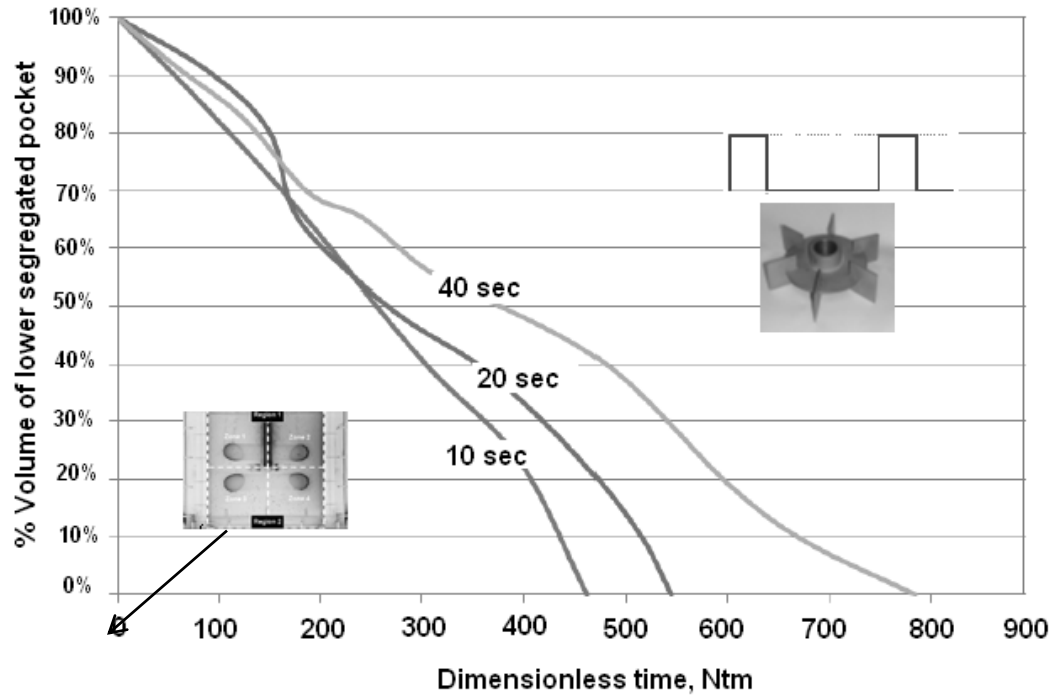


Figure 4.13: Dimensionless time, Nt_m , to reach destruction of lower unmixed pockets using square-wave application, $A_1 = 30$, with $Re = 30$ and $Re = 60$, for wave periods of 10, 20 and 40 sec

The sequences of pictures presented in Figures 4.14 and 4.15 demonstrate the chaotic mixing patterns above and below the impeller. The upper unmixed regions always form earlier than the lower unmixed regions for mixing with an amplitude fluctuation of $A_2 = 30$, shown in Figure 4.14. However, Figure 4.15 shows that it takes longer to destroy the upper unmixed pockets with a smaller amplitude fluctuation. Overall, the volume of the upper pocket is always smaller than the volume of the lower pocket probably due to the influence of the free liquid surface. Therefore, the variation of the mixing

intensities with larger amplitude and a shorter wave period enhances chaotic mixing in mechanically mixed AD.

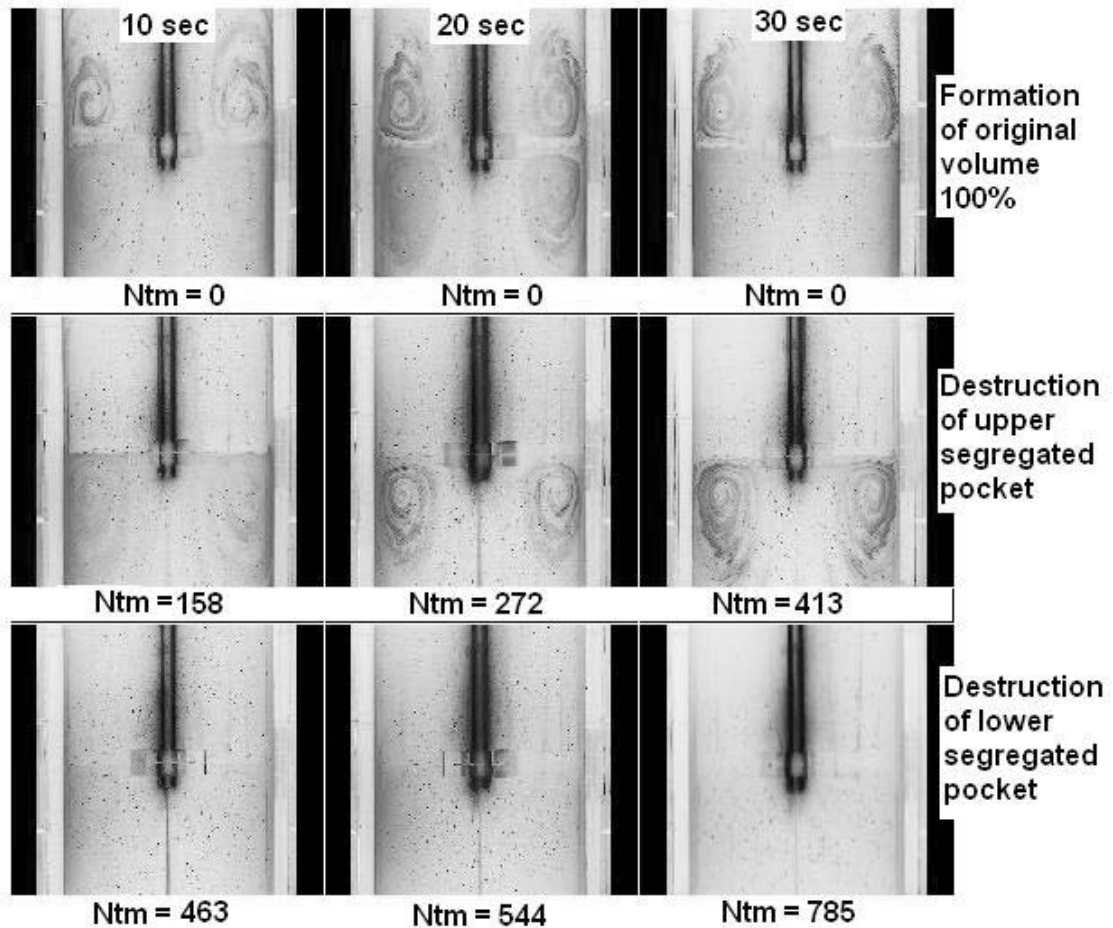


Figure 4.14: Chaotic mixing for upper and lower pockets using square-wave variation of mixing intensities with amplitude $A_2 = 30$ fluctuation with $Re = 30$ and $Re = 60$, for wave periods of 10, 20 and 40 sec

Application of *sine wave* speed mode uses the same amplitudes and wave periods to the ones used with square wave speed mode. Since a larger amplitude, $A_2 = 30$, produced better mixing in the case of square wave application, the impeller speed using sine wave

protocol uses a fixed amplitude of $A_2 = 30$ but with different wave periods: 10, 20 and 40 sec.

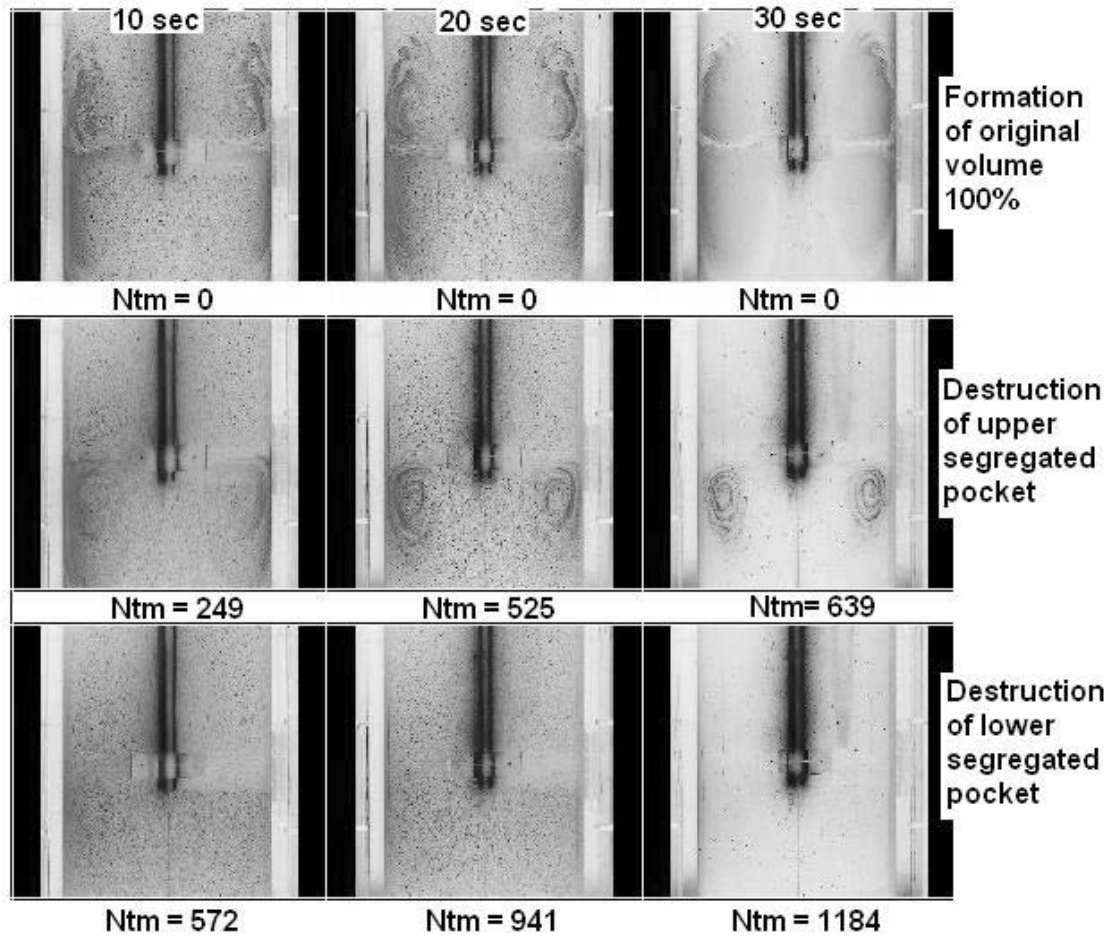


Figure 4.15: Chaotic mixing for upper and lower envelope using square-wave variation of mixing intensities with amplitude $A_1 = 20$ fluctuation with $Re = 40$ and $Re = 60$, for wave periods of 10, 20 and 40 sec

Figure 4.16 shows the evolution of the volume of unmixed region as a function of the dimensionless mixing time, Nt_m . The sine wave application with a wave period of 10 sec reduces the volume of the unmixed regions by 80% within the dimensionless time of 1,500 due to the higher frequency of the impeller rotation. The continuous change in the

impeller rotation speed up and down allows outside fluid from active mixing regions to penetrate the originally stable unmixed flow structures, leading to enhanced laminar chaotic mixing. For 20 sec period and 40 sec period application of the sine wave mixing, the volume of the unmixed flow region decreased drastically from 100% to around 20% within the dimensionless time of 5,000. However, there is no significant difference in the results for these two periods after the dimensionless time of 5,000, as shown in Figure 4.16. The change of amplitude between $Re_{max} = 60$ and $Re_{min} = 30$ requires longer time for the case of sine wave application than the square wave application. Hence, the result indicates that, for a sine wave mode of mixing with amplitude of $A_2 = 30$, changing the wave period from 20 and 40 sec have no beneficial effect on the mixing time of manure in ADs.

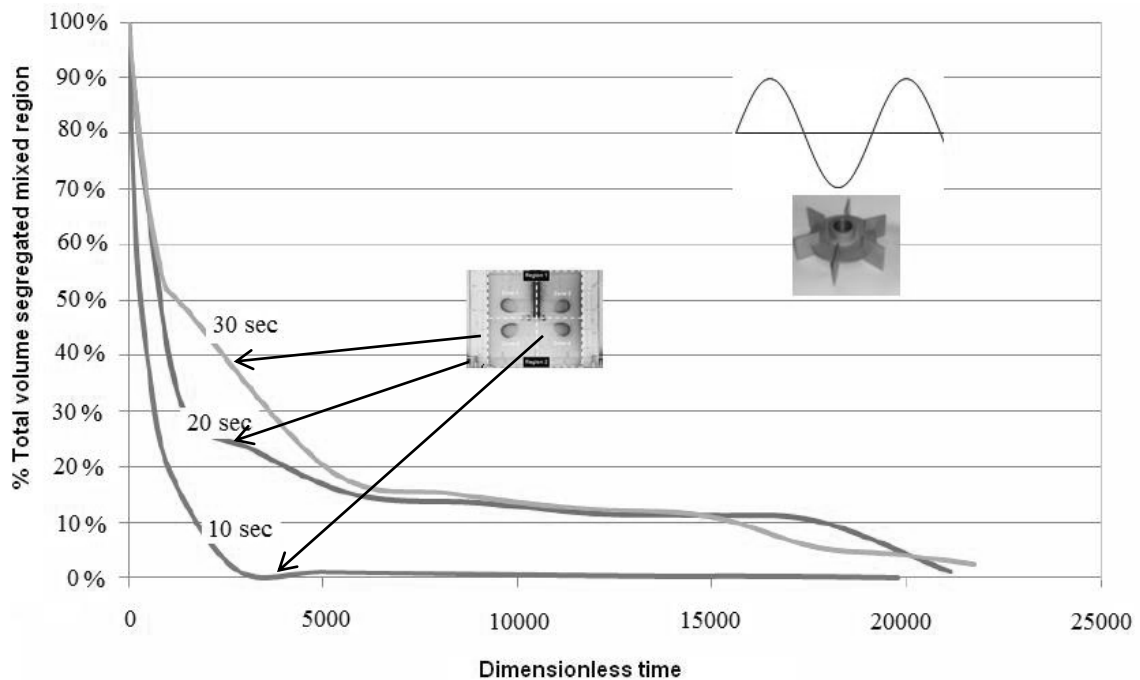


Figure 4.16: Reduction in volume of unmixed structure regions using 10, 20 and 40 sec periods with a sine wave applied at $Re = 30$ to $Re = 60$

The core of the unmixed flow region shifts gradually between P_1 and P_2 , as shown in Figure 4.17, without sudden switching effects observed during square wave mode. This smooth cyclic motion restricts convective interaction between the unmixed flow region and well-mixed region, and thus destruction of the unmixed flow region requires a longer time for the sine wave application. Hence, the volume reduction rate of the unmixed flow region is slower in this case. Therefore the unmixed flow region volume reaches an asymptotic volume at $Nt_m = 5,000$ and exhibits no further changes thereafter. Beyond $Nt_m = 5,000$, a slow diffusive mechanism is responsible for the mixing between the unmixed flow structures and well-mixed flow structures. These structures do not disappear completely for the sine wave application but only get smaller after a long time. The core of the unmixed flow structure is still visible even after several hours of mixing due to a lack of convective flow within the digester.

Yao *et al.* (1998) have also demonstrated that for a given Re , a longer mixing time is required if a longer wave period is used. Figure 4.18 shows the reduction of unmixed flow regions to $\sim 20\%$ of their original size and remaining stable regardless of further increase in Nt_m . The sine wave mode with 10 sec period requires the shortest dimensionless time of 1500 for the unmixed flow regions to reach $\sim 20\%$ of original volume, while the other two sine wave modes require an average dimensionless time of 1,500 to reach $\sim 20\%$ of the original volume. Figure 4.18 also clearly shows that the upper unmixed flow pocket structure is always smaller than the lower unmixed flow structure due to the influence of the free liquid surface.

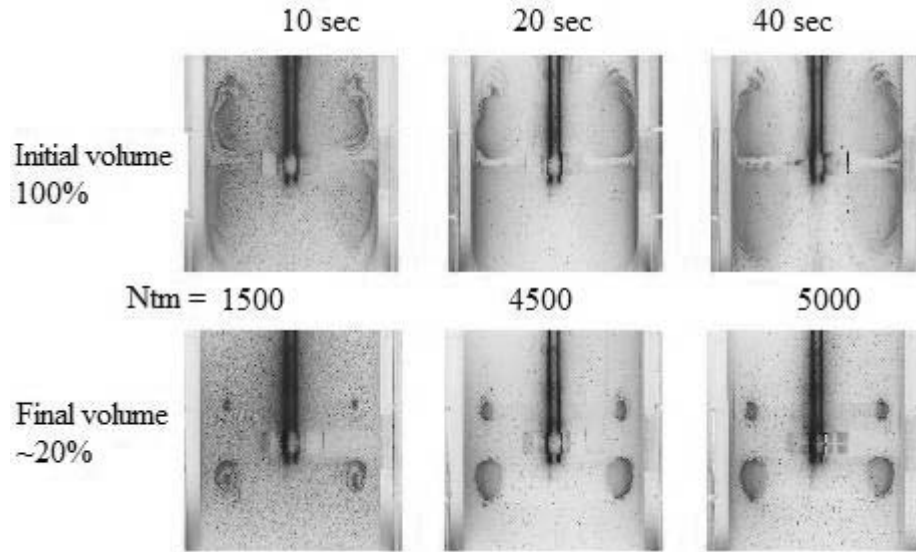


Figure 4.17: Reduction of upper unmixed structure pocket to 20% volume using 10, 20 and 40 sec periods with a sine wave applied from $Re = 30$ to $Re = 60$

The experimental work of Kato et al. (2005) shows that using unsteady mixing with sine wave modulation destroys these structures. However, their sine wave speed modulation consisted of irregular amplitude pattern (larger positive amplitude and smaller negative amplitude) whereas this work involved sine wave modulation with regular amplitude pattern (equal positive and negative amplitudes).

In addition, this work examines the effects of different impeller types on unmixed mixed zones. Figure 4.18 shows the evolution of the total unmixed region volume defined as the sum of upper and lower unmixed pockets volume as a function of dimensionless mixing time, Nt_m . Recall Nt_m equals to the total number of impeller rotations under uniform and unbaffled operating conditions. The initial volume of unmixed flow region for all impellers is more than 50% of the total liquid volume. With an increase in Nt_m , the volume of these regions for all impellers decreases until it reaches a certain constant

volume. It is clear that, even after several hours of mixing, the volume of unmixed flow regions for all impellers does not decrease below 8% of the total liquid volume. Comparison of all three impellers in Figure 4.18 shows impellers PBT and A310 perform better because the initial unmixed volume reduces from about 62% to 10% within a dimensionless mixing time of 6,000.

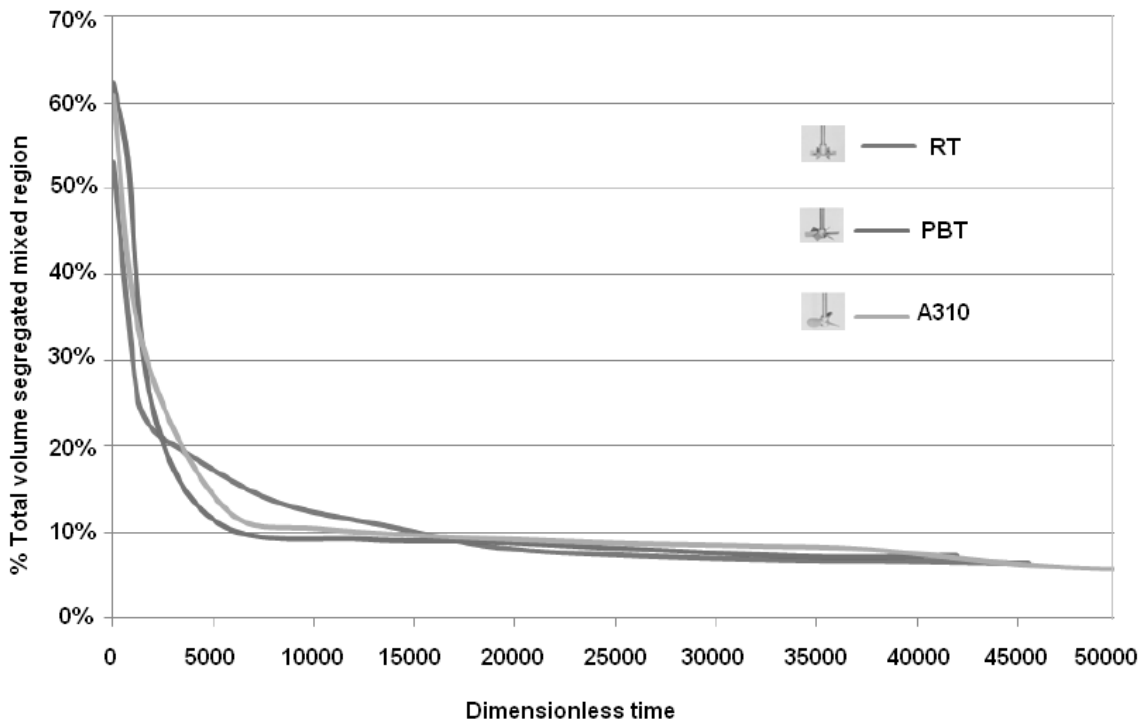


Figure 4.18: Evolution of total unmixed volume with dimensionless time, Nt_m using uniform impeller speed without baffles of $Re = 60$

However, it takes a longer dimensionless mixing time of about 15,000 for RT to reduce the volume to about same value of $\sim 10\%$ even though RT has a smaller initial unmixed volume than those for PBT and A310, as shown in Figure 4.19. These results

demonstrate that maintaining a uniform impeller speed leads to inefficient mixing of manure in AD.

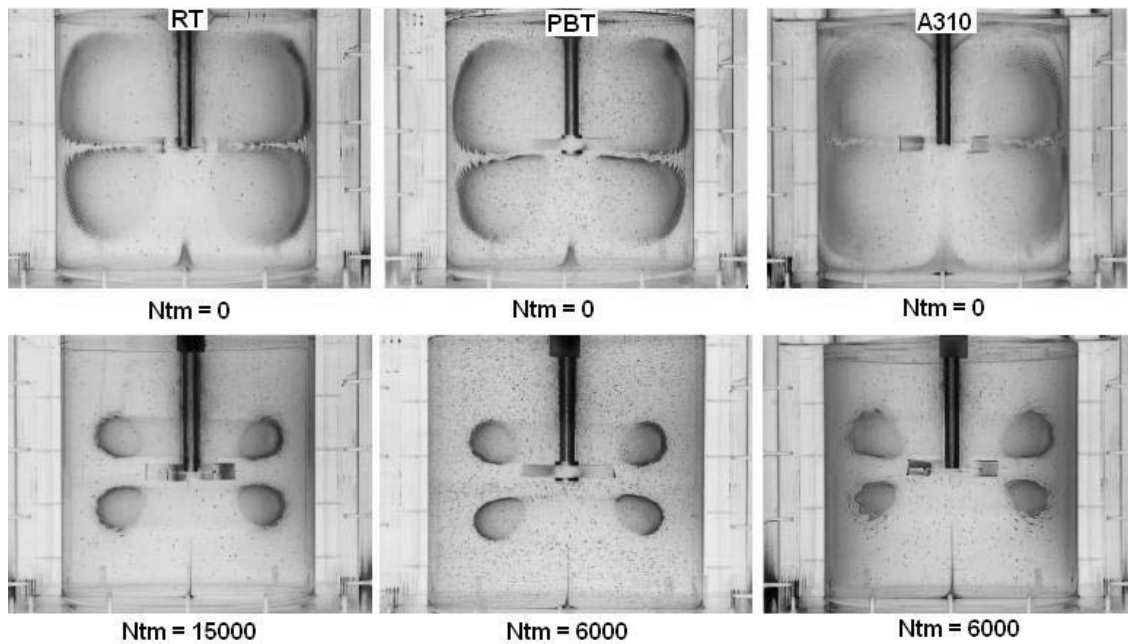


Figure 4.19: Chaotic mixing of unmixed mixed regions for impellers RT, PBT and A310 using uniform impeller speed without baffles for $Re = 60$

Figure 4.20 shows the evolution of the total volume of unmixed mixed zone as a function of Nt_m when using RT and PBT impellers with and without baffles. Both are operated using square-wave speed variation with an amplitude of 10 ($Re_{max} = 20$ to $Re_{min} = 10$) and a constant wave-period of 10 sec. Under unbaffled condition, the initial volume of unmixed zone in the digester occupies $\sim 65\%$ of the total liquid volume for both RT and PBT. With increase in Nt_m , the total unmixed volume for both impellers decreases and eventually becomes zero. This result shows clearly that rotating the impellers with square-wave variation increases the destruction rate of these unmixed flow structures.

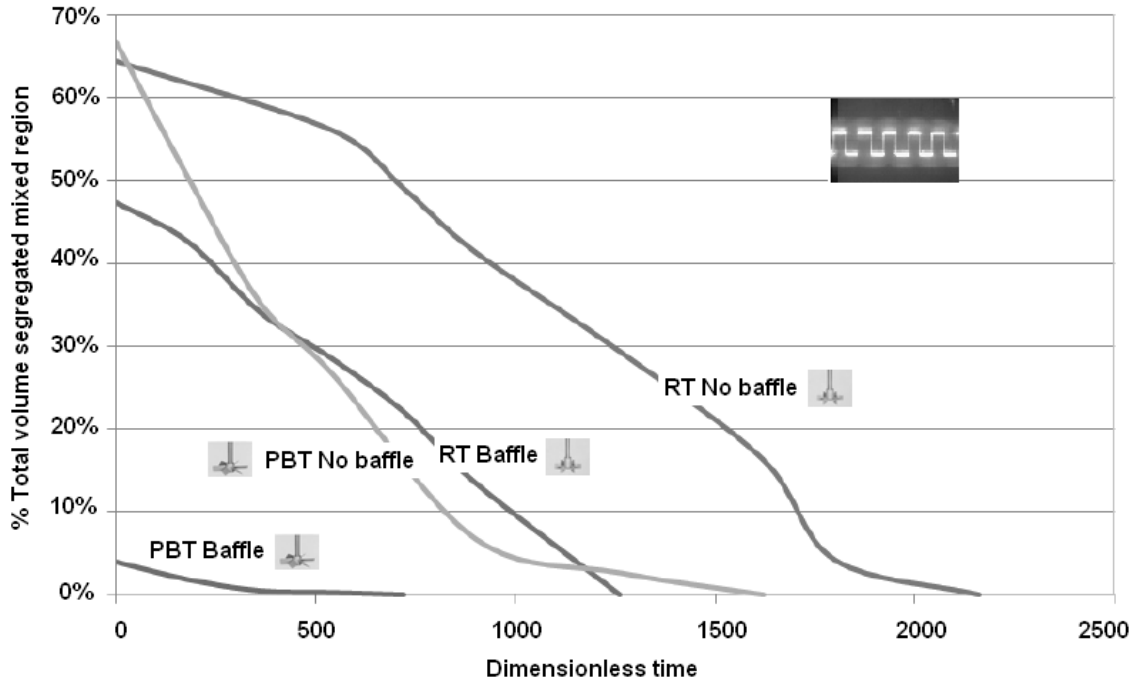


Figure 4.20: Evolution of total unmixed volume with dimensionless time, Nt_m using square-wave variation of mixing intensities with amplitude $A = 10$ fluctuation with $R = 10$ and $Re = 20$, for wave period of 10 sec

Comparison of the performance of these two impellers show the PBT leads to rapid decrease in volume of unmixed flow region than RT. The number of rotations Nt_m required for the complete destruction of unmixed flow structures using PBT is 1,600 which is lower than $Nt_m = 2,200$ required for RT.

Under baffled condition, the initial total volume of unmixed region for both impellers is smaller than observed for the unbaffled condition. Especially, the initial core of the unmixed flow volume for PBT is only about 5% of the total liquid volume. This result demonstrates the effect of baffling on volume of unmixed flow zone. For both impellers, the dimensionless time required to destroy the unmixed flow region is less than 1,250

under baffled condition. Therefore, the rate of unmixed flow regions destruction for both impellers is greater for AD with baffle than digester without baffle.

In general, consideration of the flow characteristics in the digester explains effects of baffles and impeller types in the destruction of unmixed flow regions. As the impeller rotates clockwise in the mixed digester, the sweeping motion of each impeller blade pumps the fluid from the active mixed regions into the unmixed flow structures. As shown in Figure 4.21, the fluid exchange between the unmixed flow structures, shown as bright coloured structures containing NaOH, and well-mixed region shown as darker regions containing HCl after neutralization, appears to be homogenous even before the initial formation of unmixed flow structures. When square-wave variation of mixing intensities used to operate the impeller, it promotes more stretching and folding of the unmixed flow structures as the impeller speed switches rapidly from high rpm to low rpm, thereby increasing the rate of unmixed region destruction. When the baffles are present, they restrict the volume of the unmixed flow region further to the space between the baffles and the rotating impellers, rather than the space between the digester wall and the impellers, thus creating more chaos to the unmixed flow structures in the digester.

It is also interesting to note the differences in the flow pattern and evolution of the unmixed flow structures for the two impellers. Figure 4.21 shows the evolution of unmixed flow structures and the flow pattern created by impellers PBT and RT, respectively. Impeller PBT placed at mid-liquid height creates a radial downward flow pattern under laminar regime. In addition, the blades of PBT also create a stronger

downwards perturbation, allowing more actively mixed fluids to penetrate into the lower unmixed flow structures. This motion forms envelope-like structures consisting of pockets of acidic and alkaline strands that are not homogeneously mixed. In the case of RT, the radial flow pattern created by the impeller displays very different unmixed flow structures compared to structures formed by using PBT.

Although, the RT creates an even distribution of perturbation across the bulk liquid volume in the open digester, the upper unmixed flow pockets appear smaller in volume. This is mainly because of the higher azimuthal flow circulation caused by the impeller rotation in the upper part of the digester due to the presence of the free liquid surface boundary.

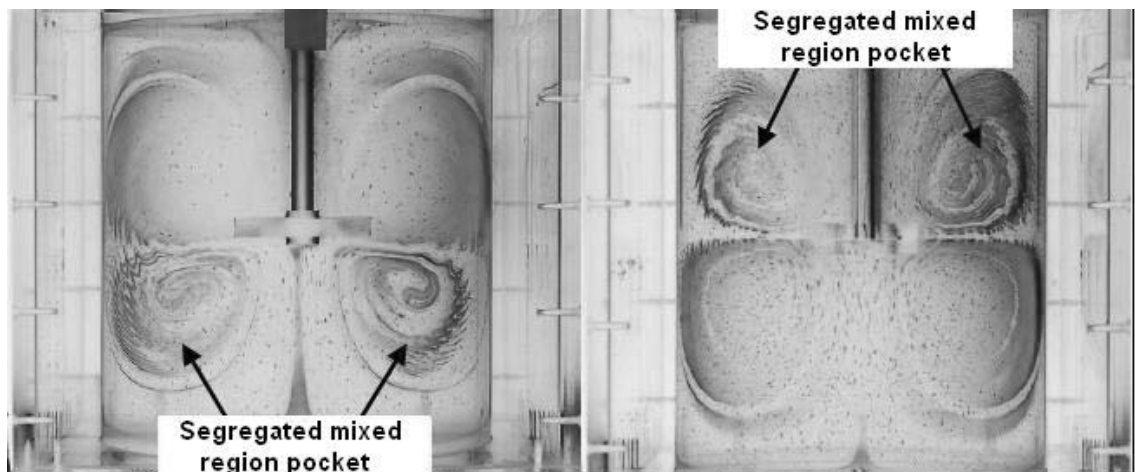


Figure 4.21: Evolution of total volume of unmixed mixed zone with dimensionless time, Nt_m , using square-wave variation of mixing intensities with amplitude $A = 10$ fluctuation with $Re = 10$ and $Re = 20$, for wave period of 10 sec under unbaffled conditions using PBT (left) and RT (right)

Under baffled condition, the initial formation of unmixed structures varies with different impeller types. Figure 4.22 shows the plot of changes in the total percentage volume of unmixed flow structures with respect to the dimensionless time, Nt_m at steady-state

speed. The initial volume of unmixed flow zone core for A310 is about 50% smaller than for RT and PBT.

However, all three impellers do not destroy the unmixed structures even after $N_{tm} = 35,000$, leaving strands of unmixed flow regions (about 2 to 5% of the total digester volume).

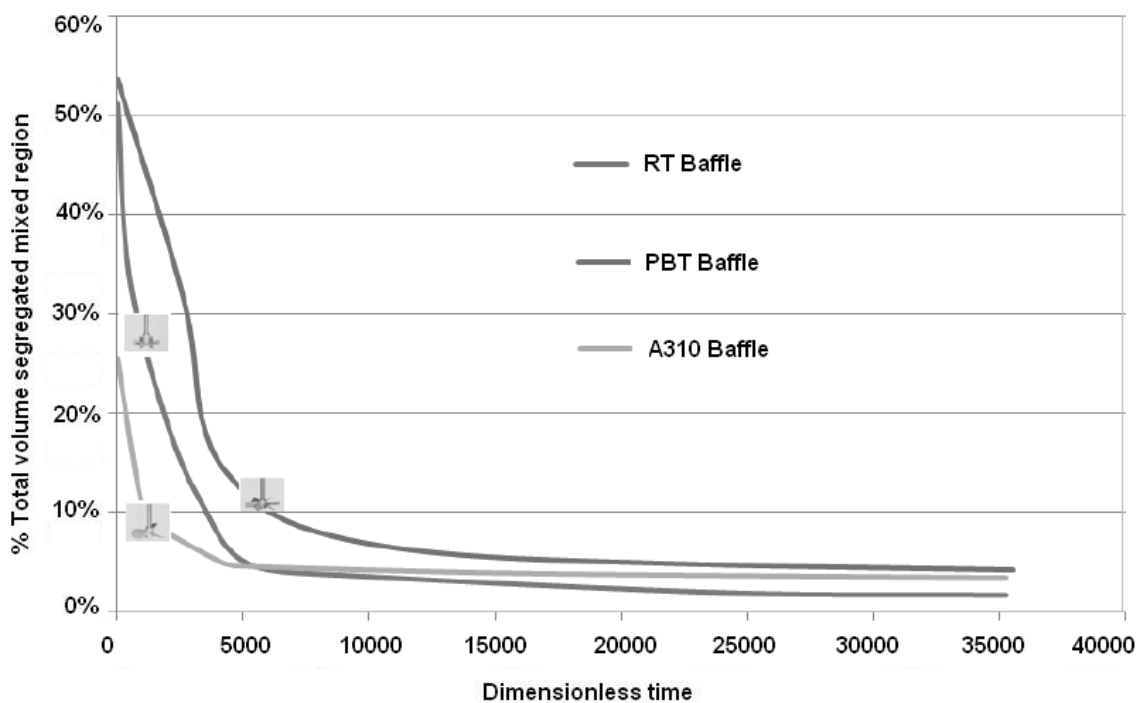


Figure 4.22: Variation of total percentage volume for unmixed core structures as function of dimensionless time, N_{tm} for different impellers and normal baffles using uniform impeller speed without baffles for $Re = 60$

Figure 4.23 shows the unmixed flow core structures that are not completely destroyed at uniform speed of impeller regardless of impeller types employed. However, using RT effectively diminishes the size of the unmixed flow core structures to about less than 2% of original total volume compared to using PBT (~ 5%) and A310 (~ 4%). The azimuthal

flow circulation and free fluid surface boundary above both using RT and A310 cause the segregation phenomenon. Using PBT with a strong radial downward flow circulation destroys the lower unmixed flow pocket and leaves the upper pocket core structures intact. Overall, the unmixed core structures are still present in all the cases (even in the presence of baffles), and they do not disappear completely.

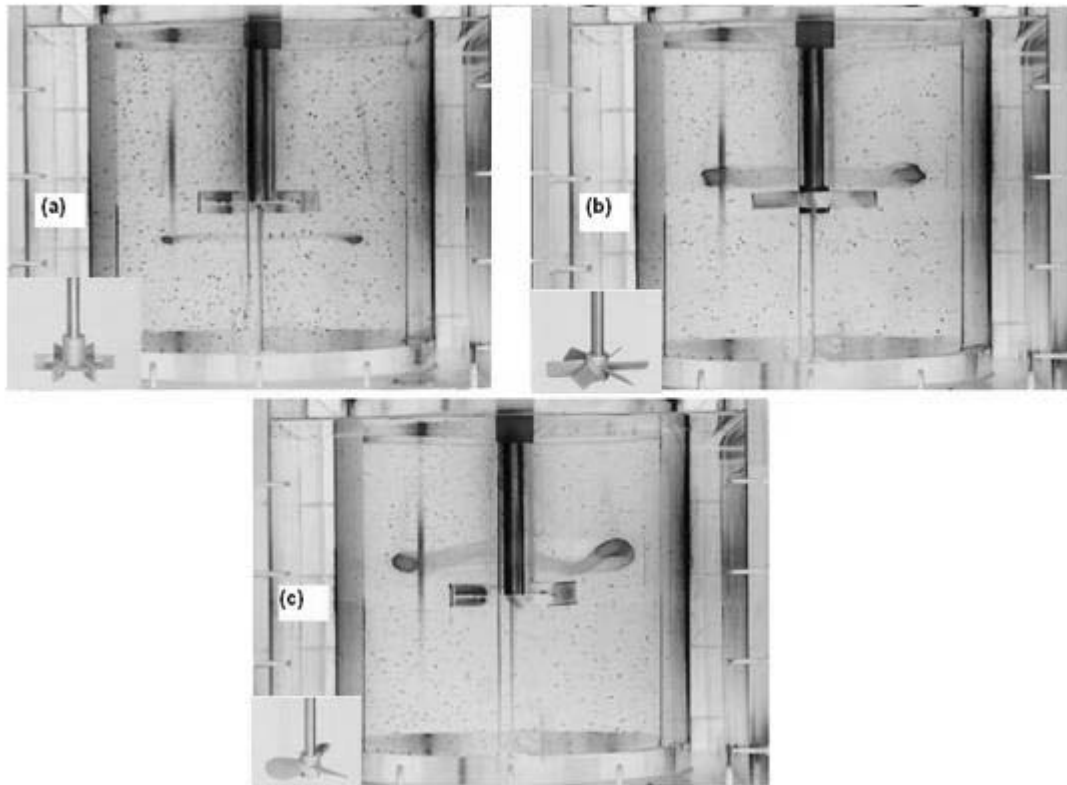


Figure 4.23: Unmixed core structures with 4-blade baffles normal to the digester wall using uniform impeller speed for $Re = 60$ uniform speed after several hours with impellers (a) RT, (b) PBT and (c) A310

The unmixed mixed structures float above and below the rotating impellers. Eventually, these structures homogenized through slow diffusion process under laminar flow regime but it takes much longer mixing time.

Finally, the effects of modified baffles shown in Figure 4.24 placed off the digester wall are investigated. Figure 4.25 illustrates the occurrences of the unmixed flow pockets for the impellers studied in the presence of modified baffles. The location of the modified baffles is the middle space between the impeller shaft and the digester wall rather than attaching it to the digester wall. The location of the modified baffles concedes to location where the core of unmixed flow pocket forms and adds difficulty to observe formation of the unmixed flow pocket. The baffles disturb the formation of unmixed structures. Therefore, the modified baffles reduce the amount of undigested solids formed behind conventional baffles located near the digester wall. In addition, the total dimensionless time for the formation and destruction of unmixed flow regions is less than 2500 (> 10 minutes). Therefore, using these modified baffles provide beneficial effects for a better mixing in AD.

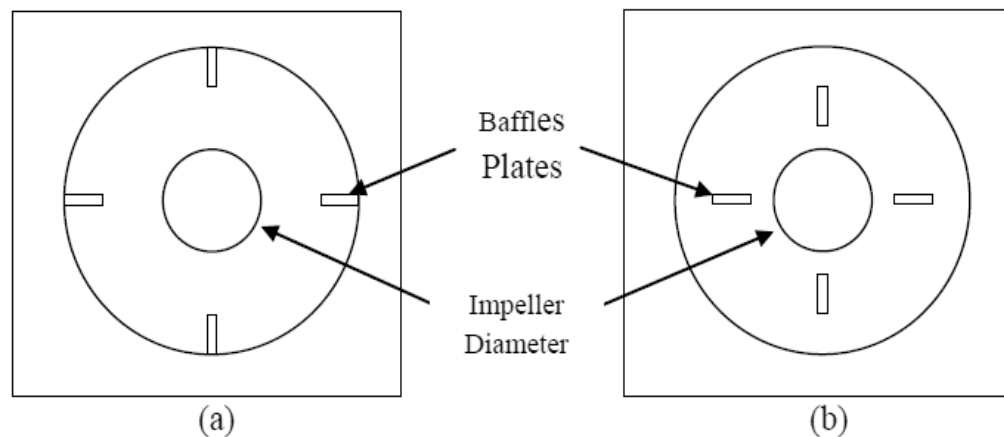


Figure 4.24: Schematic of modification of baffles: (a) normal to the wall, and (b) baffles placed away from the wall

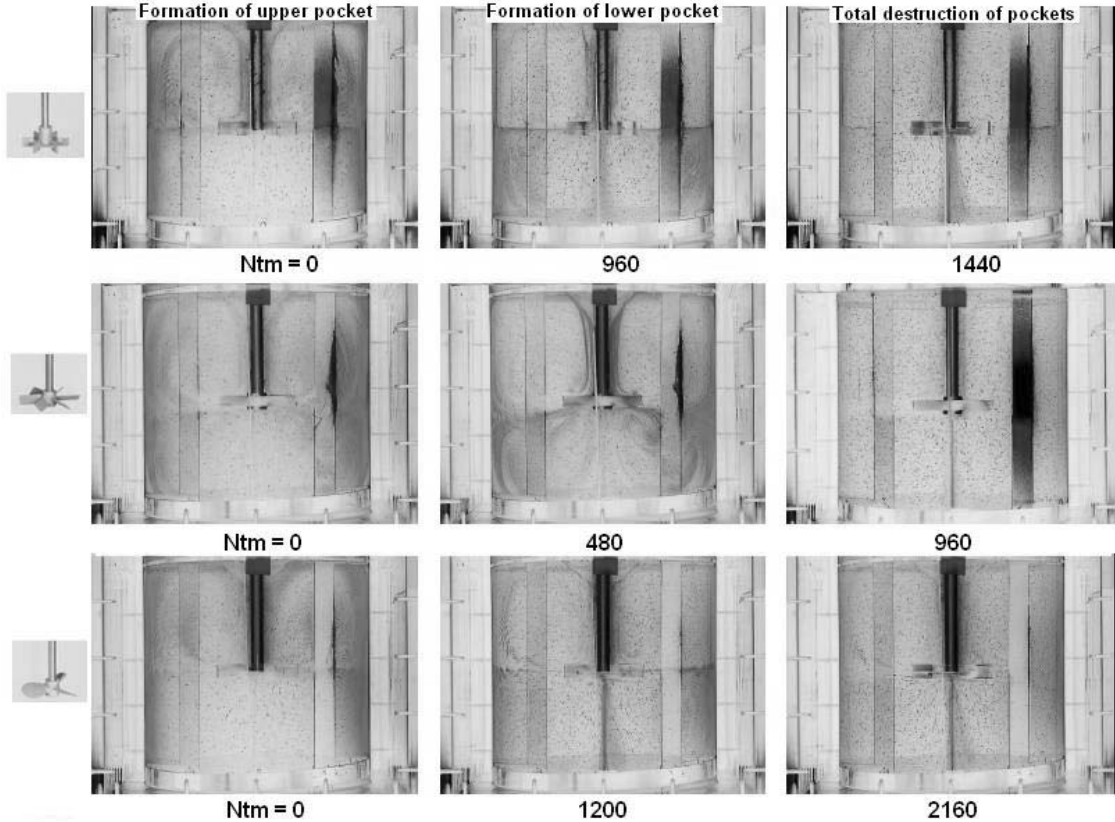


Figure 4.25: Evolution of segregated pockets with modified baffles placed away for the wall at uniform impeller speed using RT, PBT and A310 impellers and $Re = 60$

4.5 Effect of temperature change on segregated mixing regions

To measure the effect of temperature in the upper segregated mixed region and its surrounding actively mixed region, an experiment independent of the above flow visualization is conducted using two thermocouples. The positions of the two thermocouples are set in the upper segregated region, and the actively mixing region. While the HEC solution temperature is kept at 30°C , the water bath temperature surrounding the digester is changed to a fixed higher temperature of 50°C . The viscosity of the working fluid changes with temperature and hence the Reynolds number changes from 20 to 60 when the temperature increases.

Figure 4.26 shows cross sectional views of segregated mixed regime transition and summary of the transition sequence of the upper isolated pocket. At $t = 27$ min, the geometric structure of the upper isolated pocket having 3 islands collapsed and the decolorized fluid penetrated into the core torus, as shown in Figure 4.26c. The stable torus without any islands is established at $t = 35$ min and the unmixed structure region consisting of a small core torus and two large half-circle-shaped islands is observed at $t = 46$ min, as shown in Figure 4.26d and 4.26e, respectively. As shown in Figure 4.26f, the size of the half-circle-shaped islands is small as compared with the core torus.

In order to quantitatively estimate the effect of temperature change on mixing enhancement between segregated mixed region and its surrounding active mixing region, the cross-sectional area of the upper segregated region is measured. Figure 4.27 shows time variation of the cross-sectional area of the upper pocket. As compared with the steady operation at 30°C , the area of region dramatically decreased with time. This mixing enhancement is the result of dynamic change of flow structure due to decrease of viscosity when temperature increases. Hence, a temperature difference enhances the diffusion mechanism between isolated and active region more easily.

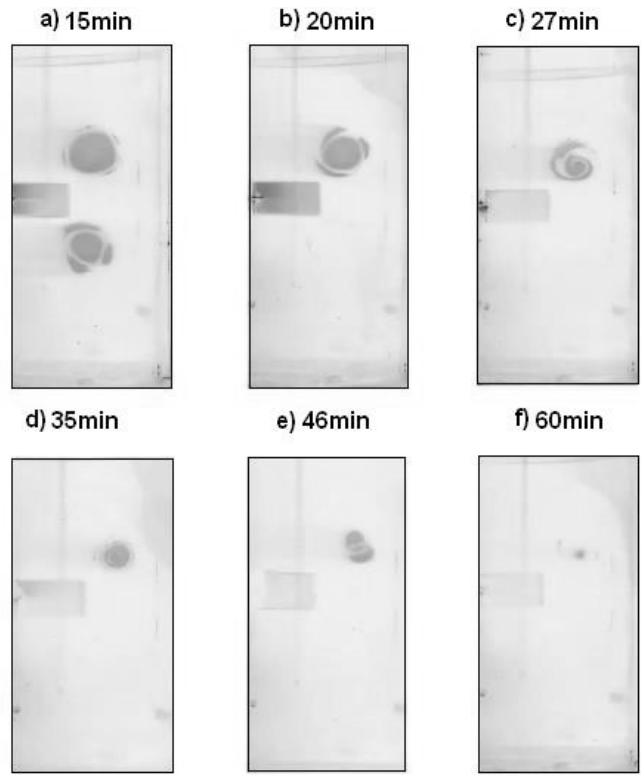


Figure 4.26: Cross sectional view showing the transition of unmixed flow structures in the vessel from $t = 15 \text{ min}$ to $t = 60 \text{ min}$ as result of temperature difference of 10°C , $Re = 30$

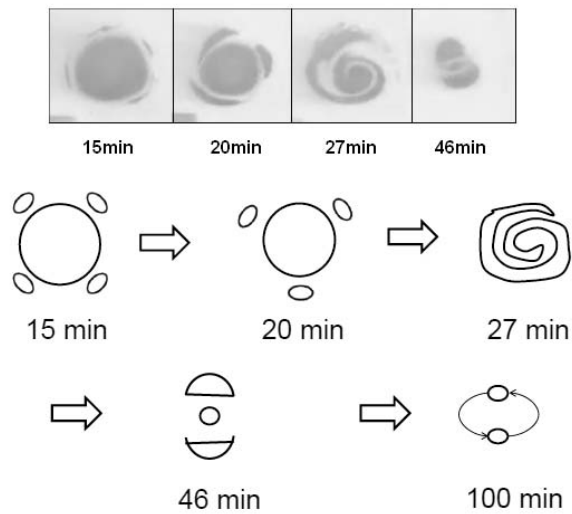


Figure 4.27: Cross sectional view showing the sequence of transition of upper chaotic flow structures in the vessel with schematic of evolution from $t = 15 \text{ min}$ to $t = 60 \text{ min}$ as result of temperature difference of 10°C , $Re = 30$

4.6 Conclusion

The unmixed flow regions that exist above and below the rotating impeller for several hours during the mixing of high viscous fluids in mixed ADs are substantial barriers to achieve efficient mixing. It is possible to eliminate the unmixed flow regions using high rotational impeller speeds; however, high shearing rates are undesirable for shear sensitive microorganisms in anaerobic digestion system. We thus investigated the impeller type and baffle effects using various speed modulation protocols to destroy the unmixed region in laminar mixing vessels with non-Newtonian flow. The following are contributions this chapter makes in this regards to the scientific literature and design practitioners

- The presence of baffles restricts the unmixed flow region volume between the digester wall and the rotating impellers, while the speed modulation promotes more stretching and folding mechanism of the unmixed flow structures. Therefore, the baffling effect and speed modulation enhance the chaotic mixing process in AD.
- Laminar mixing under $Re < 100$ could be enhanced using impeller speed modulation by changing both amplitude and wave period appropriately in a step wave mixing application
- Using shorter wave period or frequency modulation yields better results than that obtained with mere amplitude fluctuation.
- Speed modulation using sine wave protocol also helps to decrease the volume of segregated mixed regions However, these regions do not disappear completely under this protocol due to relatively slow diffusion mechanism

- A digester equipped with PBT impeller leads to higher destruction rate of the unmixed flow zones than RT and A310 impellers.
- A change in temperature transforms the segregated structures from a combination of crescent shape and torus, to narrow torus, to a spiral structure and eventually disappear.
- The temperature difference decreases the time to eliminate the segregated structures by enhancing global mixing in the stirred digester since a larger temperature difference enhances diffusion mechanism between isolated and active mixing regimes more easily. Applying step temperature change of the outer jacket enhances the elimination of these isolated mixed regions and beneficial to designing mixing processes other than AD.

5. Numerical modeling of hydrodynamics of mixed AD

Although experimental techniques are useful in understanding the hydrodynamics of digesters, these techniques are time consuming, expensive, difficult to scale properly, and are not always available. Thus, it is hard to use these experiments to characterize every digester configurations and operating conditions. As an alternative, Computational Fluid Dynamics (CFD), once validated, provides a valuable and efficient tool to understand and evaluate the hydrodynamics and mixing of digesters.

The overall flow pattern in mechanically stirred AD and the changes that are introduced when geometric and operating variables are varied have a strong impact on different mixing phenomena and mixing parameters. The mixing parameters in turn, have a significant effect on the digestion process carried out in AD system. Hence, considering the need of evaluating the CFD model with proper experimental data, we develop a CFD model of a lab-scale digester similar to the one used in Chapter 3. The CFD model developed allows a priori predictions of the flow generated in mixed AD of any configuration and the role that key geometric and dynamic parameters play that result in different operating regimes for digesters operated at different operating conditions. In addition, the results contribute to practitioners to operate properly their mixing operation in AD in regions where the desired mixing effects for an optimum performance required.

In order to achieve these objectives, the adopted methodology is to:

- i. Develop a CFD model representing the mixed digester incorporating the rheology of manure using experimental data where the $H/T = 1$ used in Chapter 6

- to predict impeller pumping flow and pumping number, impeller discharge angle, impeller power dissipation, power number and prediction of mixing time
- ii. Investigate laminar flow and the associated pumping breakdown within an AD operating with high TS manure, determine the physical mechanism responsible for the change in flow pattern from pumping to stall at very low Re and investigate the near impeller forces on the fluid particle
 - iii. Detailed investigation of transitional flow within AD digesting low to medium TS manure with characterization of near impeller mean flow forces on the fluid particle including near-impeller flow dynamics including initiation and propagation of the impeller-trailing vortex

In order to achieve these objectives, experimental tools used include a 2D and Stereo PIV for the experimental determination of the velocity profiles including the fluctuating component, the impeller pumping capacity and pumping number. The mixing time measurement uses the conductivity measurement as detailed in Chapter 3 to quantify mixing time and a strain gage-based rotary torque transducer system (Model, T6-5-Dual Range, Interface, Inc. Scottsdale, AZ) to measure the power dissipated by the impeller and a visual observation method to determine the minimum agitation speed for complete solids suspension, Njs. In addition, CFD modeling is used to predict the behavior of the system in terms of its velocity profile, Power number, Pumping number, and mixing time. CFD predictions are obtained using both a Multiple Reference Frame (MRF) model coupled, when needed, with a Volume of Fluid (VOF) model, in order to study systems in which a vortex forms.

5.1 Model geometry for lab scale digester

The lab-scaled mixed digester shown in Figure 5.1 consists of a cylindrical baffled digester of diameter $T = 0.25$ m and a six-blade Rushton impeller of diameter $D = T/3$ positioned at the centre of the digester with clearance from the bottom $C_b = T/3$.

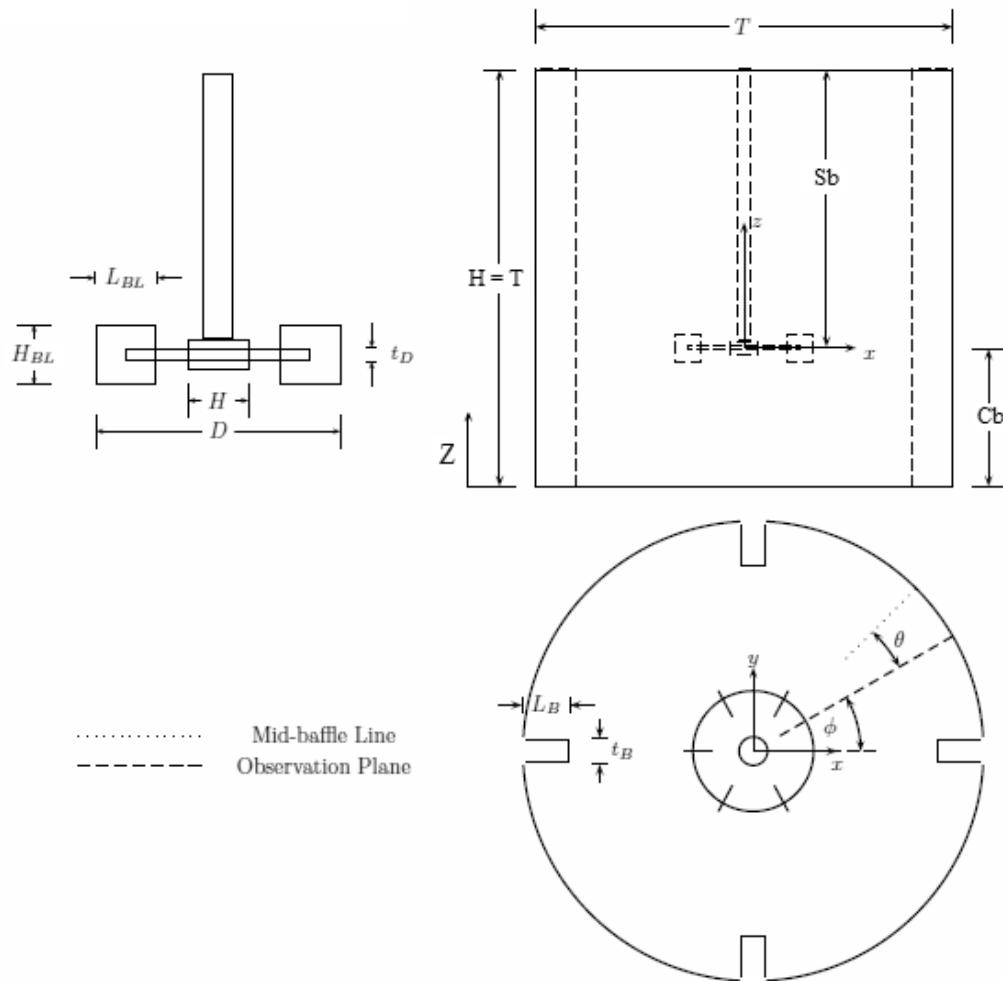


Figure 5.1: Geometry used for simulation dimensions of lab-scale digester: $T = 0.25$ m, six-blade RT impeller, $D = T/3$, $C_b = T/3$, $H_{BL} = 0.2D$, $L_{BL} = 0.25D$, $t_{BL} = 0.01T$, $L_B = T/10$ and $t_B = 0.01T$. $Re = 1, 6.9, 15.5$ for laminar, $3,000$ for transitional, and $22,500$ for turbulent cases.

The blade height, width and thickness are $H_{BL} = 0.2D$, $L_{BL} = 0.25D$ and $t_{BL} = 0.01T$ respectively. The digester contains four equally spaced baffles of width and thickness $L_B = T/10$ and $t_B = 0.01T$, respectively. The working fluid used in the simulations and experiments used for simulation validations is HEC similar to Chapter 3. The shaft of the impeller is concentric with the axis of the digester. The Reynolds number considered are 1, 6.9, 15.5 for laminar (high TS manure), 3,000 for transitional (medium TS manure) and 22,500 (low TS manure) for turbulent cases.

5.2 Governing equations

The equations solved are the continuity and momentum equations. The continuity equation is a statement of conservation of mass for a constant density fluid, and it takes the form:

$$\text{div}(\vec{v}) = 0 \quad (5.1)$$

The momentum equations are a statement of conservation of momentum in each of the three components. The three momentum equations are collectively called the Navier-Stokes equations. In addition to momentum transport by convection and diffusion, several momentum sources are also involved. In cylindrical coordinates (r, θ, z) , the momentum equations take the form (Guillard *et al.*, 200):

$$\frac{\partial(\rho u_r)}{\partial t} + \text{div}(\rho u u_r) - \rho \frac{u_r^2}{r} = -\frac{\partial p}{\partial r} + \text{div}(\tau_r) - \frac{\tau_{\theta\theta}}{r} + F_r \quad (5.2)$$

$$\frac{\partial(\rho u_\theta)}{\partial t} + \text{div}(\rho u u_\theta) + \rho \frac{u_r u_\theta}{r} = -\frac{1}{r} \frac{\partial p}{\partial \theta} + \text{div}(\tau_\theta) - \frac{\tau_{r\theta}}{r} + F_\theta \quad (5.3)$$

$$\frac{\partial(\rho u_z)}{\partial t} + \text{div}(\rho u u_z) = -\frac{\partial p}{\partial z} + \text{div}(\tau_z) + F_z \quad (5.4)$$

$$p = p_s + \frac{2}{3} \rho k \quad (5.5)$$

F_r , F_θ and F_z are the centrifugal force, the Coriolis terms and the gravity. The expressions of these three terms are (Escudié and Liné, 2004):

$$F_r = \rho(w^2 r + 2w u_\theta) \quad (5.6)$$

$$F_\theta = \rho(-2w u_r) \quad (5.7)$$

$$F_z = -\rho g \quad (5.8)$$

The viscous stress tensor defined as (Sun, 2002):

$$\bar{\bar{\sigma}} = \begin{bmatrix} \tau_{rr} & \tau_{r\theta} & \tau_{rz} \\ \tau_{r\theta} & \tau_{\theta\theta} & \tau_{\theta z} \\ \tau_{rz} & \tau_{\theta z} & \tau_{zz} \end{bmatrix} \quad (5.9)$$

where:

$$\tau_{rr} = 2\mu_e \frac{\partial u_r}{\partial r} \quad (5.10)$$

$$\tau_{\theta\theta} = 2\mu_e \left(\frac{1}{r} \frac{\partial u_\theta}{\partial \theta} + \frac{u_r}{r} \right) \quad (5.11)$$

$$\tau_{zz} = 2\mu_e \frac{\partial u_z}{\partial z} \quad (5.12)$$

$$\tau_{r\theta} = \mu_e \left(\frac{1}{r} \frac{\partial u_r}{\partial \theta} + r \frac{\partial}{\partial r} \frac{u_\theta}{r} \right) \quad (5.13)$$

$$\tau_{rz} = \mu_e \left(\frac{\partial u_r}{\partial z} + \frac{\partial u_z}{\partial r} \right) \quad (5.14)$$

$$\tau_{\theta z} = \mu_e \left(\frac{\partial u_z}{\partial \theta} + \frac{\partial u_\theta}{\partial z} \right) \quad (5.15)$$

The k- ϵ model is one of a family of two-equation models, for which two additional transport equations solved in order to compute the Reynolds stresses. The RNG k- ϵ model is a response to the empirical nature of the standard k- ϵ model Yakhot (2001). The derivation applies statistical methods on the field of renormalization group (RNG) theory rather than depending on observed fluid behaviour. It is similar in form to the standard k- ϵ model, but it contains modifications in the dissipation equation to describe better flows with regions of high strain, such as the flow around a bend or reattachment following of recirculation zone. In addition, a differential equation solves the turbulent viscosity. Several authors such as Montante *et al.* (2001), Jaworski *et al.* (2000), Launder *et al.* (2001), Lamberto *et al.* (2001) and Kelly *et al.* (2003) have used this model in the past.

The equation of the turbulent kinetic energy has the following form (Rande, 2001):

$$\frac{\partial(\rho k)}{\partial t} + \text{div}(\rho u k) = \text{div}\left(\frac{\mu_e}{\sigma_k} \text{grad } k\right) + G_k - \rho \varepsilon \quad (5.16)$$

The equation of the dissipation rate of the turbulent kinetic energy is (Zac *et al.* 2002):

$$\frac{\partial(\rho \varepsilon)}{\partial t} + \text{div}(\rho u \varepsilon) = \text{div}\left(\frac{\mu_e}{\sigma_\varepsilon} \text{grad } \varepsilon\right) + C_{1\varepsilon} \frac{\varepsilon}{k} G_k - C_{2\varepsilon}^* \rho \frac{\varepsilon^2}{k} \quad (5.17)$$

G_k is the turbulent kinetic energy production term:

$$G_k = \frac{\tau_{ij} \tau_{ij}}{2\mu_e} \quad (5.18)$$

where:

$$\mu_e = 1 + \mu_t \quad (5.19)$$

The difference between the RNG and the Standard versions is due to the onset of the next term (Jones *et al.* 2001):

$$C_{2\varepsilon}^* = C_{2\varepsilon} + \frac{C_\mu \eta^3 \left(1 - \frac{\eta}{\eta_0}\right)}{1 + \beta \eta^3} \quad (5.20)$$

where:

$$\eta = \frac{Sk}{\varepsilon} \quad (5.21)$$

Table 5.1 shows constants for turbulence model.

Table 5.1: Constants of the turbulence model

C_μ	$C1\varepsilon$	$C2\varepsilon$	σ_k	σ_ε	η_0	β
0.084	1.42	1.68	0.071	1.3	4.38	0.012

Algebraic form of a conservation equation in any control volume momentum equation is (Jaworski *et al.*, 2000):

$$A_P \Phi_P - \sum_i A_i \Phi_i = 0 \quad (5.22)$$

Since the solution of each equation at any step in an iterative calculation depends on inexact information originating from initial guessed values and refined through repeated iterations, the right hand side of the above equation is always non-zero.

This non-zero value represents the error, or residual in the solution of the equation in the control volume (Lauder *et al.*, 2001):

$$R_P = A_P \Phi_P - \sum_i A_i \Phi_i \quad (5.23)$$

The total residual is the sum over all cells in the computational domain of the residuals in each cell (Montante *et al.*, 2001):

$$R = \sum_P R_P \quad (5.24)$$

Since the total residual R defined in this manner is dependent upon the magnitude of the variable solved, it is common to either normalize or scale the total residual to gauge its changing value during the solution process. There are a number of ways to perform normalization and scaling. The change in the normalized or scaled residuals is important in evaluating the rate and level of convergence of the solution. A simulation arrives convergence when the residual mass and other quantities characterizing the flow such as the three velocity components and turbulent kinetic energy and the dissipation rate fall below 10^{-6} .

5.3 CFD modeling of mixing in a lab scale digester

5.3.1 Modeling viscosity

The viscosity of manure stimulant fluid model uses the non-Newtonian power law model in Fluent. This power law model, described as (Fluent, 2005):

$$\eta_{\min} < \eta = k \left(\frac{d\gamma}{dt} \right)^{n-1} \exp\left(\frac{T_0}{T}\right) < \eta_{\max} \quad (5.25)$$

where η is the apparent viscosity [Pa·s], η_{\min} is the lower viscosity limit, η_{\max} is the upper viscosity limit, $d\gamma/dt$ is the shear rate [s^{-1}], k is the consistency coefficient [Pa·sⁿ], n is the flow behaviour index, T is the temperature [K], and T_0 is the reference temperature. Since isothermal conditions are assumed, $T = T_0$ everywhere in the reactor, so $\exp(T_0/T) = 1$ everywhere. The consistency coefficient K and flow behaviour index n for solution of HEC obtained as described in detail in Chapter 3.

5.3.2 Volume of Fluid (VOF) method

The VOF method can model two immiscible fluids or phases by solving a single set of momentum equations and tracking the volume fraction of each of the fluids throughout the domain (Hirt *et al.*, 1987). In stirred tank applications, the VOF model is useful for tracking the shape of air-liquid interface (Sera *et al.*, 2001; Haque *et al.*, 2006; Mahmud *et al.*, 2009). In this research VOF model is used to model the air-manure simulant liquid interface in the lab-scaled digester for different liquid level. The following restrictions apply to the VOF model in Fluent:

- i. One set of momentum equations is used in the VOF model. The variables or properties in any given cells are either purely representative of one of the phases, or representative of a mixture of phases, depending on the volume fraction values.
 - a. $\alpha_i = 0$: The cell is empty (of phase i)
 - b. $\alpha_i = 1$: The cell is full (of phase i)
 - c. $0 < \alpha_i < 1$: The cell contains the interface between two phases.
- ii. All control volumes must be filled with either a single phase (e.g. gas or liquid) or a combination of both phases. The VOF model does not allow any void regions in the domain.
- iii. The VOF formulation relies on the fact that two or more phases are not interpenetrating. In another word, the model has been designed for immiscible phases.

If the interface lies inside the control volume, special treatment is used to track its position and slope in both the control volume and neighbouring cells as the calculation progresses. This procedure contains calculation of the volume fraction for secondary phase, α_i , which represents the fractional volume of the cell occupied by that phase. Since the fluid type does not change along particle paths in an incompressible, non-reacting flow, the characteristic function α_i is passively advected with the flow. The VOF model includes the solution of a scalar advection equation for the quantity of the volume fraction of the secondary phase. In this work, primary phase is manure simulant solution of HEC solution and secondary phase is air. The advection equation for the volume fraction for phase A (air) in Cartesian coordinate is (Montante *et al.*, 2001):

$$\frac{\partial \alpha_A}{\partial t} + \bar{u}_A \frac{\partial \alpha_A}{\partial x} + \bar{v}_A \frac{\partial \alpha_A}{\partial y} + \bar{w}_A \frac{\partial \alpha_A}{\partial z} = 0 \quad (5.26)$$

$\vec{v} = (u, v, w)$, velocity field

For an incompressible fluid, the conservation of mass or continuity equation is

(Guillard *et al.*, 2000):

$$\frac{\partial u_A}{\partial x} + \frac{\partial v_A}{\partial y} + \frac{\partial w_A}{\partial z} = 0 \quad (5.27)$$

Multiplying Equation 5.27 by α_A and adding it to Equation 5.26, conservation law for the volume fraction will be obtained (Sera *et al.*, 2001):

$$\frac{\partial \alpha_A}{\partial t} + \frac{\partial \bar{u}_A \alpha_A}{\partial x} + \frac{\partial \bar{v}_A \alpha_A}{\partial y} + \frac{\partial \bar{w}_A \alpha_A}{\partial z} = 0 \quad (5.28)$$

Then the volume fraction for the primary phase (HEC solution) can be simply calculated from (Mahmud et al., 2009):

$$\alpha_A + \alpha_W = 1 \quad (5.29)$$

As mentioned before, a single momentum equation is solved throughout the domain and the resulting field is shared among the phases. The governing momentum balance equation (Haque et al., 2006) is:

$$\frac{\partial u_i}{\partial t} + \frac{\partial u_i u_j}{\partial x_j} = -\frac{1}{\rho} \frac{\partial P}{\partial x_i} + \nu \nabla^2 u_i + g_i + F \quad (5.30)$$

In the momentum equations, material properties are determined based on presence of the component phases in each control volume. For the case of a two-phase flow, the density and viscosity are calculated by these equations:

$$\rho = \alpha_A \rho_A + (1 - \alpha_A) \rho_W \quad (5.31)$$

$$\mu = \alpha_A \mu_A + (1 - \alpha_A) \mu_W \quad (5.32)$$

F, the source term, in VOF simulation is the surface tension. The surface tension model in Fluent is the continuous surface force (CSF) model proposed by (Blackball *et al.* 1992).

5.3.3 Computational prediction of impeller pumping flow and pumping number

The approach to calculate N_{Qr} is similar to the one used for the experimental work mentioned in Chapter 3 with the use of computationally predicted velocities instead of experimental results. In order to compute the radial pumping number, the radial discharge flow rate, Q_r must be calculated using (Jaworski *et al.*, 2000):

$$Q_r = \int_{-w_c/2}^{w_c/2} V_{r \text{ out } r=d/2} \pi D_c dz \quad (5.33)$$

In these equations, D_c and W_c denote, respectively, the diameter and height of the cylinder surrounding the impeller where the velocities are predicted and used to calculate the pumping rate. In this work the constructed cylinder had a diameter of 4.2 cm ($r/R = 0.34$) and a height of 2 cm.

The method used to calculate radial discharge flow rate through the side surface of constructed cylinder is the net flow rate data through a selected surface on the side surface of the cylinder included by commercial software such as Fluent. As result, it is possible to predict the Radial pumping numbers, N_{Qr} for different H/T ratios and impeller off-bottom positions.

5.3.4 Computational prediction of impeller discharge angle

The impeller discharge angle is calculated using CFD simulation data and compared to that obtained experimentally. In this work, radial and axial velocity components predicted by CFD on the side surface of a cylinder around impeller with a radius r such

that $r/R = 0.34$ and height equals to the blade height, $Z_1 = 7.5$ cm and $Z_2 = 9.04$ cm are used to calculate impeller discharge angle at each point on this surface. The average of all these data of around 2, 000 points is the final impeller discharge angle reported in this study.

5.3.5 Computational prediction of impeller power dissipation and power number

In this work, the calculation of the torque applied to the impeller uses predicted values of the pressures applied at each point on the impeller blades that allows computing the tangential forces on the impeller blades. Equation 3.9 and Equation 3.10 mentioned in experimental section in Chapter 3 are used to calculate the power dissipated and hence power number from computational predictions. The pressure difference on each impeller blade and the shear stress on the blade width, disk, hub and shaft are the forces applied to the impeller in the tangential direction. The torque, Λ , from CFD simulations is (You, 2001):

$$\Lambda = \sum_i (P_1 - P_2)_i \cdot r_i \delta A_i + \sum_j \tau_j \cdot r_j \delta A_j \quad (5.34)$$

where the calculation is performed over all control cells, i corresponds to each blade and j corresponds to the thickness of the blades, disk and hubs. In this equation, r is the force arm and δA_i is the cell surface area, and P_1 and P_2 are the pressures on the front and back of the blade.

5.3.6 Computational prediction of mixing time

Numerical simulation method used here to calculate the mixing time is similar to the way it is determined experimentally. First the flow field for the system under study is computationally determined and then a blob of a tracer is numerically introduced through a vertical cylinder with radius of 0.4 cm, a height of 1cm and center point $X = 0$ cm, $Y = 6.15$ cm, $Z = 0.7$ cm away from air-liquid interface. Simulation of the mixing time requires the unsteady state transport of an inert tracer superimposed on the calculated flow field monitored until complete homogenization achieved after the convergence of the flow field. The time required to achieve a predefined level of homogeneity considered is 95%. The solution of the Reynolds-averaged species transport equation (Javed *et al.* 2006) gives the temporal and spatial distributions of the tracer concentration.

$$\frac{\partial c}{\partial t} + \frac{\partial}{\partial x_i} (u_i c) = - \frac{\partial}{\partial x_i} \left(-D_m \frac{\partial c}{\partial x_i} \right) - \frac{\partial}{\partial x_i} (u_i' c') \quad (5.35)$$

where c and c' are the mean component and fluctuating component of tracer mass concentration, respectively, and D_m is molecular diffusion coefficient. The modeling of the turbulent mass fluxes component, $u_i' c'$, uses gradient-diffusion approach (Javed *et al.* 2006):

$$\overline{u_i' c'} = -E_D \frac{\partial c}{\partial x_i} \quad (5.36)$$

where $E_D = \mu_t / \sigma_t$ is the eddy diffusivity, $\mu_t = C_\mu \rho k^2 / \varepsilon$ the turbulent viscosity, σ_t stands for the turbulent Schmidt number and is taken as 0.7, and C_μ is a constant number.

Figure 5.2 shows the record positions for the normalized concentrations of tracer as a function of time.

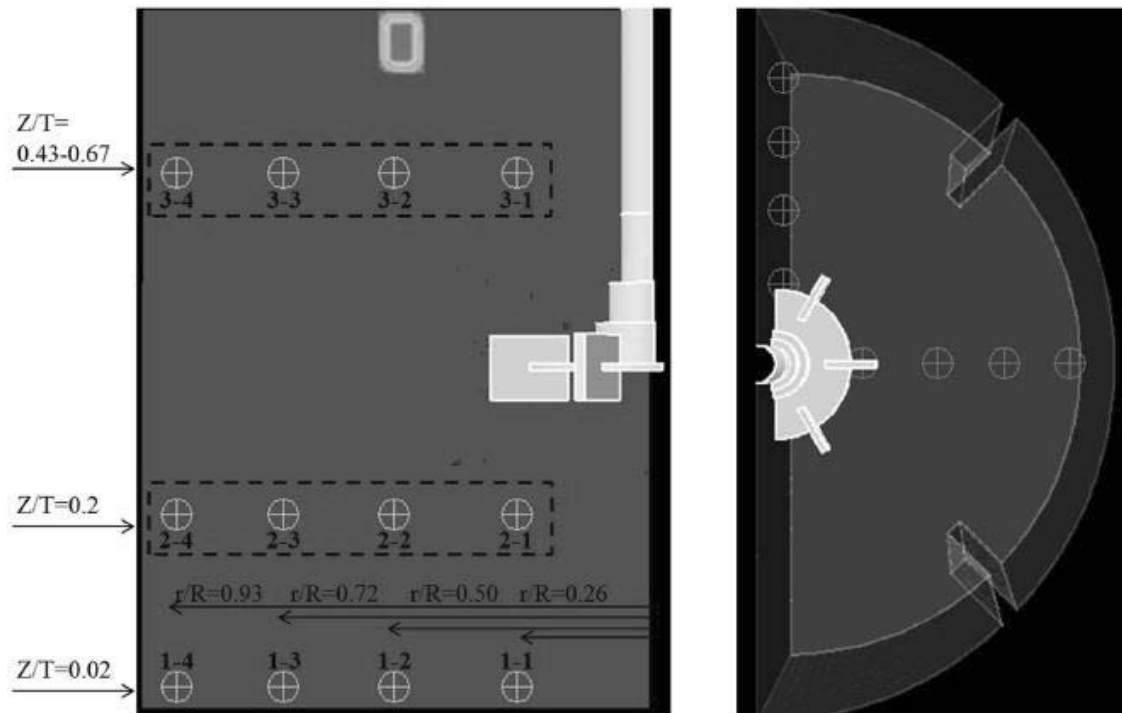


Figure 5.2: Geometric locations used to record normalized concentrations of tracer as a function of time. The square area marked red at the top of the digester is the location of tracer injection

Data at $Z/T = 0.02$ is used to study the mixing phenomena close to the digester bottom. The next two axial data sets are between the impeller and digester bottom and between impeller and air-liquid interface that enables to study the mixing time in the whole digester as impeller submergence is decreasing. The time t_{95} is the average of all data calculated to achieve 95% uniformity. The highest Z/T data location is different for

different impeller submergence ratios and it is in the middle of impeller and air-liquid interface: $Z/T = 0.43$ for $S_b/D = 0.56$ and $Z/T = 0.67$ for $S_b/D = 2.23$.

5.4 Results and discussions

The grid is generated using a commercial grid generation tool called GAMBIT (Fluent Inc., USA). The numerical simulations performed in this work span the full range of working conditions of the anaerobic digester process interest, corresponding to Reynolds number $1 - (3)10^4$. The three-dimensional, time-dependent flow field evaluation uses a finite-volume, commercial code Fluent that solves the Reynolds average form of mass and momentum balance equations for the fluid in the digester. The number of cells for the computational domain is 1,212,530 cells as illustrated in Figure 5.3. Boundary conditions are no slip at solid surfaces of wall of the digester and rotating impeller.

Preliminary grid sensitivity analysis ensured that the domain discretization shown in Figure 5.3 is refined enough to obtain grid-independent results. The maximum difference equal for the flow field calculated at pseudo steady state is 4% for the grid and a grid 1.2 times more refined in the impeller region. The flow field calculation is done at each incremental position of the impeller, exploiting a transient, sliding mesh (SM) approach described in the next section. This precise flow field characterization allows numeric reproduction of the time-dependent mixing processes with adequate accuracy. Investigation of the dispersion of species in the fully developed flow at pseudo steady state conditions allows check for the reproducibility of our results. These conditions are extremely costly and time-consuming to reproduce using full transient computations since, in the real apparatus, order 30 impeller revolutions are necessary to achieve pseudo steady state starting from fluid at rest. In order to avoid such a problem, the

explicit simulation of the start-up of agitation using the hybrid approach is important. In the hybrid approach, first an approximate flow field calculation using the multiple frame of reference (MFR) approach is performed. Then, the resulting flow information serves as a starting condition for the sliding mesh simulation.

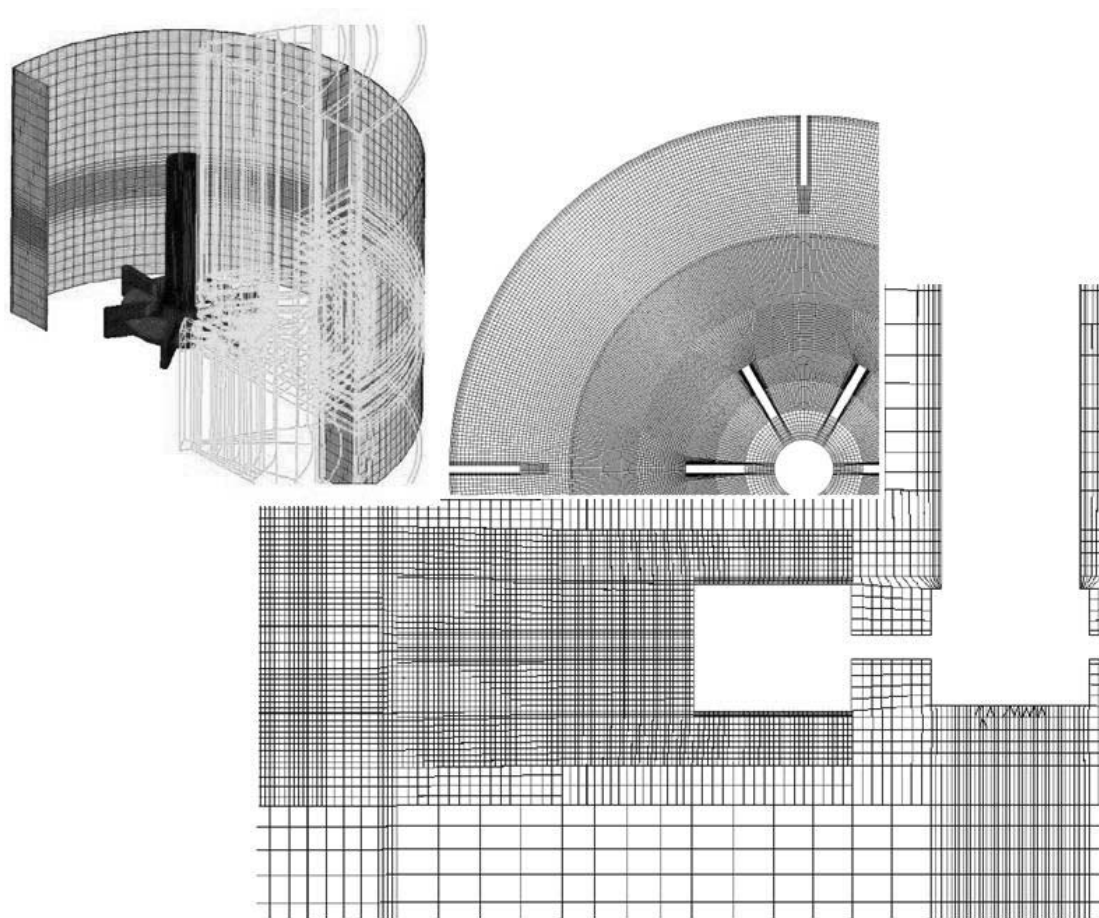


Figure 5.3: Computational grid used to perform numerical simulation with local mesh refinement. In each simulation, the computational mesh is made up of two parts: an inner rotating cylindrical volume enclosing the impeller and an outer stationary volume containing the rest of the digester

Monitoring continuously results indicates that five impeller revolutions with SM are sufficient to achieve pseudo steady state starting from the MFR solution. The calculation

of the fully developed flow field required an overall CPU time of about 50 h on an Intel (R) Core CPU processor @ 2.93GHZ, 4 GB RAM server, for each examined condition.

At pseudo steady state, we release the tracer and then solve for the mass balance equation of the injected species using the Eulerian-Eulerian approach. Use of passive tracer permits to tag the spreading of fluid as in a dye injection experiment. Density and viscosity are the same as the fluid in the digester. In these conditions, the amount of injected tracer and its physical properties have no effect on mixing time. Monitoring continuously the values of concentration at different sampling points makes it easy to follow the spreading of the tracer. The results revealed that the concentration at sampling locations becomes steady after about 16 impeller revolutions. The calculation of the dispersion of species up to well-mixed conditions requires about 150 h of CPU time on the same server for each examined condition. Validation of CFD results uses experimental data obtained as in Chapter 3 using three vertical planes located very close to the tips of the impeller blades as shown in Figure 3.6.

5.4.1 Laminar hydrodynamics

All the aforementioned observations indicate that, for low Re , significant changes take place in the flow pattern close to the impeller tip. In order to study these changes in more detail, further CFD simulations are carried out. Figures 5.4-5.6 show comparison between experimental and CFD based predictions of the variation of the normalized radial velocity V_r/V_{tip} near the upper tip of the blade where $z/T = 1/30$ at three radial locations as a function of phase angle ϕ . This angle is zero when the blade is located exactly midway between two baffles (Figure 5.1).

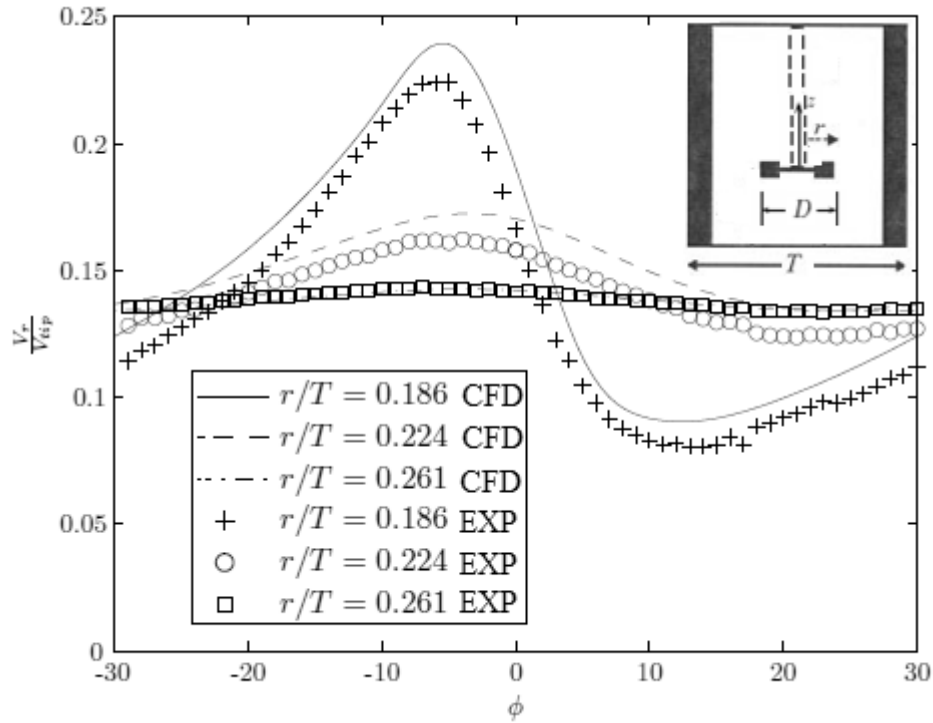


Figure 5.4: Comparison of radial velocity components obtained from numerical simulation and experiment at various normalized distances r/T for $Re = 15.5$, near upper blade tip at $z/T = 1/30$

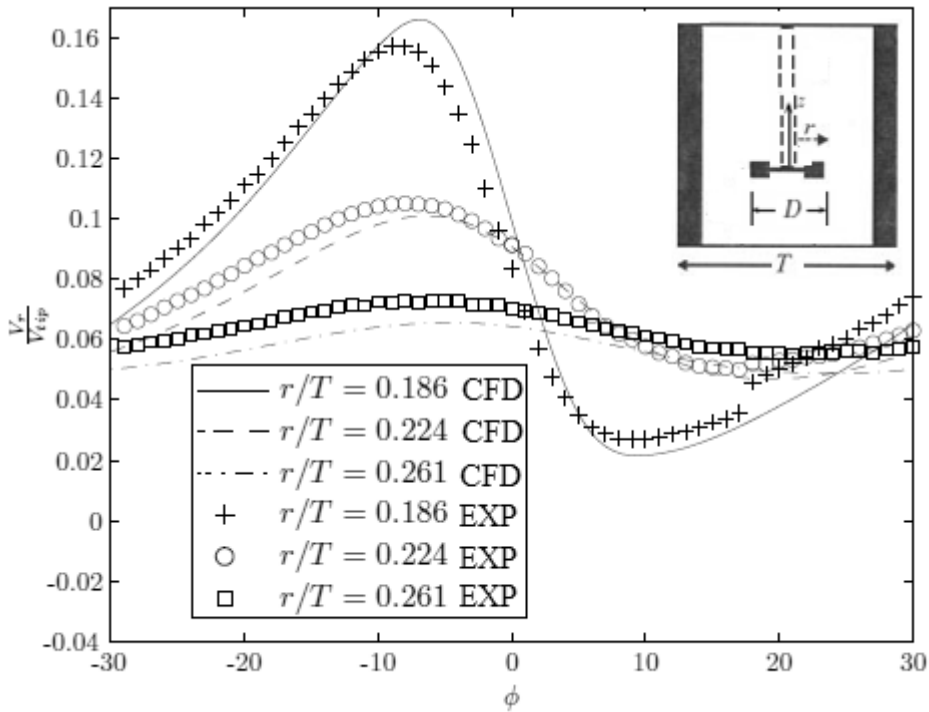


Figure 5.5: Comparison of radial velocity components obtained from numerical simulation and experiment at various normalized distances r/T for $Re = 6.9$, near upper blade tip at $z/T = 1/30$

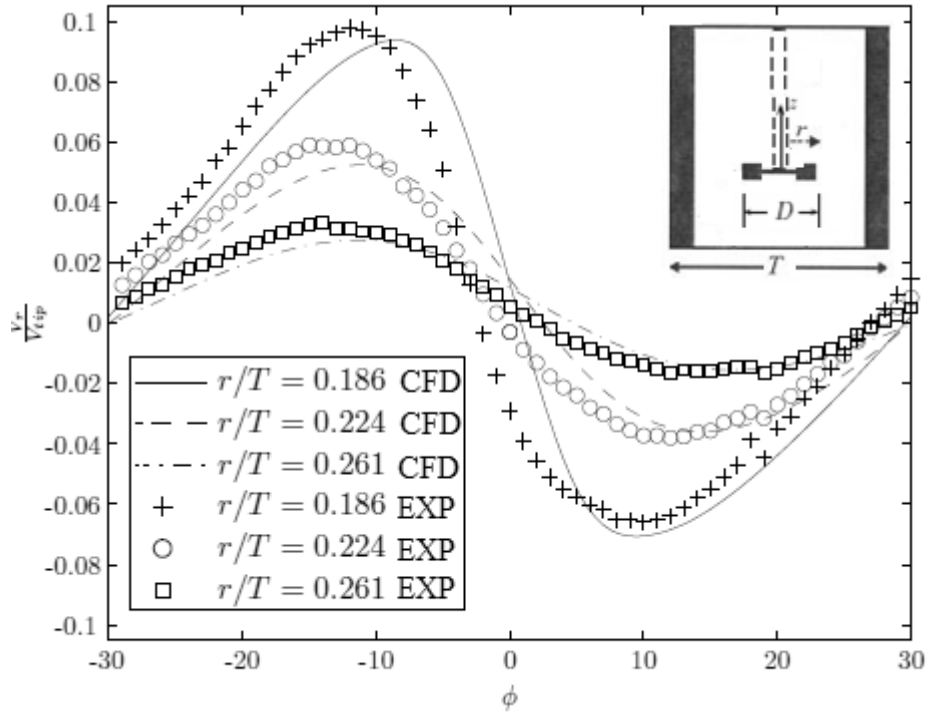


Figure 5.6: Comparison of radial velocity components obtained from numerical simulation and experiment at various normalized distances r/T for $Re = 1$, near upper blade tip at $z/T = 1/30$

Hence, in terms of the nomenclature given in Figure 5.2, the observation plane corresponds to $\theta = 0^\circ$. Note that the direction of rotation is clockwise. There is generally good agreement between experiments and predictions, especially for $Re = 15.5$ and 6.9 . However, for $Re = 1$ there is a slight shift of a few degrees in the local maximum and minimum values. Figure 5.7 shows a three-dimensional surface plot for the radial velocity at the midsection of the impeller disk-plane along with the associated location of the impeller.

For the two higher Re , both the CFD and experimental results indicate positive radial velocities for all phase angles ϕ , therefore the ensemble-averaged velocity is positive. It can be seen that for the three Re examined, the maximum radial velocity occurs near the

pressure side of the blade at $\varphi \approx -5^\circ$, which is the approximate location of the minimum radial pressure gradient as will be shown in the next section. On the other hand, the minimum radial velocity occurs near the suction side of the blade at $\varphi \approx 5-10^\circ$. As the fluid moves away from the blade in the radial direction, the variation of the radial velocity profile with blade angle, under the influence of viscosity, becomes less pronounced. Note the effect of Re on the magnitude of radial velocity: the higher the Re , the higher the magnitude of radial velocity attained. Thus, the ensemble-averaged radial velocity is reduced with a decrease in Re where $\langle V_r/V_{tip} \rangle = 0.145$ and 0.08 for $Re = 15.5$ and 6.9 respectively. This trend continues for the lowest Re resulting in almost complete stop or breakdown of pumping where the resulting average normalized radial velocity is very small, $\langle V_r/V_{tip} \rangle = 0.007$.

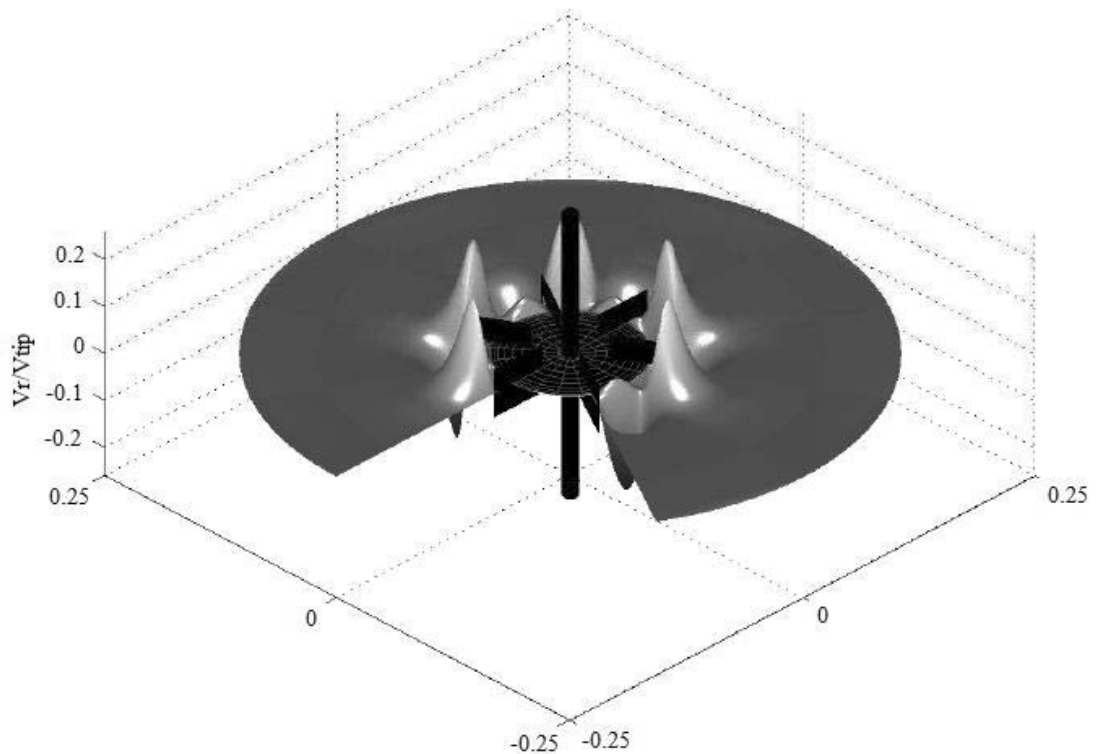


Figure 5.7: Three dimensional view of the fluid motion around the impeller for $Re = 1$ at $H_{Bl}/2$

Figure 5.8 shows radial velocity with contour plots of pressure superimposed near the impeller upper tip, for $Re = 1$. It is evident that the flow behavior is characterized by the following: Positive radial flow near the pressure-side of the blade, which vanishes at the blade tip, followed by localized reverse flow at the suction-side of the impeller blade. It is this transition from pumping, to stall and finally reverse flow at very low Re , which has previously remained unreported in the literature. Note also that the almost symmetric pressure contour magnitude on either side of the blade revealing the absence of a wake behind the blades.

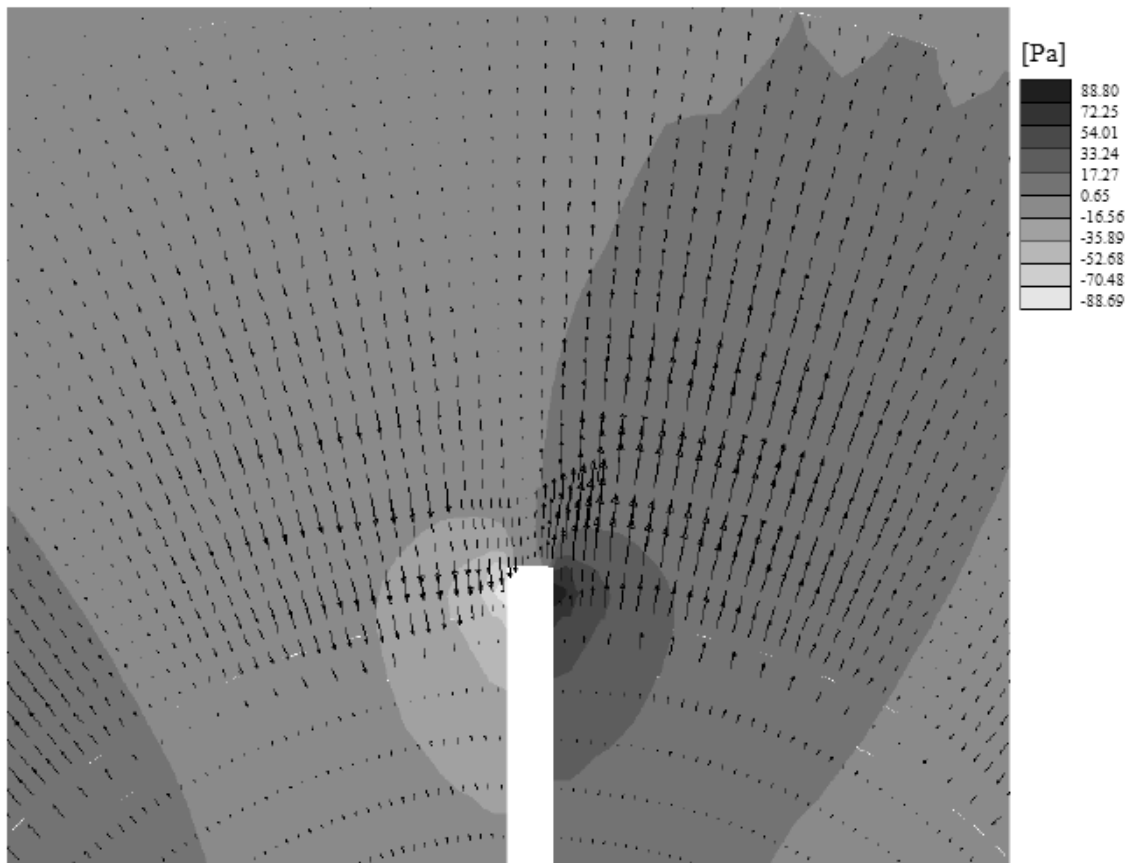


Figure 5.8: Radial velocity and pressure contours in units of Pa for $Re = 1$, in plane $z/T = 1/30$. The rotation of the blade is clockwise.

In order to explain in detail the change in flow pattern from a uniformly positive to localized reverse pumping, it is useful to investigate the forces acting upon the fluid elements in the radial direction. Specifically, two surface forces due to pressure and viscosity balance the inertial force experienced by a fluid element per unit volume that is the material derivative of velocity multiplied by density ρ_a . Figure 5.9 displays the variation of the material derivative and the two surface forces - viscous and pressure with the radial location r at $\varphi = 0^\circ$. All quantities are normalized by $\rho\omega^2D/2$, i.e. the radial inertial force per unit volume at the impeller tip. Note that the absolute maximum value of the acceleration is approximately 0.8 and not exactly 1.0 because the first radial location considered is slightly displaced from the tip. It can be seen that the maximum values for all quantities are attained near the impeller tip and then rapidly decline. For a more detailed investigation of the force variation against φ , attention is focused on a point close to the upper blade tip $z/T = 1/30$, at a radius $0.186T$, the same radial location used for the calculation of the flow number F in the previous sections.

Referring to Figure 5.10a it can be observed that the fluid acceleration is primarily negative characterized by fluid deceleration for a large interval of blade angle φ , indicating a radially inward acceleration due to the rotation of the fluid in the mixed digester. This inward acceleration is maximized at an angle $\varphi \approx 0^\circ$ which corresponds to the blade tip passing. The important qualitative difference to notice for the three Re is the increase in the relative magnitude of pressure and viscous forces compared to the inertial force with decreasing Re . $Re = 6.9$ represents a transitional case whereby pressure, viscous and inertial forces are comparable as shown on Figure 5.10b.

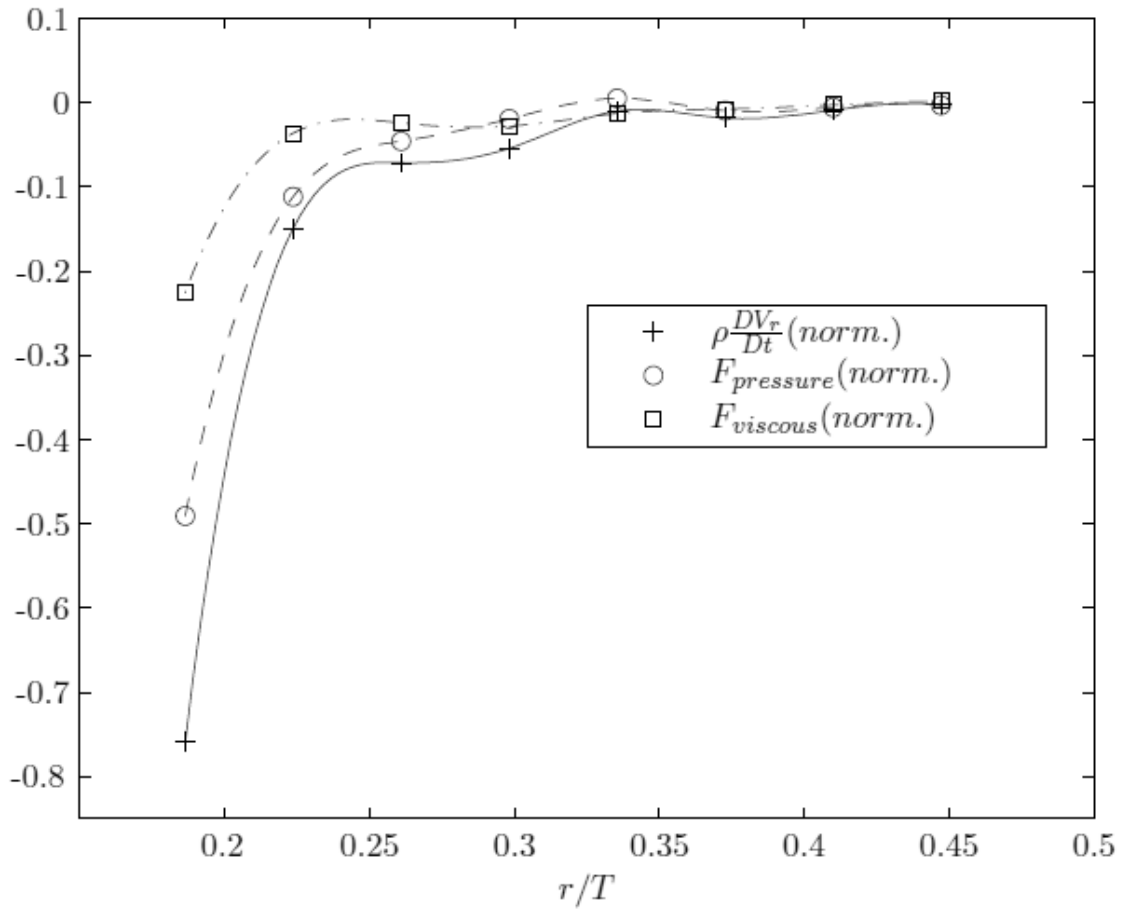


Figure 5.9: Variation of normalized acceleration, pressure and viscous forces in the radial direction for $\phi = 0^\circ$, $z/T = 1/30$ (upper blade tip) and $Re = 15.5$

However, for $Re = 1$, an interesting behavior is observed as shown in Figure 5.10c where essentially a balance exists between the pressure and viscous forces with very small values for the inertial force. In other words, the fluid behavior can be described as conforming to that of slug or creeping flow.

Since inertia is very small compared to the pressure and viscous forces, the fluid particles react instantaneously to the pressure field as shown on Figure 5.8. Clearly, the two quantities are almost perfectly in phase. Note that for purposes of illustration, the

normalized pressure force has been rescaled by dividing it by 20 in order to fit in the same graph as normalized velocity. The negative radial velocities close to the impeller disk have been reported in the past for non-Newtonian fluids, and more specifically viscoelastic materials (Bartels, 2004). Viscoelastic materials exhibit a very interesting behavior due to the presence of elastic forces in addition to the classical Newtonian inertial, pressure and viscous forces. The elastic forces act in the direction opposite to the inertial forces and cause a decrease in pumping capacity. For low rotational speeds and a highly elastic material, this can result in an inward flow at the impeller and breakdown of the pumping action.

It is found that as the Re is reduced, the net pumping capacity of the impeller is reduced as well. Fluid reciprocation in the radial direction causes to stop the pumping for Re lowest where the simulation successfully captured this behavior. A force decomposition using CFD derived measurements established the progressive strengthening of the pressure and viscous terms compared to inertial forces with reduction in Re . In fact, for the lowest Re , a balance between pressure and viscous forces where changes in fluid momentum can be neglected characterizes the flow.

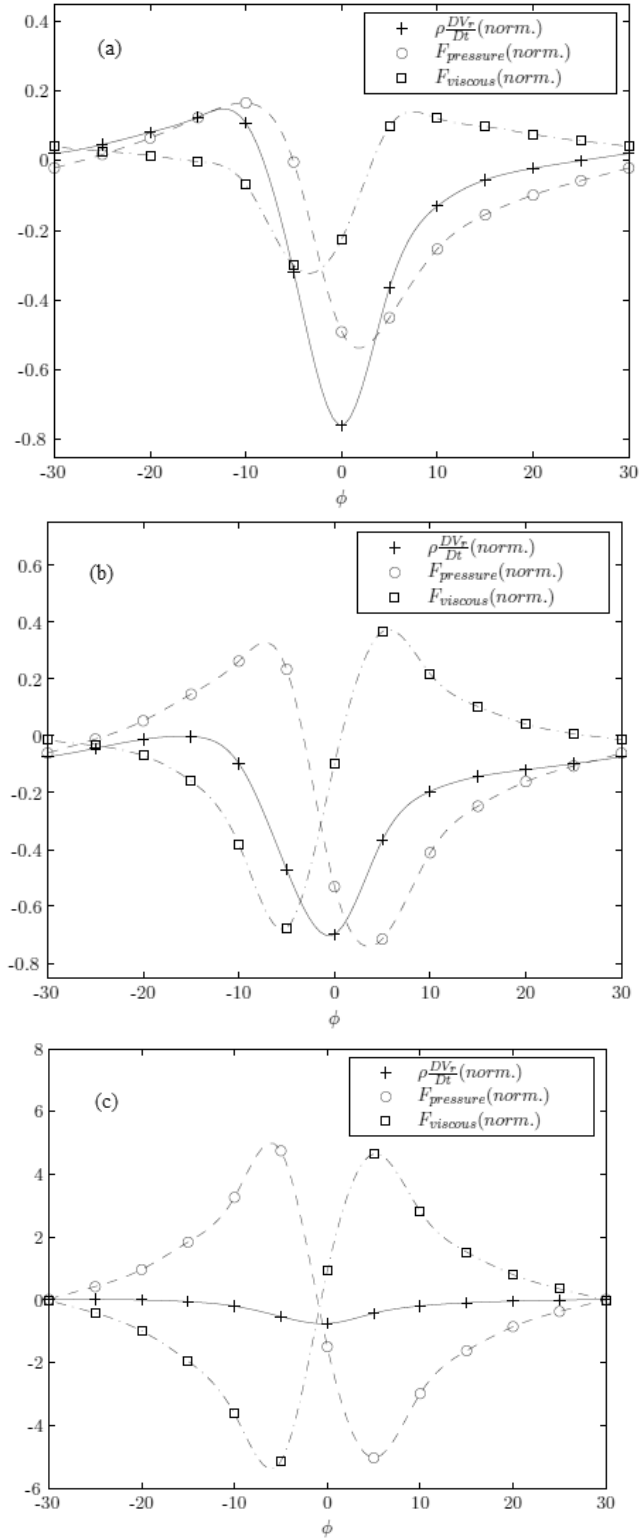


Figure 5.10: Radial force components at near upper tip location at normalized distance $r/T = 0.186$ and $z/T = 1/30$ for (a) $Re = 15.5$, (b) $Re = 6.9$ and (c) $Re = 1$

5.4.2 Transitional hydrodynamics

The geometry simulated under transitional conditions at a $Re = 3(10^3)$ is similar to that investigated under laminar flow conditions. In contrast to laminar flow mixing, where molecular diffusion and large-scale convection are the primary mixing mechanisms, turbulent flows result in enhanced mixing due to local small-scale property fluctuations i.e. larger energy containing and small scale dissipative turbulent fluctuations that serve to enhance property transport. Applications of transitional regime mixing are important for low to medium TS manure digestion. In AD, the rate of excessive product formation is often related to the mismatch between desired and actual constituent component mixing. Hence, as momentum transfer mechanisms are similar to those of species transport, knowledge of flow perturbations and hence local dissipation and turbulence intensity is important. Specifically, regions of high dissipation through property gradients, both mean-flow and turbulent fluctuation induced, correspond to regions of high mixing rates by diffusion. In addition, regions of high turbulence intensity can correspond to high turbulent species as well as momentum flux i.e. enhanced effective diffusion. Therefore, a thorough understanding of the flow physics, including flow turbulence, is important for improving mixer performance and formulating optimal mixing strategies.

Before proceeding further, the calculated mean-flow field must be validated against experimental data. Radial, circumferential and axial mean velocities, V_r , V_θ , V_z are measured in the rest frame for an identical geometry studied in Chapter 3 for an observation plane half-way between baffles where $\theta = 0$. Specifically, the curve fit for

turbulent and transitional flow normalized radial mean velocity at the disk, $z = 0$ is given as:

$$\left(\frac{\bar{V}_r}{V_{tip}}\right)_{disk} = 0.67\left(\frac{r}{R}\right)^{-0.93} \quad (5.37)$$

Figure 5.11a compares the circumferential average of simulation normalized mean-flow radial velocity V_r/V_{tip} to the correlation described in Equation 5.30 as a function of normalized radial distance r/R and indicates good quantitative agreement with experimental results. Specifically, from near the impeller tip, $r/R = 1$ to the near baffle region where the outer digester location corresponds to $r/R = 3$, divergence from the experimental results are approximately 9%. Additionally, Figure 5.11b compares simulation normalized mean-flow circumferential velocity V_θ/V_{tip} with the experimental results. Again, computational and experimental results are in good quantitative agreement with a divergence of approximately 17-20% from experimental data.

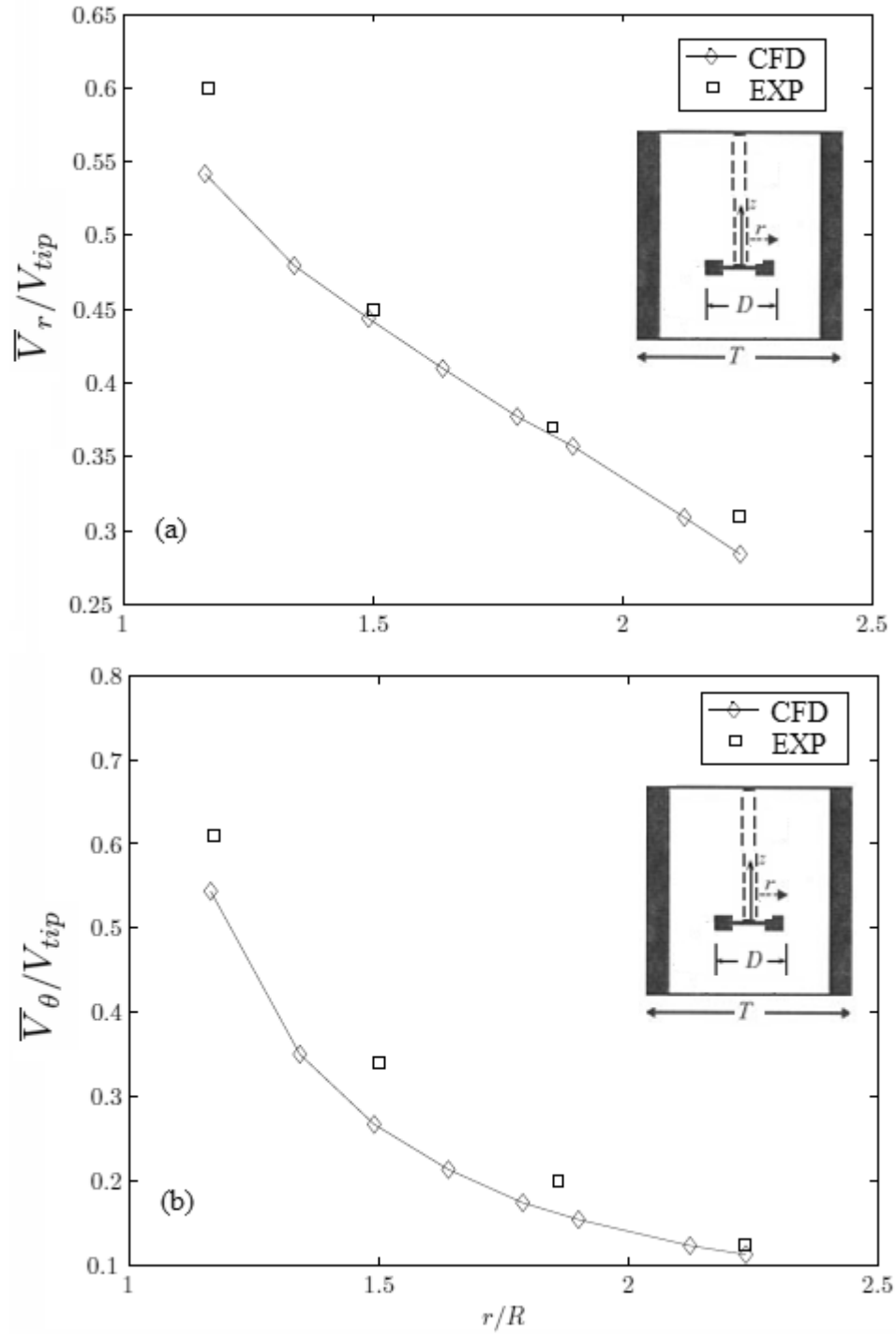
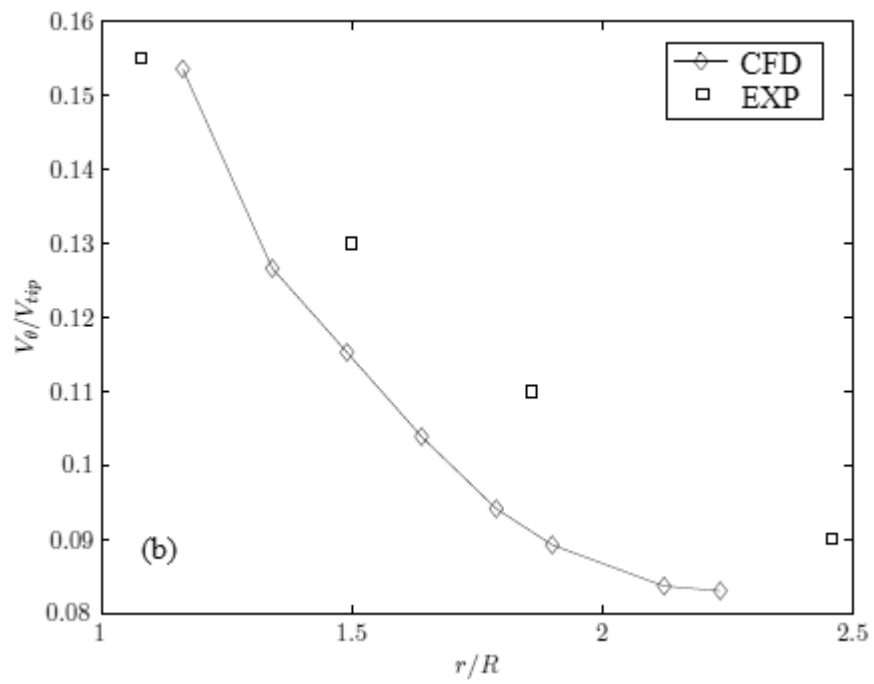
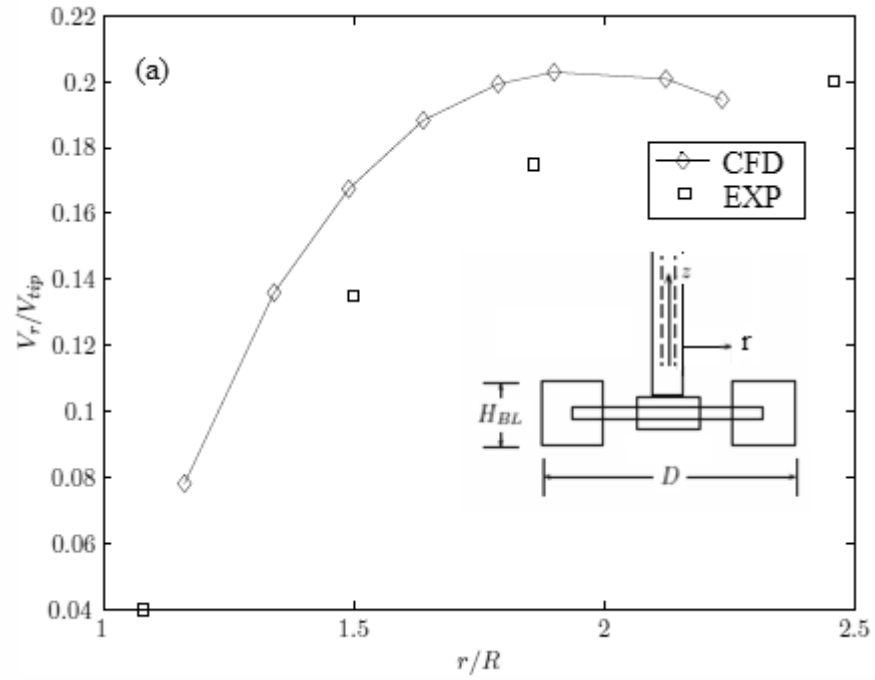


Figure 5.11: Experimental and computational results of radial and circumferential velocities normalized by the tip velocity denoted as V_r/V_{tip} and V_θ/V_{tip} at disk $x - y$ -plane for $z = 0$



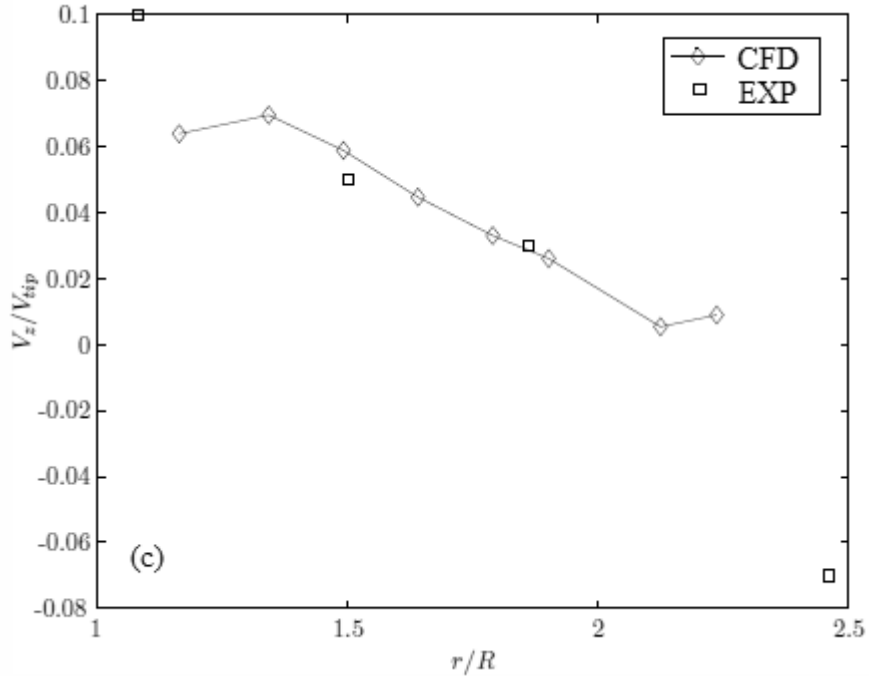


Figure 5.12: Radial V_r/V_{tip} , circumferential V_θ/V_{tip} and axial V_z/V_{tip} normalized simulated and experimentally measured mean velocity in the x-y-plane at lower blade tip, $z/(H_{BL}/2) = -1$ as a function of normalized radial position r/R .

Further comparison with experimental data are given in Figure 5.12a,b and c which illustrates radial V_r/V_{tip} , circumferential V_θ/V_{tip} and axial V_z/V_{tip} normalized simulated and experimentally measured mean velocity in the x-y-plane at lower blade tip, $z/(H_{BL}/2) = -1$ as a function of normalized radial position r/R . Again, divergence between the simulated and experimental data is approximately 18%, indicating a good correlation with experimental data.

The flow solution state at 90°-revolutions is extracted and visualized in Figure 5.13, 5.14 and 5.15. Specifically, Figure 5.10 shows x-z at $y = 0$ and disk-plane at $z = 0$ flow unit vectors and normalized velocity magnitude, indicating maximum flow $\|\vec{v}\|/V_{tip} \sim 1.0$ near the impeller and within the impeller exit stream jet. In addition, turbulence is

apparent in Figure 5.12b via the swirling, disorganized motions of various scales in the impeller stream.

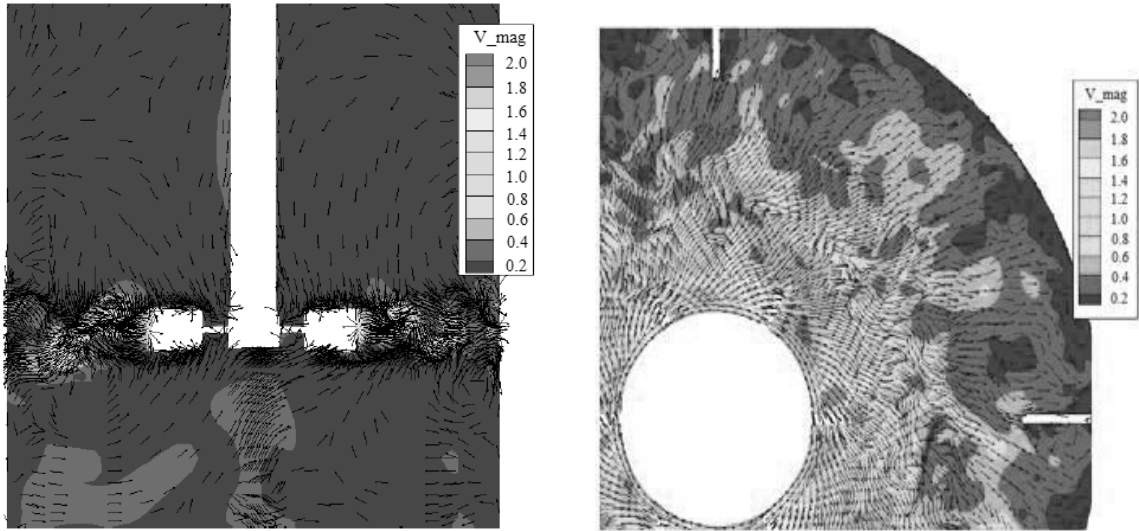
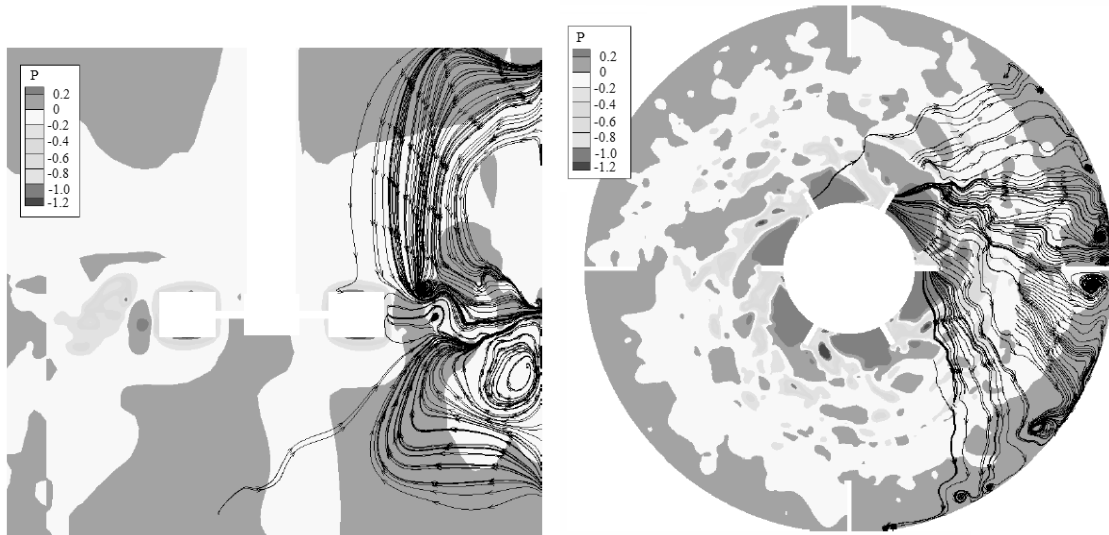


Figure 5.13: Instantaneous flow unit-vectors and normalized velocity magnitude contours $\|\vec{v}\|/V_{tip}$ at (a) $x-z, y = 0$ and (b) disk-plane, $z = 0$

The turbulent motions present within the flow are further illustrated in Figure 5.14a which visualizes eddies present via streamlines and local pressure minima associated with the local turbulence vortex cores in the impeller exit stream. Turbulent structures are also evident near the outer digester wall associated with the impeller jet flow deceleration as shown in Figure 5.14b. It should be noted that at the location $y = 0$, the outer edge of image in Figure 5.12a and 5.14a corresponds not with the outer digester wall, but to the inner baffle edge.

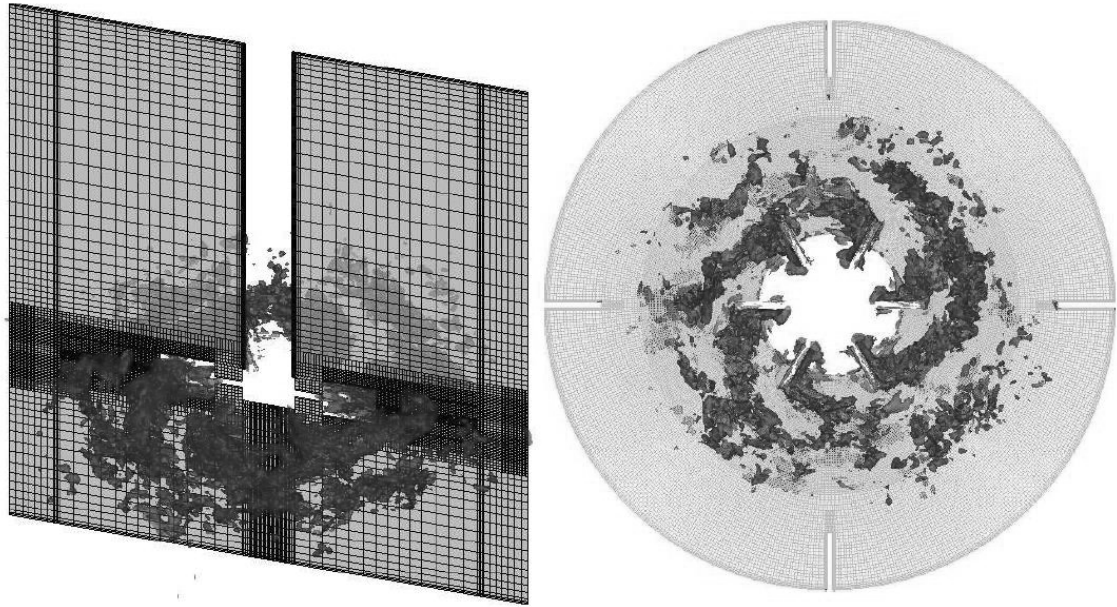


(a) $x - z$ -plane at $y = 0$ (shaft center)

(b) $y - x$ -plane at $z = 0$ (disk center).

Figure 5.14: Instantaneous flow streamlines and normalized pressure contours $P/P_{dynamic}$ based on V_{tip} . Blade rotation is clockwise

Figure 5.15 illustrates the organized motion associated with the trailing vortex that gives instantaneous swirl parameter. Specifically, Figure 5.15a indicates the presence of a turbulent wake associated with the impeller motion, while Figure 5.15b indicates that the origin of the wake is the suction side of the blade where upon the wake structure, vortex detaches from the blade and is convected outward apparently due to the bulk motion of the fluid. Note that the specific structure of the wake is difficult to discern based on examination of the instantaneous flow alone. This deficiency is addressed where the mean-flow will be used to not only establish the presence of a coherent vortex structure in the mean, but to investigate and analyze the wake (vortex) structure itself as well as the physical mechanism responsible for formation.



(a) $x - z$ -plane at $y = 0$ (shaft center)

(b) $y - x$ -plane at $z = 0$ (disk center).

Figure 5.15: Iso-surfaces of instantaneous swirl parameter at various locations in the digester indicating the presence of a turbulent wake associated with the impeller motion. The origin of the wake is the suction side of the blade whereupon the vortex detaches from the blade and convects outward due to the bulk motion of the fluid.

The mean-flow is calculated via a cell specific averaging of the flow field over 40 revolutions starting at the 50th revolution corresponding to a total simulation time of ≈ 13 sec. This yields an initial averaging based on 36 samples per revolution, or 1440 samples. Next, two global regions are specified as statistical regions to sample corresponding to the Rotor-to-sliding-mesh and Stator-to-sliding-mesh regions (Kim, 2003) as indicated in Figure 5.16. Vector quantities such as velocity are then transformed into polar coordinates yielding, over the four Stator and six Rotor-to-sliding-mesh regions, $4 * 1440 = 5760$ and $6 * 1440 = 8640$ samples for the Stator and Rotor statistical regions respectively.

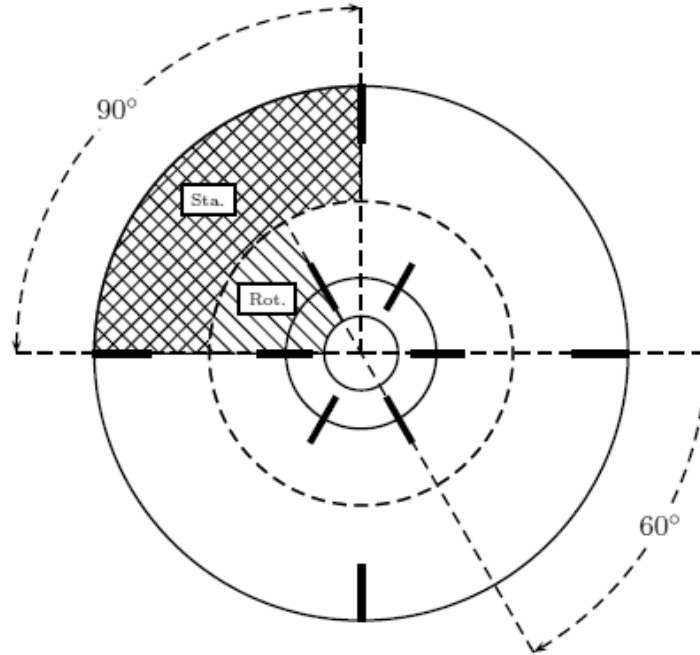
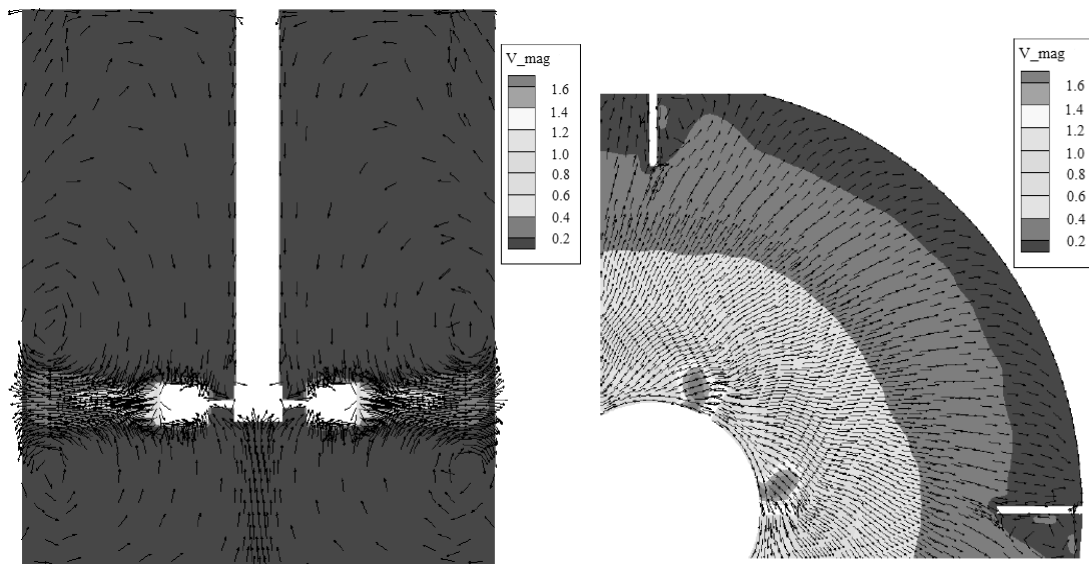


Figure 5.16: Illustration of statistical sample regions: Impeller position associated with $\theta = 0^\circ$, $\phi = 45^\circ$

The resulting statistical region mean-flow solution, now in polar coordinates, is mapped onto the flow field and converted to Cartesian coordinates. The result is a repeating flow result within the entire region based on the mapped or patterned average on a subset of the geometry i.e. Rotor/Stator statistical regions. A rotor-fixed mean-flow field for $r < R_{sliding}$ and a baffle fixed mean-flow field for $r > R_{sliding}$ where $R_{sliding}$ is the radial location of the sliding mesh interface. It should be noted that this method of averaging results in the presence of a flow and pressure discontinuity at the sliding meshes between averaged regions. This is because, as stated previously, the rotor-attached statistical region is at rest relative to the impeller while the stator-attached statistical region is at rest with respect to the outer digester region i.e. the baffles. Mean-flow properties such as $\|\bar{\vec{V}}\|/V_{tip}$, \bar{P}/P_{dynam} and the swirl parameter are illustrated in Figure 5.17-19.

Specifically, Figure 5.17 gives velocity unit-vectors and normalized velocity at the $x - z$ -plane for $y = 0$ (a) and disk-plane at $z = 0$ (b). Figure 5.17a illustrates the presence of the upper and lower bulk-flow recirculation zones above and below the disk-plane at $z = 0$ towards the outer digester wall associated with the impeller jet. Like in the instantaneous flow plots, the maximum flow $\|\bar{\vec{v}}\| / V_{tip} \sim 1.0$ near the impeller and within the impeller exit stream jet.

Figure 5.17b indicates outward flow from the impeller as well as the apparent presence of a high velocity region on the suction-side of the impeller, possibly associated with a mean-flow recirculation zone and/or wake behind the impeller.



(a) $x - z$ -plane at $y = 0$, shaft center)

(b) $y - x$ -plane at $z = 0$, (disk-plane).

Figure 5.17: Mapped mean flow unit-vectors (unit length) and normalized velocity magnitude $\|\bar{\vec{v}}\| / V_{tip}$ at various locations. The presence of the upper and lower bulk-flow recirculation zones above and below the disk-plane ($z = 0$) towards the outer digester wall are associated with the impeller jet.

To illustrate the detailed flow pattern, Figure 5.18 shows normalized mean pressure and flow streamlines i.e. impeller/digester or rotating/stationary frame streamlines based on absolute velocity. Both Figure 5.18a and b indicate outward pumping via the impeller with max or min pressure on the pressure or suction-side of the blade respectively.

Of additional interest are the upper and lower recirculation zones due to the impeller jet in Figure 5.18a impinging on the outer digester wall, as well as the separation in the mean on the suction-side of the baffle Figure 5.18b. Again, it should be noted that at the location $y = 0$, the outer edge of image in Figure 5.18a corresponds not with the outer digester wall, but to the inner baffle edge.

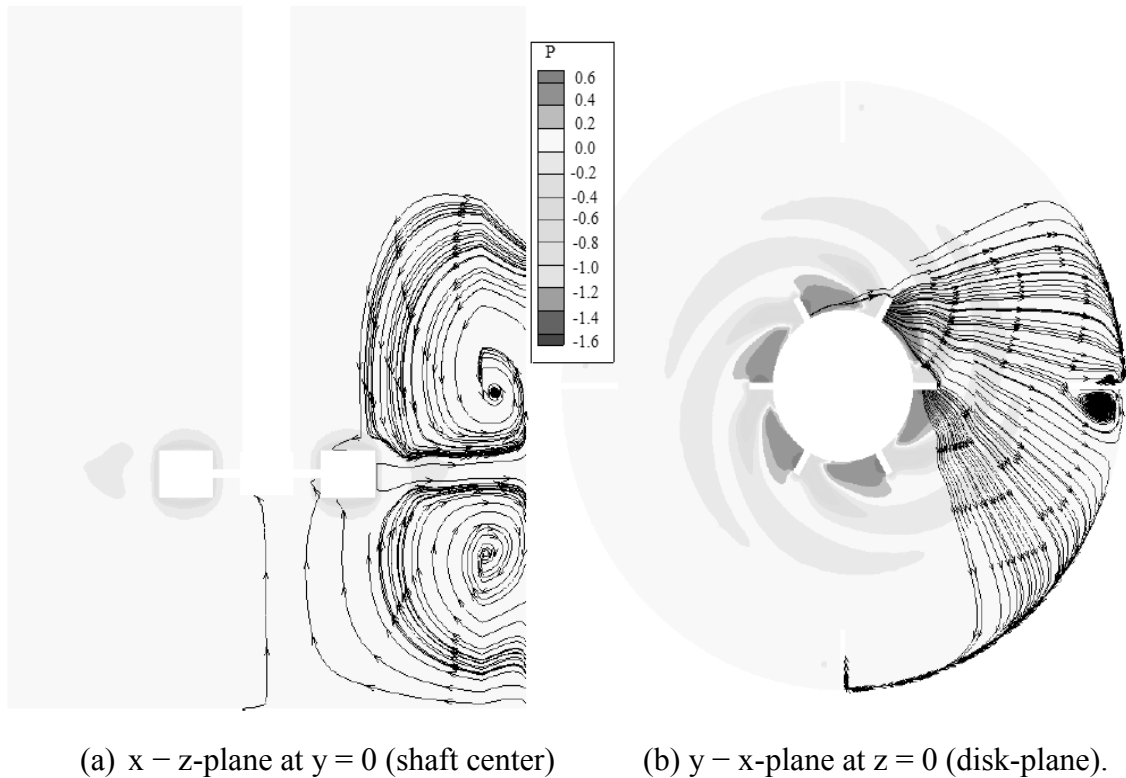


Figure 5.18: Mapped mean flow streamlines and normalized pressure P/P_{dynamic} based on V_{tip} with the upper and lower recirculation zones due to the impeller jet impinging on the outer digester wall, as well as the separation in the mean on the suction-side of the baffle

In addition, the pressure contours indicate a region of low pressure originating at the blade and subsequently convected outward with the flow. Hence, this indicates the presence of a vortex induced wake generated at the suction-side of the impeller blade. To identify these trailing vortices, the swirl-parameter is calculated based on the mean-flow. Figure 5.19 illustrates the coherent vortical structures in the form of two vortices, one above and one below the disk-plane originating at the blade suction-side, which subsequently detach and are then convected via the bulk mean-flow, outward and downstream relative to the impeller blade

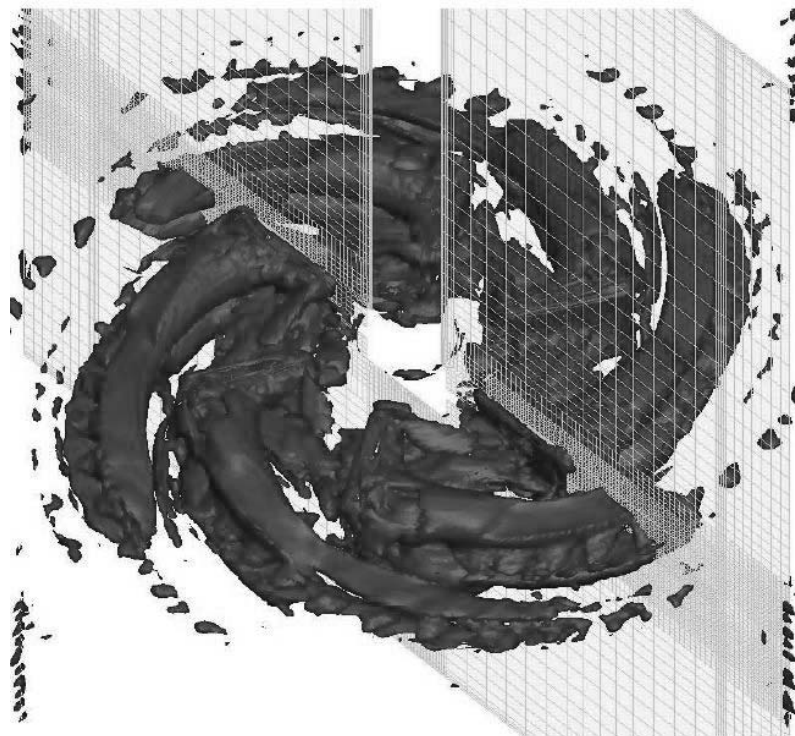


Figure 5.19: Iso-surfaces of swirl parameter for the mapped mean flow. There is a dual blade trailing on the suction-side where vortices are visible. Blade rotation is clockwise

Figure 5.20 indicates the presence of two, well-defined, vortices with origin at the blade suction-side. This establishes the presence of upper and lower vortex. Finally, unlike the

instantaneous flow snap-shot, shown in Figure 5.13, the mean-flow field appears smooth characterized by gradual spatial changes in properties such as velocity and pressure with an associated lack of turbulent structures. This suggests sufficient convergence of the statistical averaging process and hence, a sufficient number of sample flow states at least with respect to the calculation of the mean motion.

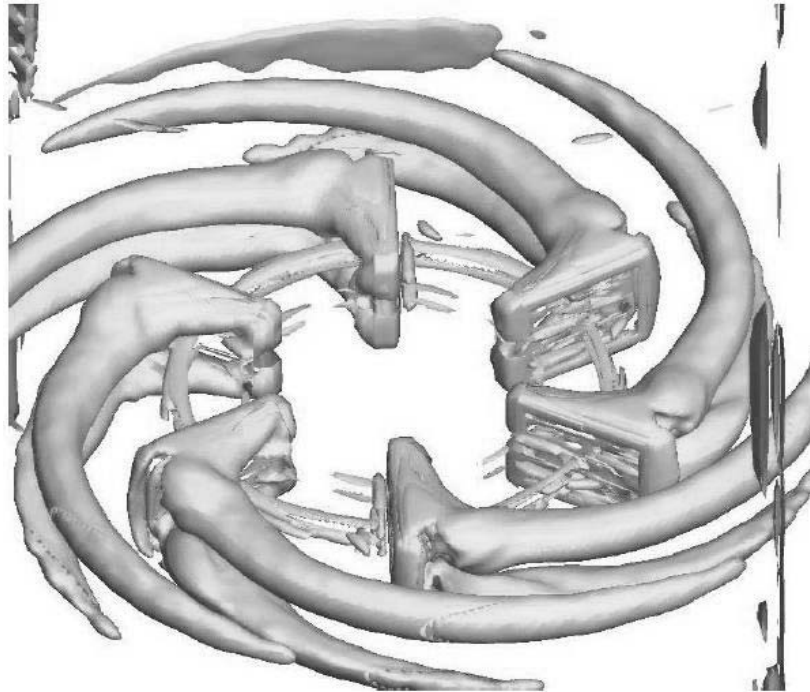
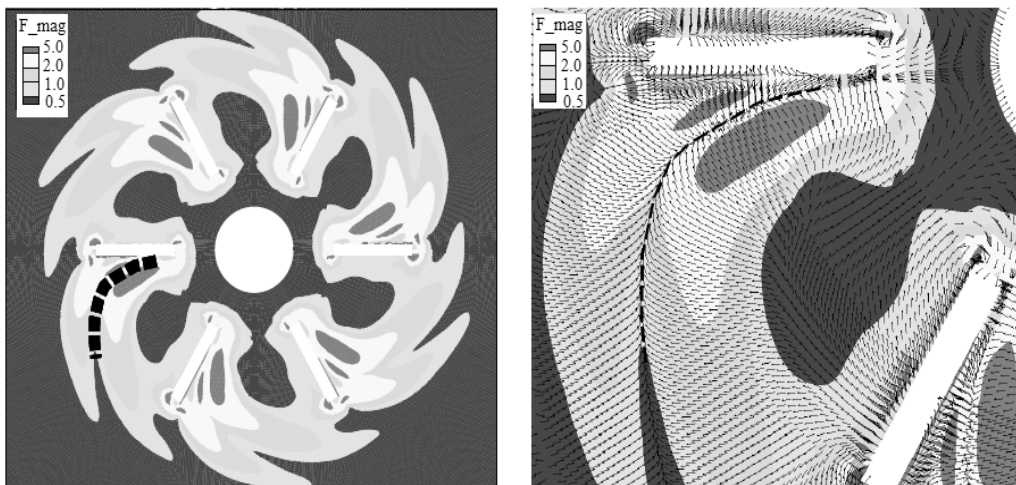


Figure 5.20: Iso-surfaces for the mapped mean flow. Dual blade trailing vortices on the suction-side are visible. Blade rotation is clockwise

The investigation of the near impeller fluid dynamics based on a mean-flow derived force decomposition not only allows for a highly detailed examination of the fundamental causal mechanisms governing the flow, but also allows for the application of a pressure force, convergence-based, detection method for identifying the spatial location of the trailing vortex core. The swirl parameter implies the presence of a vortex with initiation at the blade suction-side which is then convected outwards. Figure 5.21a

shows a contour and unit vector plot of normalized pressure force on a per unit volume basis $-\nabla P$ within the x - y -plane at axial location of one half of the blade half-height below the disk center $z/(H_{BL}/2) = -0.5$. Specifically, Figure 5.19b indicates that on the blade suction-side the convergence of the pressure force is towards a core line as signified by the dashed line. A projection of this core line onto a contour plot of pressure with pressure force unit-vectors as shown in Figure 5.19c indicates the presence of a local pressure minimum at the vortex core along the core line. Hence, an inward pressure force exists within the vortex counteracting the outward acceleration of the fluid particle due to centrifugal motion about the core. The core originates near the blade leading edge on the blade suction-side, and then detaches at a location approximately mid-cord along the blade surface. The core then moves outward under the influence of the bulk-flow, the pressure force declining as the core moves away from the impeller as indicated by the pressure force magnitude contours shown in Figure 5.19c.



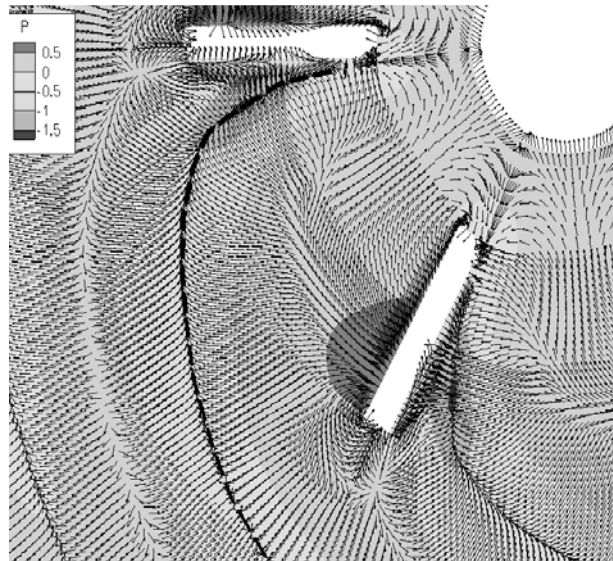


Figure 5.21: (a) Contour of normalized in-plane pressure force. (b) Near-blade contour and unit vector plot, (c) Contour of normalized pressure with pressure force unit vectors overlaid

Additional points of interest include the pressure force exerted from the pressure-side and towards the suction-side of the blade, again due to the pressure gradient as shown in Figure 5.21c. This results in acceleration of the fluid particle radially outward and away from the blade near the pressure-side tip resulting in the pumping action of the impeller and a corresponding acceleration of the flow towards the blade and inwards on the suction-side. Given the high Reynolds number of the flow at the suction-side tip, fluid particle inertia is high enough to prevent local suction-side flow halt. Recall that this is in contrast to the case of very low flow $Re \sim 1$ investigated in the laminar section where the suction-side inward pressure force results in flow stall or back-flow.

Power consumption is due to mean, periodic and turbulent dissipation, arising from the mean, periodic and perturbation flow gradients respectively. Specifically, the instantaneous power number P can be decomposed as follows:

$$P \equiv \bar{P} + \tilde{P} + P' \quad (5.38)$$

where the mean-flow contribution P is given by:

$$\bar{P} = \frac{\int_{Vol} \mu \left(\frac{\partial \bar{U}_i}{\partial x_j} + \frac{\partial \bar{U}_j}{\partial x_i} \right) \frac{\partial \bar{U}_i}{\partial x_j} dVol}{\rho N^3 D^5} \quad (5.39)$$

Calculation of the mean-flow power number via the mean-flow velocities yields

$$P = 1.78.$$

Figure 5.22 provides a more detailed treatment of mean-flow dissipation. Specifically, Figure 5.22a gives the iso-surface of normalized mean-flow dissipation per unit mass $\varepsilon_{\text{mean}}$ and indicates two general regions of high mean-flow dissipation: The first being all wetted stationary surfaces adjacent to high velocity flow such as the baffle suction-side surfaces where there exists a recirculation zone in the mean as shown on Figure 5.18b, indicating significant dissipation due to boundary-layer effects.

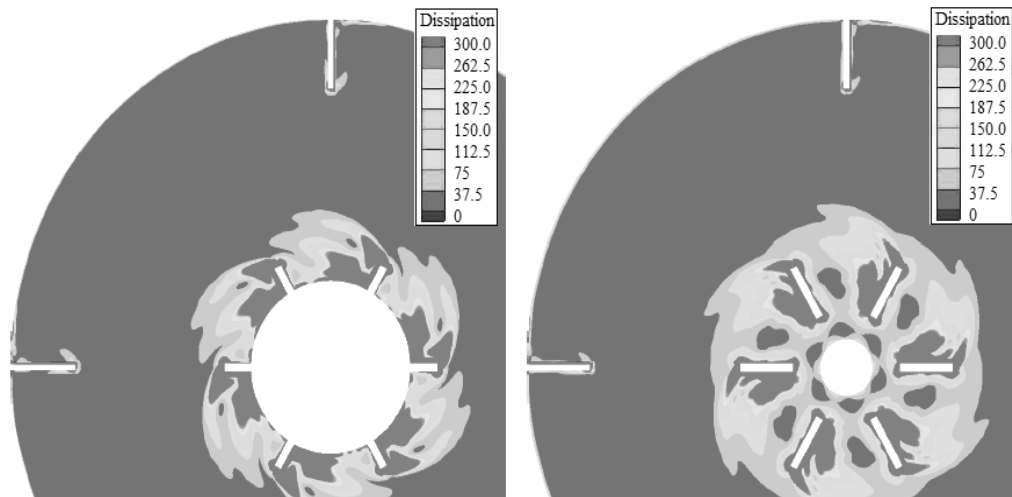
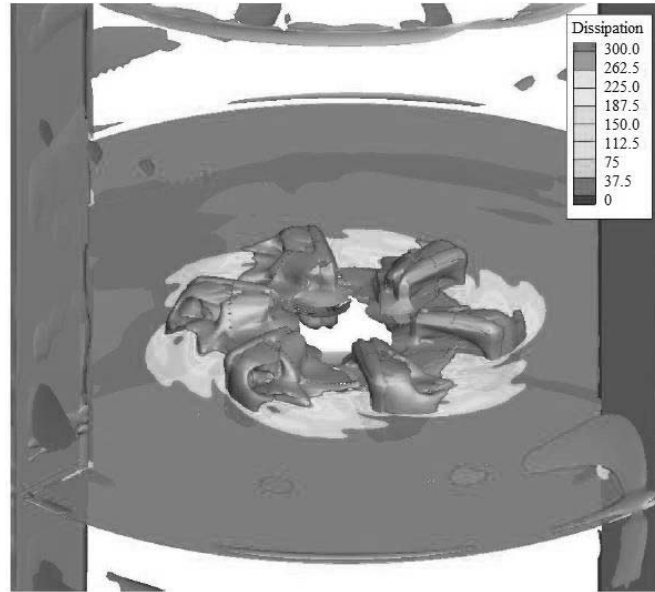


Figure 5.22: (a) Iso-surface of normalized dissipation = 300, (b) normalized dissipation at disk-plane ($z = 0$), (c) normalized dissipation in $x - y$ -plane at $z/(H_{BI}/2) = -0.5$

The second is the impeller region that exhibits significant dissipation due to the velocity boundary layer over the disk, blade edge separations and the resulting trailing-edge vortex. This can be more clearly seen by reference to Figure 5.22b and 5.22c which give normalized mean-flow dissipation ϵ in the $x - y$ -plane at $z = 0$ along the disk-plane, as well as at the half depth between disk and lower blade edge $z/(H_{BI}/2) = -0.5$.

Specifically, regions of high dissipation are at the baffle edges, blade surfaces, and especially the suction side as well as a region down-stream of the suction-side. The blade suction-side of high dissipation strengthens as one moves below, or above the disk and results from the influence of the strong swirling flow associated with the blade-trailing vortex.

Figure 5.23a gives normalized mean-flow kinetic energy k per unit mass of which high values are primarily associated with the impeller stream and trailing vortex. Specifically, Figure 5.23b gives contours of mean-flow kinetic energy k at the disk-plane at $z = 0$ and indicates a maximum just down-stream of the blade at the disk. This local maximum is associated with compression of the impeller stream via the presence of the upper and lower trailing vortices as well as flow acceleration towards the local pressure minimum associated with the vortex core. Hence, the blade pressure-side, which lacks a vortex pair, has a normalized mean-flow kinetic energy approximately equal to the tip velocity i.e. a normalized flow kinetic energy k is ≈ 1 . The same observations apply below the disk at the mid-half depth position, $z/(H_{BL}/2) = -0.5$ in the x - y -plane, where normalized mean-flow kinetic energy ranges from 1 near the blade pressure side to 2 on the suction side. Finally, for both planes as well as from the iso-surface shown in Figure 5.21a we see that the mean-flow kinetic energy rapidly declines as the fluid moves away from the blade region into the outer digester that contain relatively slow moving fluid.

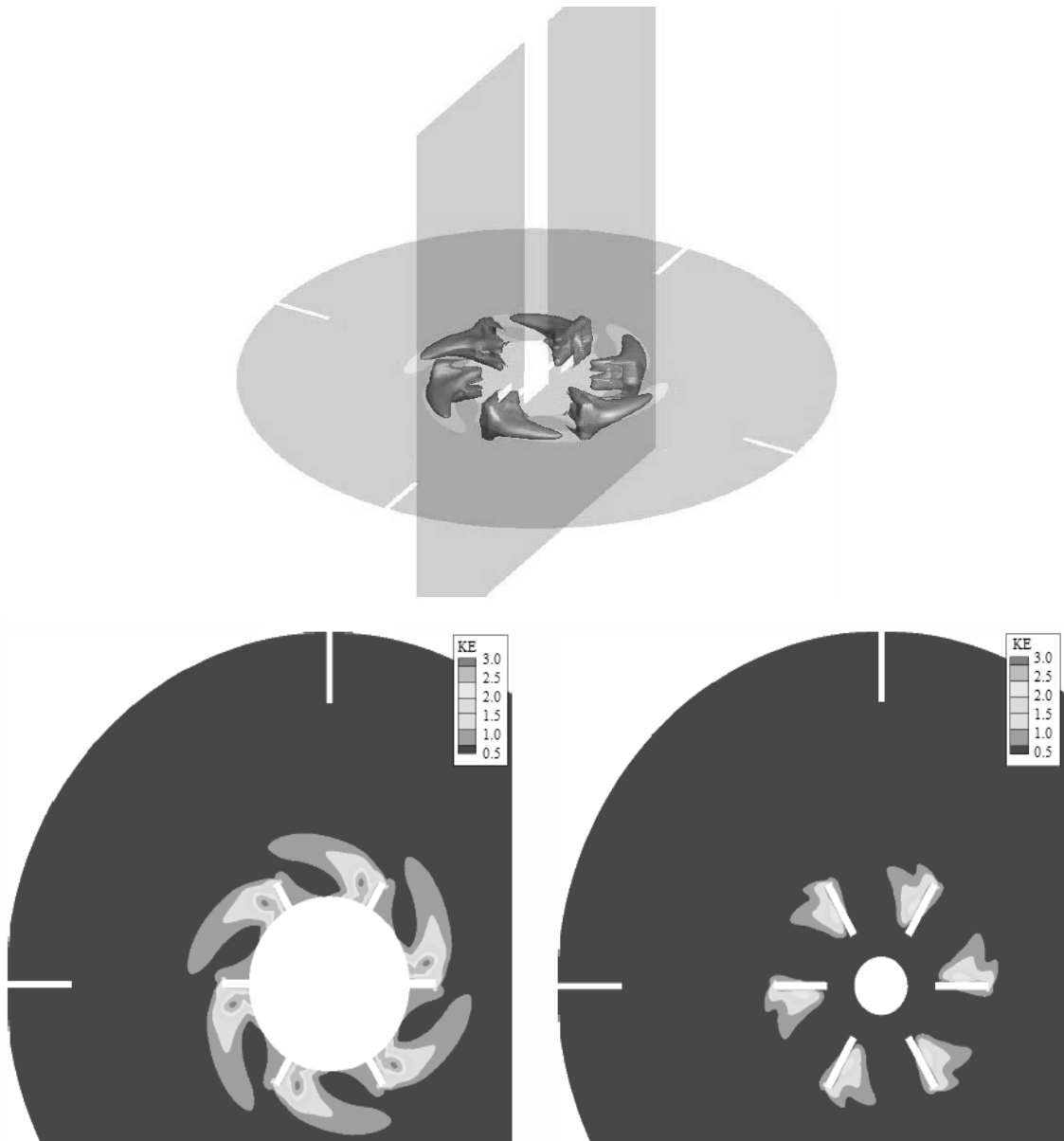


Figure 5.23: Normalized mean-flow Kinetic energy iso-surface and contours. (a) Iso-surface of normalized k/k_{vtip} of 0.75. (b) k/k_{vtip} at disk-plane, $z = 0$ (c) k/k_{vtip} in $x - y$ -plane at $z/H_{BL}/2 = -0.5$

Finally, Figure 5.24 shows normalized mean-flow kinetic energy k and dissipation ϵ just down-stream from the suction-side impeller surface at $y - z$ -plane at distance $x = 1.5t_{BL}$ from suction side surface. Specifically, Figure 5.24a shows mean-flow dissipation ϵ is locally minimized at the vortex center and increases towards the outer edge. On the other

hand, mean-flow kinetic energy k is maximized between the vortices corresponding to the maximum radial velocity associated with the impeller exit stream/jet. Conversely, the minimum mean-flow kinetic energy occurs at the upper and lower vortex outer edges opposite the central jet where the vortex relative velocity is in opposition to and counteracts the bulk flow velocity due to the presence of the jet.

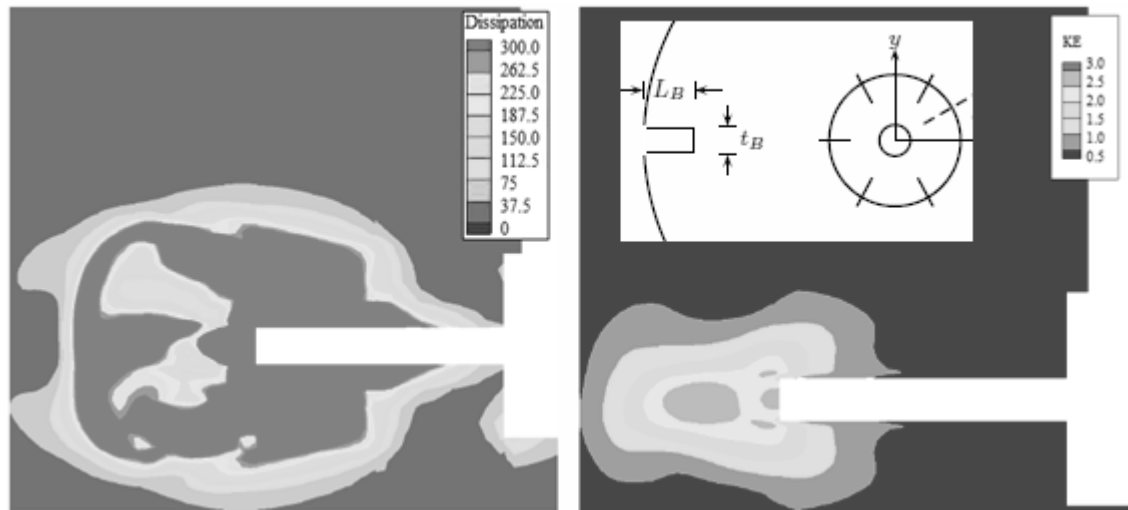


Figure 5.24: Normalized mean-flow dissipation and kinetic energy in the $x - z$ plane at distance $2t_B$ downstream from blade suction surface.

5.5 Conclusion

Anaerobic digester is an element of treatment plant completely opaque for managers. Thus, to have a computational model that allows the internal analysis at all points of the geometry is of vital importance for the analysis of the behavior and detection of possible deficiencies. In this regards the contributions this chapter makes to the scientific literature and design practitioners are:

- Computational and theoretical results with experimental validation are presented for the flow in a lab-scaled AD stirred by a Rushton turbine at low Re where $Re = 1, 6.9$ and 15.5 .
- It is found that as the Re is reduced, the net pumping capacity of the impeller is reduced as well. For lowest Re examined, pumping all but halted due to fluid reciprocation in the radial direction. CFD simulations successfully captured this behavior.
- A force decomposition using CFD derived measurements established the progressive strengthening of the pressure and viscous terms compared to inertial forces with reduction in Re. A balance between pressure and viscous forces characterizes the flow for the lowest Re where changes in fluid momentum can be neglected.
- Simulations of transitional flow for a Rushton stirred lab-scaled digester at $Re = 3(10^3)$ is performed and mean-flow properties are investigated and analyzed.
- Mean-flow properties in the impeller or baffle fixed frame are calculated and the results characterized the presence of two, well defined, trailing vortices as well as the familiar dual looped bulk-flow recirculation zones above and below the impeller stream.
- Comparison with experimentally derived mean-flow axial, radial and circumferential velocities indicates good quantitative agreement between experimental and simulation results.
- The fundamental force interactions investigated demonstrated that the flow, except very near the impeller and digester wall surfaces, is pressure driven with

an associated balance between pressure and inertial forces. This is in contrast to the case of low and very low Re flows investigated in laminar case where the interaction between pressure and viscous forces are important.

- From the calculated pressure force, a pressure force convergence based vortex core tracking procedure is used to visualize the trajectory of the trailing vortex. This trajectory is in qualitative agreement with experimental measurements of the vortex core location relative to the blade.
- The concept of a vortex relative frame is then utilized to distinctly visualize the trailing vortices. The vortices are found to originate due to the movement of fluid from the blade pressure-side, over the blade tip and toward the disk via the blade suction-side under the influence of the pressure force. The resulting recirculation zone, visible in the vortex relative and impeller frames detaches from the blade suction-side. The reason is a separation on the blade trailing edge near the blade upper/lower trailing edge.
- ✓ The calibrated model help us understand the effects of mixer geometry and operating conditions on flow mixing of non-Newtonian manure in anaerobic digesters by understanding flow inside the digester to identify possible dead zones or stratifications.

6. Effect of geometrical and operating parameters on the performance of mixing in turbulent mixed AD

The overall flow pattern in a mixed anaerobic digester and the changes that are introduced when geometric and operating variables are varied in a turbulent condition have a strong impact on different mixing phenomena and mixing parameters. These variations in turn have a significant effect on the digestion process carried out. In particular, the problem becomes huge when the total solid of the manure digested is very low in total solids, less viscous, and the turbulence intensity is high. The focus of past studies is limited to mixing vessels that have a liquid height-to-tank diameter ratio, $H/T \geq 1$. However, there are many instances where this ratio is lower than 1, as in all cases in which the digester is either emptied or filled in an anaerobic digester in batch mode. Even when the ratio, $H/T < 1$, it is important to provide a sufficient amount of agitation to attain the desired digestion process. In addition, in anaerobic digester foam is produced when organic matter decomposes and releases fatty acids that act as surfactants or surface active agents. In such cases, turbulence created on the low viscous fluid by the impeller rotation causes the fatty acids to entrain small bubbles that constitute the foam. Smaller amounts of dissolved organic matter are also released from living organisms. These foam producing molecules have one end that repels water and another end that attracts water and work to reduce the surface tension on the water surface. These fatty acids are lighter than water so float on the surface of the water as a thin film. Therefore, it is the aim of this section to determine the roles of key variables on the establishment of different flow regimes in the digester that contributes to the optimization of the mixing

process characterised by uniform mixing, suspension of solids etc. and prevent excessive foaming and sedimentation.

6.1 Methodology

To achieve these objectives, the base case configuration uses highly turbulent stirred digester with $H/T = 1$, $D/T = 1/3$, and $C = T/3$ ($S_b/D = 2.23$) as described in Chapter 5. The base case configuration is used to validate the appropriateness of the experimental technique and the computational approach used here. The impeller speed is 300 rpm corresponding to an impeller tip speed of 1.2 m/s and an impeller Reynolds number of 29,250. Since this value falls within the turbulent regime, the simulation incorporates a turbulence model to account for turbulence effects.

The simulation uses multiple references of frames (MRF) approach with the assumption of the flat air-liquid interface. In order to select the turbulence model that can best describe the experimental results, both the standard $k-\varepsilon$ model and the realizable $k-\varepsilon$ models for turbulence are tested. “SKE-CFD” denotes simulation done using the standard $k-\varepsilon$ model and “RKE-CFD” denotes simulations done using realizable $k-\varepsilon$ models in the graphs and tables. Comparisons of results obtained from each model using first-order discretization and second-order discretization show the second-order discretization are in better agreement with the experimental results. In order to assess the quality of the meshes and determine the smallest mesh size that produces mesh-independent results, the simulation considers three different mesh densities and qualities.

The Lagrangian particle motion equations for each particle are calculated based on the instantaneous local fluid velocity obtained using simulation. Contact forces acting on particles are calculated based on the Distinct Element Method (DEM). The Discrete Element Method is a numerical method to analyze the motion of a large number of particulates. In this method the particles consists of particulates, droplets, or bubbles are represented as separate entities (Fluent, 2002). Interactions between the particles are modeled explicitly using contact laws. The DEM model has proven to be versatile in modeling the behavior of granular particulates (Yuo, 2001). When coupled to fluid flow it provides a model based on first principles to describe slurry transport. Particles taken up for suspension correspond to glass beads with particle diameter d_p of 100 μm , density ρ_p of 2,500 kg/m^3 , and particle number N of 50,000.

6.2 Validation

In order to use the CFD model to optimize operation parameters, it is important to validate using experimental data obtained using PIV. There is good agreement between the experimental data and the predicted results for the velocity distribution. The velocity profiles predicted using both turbulence models denoted by SKE and RKE are close to each other but the results using RKE are in better agreement with the experimental measurements. Another approach to validate the simulations is by calculating global parameters such as the impeller Pumping number, N_Q , and the Power number, P_o . These non-dimensional numbers are constant for specific type of impellers in a given configuration and under turbulent conditions. Experimentally obtained Power number and Pumping number for the stirred digester with $C_b = T/3$ and $H/T = 1$ are compared to computationally obtained results using both SKE and RKE models. The system under

investigation here produced a double loop recirculation flow, one above and the other below the impeller. For this kind of flow pattern Q_{out} around impeller is almost identical to radial flow out, Q_r (Paul *et al.*, 2004). Therefore, the impeller Pumping number, N_Q and the impeller Radial pumping number, N_{Qr} are expected to be the same.

A summary of results are presented in Tables 6.1 and 6.2. These results show that there is good agreement between the experimental data and the computational results obtained here for N_Q and P_o . The RKE-based results for P_o agree slightly better with the experimental measurements. The pumping numbers predicted by both turbulence models are nearly same.

Table 6.1: Pumping number for $D/T = 0.31$ and $Cb/T = 0.30$

Method	N_{Qin}	N_{Qout} or N_{Qr}	Difference (%)
PIV		0.808	
SKE CFD	0.790	0.790	-2.23
RKE CFD	0.790	0.798	-1.12

Table 6.2: Power Number for $D/T=0.31$ and $Cb/T = 0.30$

Method	P_o	Difference (%)
Torque measurements	4.89	
SKE CFD	4.66	-4.70
RKE CFD	4.74	-3.07

Based on the computational results achieved, the realizable k- ϵ turbulence (RKE) model for $H/T = 1$ appeared to be slightly better than the SKE model. Therefore, the RKE model is used as the turbulent model for the remaining simulations in this Chapter.

6.3 Results and discussion (single phase)

6.3.1 Effect of impeller submergence ratio on flow pattern with $H/T < 1$

After validating the CFD simulation for $H = T$, the flow pattern and velocity field in the same lab-scale digester at different impeller submergence ratios, S_b/D , i.e. different fill ratios, H/T , are studied. Figure 6.1 shows results obtained for different impeller submergence ratios S_b/D , i.e., 2.23, $H/T = 1$: 1.24, $H/T = 0.69$: 0.98, $H/T = 0.61$: 0.77, $H/T = 0.54$, and 0.59 $H/T = 0.49$. The flow pattern predicted by CFD simulations are presented for a larger cross sectional area than the PIV measurements for better visualization purposes. The rectangular area shown in each of the CFD simulation panels corresponds to areas of the digester where PIV measurement is obtained. Figure 6.2 shows the comparison of velocity contour plots obtained using PIV data with CFD simulations. The velocity contours plots cover the same cross sectional area of the digester, both computationally and experimentally. The figures show that the CFD predictions and PIV measurements of the velocity profiles and velocity contours are in agreement for the various S_b/D values.

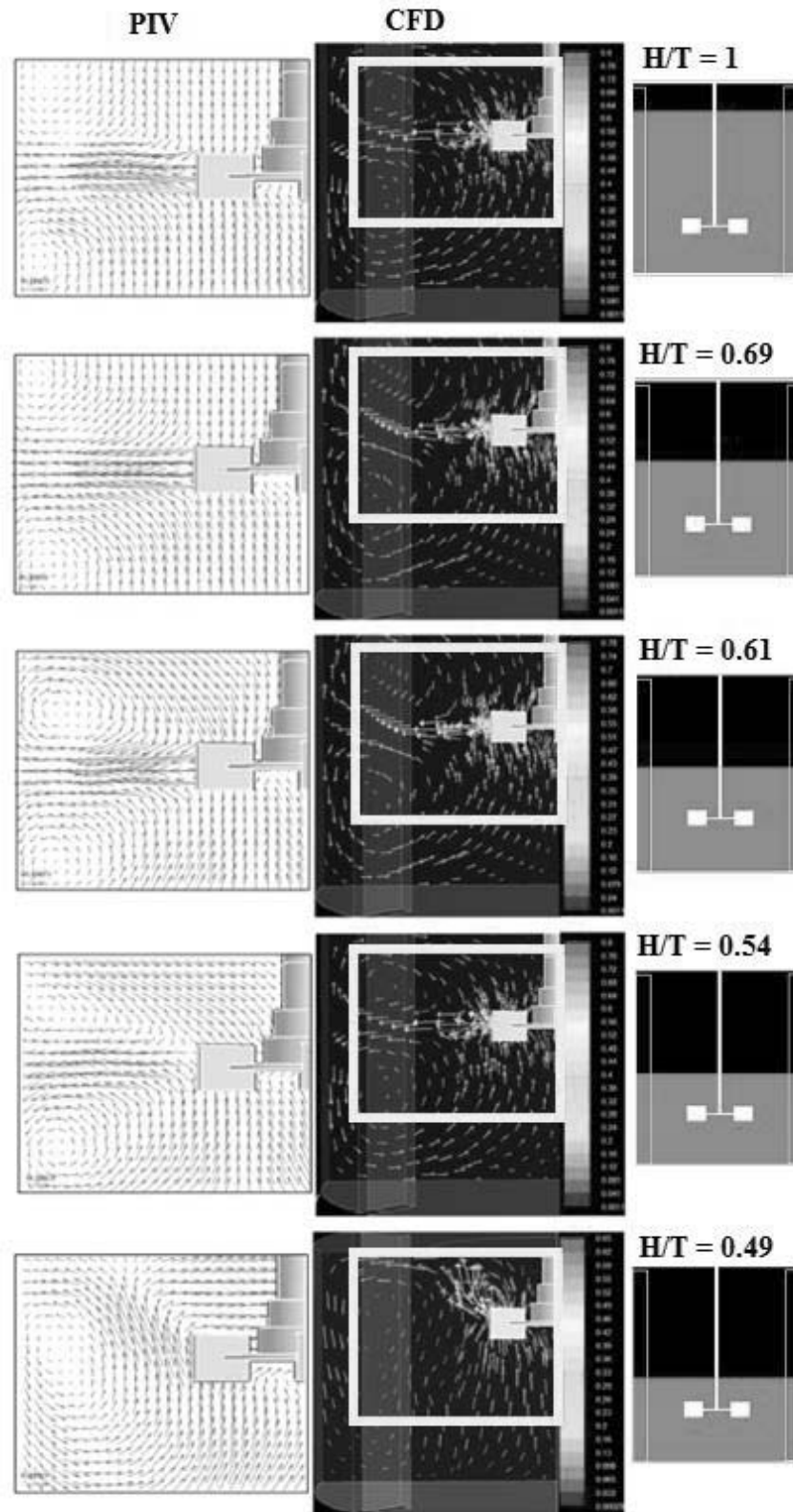


Figure 6.1: PIV measurement and CFD prediction of velocity vectors for different H/T ratios, $C_b/T = 0.30$, $D/T = 0.31$ and $N = 300$ rpm.

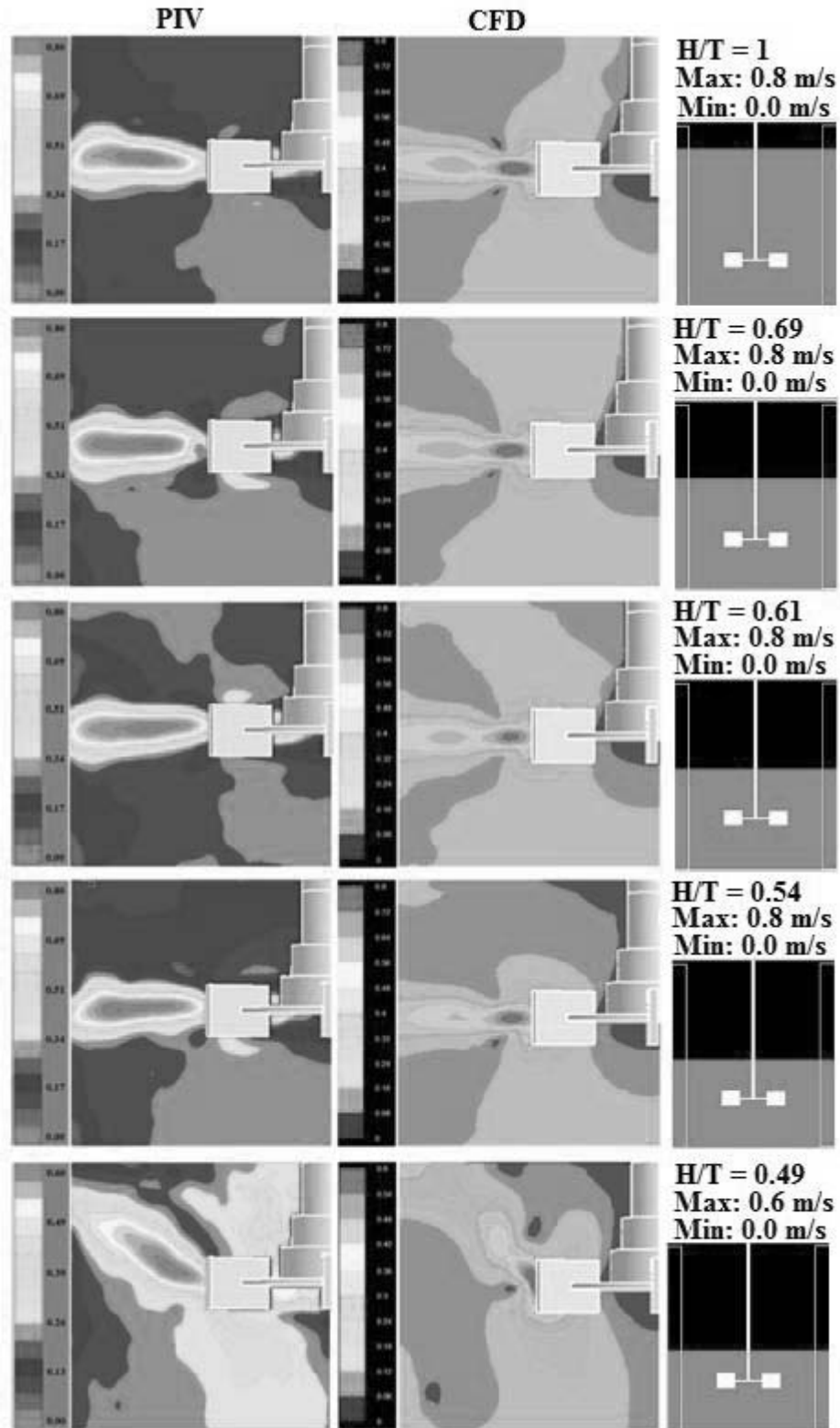


Figure 6.2: PIV measurement and CFD prediction of velocity contours for different S_b/D ratios, $C_b/T = 0.30$, $D/T = 0.31$ and $N = 300$ rpm

Additionally, it can be observed that flow pattern for $S_b/D = 0.59$, $H/T = 0.49$ is different from the other cases in both the simulations and the experimental results. When the submergence level, S_b/D reaches a value between 0.59 and 0.77, there is a suppression of the upper recirculation above the impeller. There is also a transition of the flow regime from a double loop recirculation flow (two recirculation loops one above and the other below the impeller), to a single loop up-pumping recirculation flow from top to the bottom as evident on Figure 6.1. It is possible to define a critical submergence level where above this value is the transition of flow from double loop to single loop up-pumping. For the base case stirred digester studied, the critical submergence level is $S_b/D = 0.77$, $H/T = 0.54$.

A quantitative comparison of the CFD simulation results for the radial and axial velocities for the impeller submergence ratios, S_b/D equal to 2.23 for $H/T = 1$, 1.24 (0.69), 0.77 (0.54), and 0.59 (0.49) at five different axial vertical locations in the liquid are presented in Figure 6.3. The results indicate that axial velocity profiles and radial velocities profiles are not strongly affected by sufficiently high submergence ratio i.e., S_b/D equals to 2.23, 1.24 and 0.77. However, when the flow pattern switches to the single loop up flow regime for $S_b/D = 0.59$ as shown in Figure 6.1 and Figure 6.2, both radial and axial velocities decrease. Figure 6.4 also shows the experimental velocity measurements for $S_b/D = 0.59$, validating the change in flow pattern and the weakening of the overall circulation flow.

The decrease in the radial and axial velocities that accompany the flow transition affects the mixing efficiency in mixed anaerobic digester systems, and especially solid suspension that require higher velocity field close to digester bottom to avoid particle settling. Impeller submergence ratios of 1.24 to 0.77 results in a less pronounced flow field changes. The radial velocity in upper portion of the liquid, $Z/T = 0.45$ for $S_b/D = 0.77$ is mostly negative, implying that the flow in that region is toward the impeller. However, for $S_b/D \geq 1.24$ the radial velocity is very small but positive. This observation further confirms the flow patterns for the same impeller submergence ratios presented in Figure 6.1.

The flow regime transition from double loop to single loop shown in Figure 6.1 and Figure 6.2 associates with changes in the impeller discharge angle, N_{Qr} and P_o , as shown in Figure 6.4. For relatively large impeller submergences of $S_b/D > 0.98$, $H/T > 0.61$, the average impeller discharge angle slightly points upwards between angles of $4 - 7^\circ$. However, when the submergence is closer to the critical value of $S_b/D = 0.77$, $H/T = 0.54$, the angle starts to increase and eventually reaches 60° when the flow pattern changes to $S_b/D = 0.59$, $H/T = 0.49$. Figure 6.4a shows that both computationally and experimentally obtained results predict the rapid transition. The simulations under predicted the discharge angles by 6–12%, i.e., by less than one degree for the first 2 cases and by 5 degrees for $S_b/D = 0.59$, $H/T = 0.49$.

Figure 6.4b and Figure 6.4c show the computational predictions and experimental measurements of the P_o and N_{Qr} at different H/T ratios, respectively.

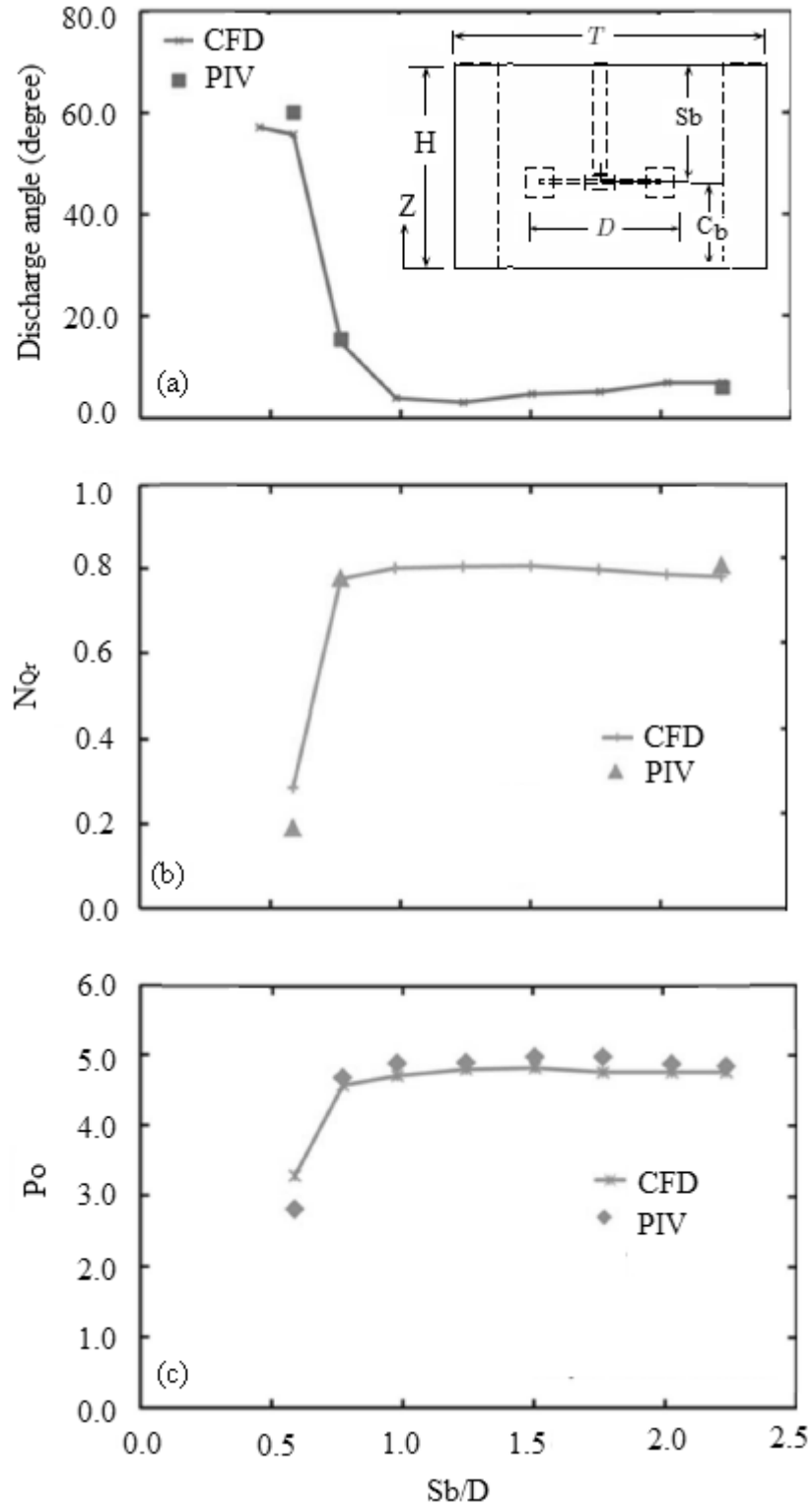


Figure 6.4: Effect of S_b/D on (a) Impeller discharge angle, (b) radial Pumping Number, N_{Qr} and (c) Power Number, P_o for different S_b/D ratios, $C_b/T = 0.30$, $D/T = 0.31$ and $N = 300$ rpm calculated from both experimental and FS-CFD Simulation data

When the impeller submergence ratio S_b/D is higher than 0.59, the submergence ratio has no effect on the N_{Qr} and P_o . However, when the impeller submergence ratio decreases to the critical level, $S_b/D = 0.77$ and reaches the $S_b/D = 0.59$ resulting in the flow pattern changes, these two dimensionless numbers decrease drastically.

The CFD predictions for P_o and N_{Qr} are in very good agreement with the experimental data for the liquid levels \geq critical submergence level of $S_b/D \geq 0.77$, $H/T \geq 0.54$, i.e., before flow pattern transition. When $S_b/D = 0.59$, the agreement is still substantial although the CFD simulations slightly over predicted P_o and N_{Qr} .

6.3.2 Effect of off-bottom clearance (C_b/T)

For both digester configurations of $H/T = 1$ and $H/T < 1$, the effect of impeller off-bottom clearance, C_b on the flow pattern and different mixing parameters such as P_o and N_{Qr} for a digester are investigated.

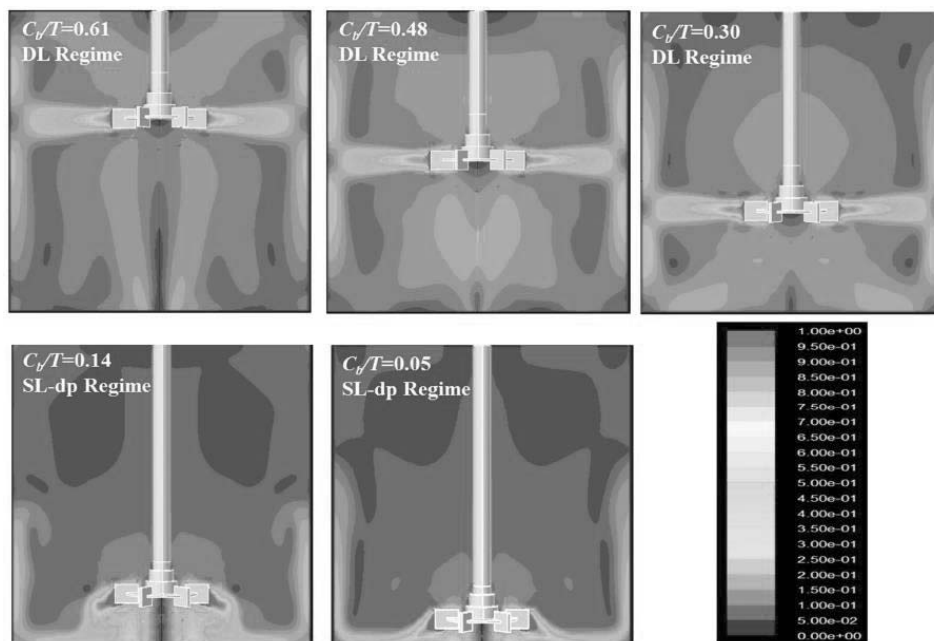


Figure 6.5: Velocity contour plots for different C_b/T , $H/T = 1$, $D/T = 0.31$, $N = 300$ rpm

Figure 6.5 shows the flow pattern predicted using simulation for decreasing C_b/T ratios equal to 0.61, 0.48, 0.30, 0.14 and 0.05.

Flow pattern transition from a double loop recirculation flow to a single loop down-pumping recirculation flow is observed when the impeller off-bottom clearance ratio, C_b/T decreases from 0.30 to 0.14. Figure 6.6 shows both experimental and numerical simulation results of the average impeller discharge angle, pumping number and power number as a function of C_b/T ratio. The average impeller discharge angles relative to horizontal line are shown in Figure 6.6a for the same impeller off-bottom clearances used in Figure 6.5. For relatively large impeller off-bottom clearances, $C_b/T > 0.14$, the average impeller discharge angles are close to zero, i.e. $C_b/T = 0.30, 0.48$ and 0.61 with corresponding angles of $6.0^\circ, 1.7^\circ$ and 0.0° , respectively. For lower impeller off-bottom clearances of $C_b/T = 0.14$ and $C_b/T = 0.05$, the flow pattern change from double loop flow regime to the single loop down-pumping regime results in abrupt decrease on the discharge angle. The impeller discharge angles near the transition point, $C_b/T = 0.14$ calculated by CFD (-23°) and measured by PIV (-20°) are in a good agreement. For a very low impeller off-bottom clearance, $C_b/T = 0.05$, the predicted value and PIV measurements are not as close as in the other cases where the predicted angle is -39° as opposed to experimentally measured angle of -27° .

Experimental data and computational predictions of N_{Qr} and P_o are in agreement for impeller off-bottom clearance ratios of 0.61, 0.48 and 0.30. However, these dimensionless numbers are slightly under predicted by simulations for C_b/T equals to 0.14 and 0.05.

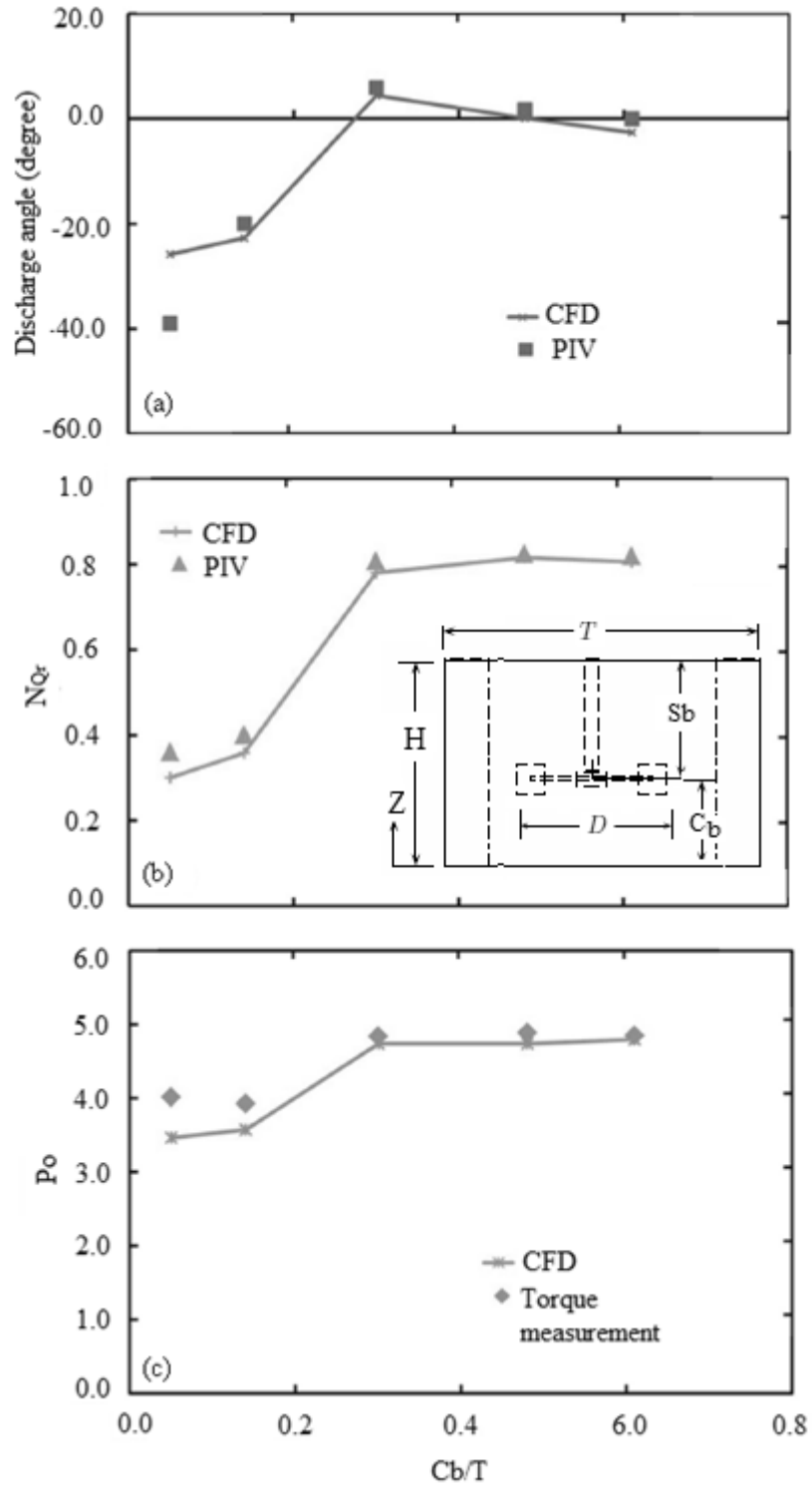


Figure 6.6: (a) Impeller discharge angle, (b) N_{qr} and (c) P_o for different C_b/T , $H/T = 1$, $D/T = 0.31$ and $N = 300$ rpm

The difference can be attributed to the highly anisotropic turbulence level between the impeller and the digester bottom which cannot be predicted well by the k- ϵ model.

Figure 6.6b and Figure 6.6c show N_{Qr} and P_o as a function of impeller off-bottom clearances respectively. N_{Qr} and P_o are nearly constant for impeller off-bottom clearance ratios, C_b/T equal to 0.61, 0.48 and 0.30. However, N_{Qr} and P_o decreases drastically with the impeller off-bottom clearance ratio decrease from 0.30 to 0.14. The C_b/T range corresponds to a flow regime transition change from double loop to single loop down-pumping, as also shown in Figure 6.5.

The ratio of S_{bcrit}/D can be defined as the critical submergence ratio at which a flow transition occurs for a given C_b/T ratio. For any given system, once S_{bcrit}/D is determined, the corresponding critical fill ratio H_{crit}/T where H_{crit} refers to the critical liquid level below which flow regime transition occurs is also known.

Table 6.3 presents a summary of the results obtained for this section in terms of critical submergence ratio. In general, the critical submergence level is found to be constant and equal to 0.77 for a D/T ratio equal to 0.31. However, when the impeller is very close to the digester bottom, $C_b/T = 0.05$ the critical submergence ratio is only 0.48. This phenomenon is the result of the effect of the interaction of the impeller with the digester bottom. Placing the impeller very close to the digester bottom increases the magnitude of this interaction.

Table 6.3: Critical fill ratios and impeller submergence ratios for different C_b/T

C_b/T	$H_{crit}(m)$	H_{crit}/T	S_{bcrit}	S_{bcrit}/D
0.05	0.060	0.24	0.050	0.48
0.14	0.090	0.38	0.060	0.77
0.30	0.134	0.54	0.059	0.77
0.48	0.176	0.72	0.059	0.77
0.61	0.202	0.82	0.059	0.77

In all cases except for very low impeller locations, $C_b/T < 0.05$, flow transition implies switching to the single loop up pumping flow regime. This regime is not directly responsible for surface air entrainment and possible impeller flooding. However, the establishment of this regime is a necessary prerequisite for significant surface air entrainment. The low recirculation zone near the impeller shaft generated by the single loop up pumping flow regime produces a vortex at higher agitation speed which then leads to air entrainment and flooding. When the impeller location is very low, $C_b/T < 0.05$ the critical submergence ratio is lower, $S_{bcrit}/D = 0.48$. However, when flow transition occurs, the result is a new regime with no circulation that produces no flow and therefore the ability of the impeller to be an effective mixer is lost.

Figure 6.7 presents additional evidence that the critical importance of S_b/D ratio on flow pattern transition where the power number is plotted against S_b/D keeping the C_b/T ratio as a parameter.

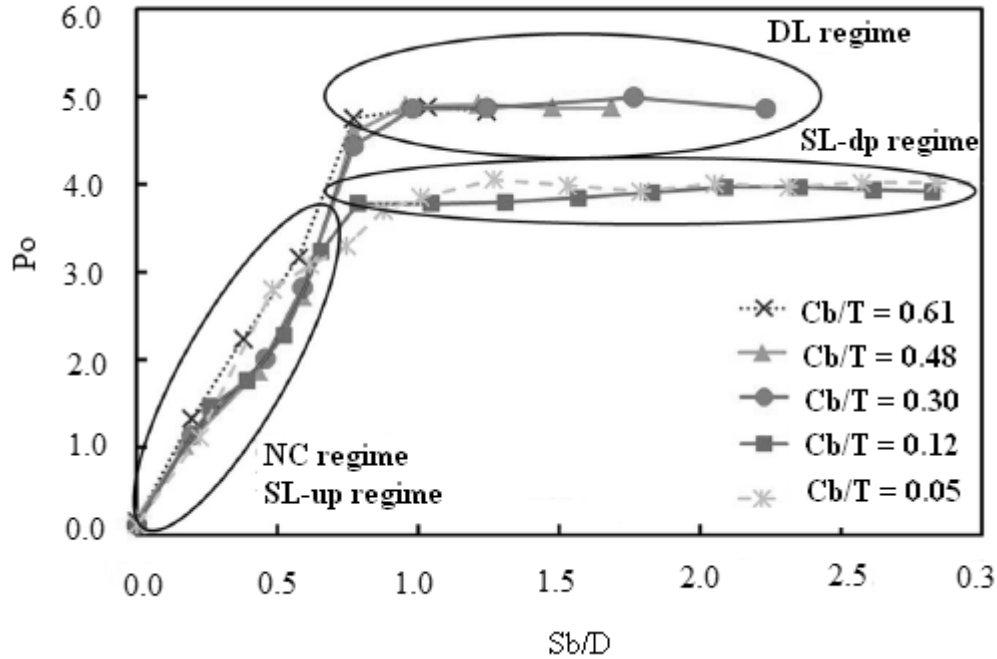


Figure 6.7: Power numbers obtained experimentally for different S_b/D at different C_b/T , $D/T=0.31$ and $N = 300$ rpm to show flow pattern transition a result of variation in C_b/T ratio

All experimental power data for different impeller off-bottom clearances are combined to show that the transition between the different regimes associate with sudden changes in power number. In Figure 6.7, the no circulation regime overlaps with the single loop up pumping flow regime. However, the no circulation regime is only observed for very low impeller off-bottom clearance, $C_b/T = 0.05$. This figure shows that the detection of a sudden power change can be used as an experimental indication that flow transition has occurred. This may be important in full-scale anaerobic digester where it is hard to visually observe the phenomenon. In addition, the flow regime diagram can be used as a guide to determine in which regime the system is operating.

6.3.3 Effect of D/T and S_b/D Ratios

After examining the effect of C_b/T on flow pattern, power numbers and pumping numbers in partially filled stirred AD, the same phenomena is studied for different impeller diameter-to-digester diameter, D/T and S_b/D on the flow regimes and flow pattern transition.

Table 6.4 shows the diameters of the impellers in the digester. The C_b/T ratio and the impeller tip velocities are kept the same irrespective of scale to 0.30 and 1.2 m/s respectively. The torque transducers data for different D/T value and impeller submergence ratios are used to determine the P_o. In addition, flow pattern changes are observed with the addition of coloured, nearly neutrally buoyant particles that follow the flow closely.

Table 6.4: Diameter of the impellers investigated

Digester diameter (m)	Impeller diameter (m)	D/T
0.25	0.055	0.22
0.25	0.065	0.26
0.25	0.078	0.31
0.25	0.093	0.37
0.25	0.108	0.43

The results for all cases are presented in Figure 6.8 in terms of P_o as a function of S_b/D ratio keeping D/T as a parameter. The Figure shows that the P_o is constant, P_o = 5 for high values of the S_b/D ratio independent of the D/T ratio although the value for each D/T ratio are different. The P_o value decreases with decrease in S_b/D ratio below a

critical value, S_{bc}/D , which depends on the D/T ratio. In all cases, a flow pattern transition from double loop to single loop up pumping regime observed as result of sudden decrease in P_o . The critical submergence ratio S_{bc}/D is larger, 1.2 for smaller D/T ratio, 0.22 and smaller, 0.54 for higher D/T ratio of 0.43. This effect can be explained by wall-impeller interaction effect. When the D/T ratio is larger, digester wall-impeller interaction is stronger. Therefore, tendency toward double loop region is higher and flow regime changes from double loop to single loop up pumping occurs at a lower impeller submergence ratio compared to anaerobic digester equipped with a smaller D/T impeller.

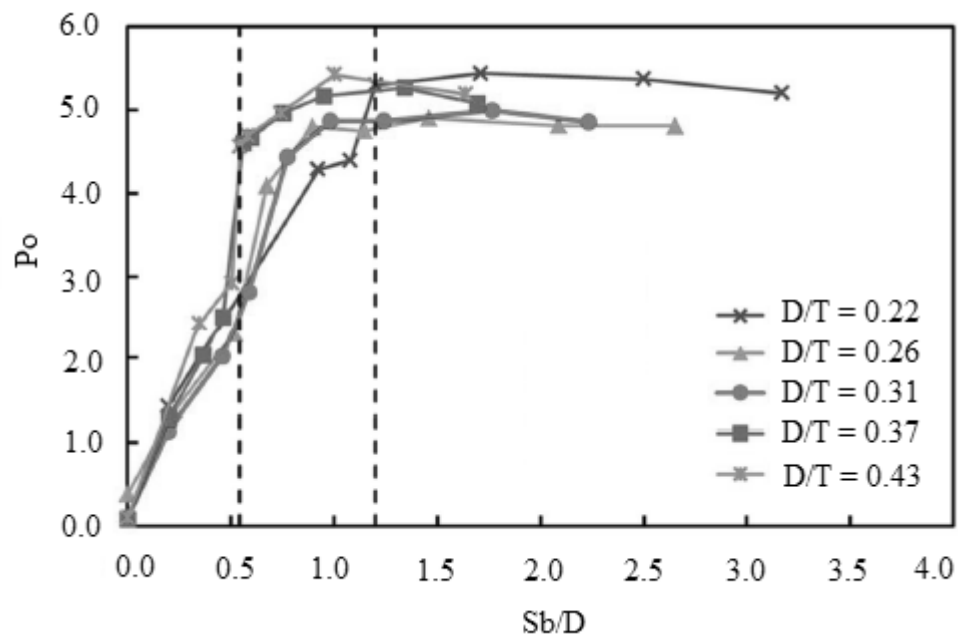


Figure 6.8: Power numbers obtained experimentally for different S_b/D at different D/T , $U_{tip}=1.2$ m/s and $C_b/T=0.30$ to show the effect of D/T variation on power number

6.4 Results and discussion (two phase)

6.4.1 Investigation of sedimentation in mixed AD

One of the purposes of mixing in anaerobic digestion processes is suspension of solid particles in liquid manure and the enhancement of mass transfer between particles and liquid manure. Therefore, it is important to quantify the particles behaviour and understand the relation between particle rising behavior from a bottom surface and mean liquid flow in a stirred anaerobic digester. To this end, the relation between particle rising behaviours and mean liquid flow pattern just around the digester bottom are investigated using Euler–Lagrangian simulations of particle behaviours rising from a digester bottom. The investigation considers four cases: unbaffled, baffled, off bottom clearance of $T/3$ and $T/2$.

Figure 6.9a portrays a particle sedimentation pattern on a digester bottom and directions of horizontal fluid flow for $C_b = T/3$ with four baffles. Figure 6.9b depicts a contour of the time-averaged vertical fluid velocity V_z immediately above the digester bottom, $Z = 0.9$ mm. The liquid flows from the front face of each baffle discharge in two directions, and mutually collide forming a twisted criss-cross stagnant area running from the four baffles. Figure 6.9a shows that the particles on the bottom are swept by the horizontal flows, forming a twisted criss-cross sedimentation pattern running from the four baffles along the stagnant area of liquid flow. Along this stagnant area, upward liquid flows are also induced as shown in Figure 6.9b. Consequently, the particles are piled up along the stagnant area, and some particles are sucked upward by the liquid flow.

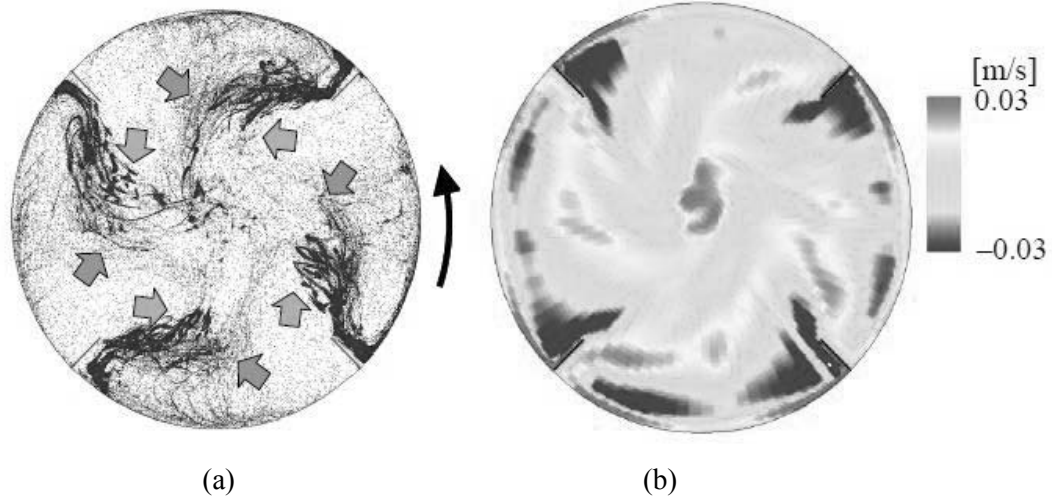


Figure 6.9: Particle sedimentation pattern on the bottom for $0.0 < z < 0.3$ mm, $C_b = T/3$ with four baffles, b) distribution of $V_{f,z}$ just above the bottom for $z = 0.9$ mm, $C_b = T/3$ baffles

For lower off-bottom clearance, $C_b = T/10$, the mean flow pattern and particle motion differ from the case of $C_b = T/3$. Figure 6.10a portrays the time-averaged fluid velocity vectors $V_{f,r-\theta}$ in the vicinity to the digester bottom, $n = 6 \text{ s}^{-1}$, $z = 0.9$ mm.

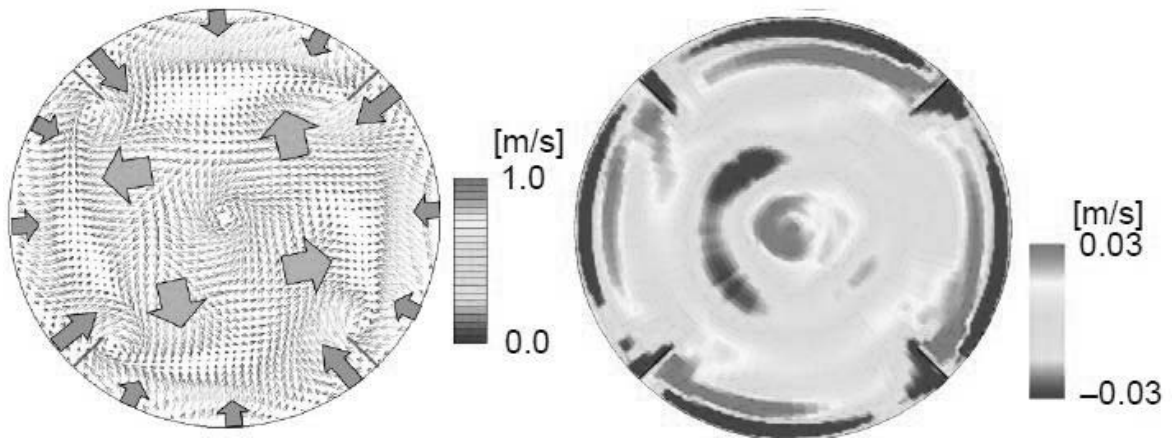


Figure 6.10: a) Horizontal fluid velocity vectors, $V_{f,r-\theta}$ just above the bottom, b) distribution of $V_{f,z}$ just above the bottom for $z = 0.9$ mm, $h = H/10$ with baffles

Figure 6.10b depicts the distribution of the time average vertical fluid velocity $V_{f,z}$ just above the digester bottom at the same condition. These figures show that the liquid flows

discharged from the impeller reach the bottom directly and then flow toward the digester wall with some elevation. The discharged flows collide with weak down-flow at around the digester wall; then proceed upward along the digester wall.

Figure 6.11a shows the particle sedimentation pattern on the bottom. Figure 6.11b shows the distribution of particles moving upward around the digester bottom. The particles on the bottom are swept toward the digester wall by the discharged flow from the impeller. Then, they pile up along the stagnant area near the digester wall. Upward liquid flows are induced along this stagnant area. Subsequently the particles are sucked upward by the flow along the wall.

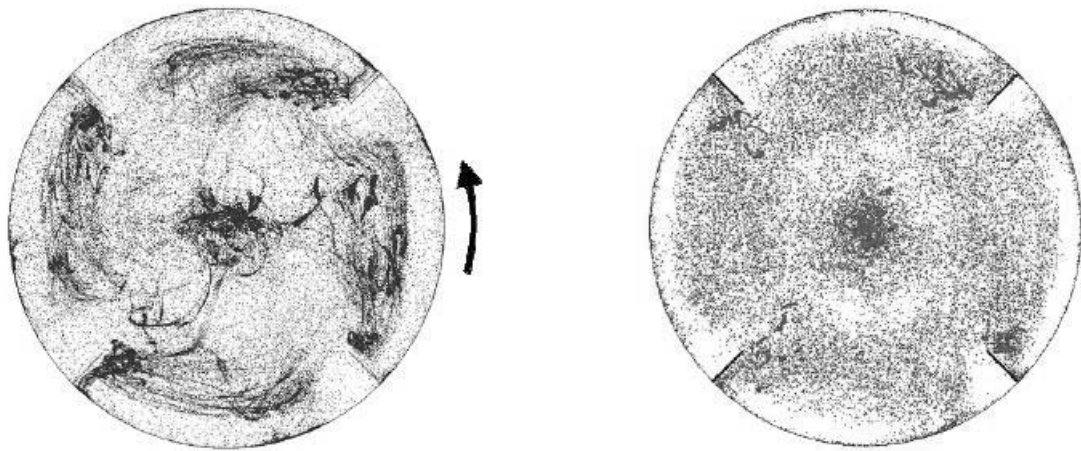


Figure 6.11: Particle sedimentation pattern on the bottom where $0.0 < z < 0.3$ mm for $C_b = T/10$ with baffles (left), and distribution of particles moving upward around the bottom where $0.3 < z < 4.0$ mm, for $C_b = T/10$ with baffles (right)

Figure 6.12a portrays the time-averaged fluid velocity vectors $V_{f,r-\theta}$ near the digester bottom, $n = 6 \text{ s}^{-1}$, $z = 0.9$ mm in the case of $C_b = T/10$ without baffles. Figure 6.12b shows

the distribution of the time-averaged vertical fluid velocity, $V_{f,z}$ just above the digester bottom, $n = 6 \text{ s}^{-1}$, $z = 0.9 \text{ mm}$.

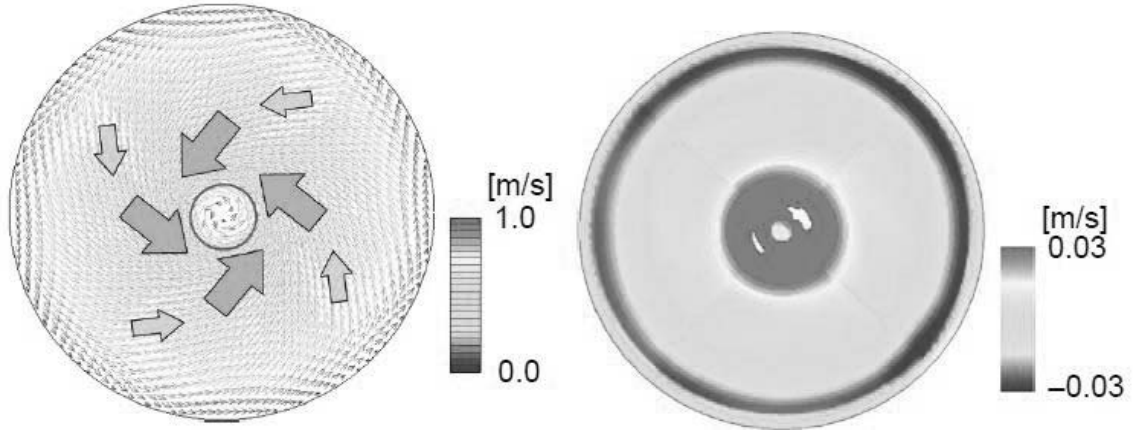


Figure 6.12: (a) Horizontal fluid velocity vectors, $V_{f,r-\theta}$ just above the bottom (b) distribution of $V_{f,z}$ just above the bottom at $z = 0.9 \text{ mm}$ for $C_b = T/3$ without baffles

In this case, liquid flows discharged from the impeller tip reach the digester wall forming a counter-clockwise rotating flow. Around the bottom, the rotating flow focuses to the center of bottom as shown in Figure 6.12a; then it induces upward flow at the center of the bottom as Figure 6.12b.

Figure 6.13a exhibits the particle sedimentation pattern on bottom, $0.0 < z < 0.3 \text{ mm}$. Figure 6.13b displays the distribution of particles moving upward around the bottom, $0.3 < z < 4.0 \text{ mm}$. The particles on the bottom are swept toward the center of digester bottom by the rotating flow. Then particles pile up at the center of the bottom where the horizontal liquid flow is stagnant as shown in Figure 6.13a. Upward liquid flows are

induced above the stagnant region. Subsequently the particles are sucked upward by the flow as shown in Figure 6.13b similarly to the pattern observed in the digester with baffles.

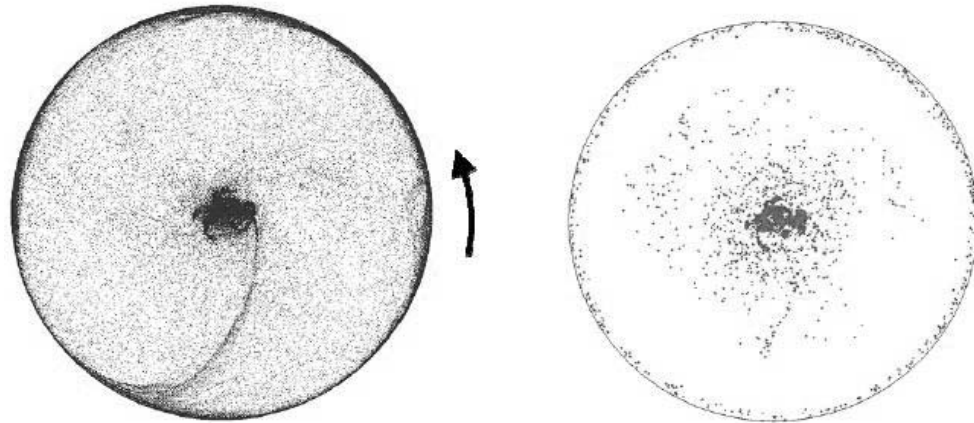


Figure 6.13: (a) Particle sedimentation pattern on the bottom for $0.0 < z < 0.3$ mm, $C_b = T/3$ without baffles (b) distribution of particles moving upward around the bottom for $0.3 < z < 4.0$ mm, $C_b = T/3$ without baffles

6.4.2 Investigation of suspension of solid in mixed AD

CFD simulation of liquid–solid mechanically agitated anaerobic digester is undertaken in this study to verify quantitatively the solid suspension characteristics since this is the vital parameter for predicting the performance of mixing in a digester. One way of checking the quality of solid suspension is by evaluating the extent of off-bottom suspension i.e., critical impeller speed for just suspended state (Barigou, M. 2004). Another way is to map the concentration profiles of solids (Bhattacharya and Kresta, 2002) in digesters to determine the extent of solid distribution i.e., solid suspension height. The method proposed by Bohnet and Niesmak (1980), which is based on the value of standard deviation, is used in the present study for the prediction of critical

impeller speed. This standard deviation method is also successfully employed for liquid–solid suspension by Khopkar et al. (2006). It is defined as:

$$\sigma = \sqrt{\frac{1}{n} \sum_{i=1}^n \left(\frac{C_i}{C_{avg}} - 1 \right)^2} \quad (6.1)$$

where n is the number of sampling locations which is used for measuring the solid holdup.

The increase in the degree of homogenisation resulting in a better suspension quality is manifested in the reduction in the value of the standard deviation. The standard deviation is broadly divided into three ranges based on the quality of suspension. For uniform suspension the value of the standard deviation σ is found to be smaller than 0.2 for just suspended condition the value of the standard deviation is between 0.2 and 0.8 and for an incomplete suspension the standard deviation value is greater than 0.8. But it is very difficult to exactly find the critical impeller speed required for the just suspended state from the values of the standard deviation. Hence we have also used another criterion which is based on the solid suspension height i.e., cloud height, $H_{cloud} = 0.9H$ along with the standard deviation method. Hence, evaluation of the quality of solid suspension and determination of the critical impeller speed uses both criteria.

Figure 6.14 shows the variation of the standard deviation values with respect to the impeller speed for RT, PBT and A310 hydrofoil impeller. The standard deviation value decreases with an increase in impeller speed for all the impellers.

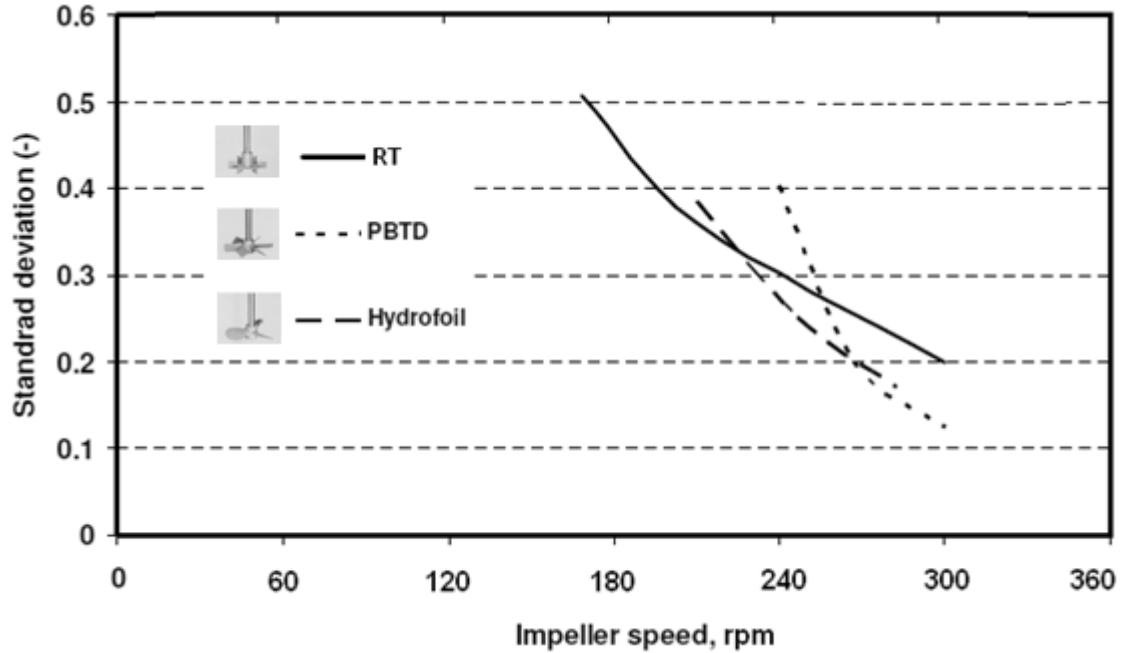


Figure 6.14: Standard deviation values obtained from CFD with respect to impeller rotational speed for RT, PBT and A315 hydrofoil impeller, particle size of 350 μm with solids loading of 10 vol. %

Figure 6.15 depicts the predicted cloud height for various impeller rotational speeds of 240, 267, and 300 rpm for the PBT impeller.

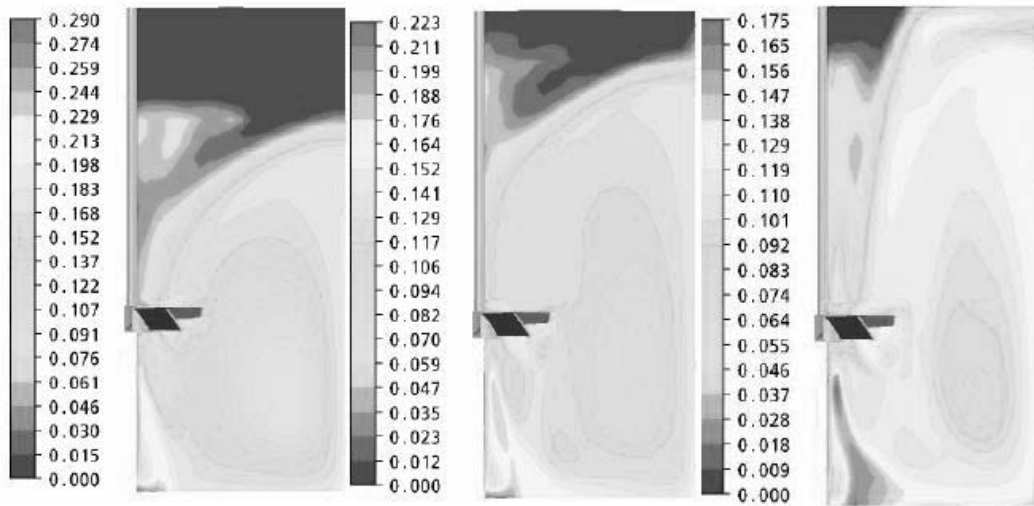
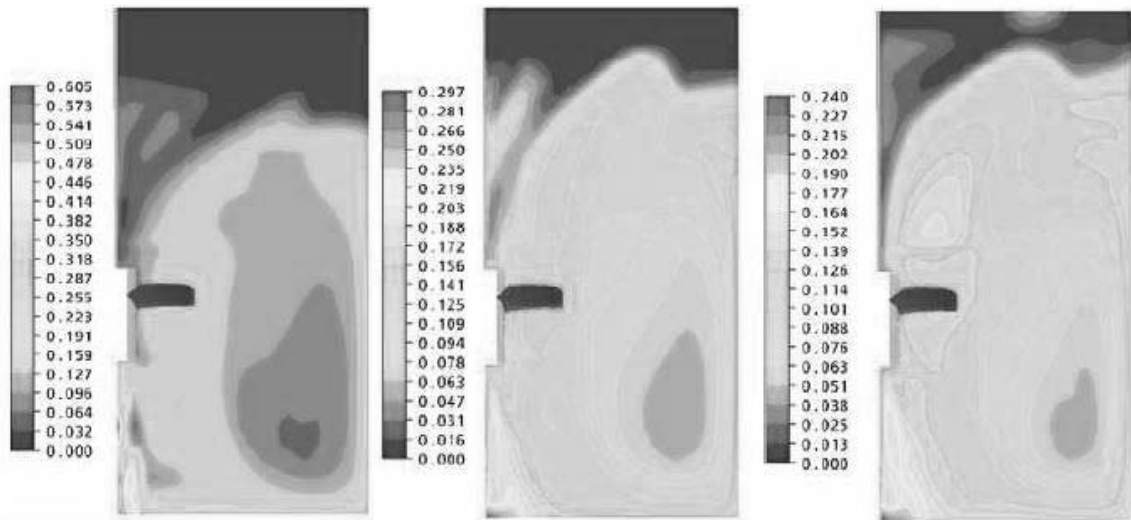


Figure 6.15: Cloud height predicted by CFD simulation for PBT impeller at different rotational speeds, particle size of 350 μm with solid loading of 10 vol. %, particle size of 350 μm

Figure 6.16 depicts the predicted cloud height for various impeller rotational speeds of 210, 246, and 282 rpm for the A310 hydrofoil impeller. It can be seen clearly from these figures that there is an increase in the cloud height with an increase in the impeller speed. The values of the standard deviation and cloud height obtained by CFD simulation along with experimental values for the three types of impellers are presented in Table 6.5. Based on these two criteria, it is found that the critical impeller speed required for PBT is 267 rpm which agrees very well with the experimental observation. It has to be noted again that both these criteria have to be satisfied for the determination of the critical impeller speed.



(a) 210 rpm, $H_s/H = 0.8$ (b) 246 rpm, $H_s/H = 0.88$ (c) 282 rpm, $H_s/H = 1.0$

Figure 6.16: Cloud height predicted by CFD simulation for A310 hydrofoil impeller at different rotational speeds, particle size of $350 \mu\text{m}$ with solid loading of 10 vol. %

The comparison of different types of impellers with regard to their suspension ability is investigated in terms of power number. The power consumption is calculated as the

product of torque on the impeller blades and the angular velocity. This is then used for the estimation of power number which is expressed as follows:

$$N_p = 2\pi NT / \rho_s N^3 D^5 \quad (6.2)$$

where torque (T) exerted on all blades is computed from the total momentum vector, which is computed by summing the cross products of the pressure and viscous forces vectors for each facet on the impeller with the moment vector.

Table 6.5: Effect of impeller type on the quality of suspension, particle size of 350 μm with solid loading of 10 vol. %

Type of impeller	Critical impeller speed, rpm		Standard deviation, σ	Cloud height
	Experimental	CFD		
RT	-	3.50	0.36	0.90
PBT	4.45	4.45	0.21	0.91
Hydrofoil	-	4.10	0.25	0.88

The predicted values of power number are compared with experimental data and are shown in Table 6.6. It can be observed that the values predicted by CFD simulations agree reasonably well with the experimental values. It can also be seen from the table that the suspension performance in terms of power number is different for different impeller designs. The lowest power consumption is observed for A310 hydrofoil impeller and highest for RT impeller. This indicates that the impeller which directs the flow downward having mainly axial component and has the least power number is most energy efficient.

Table 6.6: Experimental and predicted values of power number for digester equipped with RT, PBT and Hydrofoil impellers.

Type of impeller	Power number, P_o	
	Experimental	CFD
RT	6.0	5.00
PBT	1.67	1.55
Hydrofoil	1.5	1.37

6.4.2.1 Effect of eccentricity of impeller shaft

The eccentricity of an off-centered mechanical mixing system in anaerobic digester is defined as $R/T \times 100$ (%), where R is the radial distance from the shaft to the digester centerline. Eccentricities of 0%, 5%, 10%, and 15% corresponding to 0, 0.0125, 0.0250 and 0.0375 off-center distances as shown in Figure 6.17 are investigated. The four positions are defined as P_1 , P_2 , P_3 , and P_4 , corresponding to the eccentricities of 0%, 5%, 10%, and 15%, respectively. Mixing is provided using a hydrofoil impeller. The critical agitation speed for just drawdown of floating particles, N_{JD} and the impeller tip velocity U_{tip} are 9.83 m/s and 2.32 m/s, respectively.

In order to quantitatively analyze the effect of the shaft eccentricity on the flow in anaerobic digester, Figure 6.18a and 6.18b show the axial profiles of the mean axial and radial components, respectively, of the velocity near the wall, $r/T = 0.96$ for different shaft positions, P_1 to P_4 at a floating particle concentration of 1.0 vol %. Upward direction is defined as the positive direction of the axial velocity. The positive direction of the radial velocity is from the shaft towards the wall. The whole set of measurements (not reported here) shows that from P_1 to P_4 , the averaged axial velocity increases by

about 50 %, from 0.030 m/s to 0.0453 m/s and the averaged radial velocity increases by about 1/3, from 0.0198 m/s to 0.030 m/s at constant agitation speed.

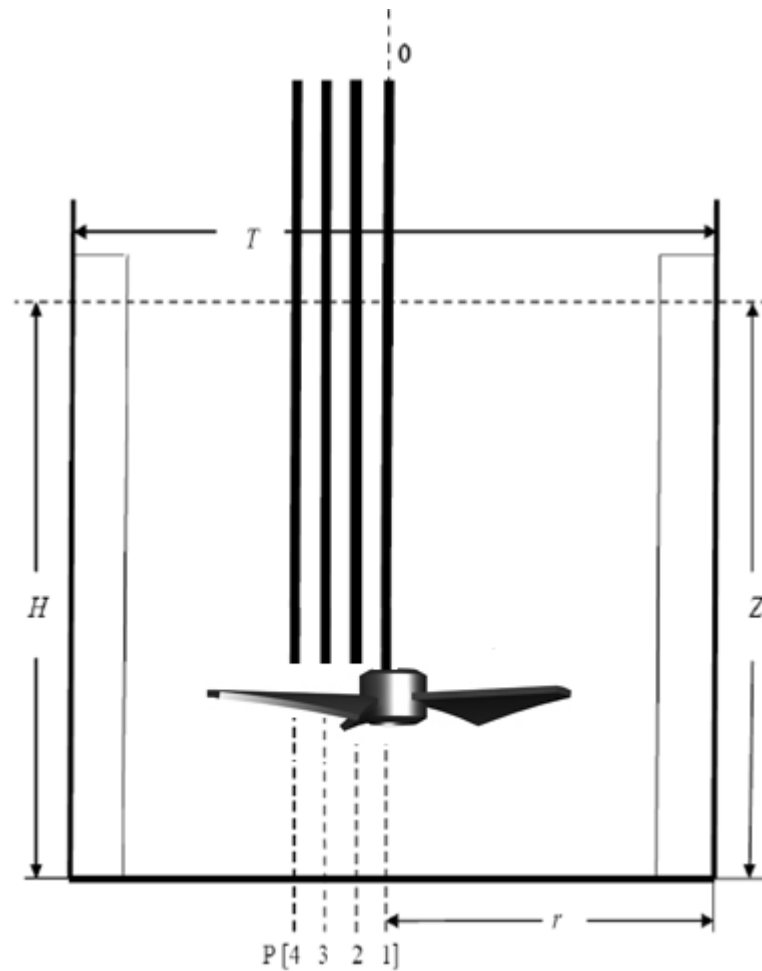


Figure 6.17: Schematic of experimental setup to examine the effect of impeller shaft position on mixing of floating particles in lab-scale digester

The increase in velocity implies that during the suspension of floating particles in stirred digester, an off-centered shaft at a lower agitation speed can provide about the same mixing performance and power consumption as a centered shaft at a higher speed.

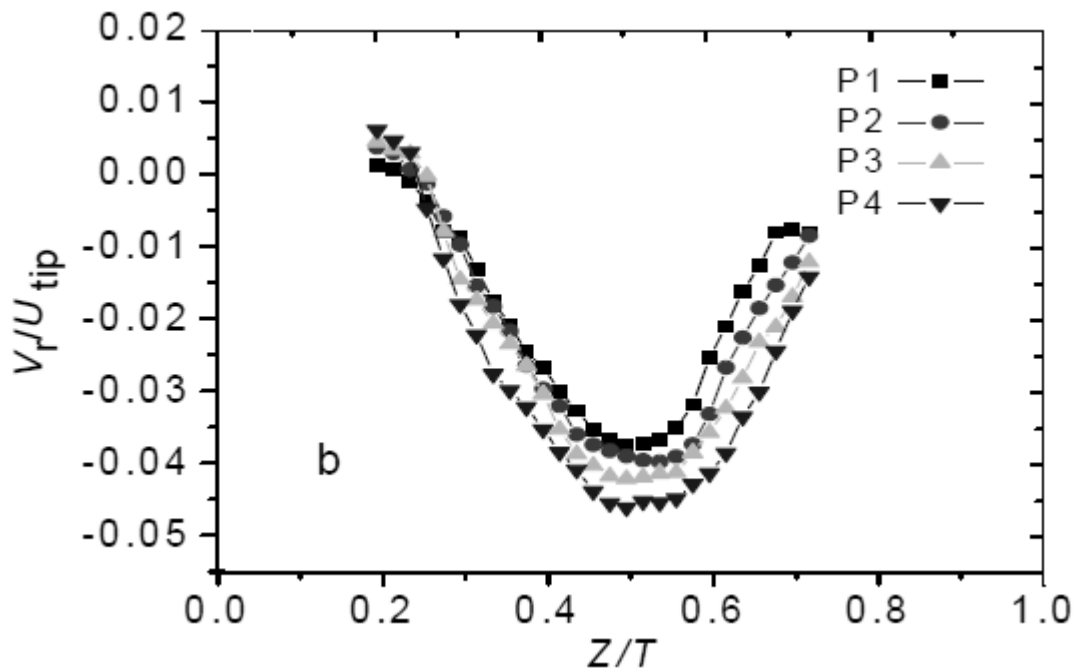
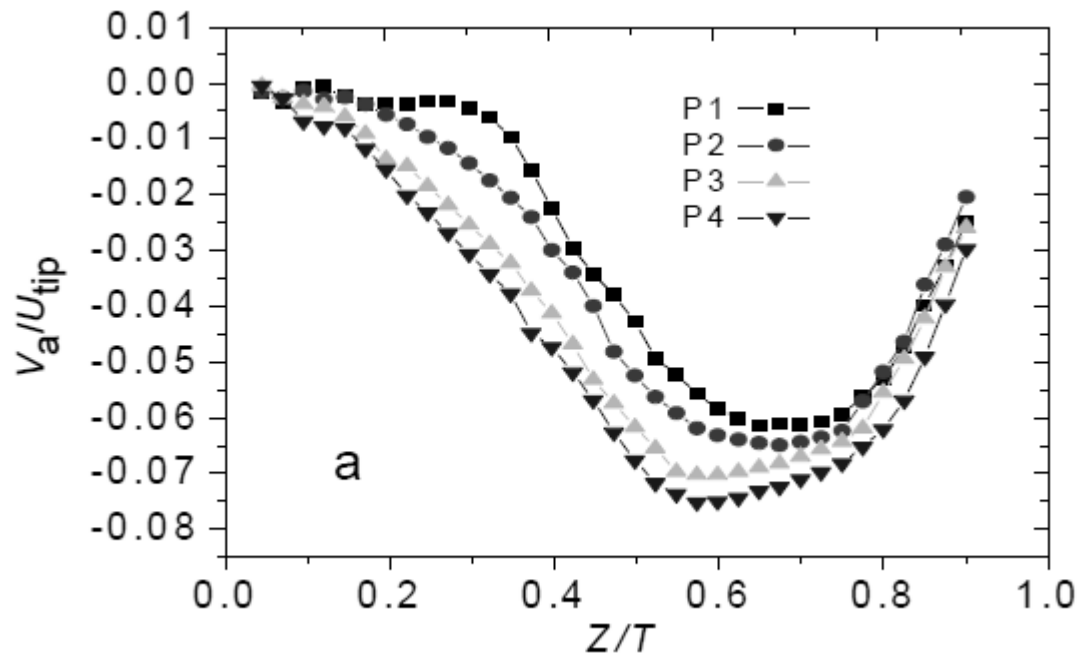


Figure 6.18: Axial profile of (a) mean axial velocity (b) radial velocity at different eccentricity, $r/T = 0.96$

Table 6.7 shows the critical agitation speed, N_{critical} and power consumption for the just drawdown of floating particles at the concentration of 1.0 vol %. The value of N_{critical} decreases from 9.83 s^{-1} at 0% eccentricity to 7.67 s^{-1} at 15% eccentricity. Correspondingly, the specific power consumption decreases from $0.38 \text{ W}\cdot\text{kg}^{-1}$ to $0.185 \text{ W}\cdot\text{kg}^{-1}$. In this case, the off-centered agitators can reduce the power consumption needed for just drawdown of floating particles to about 49 % of that in a centered shaft stirred digester.

Table 6.7: Effects of off-centered shaft on N_{critical} and power consumption

Positions	E (%)	$N_{\text{JD}} (\text{s}^{-1})$	$P_{\text{m}} (\text{W}\cdot\text{kg}^{-1})$	$P/P_{\text{Centre}} (\%)$
P1	0.0	9.83	0.38	100
P2	5	9.17	0.312	82.0
P3	10	8.33	0.234	61.6
P4	15	7.67	0.185	48.7

The averaged rising velocity of floating particles in the stagnant liquid is found to be $0.066 \text{ m}\cdot\text{s}^{-1}$. Based on the same volume, the equivalent diameter d_p for a spherical shape is 3.44 mm corresponding to the cylindrical shape of $\Phi 3.6\times 2.1$ mm. The particle rising velocity in the lab-scale digester, U_s is calculated from Equation 6.3, proposed by Fajner *et al.* (2008), and compared with the liquid velocity in the stirred AD, V_a in Table 6.8.

$$U_s/U_t = 0.32 \tanh \left[19 \left(\lambda/d_p \right) \left(\Delta\rho/\rho \right)^{0.5} - 1 \right] + 0.6 \quad (6.3)$$

where U_s - particle rising velocity in stirred tank, $\text{m}\cdot\text{s}^{-1}$

U_t - terminal rising velocity, $\text{m}\cdot\text{s}^{-1}$

λ/d_p ratio of the Kolmogorov micro scale length to the particle diameter.

The Kolmogorov micro scale length estimated by:

$$\lambda = (\nu^3/\varepsilon)^{0.25} \quad (6.4)$$

where ν is the kinematic viscosity of liquid phase and ε is the average power consumption per unit mass.

The ratio between the rising velocity in the stirred digester and that in the stagnant liquid, U_s/U_t , is calculated by using Equation 6.3 to be 0.365, giving a U_s of 0.0241 m·s⁻¹. The averaged rising velocity of floating particles in the stagnant liquid is about 2.74 times the rising velocity of the floating particles in the digester. Also the axial velocity of the liquid phase in the digester V_a (0.0%) is about 5.81 times the rising velocity of the floating particles in the digester, as shown in Table 6.8. The floating particles move much slower than the liquid, and the relative drag effect of the slow moving floating particles on the liquid can explain the decreasing velocity of the liquid even when both the liquid and floating particles are moving upwards at $r/T = 0.15$.

Finally, the experimental results show that the effect of turbulence on the rising velocity of floating particles is very high, confirming the significant role of turbulence in reducing the rising velocity of the floating particles and exhibit the same behavior as the settling ones.

Table 6.8: Effect of turbulence on floating particles at constant agitation speed of 9.8 s^{-1}

Ut	Measured U_s [$\text{m}\cdot\text{s}^{-1}$]	Calculated from Eq. (1) [$\text{m}\cdot\text{s}^{-1}$]	U_s/Ut [$\text{m}\cdot\text{s}^{-1}$]	V_a (0.0 vol %) [$\text{m}\cdot\text{s}^{-1}$]
0.066		0.0241	0.365	0.14

6.4.2.2 Effect of shape of digester bottom on mixing performance

The effect of the digester design on the hydrodynamic structure is carried out in three digesters; cylindrical digester, curved digester and spherical digester; equipped with a PBT impeller. The power consumption of these stirred digesters is calculated to choose the most effective system.

Figure 6.19 presents the distribution of the mean velocity in the vertical plane containing the blade. The impeller generates a radial jet developed from the blade and propagates in the lower part of the digester. At the proximity of the sidewall, the radial jet has been transformed into two axial jets upward and downward. In addition, there appears a recirculation loop located in the upper zone of the digester. At the curved bottom of the digester, a secondary recirculation loop appears just below the turbine. Beyond the area swept by the turbine, the mean velocity decreases gradually and becomes very low at the top of the cylindrical digester. Globally, it's noted that the appearance of the maximum values wake developed in the area swept by the turbine. Moreover, the mean velocity decreases gradually away from the impeller and becomes very low at the bottom and at the top of the digester. The discharge jet is more intense in the curved digester and it reaches the sidewall. The recirculation loop is more extended in the upper part of this digester and reduces the stagnant fluid zone. At the curved bottom, the second recirculation loop is appeared in the lower part of the curved digester that proves a

significant fluid circulation. The curved bottom is characterized by the total disappearance of the dead zones initially located at the bottom of the cylindrical digester. Contrary to the spherical digester, in the upper part the dead zones are more developed and the recirculation loop is located near the turbine that proves the decrease of the fluid motion. Thus, we can deduce that the curved bottom reduces the stagnant areas and promotes more uniformity throughout the volume of the digester without having to modify the external geometry of the upper surface of the digester.

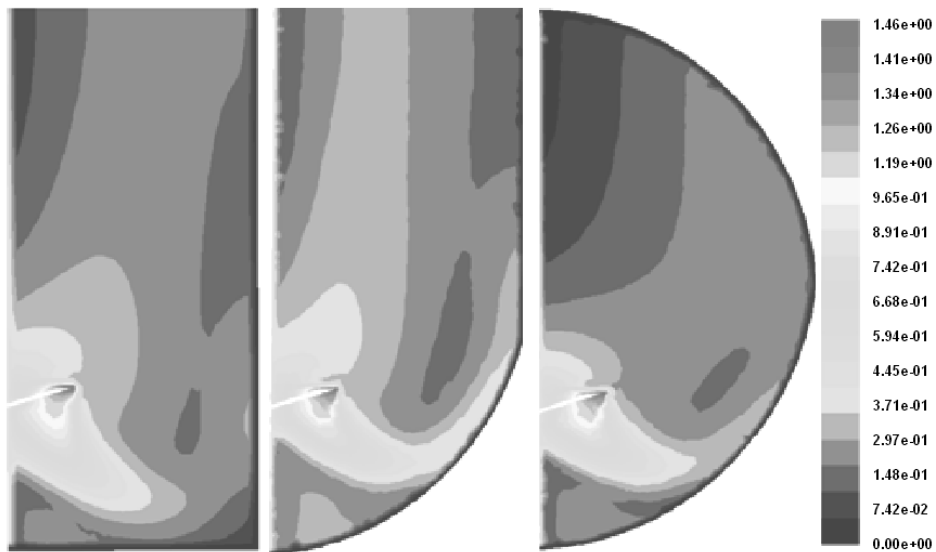


Figure 6.19: Contour plot of radial profiles of the axial velocity component for cylindrical, curved and spherical digester equipped with PBT impeller showing the distribution of the mean velocity in the vertical plane containing the blade. The impeller generates a radial jet developed from the blade and propagates in the lower part of the digester.

Figure 6.20 presents the distribution of the turbulent kinetic energy in the vertical plane containing the blade. In each system, the wake of the maximum values of the turbulent kinetic energy appears on the mechanical source and develops within the fluid to reach

the sidewall of the tank. Also, it's noted that the turbulent kinetic energy is more extended in the case of the spherical digester.

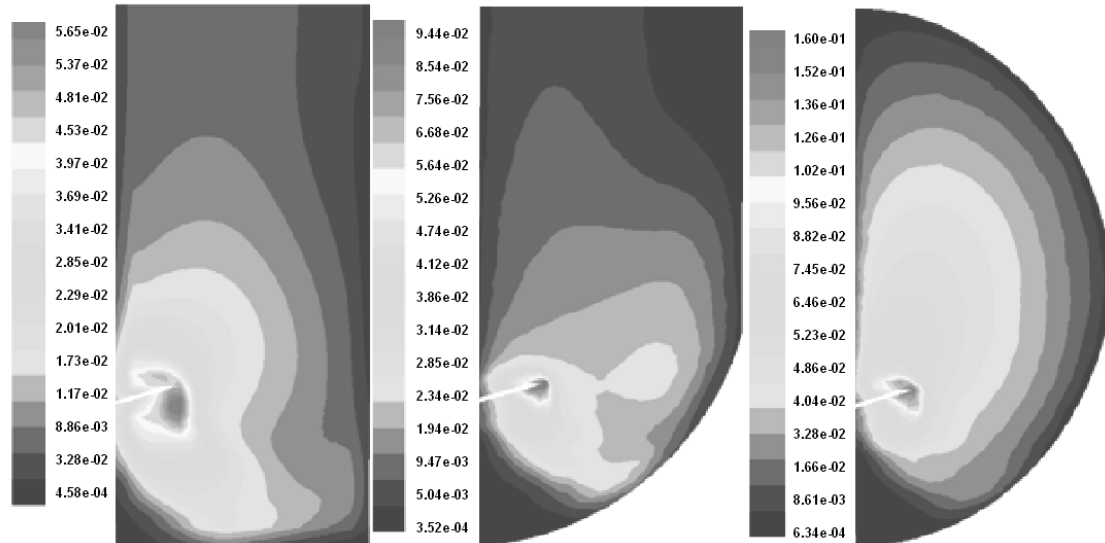


Figure 6.20: Distribution of the turbulent kinetic energy in vertical plane containing the PBT blade for cylindrical, curved and spherical digester equipped with PBT impeller

Figure 6.21 shows the distribution of the dissipation rate of the turbulent kinetic energy in r-z plane containing the blade. Globally, it's noted that the dissipation rate is very low in each system. The maximum values are concentrated around the PBT turbine. This is explained by the transformation of the energy provided by the rotating action of the turbine as heat within the fluid.

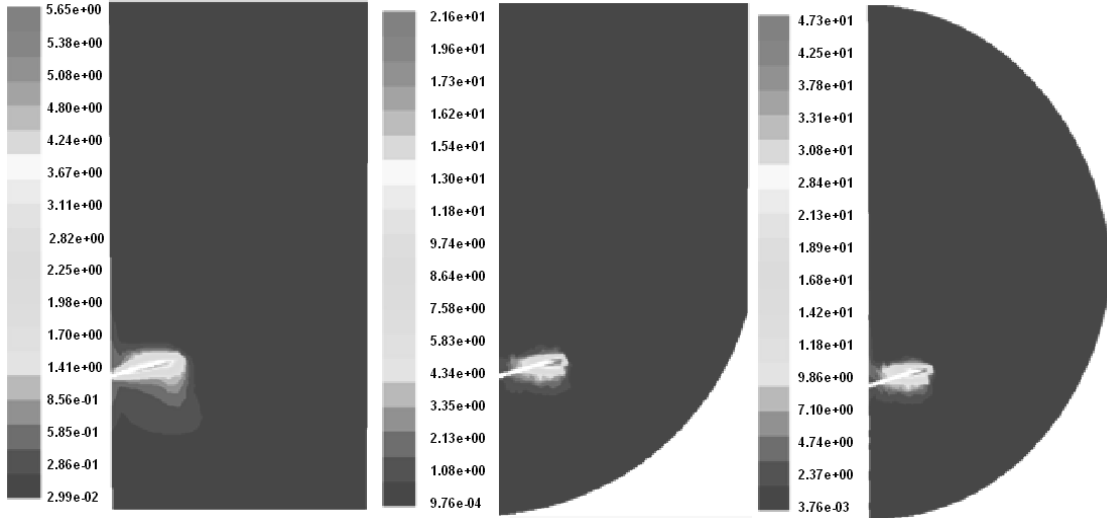


Figure 6.21: Distribution of the dissipation rate of the turbulent kinetic energy in r-z plane for cylindrical, curved and spherical digester equipped with PBT impeller

Figure 6.22 presents the variation of the power number P_o depending on the Reynolds number Re with a pitched blade turbine PBT placed respectively in the cylindrical, the curved and the spherical tank. Globally, the energy dissipation defined within the fluid increases with the curved bottom of the digester.

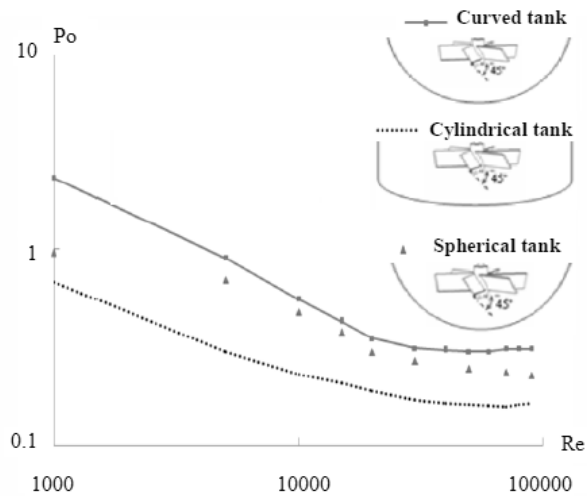


Figure 6.22: Evolution of the power number as a function of Re for cylindrical, curved and spherical digester equipped with PBT impeller

Therefore, we can deduce that the curved digester is the best system because the presence of the curved bottom improves the quality of the mixture in anaerobic digester. So, this system consumes slightly more of the energy dissipation than the other systems and is optimum for solids suspension because the bottom shape aids in directing the flow.

6.4.2.3 Optimization of suspension in mixed AD

A horizontal plane across the impeller is created, as shown in Figure 6.23, so that surface integration can be conducted to quantify the amount of axial flow passing through the impeller for each trial condition.

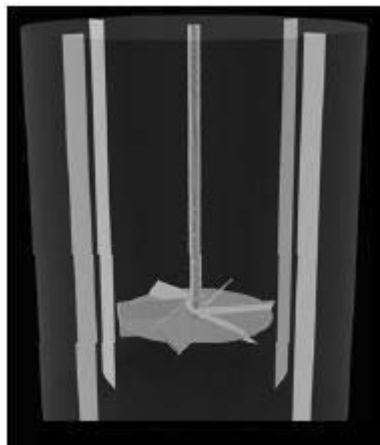


Figure 6.23: Horizontal plane for surface integration to quantify the amount of axial flow passing through the impeller in a flat bottom digester equipped with PBT impeller

Such an approach enables the determination of the axial flow, minus the radial flow component. The amount of axial flow generated is taken as the key performance indicator. The reason is because it is the axial flow component that pushes the particles to the digester bottom where they are then deflected by the digester bottom causing the particles to travel in the upward direction. In other words, the cloud height is dependent on the amount of axial flow discharge by the impellers.

The investigation concerns to optimize parameters that have a profound effect on the ability of an anaerobic digester to suspend particles are investigated numerically, namely: baffle width to digester diameter ratio, B_w/T , baffle spacing of the wall of digester to digester diameter ratio, B_s/T , number of baffle, N_B , impeller rotational speed, N , number of blades, N_{BL} , impeller diameter to digester diameter ratio, D/T and number of impeller, N_I . Overall, these variables constitute the crucial parameters that determine the success of a given reactor configuration in suspending particles in anaerobic digesters for optimum biogas production. The results presented are for a lab-scale anaerobic digester equipped with PBT impeller and four wall baffles.

Figure 6.24 shows the relationship between the mass flow rate and the baffle width to digester diameter ratio. Its behavior is governed by a third-order polynomial expression, having a good correlation coefficient, $R = 0.9899$. The expression is given by:

$$\dot{m} = -380882 \left(\frac{B_w}{T}\right)^3 + 53465 \left(\frac{B_w}{T}\right)^2 + 1189 \left(\frac{B_w}{T}\right) + 1027 \quad (6.5)$$

For optimum performance, $H_w/T = 0.1036$

The purpose of baffles is to convert radial flow into axial flow. The maximum value is at $B_w/T = 0.1036$, which explains why most baffles in the anaerobic digesters have widths ranging from 1/12 to 1/10 because beyond 1/10, the mass flow rate would drop. When the baffle widths are too small, the flow resistance is small which means the amount of radial flow converted to axial flow is minimal.

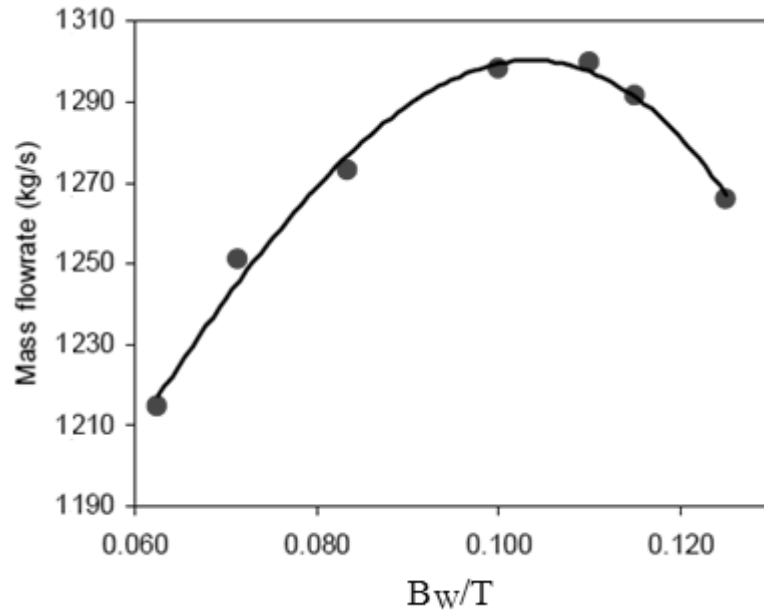


Figure 6.24: Mass flow rate vs. baffled width to digester diameter ratio for digester equipped with PBT impeller

An increase in the conversion can be achieved by widening the baffle width since doing so will increase the amount of flow resistance. But as the baffle width is further widened, too much flow resistance is provided by the baffles to such extent that not much radial flow is there to be converted to axial flow. As a consequence, beyond $B_w / T = 0.1036$, the mass flow rate started to drop. From here it can be seen that for standard wall baffles, the optimum B_w / T ratio is 1/10.

Figure 6.25 shows the power consumption as a function of the baffle width, and this is described by the polynomial model:

$$P = -288907 \left(\frac{B_w}{T} \right)^2 + 64864 \left(\frac{B_w}{T} \right) + 2762 \quad (6.6)$$

with $R = 0.9872$.

From Equation 6.6, increasing B_w/T value from 0.063 to 0.10 corresponding to equivalent increase by 58.73% will increase the power consumption by 369.6%. Increasing the B_w/T value from 0.10 to 0.15 equals to 50% increase will cause a reduction in the flow rate by 44.07%.

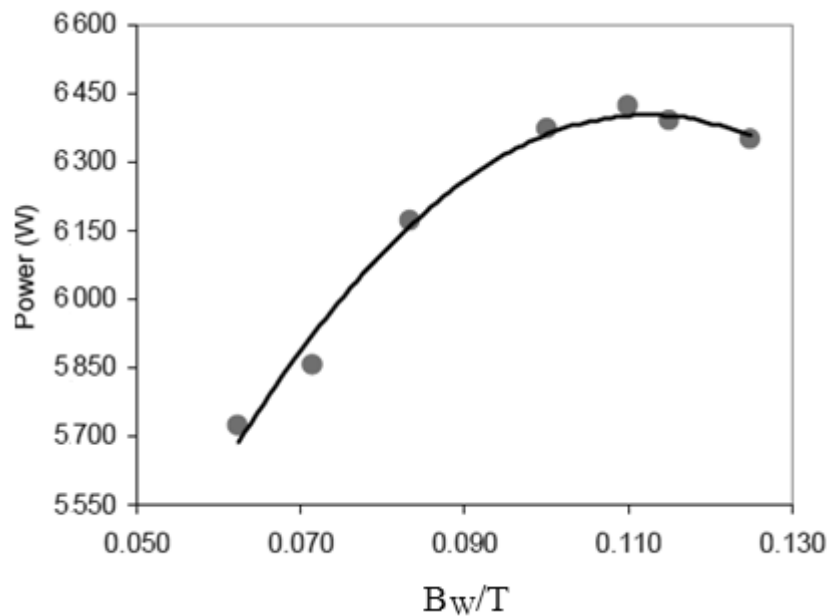


Figure 6.25: Power consumption vs. baffle width to digester diameter ratio for digester equipped with PBT impeller

Figure 6.26 shows the relationship between the mass flow rate and the baffle spacing to digester diameter ratio and is governed by the following fourth-order polynomial expression with good regression of 0.9961:

$$\dot{m} = 3767663 \left(\frac{B_s}{T}\right)^3 - 74426 \left(\frac{B_s}{T}\right)^2 + 3529 \left(\frac{B_s}{T}\right) + 1207 \quad (6.7)$$

The maximum value is at $B_s/T = 0.031$

Baffle clearance, $B_s/T = 1/32$ produces peak mass flow rate whereas for small B_s/T value, it is important to locate far away from the impellers and therefore do not contribute significantly to the flow resistance. This implies that not much radial flow is converted to axial flow. As the clearance widens, the baffles are closer to the impellers thereby converting most of the radial flow to axial flow. This automatically maximizes the mass flow rate in the axial direction.

However, as the clearance is further widened, the flow resistance drops because the clearance is large enough for the manure fluid flow behind the baffles with minimal interruption. This means that placing the baffles too far away from the digester wall will cause a reduction in the axial flow rate because the baffles do not convert enough radially oriented flow to axially oriented flow.

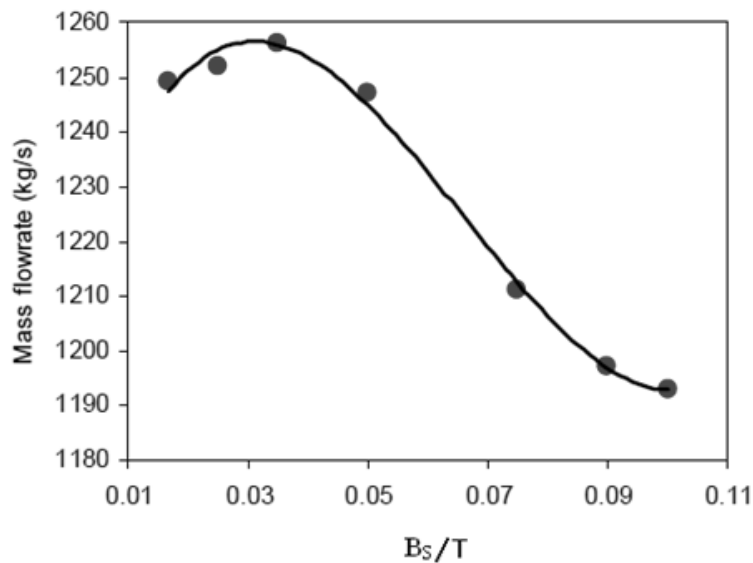


Figure 6.26: Mass flow rate vs. off bottom to reactor diameter ratio for digester equipped with PBT impeller

Figure 6.27 shows the power consumption as a function of various values of B_S/T expressed with a good regression of 0.9942 as:

$$P = 884245 \left(\frac{B_S}{T}\right)^3 - 219838 \left(\frac{B_S}{T}\right)^2 + 13047 \left(\frac{B_S}{T}\right) + 5695 \quad (6.8)$$

The peak power consumption occurred at $B_S/T = 0.03872$. The power increases from 1/60 to 1/30 and beyond this B_S/T value, the power consumption starts to decrease. At small B_S/T value, the baffle presents negligible resistance to flow. As the spacing widens, the baffles are closer to the impellers therefore contributing more flow resistance. However, as the spacing is further widened, the flow resistance drops because the spacing is large enough for the fluid flow to pass behind the baffles with minimal interruption. This phenomenon causes a reduction in the power consumption.

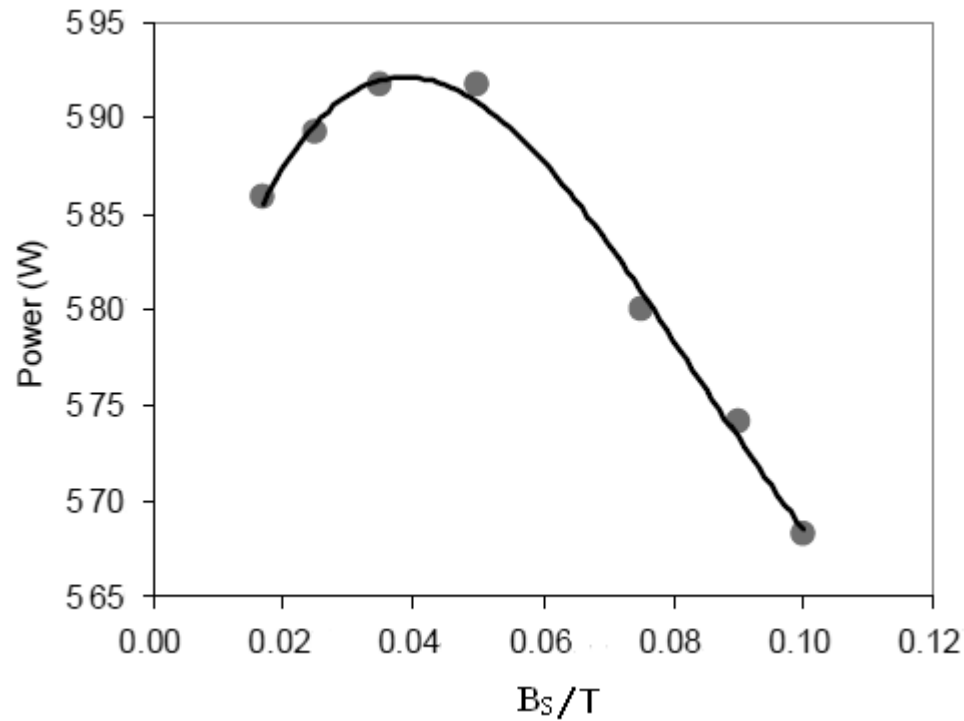


Figure 6.27: Power consumption vs baffled spacing to reactor diameter ratio for digester equipped with PBT impeller

Figure 6.28 shows the relationship between the mass flow rate and number of baffles, N_B which is governed by the following quadratic polynomial expression with good regression of 0.9991:

$$\dot{m} = -11.93N_B^2 - 149.3N_B + 844.8 \quad (6.9)$$

Using Equation 6.9, increase in the number of baffles from 2-3, 3-4, 4-5 and 5-6 results in an increase in axial flow rate by 8.1%, 5.6%, 3.4% and 1.4% respectively.

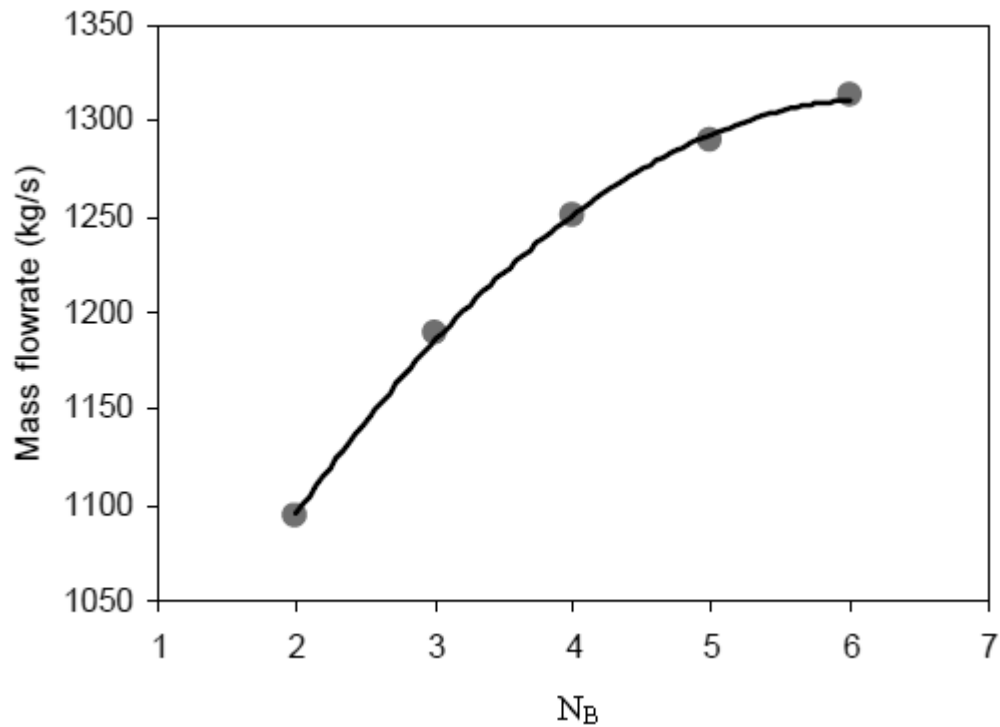


Figure 6.28: Mass flow rate vs. number of baffle for digester equipped with PBT impeller

Figure 6.29 shows the power consumption as a function of the number of baffles with a curve fit represented by a linear function with regression of 0.9928 with the form:

$$P = -220.42N_B + 4967 \quad (6.10)$$

From Equation 6.10, the power consumption will increase by 4.076% for every additional baffle installed in the digester mixing system.

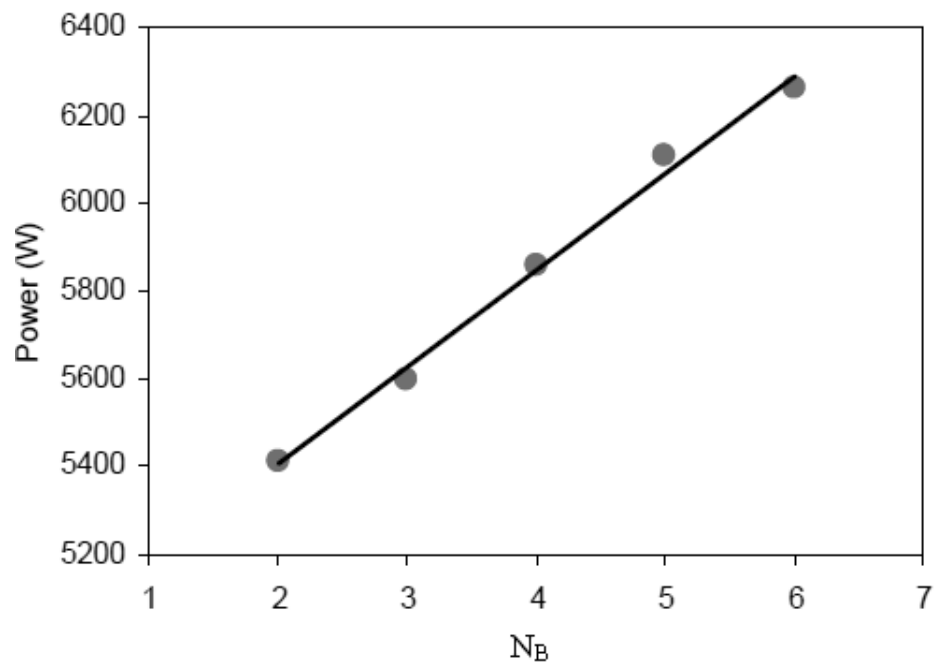


Figure 6.29: Power consumption vs. number of baffle for digester equipped with PBT impeller

Figure 6.30 shows that the flow rate increases proportionally with increase of the impeller rotational speed, which follows a linear relationship, with regression of 1. It can be expressed as:

$$\dot{m} = 15.65N \quad (6.11)$$

From Equation 6.11, an increase in the speed by 1% results in 1% increase in the axial mass flow rate. The recommended impeller rotational speed is any speed that is much greater than the just suspended speed, N_{js} .

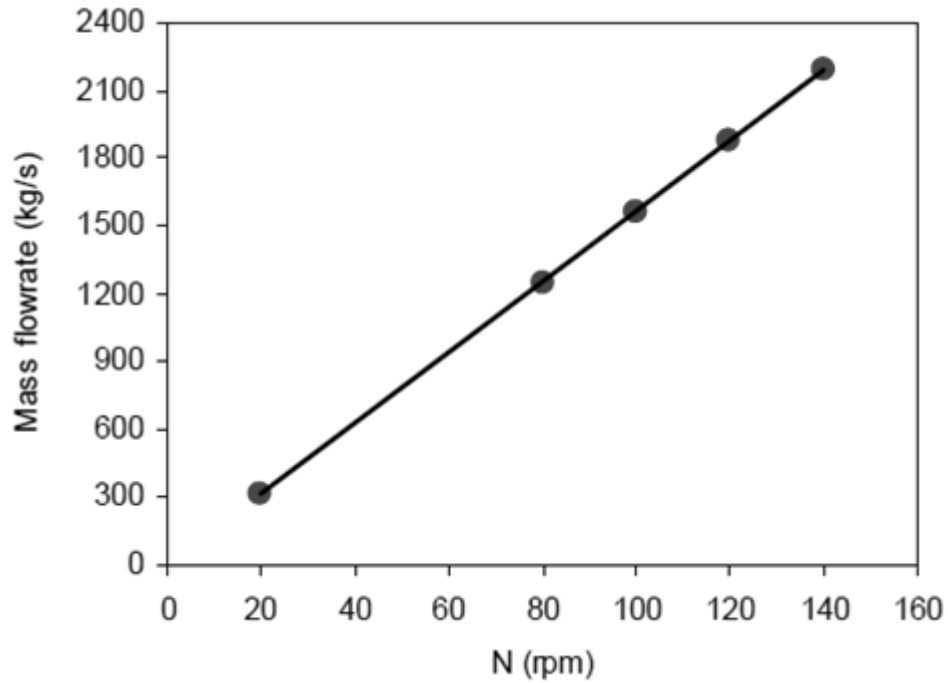


Figure 6.30: Mass flow rate vs. N (rpm) for digester equipped with PBT impeller

N_{js} is defined as the minimum rotational speed required lifting the particles from the tank bottom and that no particles remain on the digester bottom for any longer than 1-2 seconds. N_{js} can be obtained via the Zwietering correlation (Montante *et al.*, 2001), which is given as:

$$N_{js} = Sv^{0.1} \left[\frac{g(\rho_s - \rho_l)}{\rho_l} \right]^{0.45} X^{0.13} d_p^{0.2} D^{-0.85} \quad (6.12)$$

where:

S = Zwietering constant -

ν = kinematic viscosity $\text{m}^2 \text{s}^{-1}$

g = gravitational constant m s^{-2}

ρ_s = density of solid media kg m^{-3}

ρ_l = density of liquid media kg m^{-3}

X = solid loading -

d_p = diameter of solid particles m

D = impeller diameter m

Figure 6.31 shows that the power consumption relationship with the impeller rotational speed followed a power function with a regression of 1. It can be expressed as:

$$P = 0.0103(N)^{3.0222} \quad (6.13)$$

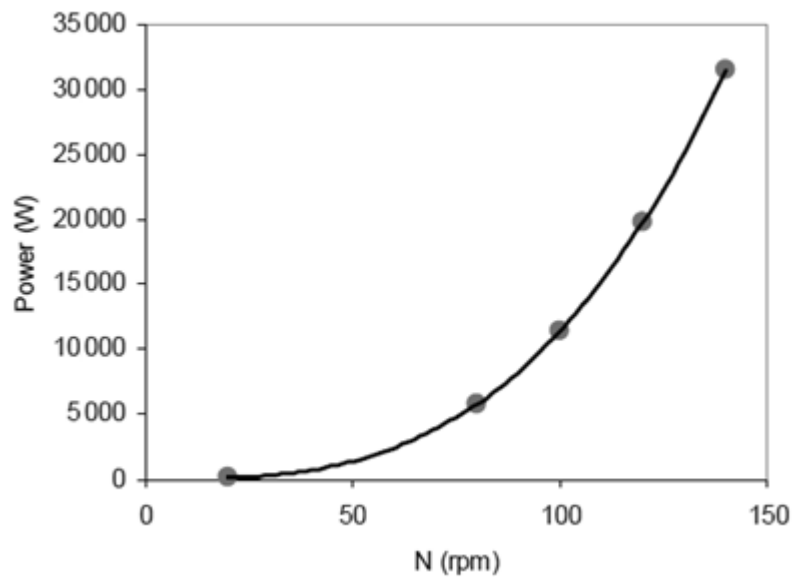


Figure 6.31: Power consumed vs. N(rpm) for digester equipped with PBT impeller

Based on Equation 6.13, increasing the speed by 300% from 20rpm to 80rpm will increase the power consumption by 5,812%, that is, a 1% increase in the speed in this

range will increase the power consumption by 19.37%. Increasing the speed from 80rpm to 140rpm (75%) will increase the power consumption by 442.7%. Therefore for every percent increase in the speed, the power consumed increases by 5.902%.

Figure 6.32 shows the relationship between the mass flow rate and the number of blades on an impeller and is governed by the following model:

$$\dot{m} = \frac{aN_{BL}}{1+bN_{BL}} \quad (6.14)$$

where \dot{m} represents mass flow rate and N_{BL} represents the number of blades. Data regression to Equation 6.14 yielded $a = 1667$ and $b = 1.167$ with a correlation fit of 0.9992. The increase in mass flow rate when the number of blades is increased from 2 to 3 blades is 11%, from 3 to 4 blades is 5.851%, from 4 to 6 is 6.287% and from 6 to 8 blades is 3.2%.

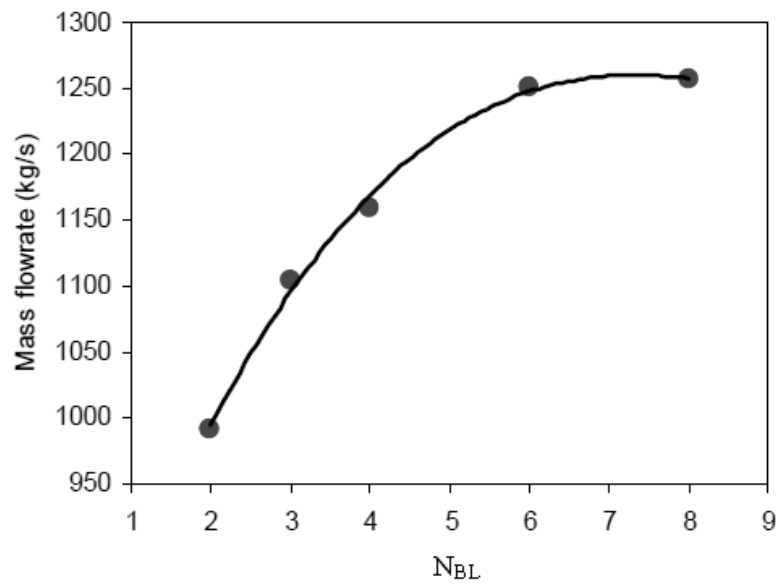


Figure 6.32: Mass flow rate vs. number of blades for digester equipped with PBT impeller

Increasing the number of blades from 6 to 8 did not return a significantly higher mass flow rate value. From a practical standpoint, a 6-bladed impeller is recommended.

Figure 6.33 shows that the power consumption as a function of the number of blades described by quadratic polynomial function with a regression of 0.9994, which can be expressed as:

$$P = -50.07(N_{BL})^2 + 1241(N_{BL}) + 201.9 \quad (6.15)$$

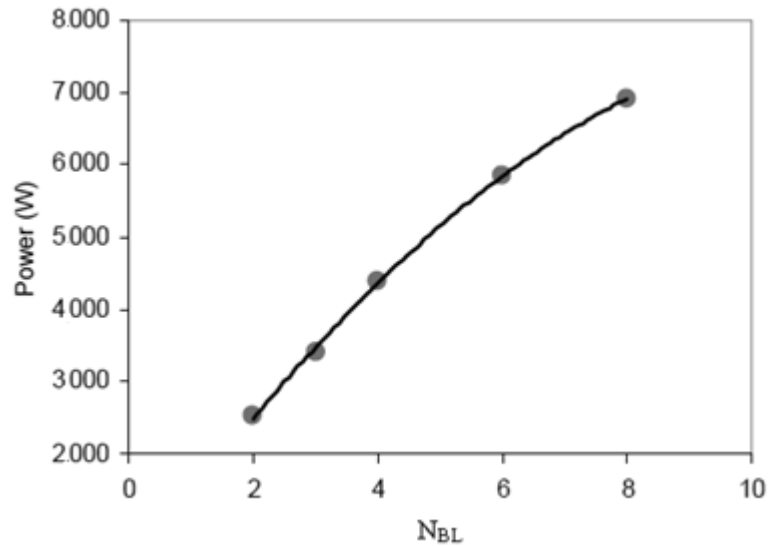


Figure 6.33: Power consumed in Watts vs. N_{BL} for digester equipped with PBT impeller

Referring to Equation 6.15, increasing the blades from 4 to 6 will increase the power consumption by 33.91% and 18.48% from 6 to 8 blades.

Figure 6.34 shows the relationship between the mass flow rate and the impeller diameter to digester diameter ratio and is governed by the following third-order polynomial expression:

$$\dot{m} = -31491 \left(\frac{D}{T}\right)^3 + 29886 \left(\frac{D}{T}\right)^2 - 4648 \left(\frac{D}{T}\right) \quad (6.16)$$

with regression value of 0.9875.

Simple differentiation at the turning point shows that the maximum value is located at $D/T = 0.54$.

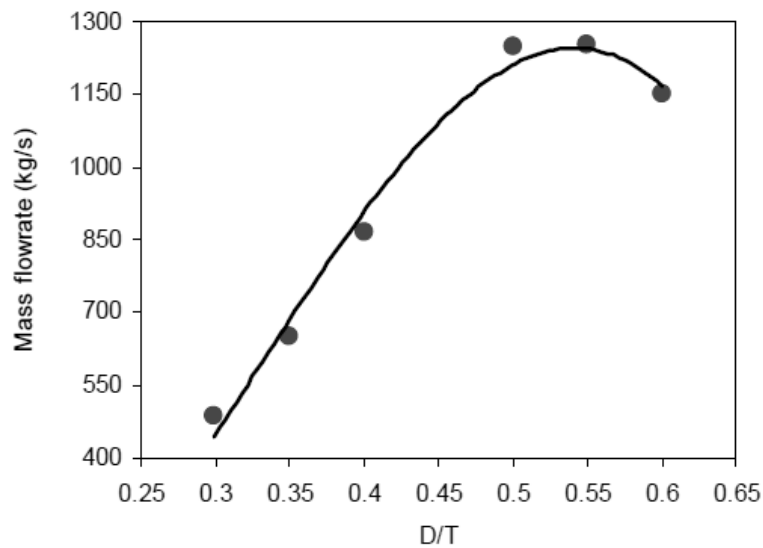


Figure 6.34: Mass flow rate vs. D/T for digester equipped with PBT impeller

From Equation 6.16, increasing the ratio from $D/T = 0.3$ to $D/T = 0.54$ increased the mass flow rate. However, increasing the D/T value beyond the maximum value caused a reduction in the mass flow rate. From $D/T = 0.3$ to $D/T = 0.4$ with 33% increment, the increase in mass flow rate is 104%, from $D/T = 0.4$ to $D/T = 0.55$ with 37.50% increment), the increased is 37.25% and from $D/T = 0.55$ to $D/T = 0.6$ with 9.09% increment, the reduction in flow rate is 6.265%. For optimum performance: $0.5 \leq D/T \leq 0.55$.

The reduction in the mass flow rate when the D/T ratio is increased to value beyond the maximum value may be attributed to the change in the flow profile discharged by the impellers i.e. the amount of fluid that passed through the horizontal plane decreased per unit time.

Figure 6.35 shows that the power consumed when D/T is increased from 0.3 to 0.6 follows an exponential relationship with a good regression of 0.9956 in the form:

$$P = 27.19e^{10.63\left(\frac{D}{T}\right)} \quad (6.17)$$

From Equation 6.17, when D/T is increased from D/T= 0.3 to D/T = 0.4, the increased in power consumption is 190%, from D/T = 0.4 to D/T = 0.55, the increased power consumption is 393% and from D/T = 0.55 to D/T = 0.6, the increased in power consumption is 70.15%.

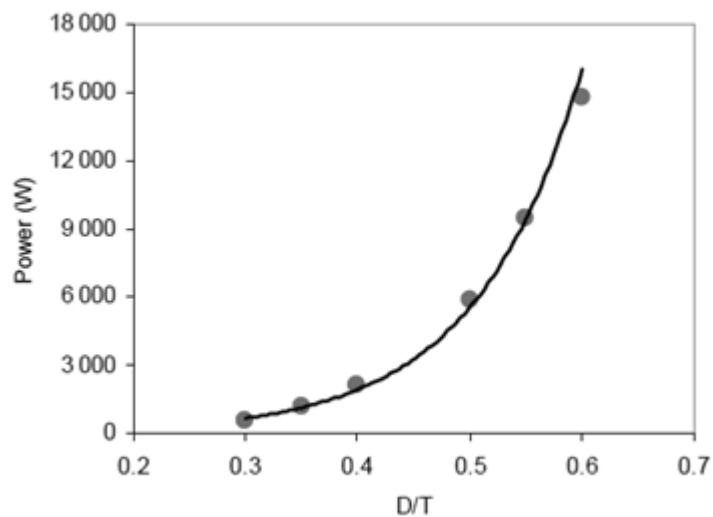


Figure 6.35: Power consumed in Watts vs. D/T for digester equipped with PBT impeller

The huge increase in the power consumption between $D/T = 0.4$ to $D/T = 0.55$ reflects the high increase in the flow rate. Although the power consumption is higher in this D/T range, it is required to achieve process objective.

Figure 6.36 shows the relationship between the axial mass flow rate and the number of impellers installed on the same shaft can be expressed as:

$$\dot{m} = 1250N_I^{0.0524} \quad (6.18)$$

with a correlation coefficient of 0.9991.

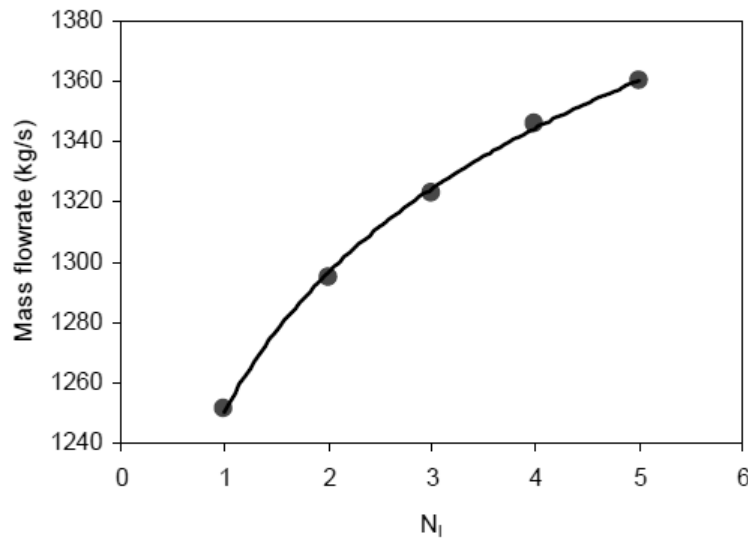


Figure 6.36: Mass flow rate vs. N_I for digester equipped with PBT impeller

Figure 6.37 shows the relationship between the power consumed by the process and the number of impeller installed on the same shaft can be expressed as a quadratic function in the form:

$$P = -415.5N_I^2 + 4181N_I + 1991 \quad (6.19)$$

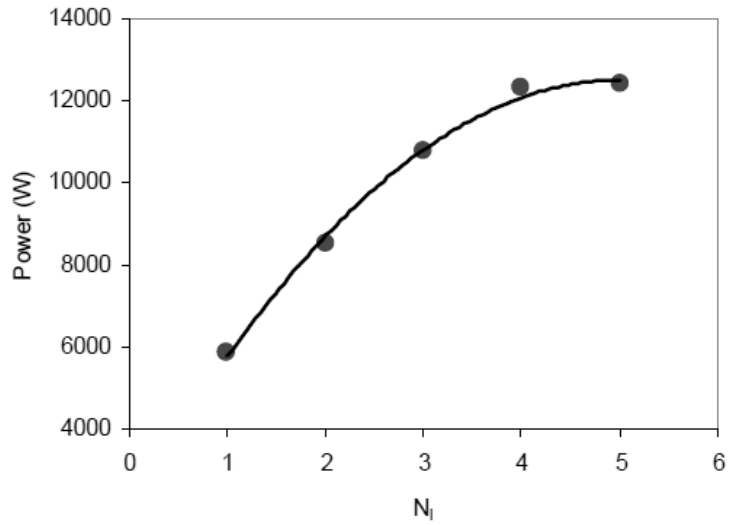


Figure 6.37: Power consumed vs. N_1 for digester equipped with PBT impeller

The percentage increment in the power consumed as a function of the increment in the number of impeller is best represented by the bar chart as shown in Figure 6.38.

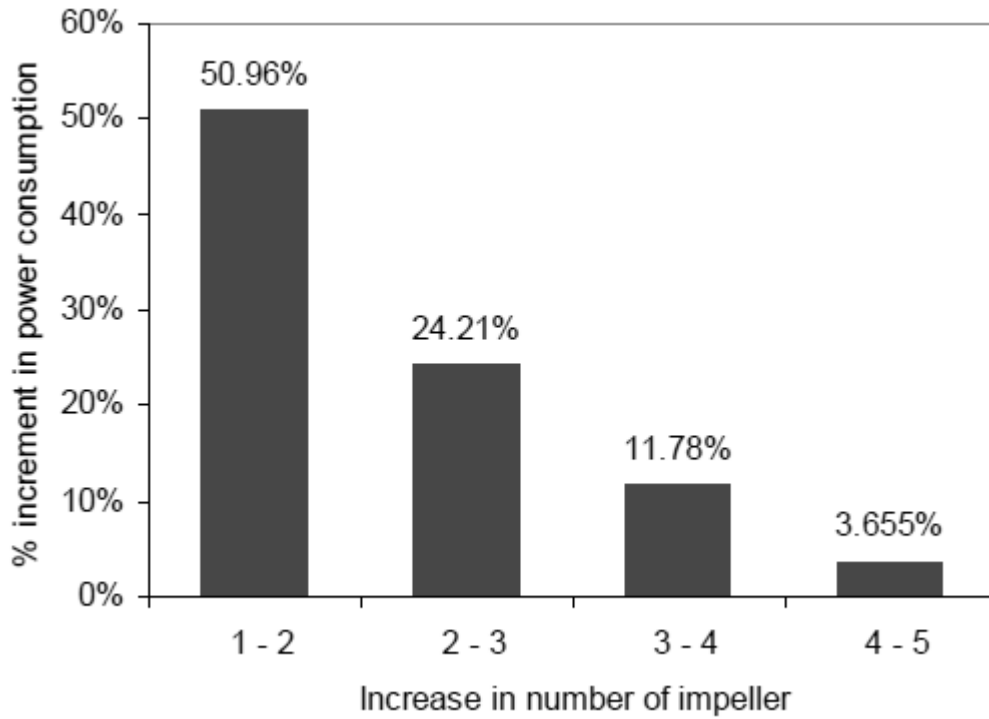


Figure 6.38: Percentage increment in power consumption vs. increase in N_1 for digester equipped with PBT impeller

The summary of the optimum operating range for each variable can be best represented by a design template shown in Figure 6.39, where H and T denote liquid height and digester diameter respectively. This template provides a convenient means of optimizing a mechanically mixed anaerobic digester without having to conduct time-consuming physical experiments and provides the user a direct route to optimization.

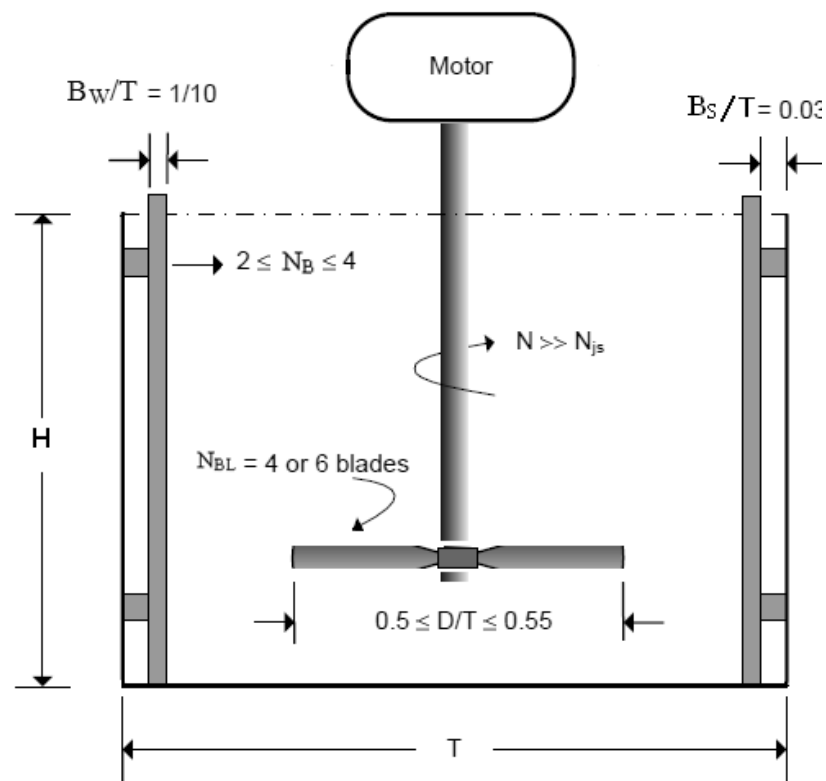


Figure 6.39: For $H/T \leq 1.4$, $N_I = 2$, since beyond this number, the increase in the flow rate did not warrant the increase in the power consumption

6.5 Conclusion

The study in this Chapter characterized in detail the hydrodynamic changes that occur when H/T is decreased, and determined the minimum liquid levels and the critical

impeller submergence for different impeller off-bottom distances, impeller diameters and agitation speeds where adequate mixing process can still be achieved, both in a single liquid phase and in solid-liquid suspensions. The critical impeller submergence ratio S_b/D is identified below which the macroscopic flow pattern generated by the impeller changes substantially, transitioning from either a "double-loop" recirculation flow or a "single-loop" recirculation flow depending on the impeller clearance off the tank bottom to an upward "single-loop" recirculation flow. In addition, below the same critical S_b/D is characterized by significant drop in Power number and radial Pumping number; difficulty to attain solid suspension at any agitation speed; sudden increase in the mixing time; formation of vortex, facilitation of air entrainment, and impeller flooding. This is the first time that such hydrodynamic regime change has been reported and characterized. This regime is not only associated with reducing mixing effectiveness, but can also explain why phenomena such as air entrainment and loss in impeller pumping capacity occur at low H/T ratios in anaerobic digester. There is a critical impeller submergence ratio S_b/D below which the power number and radial pumping number drop significantly, solid suspension cannot be attained at any agitation speed and mixing time increases suddenly. Power draw influences heat and mass transfer processes, mixing and circulation times in the digester. The costs associated with power draw contribute significantly to the overall operation costs of the digester plant. Therefore, it is desired that the mixing process is performed for submergence greater than the critical impeller submergence ratio S_b/D to mix efficiently and with a minimum expense of energy required to achieve the objective established a priori.

In addition, Eulerian multi-fluid approach along with standard k- ϵ turbulence model has been used to study the solid suspension in liquid-solid mechanically agitated anaerobic digester. CFD predictions are compared quantitatively with experimental data in terms of critical impeller speed based on the criteria of standard deviation method and cloud height. An adequate agreement is found between CFD prediction and the experimental data. The numerical simulation has further been extended to study the effect of digester shape, impeller design for RT, PBT and A310 Hydrofoil, impeller speed and particle size (200–650 μm) on the solid suspension in liquid–solid manure anaerobic digester.

The behavior of parameters having profound impact on the ability of a mixed anaerobic digester to suspend particles has been investigated. The behavior of each variable is adequately described by a polynomial model from numerical modeling. The underlying reasons responsible for the behavior of each variable under investigation is also provided. Results show that out of the six variables investigated, four variables have operating range where performance is at its optimum. Based on the results from the numerical simulations, optimized relation of these variables as a function of digester diameter are provided.

7. Effect of mixing strategy on methane production on lab and pilot scaled AD

Mixing of digester contents creates a homogeneous substrate preventing stratification and formation of a surface crust, and ensures solids remain in suspension. Bacteria, substrates and liquid consequently have an equal retention time where solids retention time, SRT will be equal to hydraulic retention time, HRT. Further, mixing also enables heat transfer, particle size reduction as digestion progresses and in release of produced gas from the digester contents. Despite the importance of mixing in achieving efficient substrate conversion, optimum mixing pattern and duration of mixing is a subject of much debate since the results are scale dependent. Therefore, the aim is to conduct test using both lab-scale and pilot scale ADs to contribute to a better understanding of the effect of mixing strategies on process performance and methane production.

In order to achieve these objectives, Section 7.1 presents the experimental set up, material and methodology to investigate the effect of mixing in lab-scale and pilot scale digesters followed by the results and discussions in Section 7.2. Finally, Section 7.3 presents concluding remarks regarding effect of mixing intensities and duration on anaerobic digestion process.

7.1 Experimental setup, materials and methods

7.1.1 Lab scale studies

The lab-scale test involves 4 identical lab-scale digesters R_1 , R_2 , R_3 and R_4 . Each lab-scale anaerobic digestion system consists of Continuously Stirred Digester Reactor

(CSTR). It is a 10.0 l PVC cylinder with the dimension of 19.0 cm inner diameter and 35.5 cm height. Sludge occupies 8.0 L of the digester while the remaining 2.0 L is the headspace for the digester. The digester operates at mesophilic conditions around 38°C with batch-mode feeding. Figure 7.1 displays the sketch of the lab-scale system. A hose pump feeds and discharges the digester using U-tube to control the feeding and discharge process with precision. An electric motor using flat blade impeller provides the digester with continuous mixing. A water tub keeps the temperature of the reactors at 38°C.

We did on-line measurements of the biogas production, biogas pressure and pH and performed a weekly check to the Total COD, Total Suspended Solids, TSS, and Volatile Solids, VS. The VFA measurement uses gas chromatography periodically. The specification of analysis methods for our experiments can be found from Ivanova (2000).

Regular intermittent pumping approximates a continuous operation of digesters. A cycle time selected is 1-h duration. This is the time interval required to feed the digesters with simultaneous withdrawal from overflows, mix the individual digester contents, and provide quiescent settling of the suspended solids in the digesters in the above sequence. The set up for feeding turns on for 1 minute every hour. There is no mixing provided to digester R_1 while subjecting R_2 , R_3 , and R_4 to alternate on-off mixing periods. The test considers two mixing durations of 45 and 15 min/h designated as T-1 and T-2, respectively. The performance of the digesters under steady-state conditions for the two mixing durations, T-1 and T-2 further studied. Here, the basis for the selection of the

steady-state periods is on the minimization of the standard deviation of the mean effluent TCOD concentrations from each digester. The steady-state period during T-1, mixing duration at 45 min/h is from day 41 to day 65; the steady-state period during T-2, mixing duration at 15 min/h is from day 125 to day 149 designated as steady-state periods of CASE-1 and CASE-2, respectively.

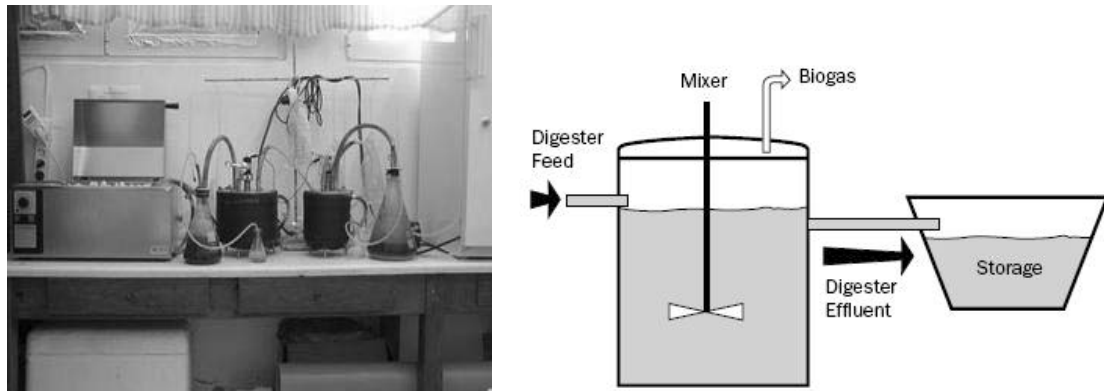


Figure 7.1: Schematic of lab-scaled digester used for performance test of different mixing duration and intensities on gas production

Mixing intensities are indirectly measured in terms of impeller speeds, rpm. The primary objective in this case is biological solids suspension at low mixing intensities. Three speed levels considered are 20, 50, and 100 rpm for R₂, R₃, and R₄, respectively. The lowest mixing intensity at 20 rpm is much greater than that required for laminar flow, $Re \leq 400$, but is just sufficient to achieve "off bottom suspension" of the sludge bed. At 100 rpm, the mixing intensity approached the level of fully turbulent flow, $Re \geq 10^3$, achieving complete uniformity of the digester contents.

To evaluate the effects of mixing on the lab-scaled anaerobic digesters under investigation, the study involves monitoring and recording of the following data:

- a) Operational data: Regular control of preset rates of feed flow and recirculation as well as impeller speeds. It also requires monitoring of effluent pH, alkalinity, and volatile acids, VA concentrations to insure system balance.
- b) Performance data: These include total COD (TCOD), soluble COD (SCOD), suspended solids, SS, and volatile suspended solids, VSS concentrations in the feed and effluents, as well as biogas production.

Sampling takes place at the beginning and the end of each new feed interval for the feed and effluent, respectively. The analysis of biogas volume and composition including CH₄, CO₂, and other gases is at the end of the feed interval. The basis for the determination of percent removals of TCOD (SCOD), SS (VSS), methane production rates and methane yields are the average volumetric feed and gas rates.

7.1.2 Pilot-scale studies

The pilot scale experiment uses a pilot-scale plant with capacity of 800 L built from a used stainless steel tank as shown in Figure 7.2. The top of the digester is fitted with a stainless steel top plate. The top plate supports the mixer, mixer motor, gas sampler, safety and pressure valve and a level switch. The digester wall includes a feed valve, three effluent outlet valves, three temperature probes and sampling ports. There is one outlet at the bottom the digester to remove sediment. Pumping hot water through a stainless steel coil fitted inside the digester maintains the digester stable at $38 \pm 1^\circ\text{C}$. A circulation pump circulates hot water between the heater and the digester using a circulation pump.

Digester feeding involves pumping the feed from a feed container of 800 L semi-continuously at 8 hr. interval. A high-speed mixer (450 rpm) thoroughly mixes the feed for 15 min prior to each feeding. A low speed top mounted mixer shaft with impeller driven by a geared DC motor with 0.25 kW, 5000 rpm mixes the digester contents. The location of effluent removal is the middle portion of the digester. The pumps used for pumping feed and effluent operate for 50 seconds every 8 hours with a flow rate of 10 L/minute. Measurement of biogas from digester uses a residential diaphragm gas meter. Relay timers and a two-channel 24 hours/7 day programmable time switch automatically controls pumps and mixers.

The digester operates with a liquid working volume of 500 l out of the total digester volume of 800 l with a HRT of 20 days and 38 ± 1 °C temperature. At start-up, the digester contains 450 l of inoculum and 30 l of fresh animal waste. Daily feeding commences after approximately 10 days when methane content in the biogas reached 50%. Fresh manure goes to the digester three times a day with 8 hr. interval and gradually increased to 25 L/day corresponding to 20 days HRT. Prior to each feeding, it is important to remove an equal amount of effluent from the middle part of the digester. During continuous mixing, the mixer operates at 100 rpm. While under alternating mixing strategy with square wave, the mixer operates at 100 rpm for 3 hours with an interval of 2 hours of stoppage. Efforts have been made to maintain more or less similar feed characteristics throughout the run by diluting the fresh manure to a nominal TS level of 6-7%. However, feed batch changes remained the main source of disturbances.

Sequencing of mixing periods with feed batch changes helps to obtain periods without feed batch change before or after changing the mixing strategy.

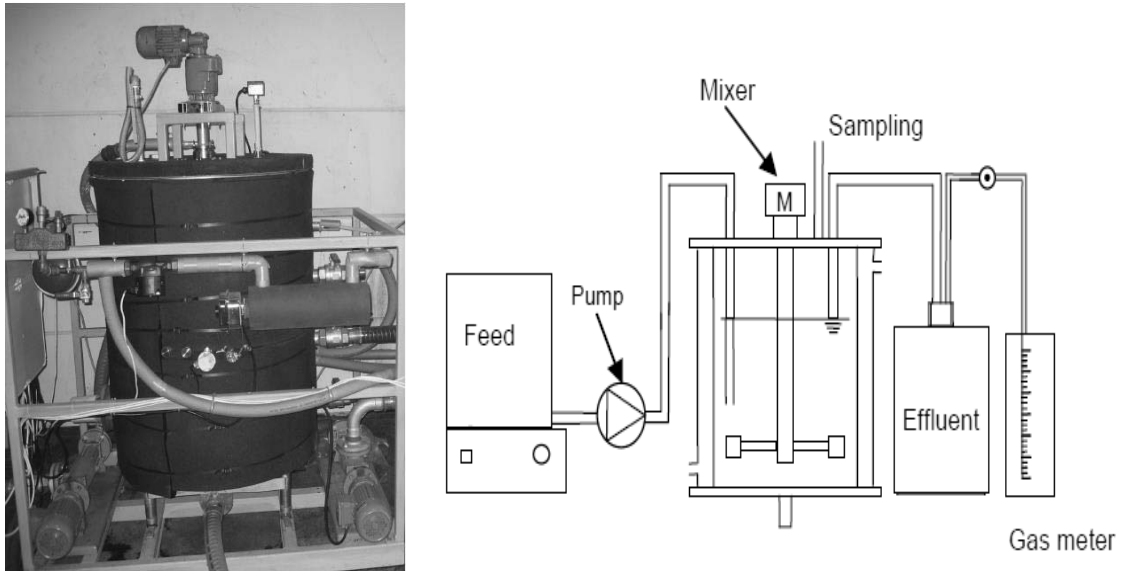


Figure 7.2: Schematic of pilot-scaled anaerobic digester used to test the effect of mixing on the performance of anaerobic digestion process

Specific biogas yield is calculated from the detailed data as the daily biogas production, divided by a weighted average of VS feed over a period stretching 8 days backward. The weighted average defines the effective VS basis for degradation to be represented by 57% of VS feed from the 3 most recent days, 29% of VS from the previous 3 days and 14% of VS from the last 3 days.

7.2 Experimental results

7.2.1 Lab-scaled anaerobic digester

In this study, the lab-scaled digester uses five separate batches of animal waste shipped to the laboratory for use. The raw waste characteristics are not consistent in all

shipments. While the average TCOD loading rate is adjusted to, the average SCOD, SS, and VSS loadings varied significantly while adjustment of $0.5 \text{ kg}/(\text{m}^3 \cdot \text{d})$ applied to the average TCOD loading. Figure 7.3 shows the large increase in SCOD loading from batch 1 to batch 2 and from batch 3 to batch 4 with a corresponding decrease in SS and VSS loadings during these periods.

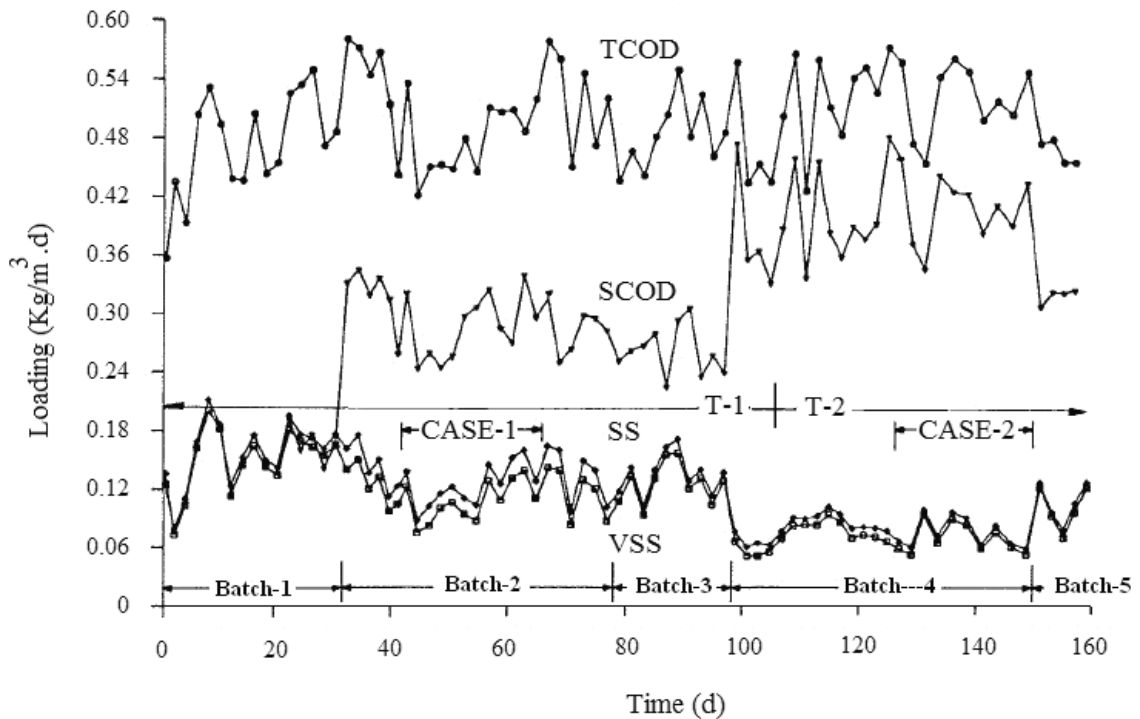


Figure 7.3: Average loadings to the lab-scaled digesters as a function of time during T-1, mixing duration at $45 \text{ min}/\text{h}$ is from day 41 to day 65; the steady-state period during T-2, mixing duration at $15 \text{ min}/\text{h}$ is from day 125 to day 149 designated as steady-state periods of CASE-1 and CASE-2, respectively

The ranges of average TCOD, SCOD, SS, and VSS concentrations in the five batches are $3,266\text{-}3,595$, $1,211\text{-}2,806$, $544\text{-}1,128$, and $489\text{-}1,067 \text{ mg}/\text{L}$, respectively. The corresponding overall average concentrations are $3,458$, $2,218$, 830 , and $753 \text{ mg}/\text{L}$,

respectively indicating batch 4 had the highest TCOD and SCOD and lowest SS and VSS concentrations among the five batches.

Overall pH, alkalinity, and VA concentrations in the digester effluents are quite stable over the duration of the experiments. The values of pH ranged from 7 to 8; alkalinity ranged from 854 to 1,634 mg/L as CaCO₃. Increasing mixing intensities accelerated the digester start-up under the conditions studied. Volatile acids concentrations dropped to below 10 mg/L in 34.5d for R₁, 17.5d for R₂, and less than 5d for R₃ and R₄. Variations in biogas production rates appeared quite normal. There are noticeable decrease and immediate recovery in gas production at each batch change.

Based on impeller speed, it is possible to estimate the motor torque delivered to the shaft, and power loss due to tube guide friction, the impeller power delivered to each digester provided with mixing according to Holland and Chapman (1966). Thus, the power-to-volume ratios, P/V corresponding to impeller speeds of 20, 50, and 100 rpm in this study are approximately 270, 700, and 1,500 W/m³, respectively. The minimum impeller speed of 20 rpm is necessary to achieve off-bottom suspension of sludge and, hence, adequate mixing for the given digester configurations. The relative impeller speeds used here are appropriate to serve the purpose of demonstrating the effect of mixing intensity on anaerobic digester performance.

Figures 7.4-7.7 presents digester input and output in terms of organics and solids concentration units for the entire study period. Figure 7.4 shows the variations in

concentrations of TCOD and SCOD in the feed. Minimization of the variations in feed TCOD in the experiments help to maintain a constant TCOD loading to the digesters. However, such variations of 2,850-3,998 mg/L for the most part are inevitable, considering the nature of the waste and the preparation requirements. The uncontrolled feed SCOD concentrations increases significantly from batch 1 to batch 2 and from batch 3 to batch 4, explaining for the corresponding increase in SCOD loadings during these periods.

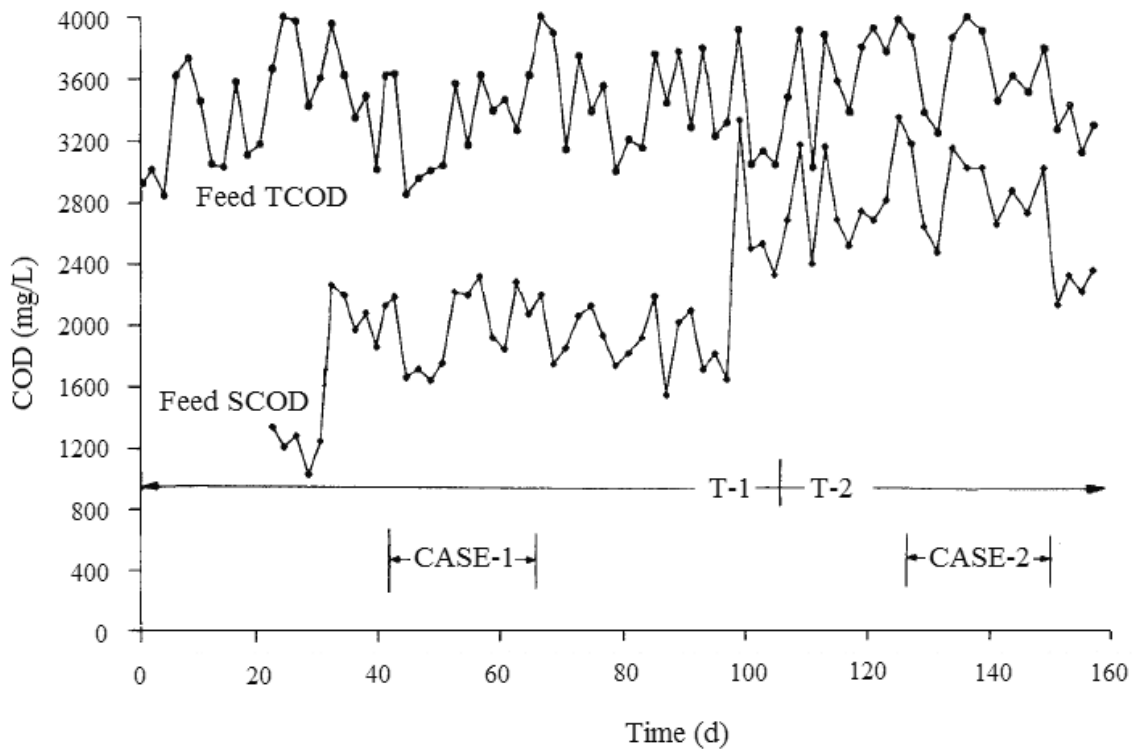


Figure 7.4: TCOD and SCOD concentrations in the feed as a function of time during T-1, mixing duration at 45 min/h is from day 41 to day 65; the steady-state period during T-2, mixing duration at 15 min/h is from day 125 to day 149 designated as steady-state periods of CASE-1 and CASE-2, respectively

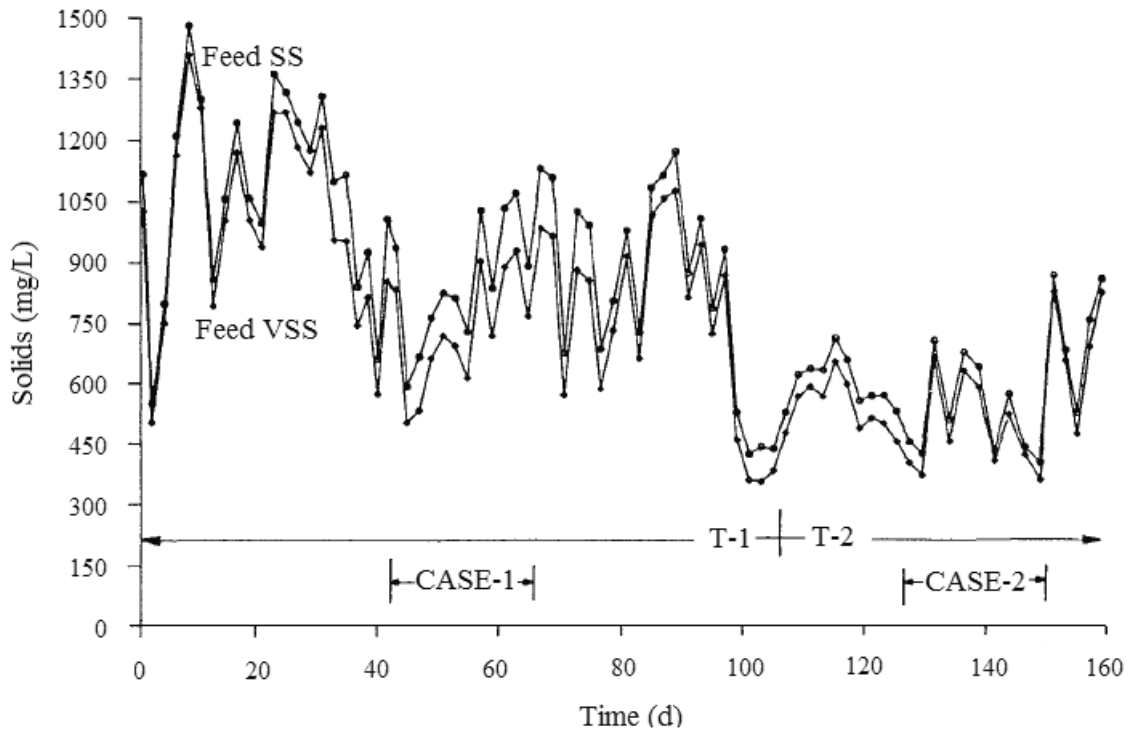


Figure 7.5: SS and VSS concentrations in the feed as a function of time during T-1, mixing duration at 45 min/h is from day 41 to day 65; the steady-state period during T-2, mixing duration at 15 min/h is from day 125 to day 149 designated as steady-state periods of CASE-1 and CASE-2, respectively

Figure 7.5 presents the variations in SS and VSS concentrations in the feed. Significant variations in feed SS and VSS concentrations throughout the investigation are illustrated. The decreases in SS and VSS concentrations roughly between days 30 and 100 and between days 100 and 150 complement the corresponding increases in SCOD concentrations to give an approximately constant TCOD loading in these periods.

Figure 7.6 shows the effluent TCOD and SCOD concentrations of the four digesters. These concentrations appeared to decrease gradually with time in R_1 without mixing. The overall response of R_2 with mixing at 20 rpm is very consistent, showing relatively

small variations in effluent TCOD and SCOD concentrations with time. The higher degrees in mixing in R₃ and R₄ compared to R₂ increased effluent TCOD variability. This is due to the higher concentrations of solids escaping the digesters at higher mixing intensities, especially in the case of R₄ with mixing at 100 rpm.

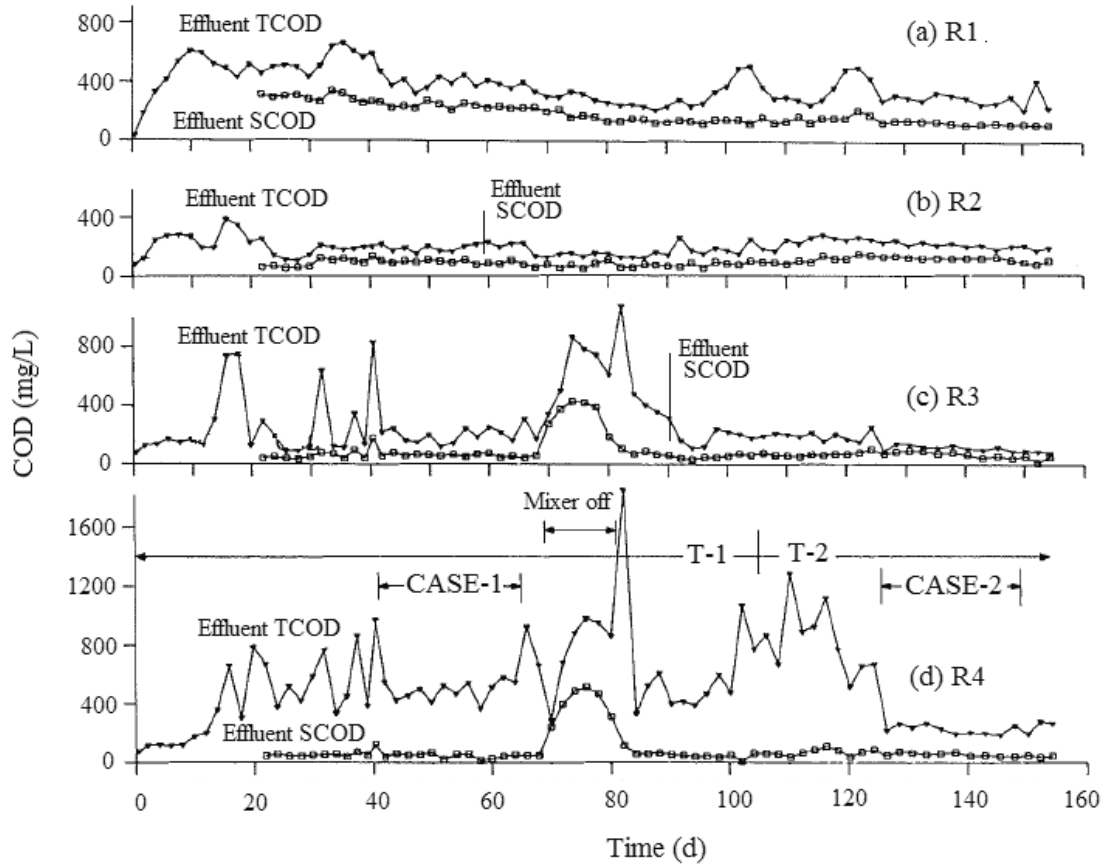


Figure 7.6: TCOD and SCOD concentrations in lab-scaled digester effluents as a function of time for mixing intensities corresponding to impeller speed of 20, 50, and 100 rpm for R₂, R₃, and R₄ respectively

The high variability of effluent TCOD concentrations compared with SCOD concentrations is, of course, due to the incorporation of solids in the TCOD tests.

Overall, the effluent SCOD concentrations in R₂, R₃, and R₄ are lower than R₁, apparently attributed to the effect of mixing.

Figure 7.7 shows the effluent SS and VSS concentrations of the four digesters. Similar to the variability in effluent TCOD concentrations, the variability in effluent SS and VSS concentrations is the lowest in R₂ and the highest in R₄. The effluent SS and VSS concentrations in R₄ between days 103 and 119 are even higher than in the feed. As a result, there is a net loss of biological solids from R₄ during this period. Usually, this would lead to reduced biodegradation. However, effluent SCOD concentrations from R₄ in the same period appeared to be unaffected as shown on Figure 5d; also, VA concentrations did not reveal any abnormality. The high degree of mixing in R₄ that provided high uniformity in digester content might have acted in a remedial manner.

Figures 7.6 and 7.7 reveal a tendency towards increased process instability in terms of TCOD and solids concentrations in the effluent as mixing intensity increases from 20 to 100 rpm. Reduction of mixing duration during T-2 after day 110 resulted in more time available for solids settling. As a result, effluent TCOD and SS (VSS) concentrations started to stabilize. However, it took approximately 20 days before R₃ and R₄ reached steady state.

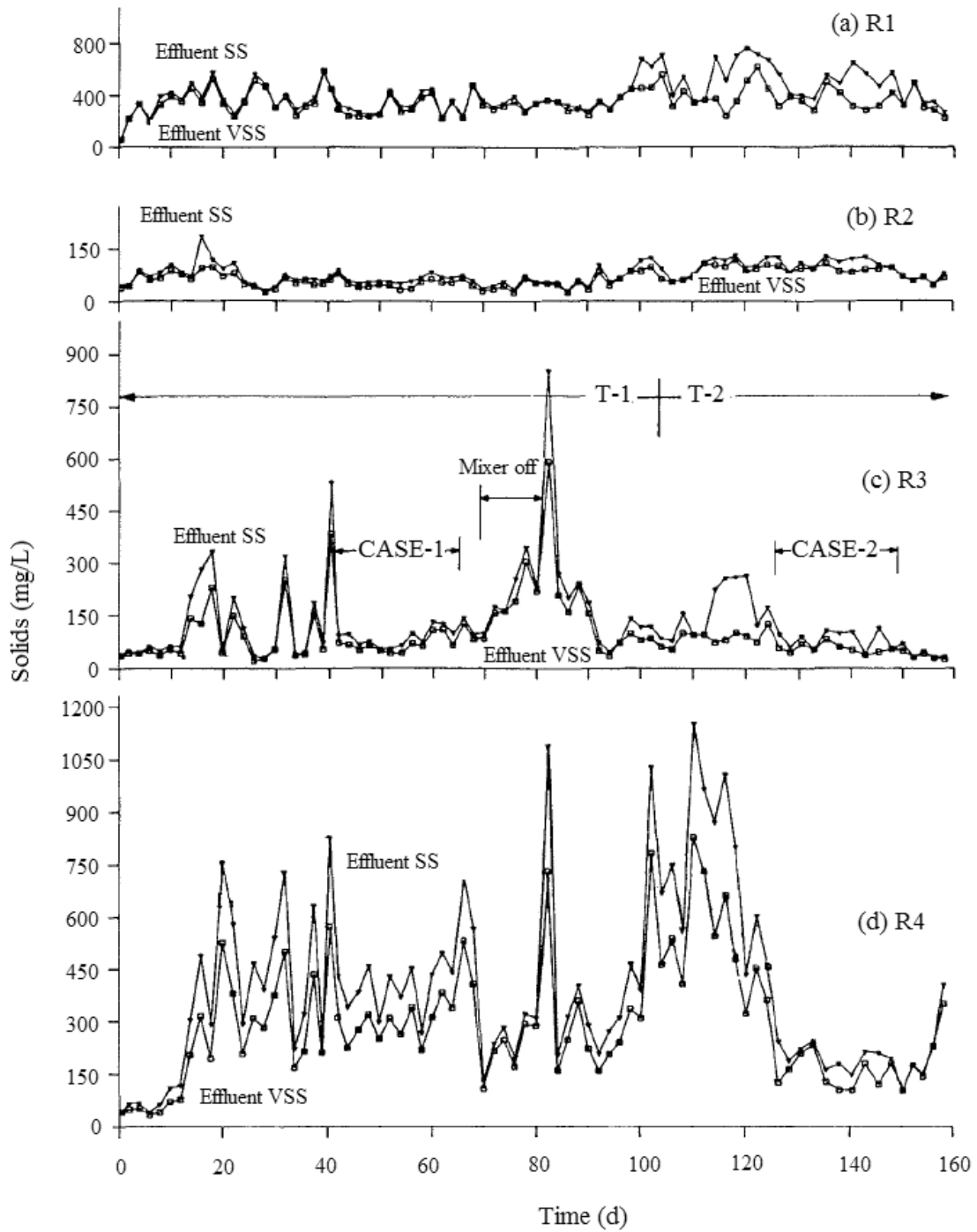


Figure 7.7: SS and VSS concentrations in digester effluents as a function of mixing intensities corresponding to impeller speed of 20, 50, and 100 rpm for R₂, R₃, and R₄ respectively

The biogas methane content from each digester is very consistent, showing no trends or major deviations from the mean with changes in feed characteristics, digester maturity, or mixing duration. Over the entire period of study, the mean CH₄ contents in the biogas are 73.5 %, 76.5 %, 76.4 %, and 75.5 % for R₁, R₂, R₃, and R₄, respectively. The corresponding CO₂ contents are 22.5%, 20.7%, 21.0%, and 21.1%, respectively. Visually, there is not much difference in biogas composition among the four digesters. However, it can be shown statistically by means of t-tests at $\alpha = 0.05$ and $n = 18$ that there is a significant difference between methane contents in digesters with and without mixing i.e., any one of R₂, R₃, and R₄ versus R₁ and between R₂ and R₄ at 20 and 100 rpm, respectively. This suggests that the degree of mixing had an influence on the methane content of the biogas. The above also shows that R₂ generated the highest methane content. In terms of methane yield during the entire period of study, R₁, R₂, R₃, and R₄ produced 0.315, 0.354, 0.352, and 0.370 m³ CH₄/kg TCOD removed, respectively. This shows that methane yield tended to increase with mixing intensity within the range of impeller speeds used. Figures 7c-d and Figure 6c-d indicates that disturbances in effluent qualities of R₃ and R₄ occurred in days 69- 81. These are due to the shutoff of the mixers in R₃ and R₄ during this period.

Table 7.1 presents the steady-state performance results of the digesters. The observed ranges of steady-state percent removals of organics and solids are: TCOD from 85.0% to 96.9%; SCOD from 87.8% to 98.0%; SS from 52.7% to 92.5%; and VSS from 59.3% to 93.2%.

Table 7.1: Steady-state performance results

Parameter	Period	Feed	Effluent			
			R ₁	R ₂	R ₃	R ₄
<i>Organics and solids concentration (removals in parenthesis)</i>						
TCOD (mg/L)	CASE-1	3,290	399 (87.9%)	196 (94.0%)	194 (94.1%)	493 (85.0%)
	CASE-2	3,654	298 (91.3%)	209 (94.3%)	114 (96.8%)	228 (93.8%)
SCOD (mg/L)	CASE-1	1970	240 (87.8%)	97 (95.1%)	63 (96.8%)	46 (97.7%)
	CASE-2	2865	133 (95.4%)	118 (95.9%)	75 (97.4%)	56 (98.0%)
	CASE-1	843	116 (86.2%)	63 (92.5%)	87 (89.7%)	399 (52.7%)
	CASE-2	526	179 (66.0%)	110 (79.1%)	82 (84.4%)	198 (62.4%)
	CASE-1	725	105 (85.5%)	49 (93.2%)	67 (90.8%)	295 (59.3%)
	CASE-2	483	125 (74.1%)	92 (81.0%)	56 (88.4%)	153 (68.3%)
<i>Methane production</i>						
CH ₄ rate (L/d)	CASE-1	-	0.86	1.07	1.04	1.05
	CASE-2	-	1.06	1.19	1.19	1.15

In general, percent removals of SCOD and VSS are higher than TCOD and SS, respectively. Methane production rates range from 0.86 to 1.19 L/d during the same periods.

Among the effluent organics and solids parameters listed in Table 7.1, only effluent SCOD decreased in concentration at higher mixing intensities during CASE-1 and CASE-2. The others, Effluent TCOD, SS, and VSS all show higher values in R₁ without mixing and R₄ with highest mixing than in R₂ and R₃. For these latter groups of parameters, there seemed to be a minimum value within the range of mixing intensities studied. On the other hand, methane production rate appeared to be the highest from R₂ at 20 rpm during both steady-state periods.

Figure 7.8 shows the percent removals of TCOD, SCOD, SS, and VSS with respect to mixing intensities for both CASE-1 and CASE-2. The general behaviors of these parameters during both steady-state periods are similar. During CASE-1, percent removals of TCOD, SS, and VSS revealed an optimum mixing intensity towards the lower side of the 20-50 rpm range. During CASE-2, the optimum mixing intensity appeared to have shifted to the higher side of this range. This indicates that for reduction in mixing duration, there is a need to increase the mixing intensity to achieve optimal removals of organics and solids in the systems studied.

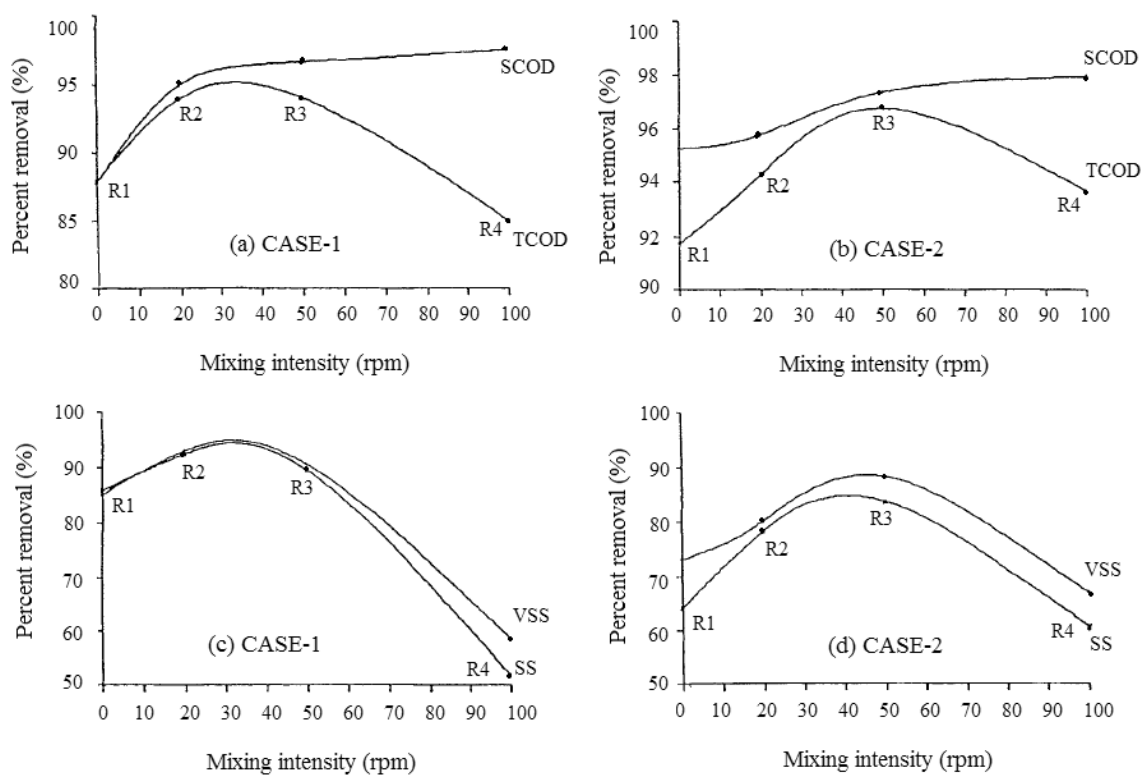


Figure 7.8: Steady-state percent removals of organics and solids versus mixing intensities corresponding to impeller speed of 20, 50, and 100 rpm for R₂, R₃, and R₄ respectively

In contrast, SCOD percent removals kept on increasing with mixing intensities. During CASE-1, the increase is high between 0 and 20 rpm corresponding to 87.7% to 95%, and then gradually reaches 97.6% SCOD removal at 100 rpm. As mentioned before, an impeller speed of 20 rpm for the configuration used is just sufficient to cause off-bottom suspension of the settled sludge. It seems that when the power level exceeded the off bottom suspension point during CASE-1, the rate of SCOD removal is reduced i.e., not much improvement is achieved. During CASE-2, SCOD removals also increase with mixing intensities from 95.3 % at 0 rpm to 98 % at 100 rpm.

However, the greatest increase had shifted to a higher mixing intensity range of 20-50 rpm; further increase is small beyond this range. This also indicates that reduction in mixing duration requires increase in mixing intensity to achieve optimal SCOD removal.

Table 7.2 summarizes the steady-state results on methane gas production from the digesters. The results show that all values are higher for R₂, R₃, and R₄ than for R₁. While the differences in methane production among R₂, R₃, and R₄ are not large, those between the digesters with and without mixing are more substantial. Thus, mixing the digester content at the intensities and durations studied enhances methane gas production rate and methane yield.

Methane yields based on TCOD removal are not much different during CASE-1 and CASE-2 for all digesters; the yields based on SCOD removal are all lower during CASE-2 than during CASE-1. However, methane production rates, L/m³.d are higher during CASE-2 than during CASE-1 for digesters with or without mixing. The latter

contradicts some results reported in the literature indicating that methane production decreases with a reduction in mixing duration (Mills 1979; Smith et al. 1979; Hashimoto 1982). The methane production rates and yields from R₁ are also inconsistent in the two steady-state periods. Supposedly, they should be the same during CASE-1 and CASE-2, since there is no mixing in R₁.

Table 7.2: Methane production during steady-state periods

Digester	CH ₄ production rate (L/(m ³ .d))		CH ₄ (m ³ /Kg COD removed)			
			TCOD basis		SCOD basis	
	CASE-1	CASE-2	CASE-1	CASE-2	CASE-1	CASE-2
R ₁	122.4	150.7	0.292	0.316	0.494	0.389
R ₂	152.6	169.4	0.339	0.346	0.564	0.434
R ₃	148.6	170.6	0.343	0.344	0.563	0.437
R ₄	149.4	164.6	0.358	0.355	0.526	0.409

The controversies are due to one important uncontrollable factor which has not been accounted for - the soluble fraction, SF equals to the ratio SCOD/TCOD (Smith *et al.* 1979), of organics in the manure supply. Soluble fractions of the feed during CASE-1 and CASE-2 are 0.584 and 0.780, respectively. Thus, higher SF, rather than shorter mixing duration for CASE-2, actually resulted in a higher methane production rate, L/m³.d. When the organics are more soluble, they are more readily and easily biodegradable; hence, more biogas is produced. As seen in Figures 7.8a and 7.8b, higher SCOD removals occurred during CASE-2 than during CASE-1 or more correctly, at higher SF than at lower SF of the organics. This means that lower methane yield, m³/(kg

SCOD removed is expected at higher SF, as is shown in the last two columns of Table 3. It can be shown that there is actually a significant negative correlation between methane yield in terms of SCOD removal and SF at the 5% level of significance, $r = -0.83$. Therefore, change in the SF of the feed, due to a change in SCOD concentration significantly affected the methane production rate and methane yield.

To remove the possible influence of different feed characteristics on digester performance, the results of each digester with mixing is expressed as a ratio to R1 without mixing. Figure 7.9 shows the performance of the digesters normalized with respect to R1. In general, Figure 7.6a shows the percent removals of TCOD and SCOD by digesters with mixing are better than R₁ without mixing. Furthermore, the reduction in mixing duration from CASE-1 to CASE-2 has a negative effect on both TCOD and SCOD percent removals, with the exception of TCOD percent removal by R₄. As observed before, the normalized SCOD percent removal curves in Figure 7.9a also show higher SCOD percent removals at higher mixing intensities, but the increase is negligible between 50 and 100 rpm for both CASE-1 and CASE-2. The normalized TCOD percent removal curve for CASE-1 peaks at a mixing intensity of 30 rpm, whereas that for CASE-2 peaks at 50 rpm.

The normalized solids removal curves in Figure 7.9b clearly show the adverse effect of high-level mixing. Suspended solids and volatile suspended solids percent removals by R₄ are all lower than those by R1 during both CASE-1 and CASE-2. This is due to the

substantial loss of solids in the effluent at the high mixing intensity used at 100 rpm. However, moderate degree of mixing is obviously advantageous. The normalized SS and VSS percent removal curves in Figure 7.9b appear to peak at a mixing intensity of 30 rpm during CASE-1 and at 50 rpm during CASE-2. The reduction in mixing duration from CASE-1 and CASE-2 resulted in a considerable improvement of SS and VSS percent removals for all digesters with mixing, especially for R₄. This explains the improvement in TCOD percent removal by R₄ from CASE-1 to CASE-2 shown on Figure 7.9a.

Figure 7.9c shows methane production rates by all digesters compared to R₁ during the steady-state periods. The results show normalized methane production rates from digesters with mixing decreases from CASE-1 to CASE-2, instead of the apparent increases shown in Table 7.2. Figure 7.6d illustrates similar results from the normalized methane yield curves. In particular, methane yield based on TCOD percent removal is considerably more sensitive to the reduction in mixing duration than that based on SCOD percent removal. Removing the effect of changing feed characteristics reveals the advantages of longer mixing durations in terms of higher methane production rate and higher methane yield. Both Figures 7.9c and 7.9d show higher methane production rates and higher methane yields with mixing than without mixing. They also show that the optimum mixing intensity for maximum methane production appears to be between 20 and 50 rpm for the conditions of this study.

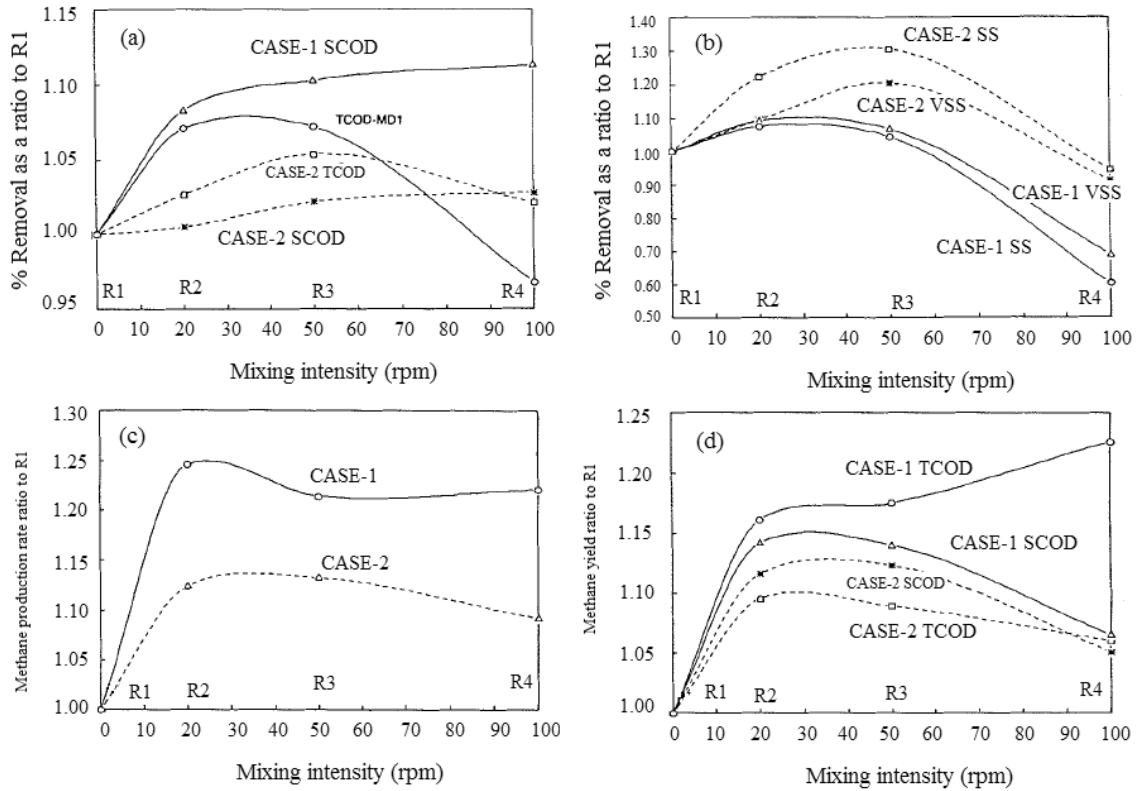


Figure 7.9: Normalized steady-state digester performance versus mixing intensities corresponding to impeller speed of 20, 50, and 100 rpm for R₂, R₃, and R₄ respectively

The above analysis clearly demonstrates that mixing intensity and mixing duration and their joint effect significantly affect the steady-state performance of the anaerobic digesters in treating agricultural and industrial waste. Statistical tests conducted to verify such an effect uses a two-factor analysis of variance based on normalized data. The results show that digester performance in terms of percent removals of TCOD, SCOD, SS, and VSS as well as methane production rate and yield are significantly affected by the main effects of the mixing intensity and mixing duration levels studied and by their interaction ($\alpha = 0.05$).

7.2.2 Effect of mixing on the performance of pilot-scale AD

Figure 7.10 illustrates the results for the performance of the pilot scale digester in terms of biogas production.

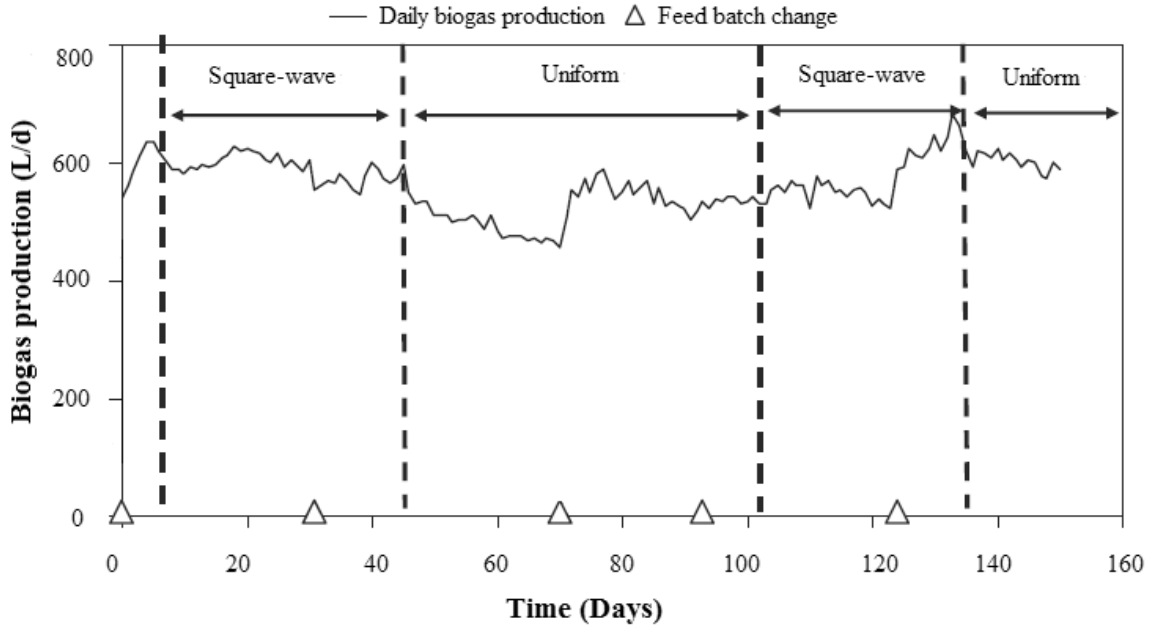


Figure 7.10: Effect of modes of mixing on biogas production. During continuous mixing, the mixer operates at 100 rpm while under alternating mixing strategy with square wave, the mixer operates at 100 rpm with interval of 2 hours every 3 hours of mixing.

Fig. 7.12 illustrates the level of stability obtained throughout the period in terms of VFA level. VFA level is higher during the first part of the experiment in the range of 2-4 g/l, probably due to remaining start-up adaptation, but fell to a low and constant level of 1 g/l in the latter part of the run as shown in Figure 7.12 .

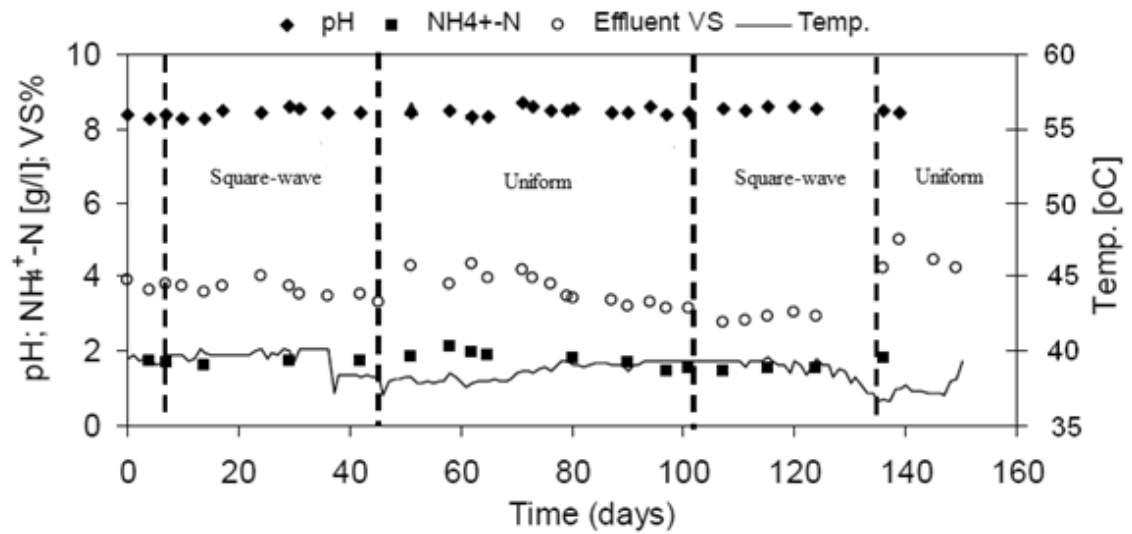


Figure 7.11: Performance of digester to different modes of mixing. During continuous mixing, the mixer operates at 100 rpm while under alternating mixing strategy with square wave, the mixer operates at 100 rpm with interval of 2 hours every 3 hours of mixing.

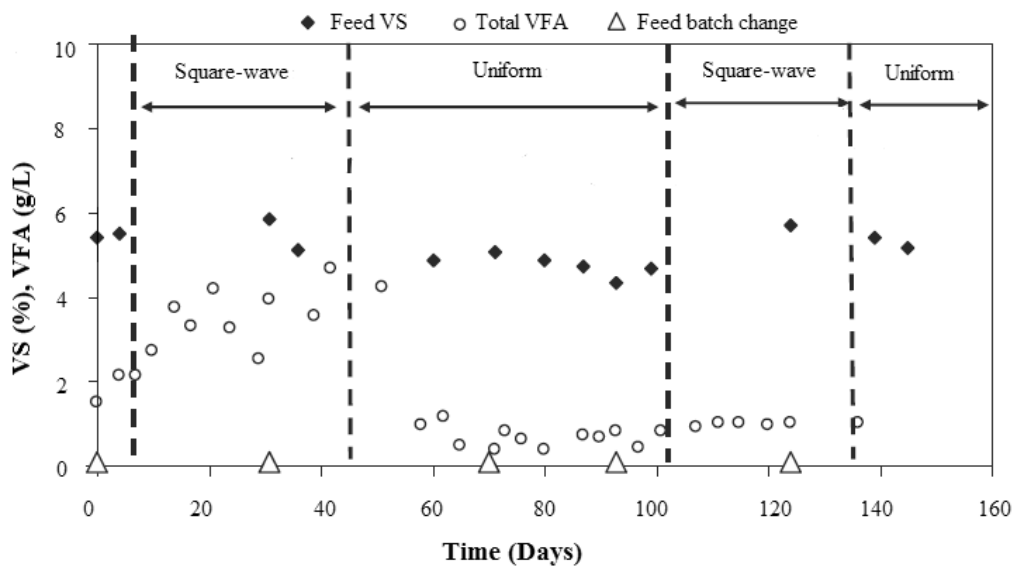


Figure 7.12: Process performance during anaerobic digestion with steady state and square wave modes of mixing application where the mixer operates at 100 rpm with interval of 2 hours every 3 hours of mixing.

Figure 7.13 shows average specific biogas yield that is the primary evaluation parameter. Results indicate that the specific biogas yield obtained during periods with alternating mixing is 2.5-14.6% higher than the yield obtained with continuous mixing, with an average value of 7%. In addition, the effluent VS level is generally lower during the periods of alternating mixing, which indicate that this mixing strategy resulted in stratification of digester content and thus minimized VS loss.

Although there is a significant variation in biogas yield when changing mixing strategy, the tendency is the same for every change, and thus considered as a statistically reliable observation. Variations observed are likely the result of other disturbances, temporarily affecting process performance. The period prior to the first change from continuous to alternating mixing is relatively short and is affected by a disturbance characterized by shift in specific biogas yield related to feed batch change. Furthermore, Figure 7.13 shows that there is a VFA build-up in the initial phase of the alternating mixing, which may not be related to the mixing strategy, reducing biogas yield during the alternating mixing period and thus resulting in a relatively small change in yield. Likewise, the relatively large step observed in Figure 7.13 when switching back to continuous mixing on day 32 may be affected by a temperature disturbance shortly before shifting the mixing strategy (which is also the case second time at day 135), and the general shift in VFA level in this period. It is obvious that the third feed batch started at day 70 must have been with VS with higher biogas potential. However, the process appears to have stabilized before initiation of the second alternating mixing period.

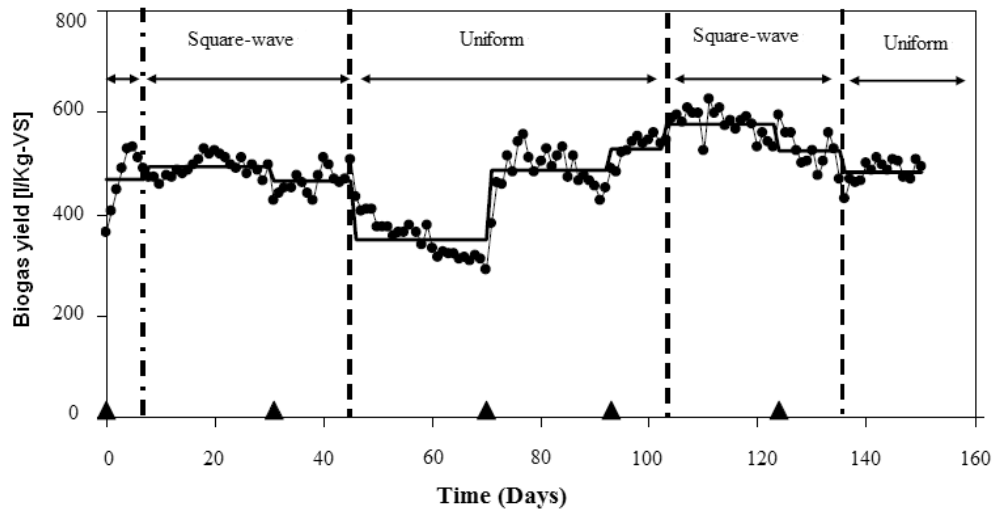


Figure 7.13: Effect of mixing mode on specific biogas yield during anaerobic digestion. During uniform mixing, the mixer operates at 100 rpm while under alternating mixing strategy with square wave, the mixer operates at 100 rpm for 3 hours with an interval of 2 hours stoppage time.

The results indicate that mixing strategy can positively affect biogas production in the pilot scale digester. The improved biogas production under alternating mixing compared to continuous mixing contributes to better solids and biomass retention in the digester. Biogas yield improvement appear to be of the order 7% from the present experiments, which is of significant importance for existing and new full scale biogas plants, as the improvement method involves virtually no cost, except a revised control strategy for digester mixing. These results are in accord to Dague et al. (1971) who have also reported that shifting from continuous mixing to alternating mixing of 2 min of mixing/h resulted in significantly higher gas production during the anaerobic treatment of a liquid waste stream. The increase in biogas production results from an improved solids

retention due to better bio flocculation in the alternatively mixed digester operating on square wave mode.

The choice of a 2 hour mixer stoppage is based on previous settling experiments (U of MN Extension, 2006) showing that most stratification of solids occurred within this period, but also considering practical possibilities on most full-scale biogas plants operating with discharge intervals in the range of 4-10 hours. During this “non-stirring” period, the lighter fiber fraction floats to the surface by floatation while the heavier solids settle to the bottom by gravity leaving the middle portion with low solids content. Removal of effluent from the middle layer with lowest solids content at the end of the “non-stirring” period had resulted in retaining the solids from upper and lower layers with higher VS content for further degradation and minimizing effluent loss. Previous research also showed that optimal bio-methane production of cattle manure obtained when the effluent discharge point is at the middle of the liquid level in a biogas plant (Schofield and Rees 1988; Ong *et al.*, 2000). Hence, separation of digester contents within the digester through withholding mixing can effectively serve as an operating strategy to optimize biogas production in full-scale plants. However, it is necessary to pay attention when operating at high TS/VS mixtures as high straw/fiber content can lead to formation of solid floating layer that may overload mixer when starting after a “non-stirring” period. Moreover, accumulation of solids in the bottom can reduce the effective working volume. To avoid these two operational problems, it is helpful to either discharge effluent from the middle layer with digester periodically operated in

continuous mixing mode or occasional discharge from the bottom rather than the middle layer.

7.3 Conclusions

The study of the effects of mixing intensity and mixing duration on the anaerobic digestion uses four laboratory-scale digesters. Mixing intensities for digesters R₁, R₂, R₃, and R₄ are set at impeller speeds of 0, 20, 50, and 100 rpm, respectively. Two mixing durations at 45 and 15 min/h are considered. Increasing mixing intensities under the conditions studied accelerated the digester start-up. The levels of mixing intensity and mixing duration used and their joint effect significantly affected digester performance with respect to organics and solids removals. Process instability in terms of variations in effluent TCOD and SS (VSS) concentrations increased as mixing intensity increased from 20 to 100 rpm. Effluent SCOD concentrations decreased at higher mixing intensities during both steady-state periods. Steady-state percent removals of SCOD, 87.8 % -98.0% and VSS, 59.3% -93.2% are generally higher than values of TCOD, 85.0% -96.9 % and SS, 52.7% -92.5 %, respectively, by all digesters under the conditions studied. The observed results suggest that when mixing duration is reduced for the same cycle time, mixing intensity must be increased to achieve optimal removals of organics and solids. Mixing at the highest impeller speed studied at 100 rpm caused substantial solids loss in the effluent. Reduction in mixing duration from 45 to 15 min/h resulted in considerable improvement in SS (VSS) removal efficiencies for all digesters with mixing; however, this generally had a negative effect on TCOD and SCOD percent removals. Methane production rate, L/mL d and methane yield, m/kg COD removed are enhanced by mixing; however, both decreased relative to those from R₁ when mixing

duration is reduced from 45 to 15 min/h. Over the entire study period, methane yield ranged from 0.315 to 0.370 m³/kg TCOD removed; methane content in the biogas is 2%-3% higher from digesters with mixing than that without mixing. Higher soluble fraction of organics in the feed increases methane production rate but decreases methane yield. The mixing intensities studied had a significant effect on SCOD utilization rate. The rates of SCOD utilization in R₄ where mixing intensity is the highest are significantly higher than the other three digesters during both steady-state periods ($\alpha = 0.05$).

In case of pilot scale digester, the specific biogas yield obtained during periods with step wave mixing is 2.5-14.6% higher than those obtained with continuous mixing, with an average value of 7%. The increase in biogas production can be attributed to solids retention due to better bioflocculation in the step function mixing reactor. This finding has a significant importance for existing and new full scale biogas plants, as the improvement method involves virtually no cost, except a revised control philosophy for digester mixing. The effluent VS level was also generally lower during the periods of intermittent mixing, which indicate that this mixing strategy resulted in stratification of digester content and thus minimized VS loss.

8. Conclusion, contributions and recommendations

Section 8.1 lists accomplished tasks, conclusions drawn and contributions made to the community of anaerobic digester designers. Section 8.2 indicates some of the issues the author encountered during the research and recommendations worth considering to expand on the knowledge gained from this work.

8.1 Conclusions and contributions

The present successfully investigated, described and characterized the distinct flow regimes existing within a mixed anaerobic digester at various operational conditions using experimental and numerical approaches. As a result, mixing is characterized and outputs are provided to identify optimum mixing regimes for digesters depending on their sludge rheology, operational regimes, digester dimensions and mixing systems. In addition, we identified relationships useful to optimize the choice of operational parameters. The next section lists summary of contributions to the knowledge of mixing in anaerobic digesters from both experimental and numerical work done.

8.1.1 Significance of experimental work

- (a) A new candidate transparent fluid model material to mimic the manure behavior is rheologically characterized and parameters affecting the viscosity are investigated.
 - The power equation indicated that the consistency coefficient increased non-linearly with an increase in concentration.
 - Mathematical models are developed for prediction of the consistency coefficient as a function of temperature and concentration.

- Apparent viscosity decreases fast at higher concentration than low concentration at increasing shear rates
- (b) Investigated mixing times and power in anaerobic digester with non-Newtonian fluids, determined the characteristic shear rate in mixed anaerobic digester in which mixing takes place in order to estimate a viscosity which can be used to correlate the mixing time data, and used the correlation to explain the effect of non-Newtonian behaviour of manure on the mixing process in the digester
- mixing time depends on the probe and injection locations
 - the efficiency of mixing based on mixing times indicates dependence on the geometry of the digester and impeller, as well as on the properties of the fluid
 - each impeller has a critical Reynolds number, above which $N\theta$ is constant and below which $N\theta$ increases with decreasing Reynolds number
 - Developed a robust method to obtain the apparent viscosity of manure in anaerobic digester based on the estimation of the average shear stress in the fluid at the surface of the digester wall and base by relating the torque to the tangential velocity gradient of the fluid at the digester wall and base and the pressure drop due to the fluid impinging on the baffles to the shaft torque.
 - The analysis of the effect of power input on mixing time shows that there are potential savings to be made in the capital cost of an agitator if an impeller with a low power number is chosen.

- Data from all impellers under investigation are correlated using three dimensionless groups namely power number, P_o , Reynolds number, Re and Fourier number, F_o
- (c) Investigated the presence, location and size of segregated mixed structures that exist in anaerobic digesters
- Impeller speed modulation of square wave and sine wave protocols induce chaotic mixing by enhancing the stretching and folding of fluid within the segregated regions
 - The combination of larger amplitude and shorter wave period for square wave protocol modulation intensifies the mixing process, resulting in the faster destruction of segregated structures
 - Transition of the segregated structure results from the dynamic change of flow structure due to increase of the Reynolds number with decrease of viscosity when temperature increases.
- (d) Effect of mixing on the performance of anaerobic digesters using lab and pilot scaled digesters. The study concerns with mixing intensity and duration effect on performance of AD and results showed that:
- Reactor start-up appeared to be accelerated by increasing mixing intensities under the conditions studied.
 - The levels of mixing intensity and mixing duration used and their joint effect significantly affected reactor performance with respect to organics and solids removals.

- Process instability in terms of variations in effluent TCOD and SS (VSS) concentrations increased as mixing intensity is increased
- The rates of SCOD utilization in the digester where mixing intensity is the highest are significantly higher than those in the other three reactors during both steady-state periods
- Reduction in mixing duration resulted in considerable improvement in SS (VSS) removal efficiencies for all reactors with mixing; however, this generally had a negative effect on TCOD and SCOD percent removals.
- Methane production rate, L/mLd and methane yield, m/kg COD removed are enhanced by mixing; however, both decreased when mixing duration is reduced

8.1.2 Significance of numerical work

Developed a fully 3D numerical model with experimental validation to predict the behavior of manure in a mechanically mixed anaerobic digester in terms of its velocity profile, Power number, Pumping number, and mixing time. The model:

- Incorporates non-Newtonian flow behaviour of manure
- adopts both multiple frames of reference and sliding grid approaches where no experimental data is needed; instead, the impeller is explicitly simulated
- computes power consumption, pumping capability, fluid dynamic efficiency, and mixing time to homogeneous distribution from point-wise release of a scalar

The findings can be summarized as:

i. For laminar flow:

- Identified three different flow patterns for laminar mixing in a Rushton stirred anaerobic digester: Pumping, stalled and reverse flow.
- Identified the dominant forces present within the digester using computational methods and force decomposition.

ii. For the case of transitional flow:

- The sources of and physical mechanisms responsible for the impeller induced macro-instabilities i.e. blade trailing vortices are identified.
- The pressure and viscous forces in the mean flow field are calculated and used to establish causal mechanisms responsible for the vortex formation in detail.

iii. For turbulent flow:

- characterized in detail the hydrodynamic changes that occur when H/T is decreased, and determined the minimum liquid levels and the critical impeller submergence for different impeller off-bottom distances, impeller diameters and agitation speeds where adequate mixing process can still be achieved, both in a single liquid phase and in solid-liquid suspensions.
- Identified a critical impeller submergence ratio S_b/D below which:
 - the macroscopic flow pattern generated by the impeller changes substantially, transitioning from either a double-loop recirculation flow or a single-loop recirculation flow depending on the impeller

clearance off the digester bottom to an upward single-loop recirculation flow;

- the Power number and Radial pumping number drop significantly;
- solid suspension cannot be attained at any agitation speed;
- mixing time increases suddenly;
- vortex formation occurs, air entrainment is significantly facilitated, and impeller flooding typically results
- specific power required for just-off-bottom suspension increases rapidly with the solids concentration

All above mentioned findings are significant pieces of knowledge for designers in the anaerobic digester community to optimize the digestion process in a digester system as whole to stabilize process, maximize gas production, minimize scum and foam formation, and prevent solids deposition in the digester.

8.2 Recommendations

This study has considered the velocity gradient as a tool to demonstrate the importance of zones of minimal mixing in a digester on biogas production. In order to achieve this, computational fluid dynamics (CFD) models are used to calculate local velocity gradients in laboratory-scale digesters at a range of mixing speeds. These models mimicked experimental work undertaken to determine the change in biogas production from laboratory-scale, mechanically-mixed anaerobic digesters when the mixing speed was altered. The experimental results were considered in conjunction with the results of the CFD models to demonstrate the importance of pockets in the digester which

experience low velocity gradients. Consideration of the intermediary link between mixing and microbiology can provide a potential explanation for the findings of this research.

(b) Substrate composition information is important for simulating and optimizing anaerobic digestion processes and reactors. Substrate composition determines the process pathways and influences the overall process in high rate anaerobic reactors. The substrate composition is even more important and considered as the bottle neck for high solids digestion due to the importance of the hydrolysis step. Therefore, it will be beneficial if comparison of different high solids mixed digester system designs for given solid waste are performed.

(c) High shear condition has a negative effect on anaerobic digestion process. Our hypothesis for this adverse effect of high intensity mixing are related to the disruption of spatial juxtaposition between hydrogen-producing syntrophic bacteria and their methanogenic partners, prevention of growth of methanogenic zones required for methane conversion or increased hydrolysis rates. Hence, we recommend that further studies to be conducted to evaluate the response of anaerobic microorganisms to high shear present in anaerobic digester. It will be beneficial if digester performance data and molecular microbial techniques be used to link dynamics of the microbial community to the change in shear conditions in the mixed anaerobic digester.

(d) Microbial floc structure analysis with fluorescence in situ hybridization can shed light if microbial floc size distributions are affected under increased shear conditions or not, if before, during, and after a high shear period, indicating that syntrophic interactions were intact or not. In conducting the present research program a number of

important questions arose which could not be answered as part of this work. It is recommended that the following could form part of any future investigation into the area of solid-liquid mixing:

(e) It appears that there is more than one mechanism responsible for solids suspension. It would be valuable to design experiments in which only one mechanism is controlling and hence study the suspension behaviour accordingly. In addition, laser measurements of velocity and energy distribution at digester base are recommended. This information aid to clarify the nature of suspension mechanism(s) at just suspension condition. The flow pattern of an impeller has been shown to have a substantial influence on solids suspension and distribution but these effects are virtually impossible to quantify by normal experimental means. A computational fluid dynamics study on flow interactions and their effects on solid-liquid mixing may be the most effective way of clarifying this area.

In view of the similarities between the suspension of particles, fluidization, transportation of sediments and solids, a comparative study of present knowledge in these processes would be a fruitful investigation. This study demonstrates that power number increases with digester sizes. This does not affect the validity of the scale-up rules as long as geometrical similarity is assumed. However, it will certainly affect the choice of motor and gear box. Further study is necessary to clarify the effect of scale on power number.

References

- Alvarez-Hernández, M.M., Shinbrot, T., Zalc, J., Muzzio, F.J. (2002). Practical chaotic mixing, *Chemical Engineering Science*, 57, 3749–3753.
- Agote, I., Odriozola, A., Gutierrez, M., Santamaria, A., Quintanilla, J., Coupelle, P., Soares, J. (2001). Rheological study of waste porcelain feedstocks for injection moulding. *Journal of the European Ceramic Society* 21, 2843–2853.
- Amanullah, A., Hjorth, S.A., Nienow, A.W. (1997). Cavern sizes generated in highly shear thinning viscous fluids by SCABA 3SHP1 impellers, *Transactions I. Chem.E.*, 75(C), 232–238.
- Anandha Rao, M., Brodkey, R.S. (1972). Continuous flow stirred digester turbulence parameters in the impeller stream, *Chemical Engineering Science*, 27, 137–156.
- ARC 2003(1) Campbell, Stewart: An inventory of bioprocesses to enhance industrial efficiency in the energy, forestry, pulp and paper, mining, chemical and plastics industrial sectors. Alberta Research Council, Report prepared for Environmental Biotechnology Advancement Division Environmental Protection Services, Environment Canada, March 3, 2003.
- Armenante, P.M., Chou, C.C. (1996). Velocity profiles in a baffled vessel with single or double pitched-blade turbines, *A.I.Ch.E. Journal*, 42(1), 42–54.
- Ascanio, G., Foucault, S., Tanguy, P.A. (2004). Time-periodic mixing of shear-thinning fluids, *Chemical Engineering Research and Design*, 82(A9), 119–1203.
- Aubin J., Mavros P., Fletcher D.F., Bertrand J., Xuereb C. (2001). Effect of axial agitator configuration (up-pumping, down-pumping, reverse-rotation) on flow patterns generated in stirred vessels, *Chem. Eng. Res. Des.*, 79, 845–856.
- Aubin, J., Naude, I., Bertrand, J., Xuereb, C. (2000). Blending of Newtonian and shear thinning fluids in a digester stirred with a helical screw agitator, *Chemical Engineering Research and Design*, 78(A), 1105–1114.
- Bakker, A., Fasano, J.B. (1994). Time dependent, turbulent mixing and chemical reaction in stirred digesters, *A.I.Ch.E. Symposium Series*, 299, 71–77.
- Bakker, A., K. J. Myers, R. W. Ward, and C. K. Lee, (1996). The laminar and turbulent flow pattern of a pitched blade turbine, *Trans. IChemE*, 74A, 485.
- Bakker, A., Myers, K.J., Ward, R.W., Lee, C.K. (1996). The laminar and turbulent flow pattern of a pitch blade turbine, *Chemical Engineering Research and Design*, 74(A), 485–491.

- Bakker, R.A., van den Akker, H.E.A. (1994). A computational study of chemical reactors on the basis of micromixing models, *Chemical Engineering Research and Design*, 72(A), 733–738.
- Bakker, R.A., van den Akker, H.E.A. (1996(a)). A Lagrangian description of micromixing in a stirred digester reactor using 1D-micromixing models in a CFD flow field, *Chemical Engineering Science*, 51(11), 2643–2648.
- Balhoff, M.T., Thompson, K.E. (2004). Modelling the steady flow of yield-stress fluids in packed beds, *A.I.Ch.E. Journal*, 50(12), 3034–3048.
- Barigou, M. (2004). Particle tracking opaque mixing systems: An overview of the capabilities of PET and PEPT, *Chemical Engineering Research and Design*, 82(A9), 1258–1267.
- Barrue, H., Xuereb, C., Pitiot, P., Falk, L., Bertrand, J. (1999). Comparison of experimental and computational particle trajectories in a stirred vessel, *Chemical Engineering & Technology*, 22(6), 511–52.
- Batstone D.J., Keller J., Angelidaki I., Kalyuzhnyi S. V., Pavlostathis S. G., Rozzi A., Sanders W. T. M., Siegrist H. and Vavilin V. A. (2002a). Anaerobic Digestion Model No.1 (ADM1). IWA Task Group for Mathematical Modelling of Anaerobic Digestion Processes, IWA Publishing, London, UK.
- Bello-Mendoza, Ricardo; Sharratt, Paul N., (1998). Modeling the effects of imperfect mixing on the performance of anaerobic reactors for sewage sludge treatment, *Journal of Chemical Technology & Biotechnology*, 71(2), 121–130.
- Ben-Hasson, R.M., Ghaly, A.E.; Singh, R.K. (1985). Design and evaluation of no-mix energy efficient AD. Proceedings, Annual Meeting, Canadian Society of Agricultural Engineering, June 23-27, Charlottetown, P.E.I.
- Bhattacharya, S., Kresta, S.M. (2002). CFD simulations of three-dimensional wall jets in a stirred digester, *The Canadian Journal of Chemical Engineering*, 80, 695–709.
- Bittorf, K.J., Kresta, S.M. (2000). Active volume of mean circulation for stirred digesters agitated with axial impellers, *Chemical Engineering Science*, 55, 1325–1335.
- Bittorf, K.J., Kresta, S.M. (2001). Three-dimensional wall jets: axial flow in a stirred digester, *A.I.Ch.E. Journal*, 47(6), 1277–1284.
- Björnsson L. (2000). Intensification of the biogas process by improved process monitoring and biomass retention. PhD Thesis, Department of Biotechnology, Lund University, Sweden.

- Boe K. (2006). Online monitoring and control of the biogas process. PhD Thesis, Institute of Environment & Resources, Technical University of Denmark, Lyngby, Denmark.
- Bonhotal, J. (2001). Managing manure solids. Dairy Manure Systems: Equipment and Technology. Natural Resource, Agriculture, and Engineering Service NRAES-143. Cornell University, Ithaca, New York.
- Borghesani, A. F. (1988). Non-Newtonian flow behaviour of coal-fuel oil suspensions. In: N. P. Cheremisinoff (Ed.), *Encyclopedia of Fluid Mechanics, Rheology and Non-Newtonian Flows*, 7(89). Houston, Gulf publishing company.
- Brucato, A., Ciofalo, M., Girsafi, F., Micale, G. (1998). Numerical prediction of flow fields in baffled stirred vessels: A comparison of alternative modeling approaches, *Chemical Engineering Science*, 53(21), 3653–3684.
- Brucato, A., Ciofalo, M., Girsafi, F., Tocco, R. (2000). On the simulation of stirred digester reactors via computational fluid dynamics, *Chemical Engineering Science*, 55, 291–302.
- Bugay, S., Escudié, R., Liné, A. (2002). Experimental analysis of hydrodynamics in axially agitated digester, *A.I.Ch.E. Journal*, 48(3), 463–475.
- Bujalski, J.M., Jaworski, Z., Bujalski, W., Nienow, A.W. (2002(b)). The influence of the addition of position of a tracer on CFD simulated mixing times in a vessel agitated by a Rushton turbine, *Chemical Engineering Research and Design*, 80(A), 824–831.
- Bujalski, W., Jaworski, Z., Nienow, A.W. (2002(a)). CFD study of homogenization with dual Rushton turbines – comparison with experimental results, Part II: The multiple reference frames, *Chemical Engineering Research and Design*, 80(A), 97–104.
- Bujalski, W., Nienow, A.W., Chatwin, S., Cooke, M. (1986). The dependency of scale and material thickness of power numbers of different impellers, *International Conference on Mechanical Agitation*, 1, 37-42.
- Bujalski, W., Nienow, A.W., Chatwin, S., Cooke, M. (1987). The dependency on scale of power numbers of Rushton disc turbines, *Chemical Engineering Science*, 42(2), 317–326.
- Burke D.A. (2001). Dairy waste anaerobic digestion handbook. Options for recovering beneficial products from dairy manure. Environmental Energy Company, Olympia, WA, USA.
- Campola, M., Sbrizzai, F., Soldati, A. (2003). Time-dependent flow structures and lagrangian mixing in a Rushton-impeller baffled-digester reactor, *Chemical Engineering Science*, 58, 1615–1629.

- Carreau, P.J. (1972). Rheological equations from molecular network theories. *Trans. Soc. Rheol.*, 16, 99–127.
- Casey, T.J., (1986). Requirements and methods for mixing in ADs. Anaerobic digestion of sewage sludge and organic agricultural wastes, 90–103.
- Chaouuki, J., Larachi, F., Dudukovic, M.P. (Eds) (1997). Non-invasive monitoring of multiphase flows, *Elsevier, Amsterdam*.
- Chen, T.; Chynoweth, D.P.; Biljetina, R., (1990). Anaerobic digestion of municipal solid waste in a non-mixed solids concentrating digester. *Appl. Biochem. Biotechnol.* 24/25, 533–544.
- Chhabra, R.P. & Richardson, J.F. (1999). Non-Newtonian flow in the process industries: Fundamentals and engineering applications. Butterworth Heinemann.
- Chung, K.H.K., Barigou, M., Simmons, M.J.H. (2007) Reconstruction of 3-D flow field inside miniature stirred vessels using a 2-D PIV technique, *Chemical Engineering Research and Design*, 85(5), 560–567.
- Cicek N., Lambert S., Venema H.D., Snelgrove K.R., Bibeau E.L. and R. Grosshans (2006). Nutrient removal and bio-energy production from Netley-Libau Marsh at Lake Winnipeg through annual biomass harvesting, *Biomass and Bioenergy*, 30(6), 529–536.
- Ciofalo, M., Brucato, A., Grisafi, F., Torraca, N. (1996). Turbulent flow in closed and free-surface unbaffled digesters stirred by radial impellers, *Chemical Engineering Science*, 51(14), 3557–3573.
- Conklin A.S., Chapman T., Zahller J.D., Stensel H.D. and Ferguson J.F. (2008). Monitoring the role of aceticlasts in anaerobic digestion: Activity and capacity. *Water Research*, 42(20), 4895–4904.
- Couerbe, G., Fletcher, D.F., Xuereb, C., Poux, M. (2008). Impact of thixotropy on flow patterns induced in a stirred digester: Numerical and experimental studies, *Chemical Engineering Research and Design*, 86, 545–553.
- Dague, R.R.; McKinney, R.E.; Pfeffer, J.T. (1970). Solids retention in anaerobic waste treatment systems. *J. Water Pollut. Control Fed.* 42 Part 2, R29–R46.
- Derksen, J. (2001). Assessment of large eddy simulations for agitated flows, *Chemical Engineering Research and Design*, 79(A), 824–830.

- Derksen, J., van den Akker, H.E.A. (1999). Large Eddy simulations on the flow driven by a Rushton turbine, *A.I.Ch.E. Journal*, 45(2), 209–221.
- Diaz L. and Trezek G. (1977) Biogasification of a selected fraction of municipal solid wastes. *Compost Sci.* 8–13.
- Dolfing, J., and Harrison, B. K. (1992). Gibbs free energy of formation of halogenated aromatic compounds and their potential role as electron acceptors in anaerobic environments. *Environ. Sci. Technol.* 26, 2213–2218.
- Ducoste, J.J., Clark, M.M. (1999). Turbulence in flocculators: Comparison of measurements and CFD simulations, *A.I.Ch.E. Journal*, 45(2), 432–436.
- Edwards, M.F., Godfrey, J.C., Kashani, M.M. (1976). Power requirement for the mixing of thixotropic liquids, *Journal of Non-Newtonian Fluid Mechanics*, 1, 309–322.
- Eggels, J.G. (1996). Direct and large-eddy simulations of turbulent flow using the lattice-Boltzmann scheme, *International Journal of Heat and Fluid Flow*, 17, 307–323.
- Ein-Mozaffari, F., Bennington, C.P.J., Dumont, G.A., Buckingham, D. (2007). Measuring flow velocity in pulp suspension mixing using ultrasonic Doppler velocimetry, *Chemical Engineering Research and Design*, 85(A5), 591–597.
- Elson, T. P. (1990). The growth of caverns formed around rotating impellers during the mixing of a yield stress fluid, *Chem. Eng. Communication.*, 96, 303–319.
- Elson, T. P. (1998). Mixing of fluids possessing a yield stress, Proc. 6' European Conference on Mixing, 485–492, Pavia, Italy, BHRA, 24 - 26 May 1988.
- Elson, T.P. (1990). The growth of caverns formed around rotating impellers during the mixing of a yield stress fluid, *Chemical Engineering Communication*, 96, 303–319.
- Elson, T.P., Cheesman, D.J. (1986). X-ray studies of cavern sizes and mixing performance with fluids possessing a yield stress, *Chemical Engineering Science*, 41(10), 2555–2562.
- Environment Canada. (2001). Technical Bulletins on Landfill-Gas-to-Energy from the National Office of Pollution Prevention, Ottawa, Ontario, Canada.
- EPA (2005). Anaerobic Digestion: Benefits for Waste Management, Agriculture, Energy, and the Environment. Discussion Paper. Environmental Protection Agency of Ireland, Wexford, Ireland.

- Escudié, R., Bouyer, D., Liné, A. (2004). Characterization of trailing vortices generated by a Rushton turbine, *A.I.Ch.E., Journal*, 50(1), 75–86.
- Escudié, R., Liné, A. (2003). Experimental analysis of hydrodynamics in a radially agitated digester, *A.I.Ch.E. Journal*, 49(3), 585–603.
- Escudié, R., Liné, A. (2006). Analysis of turbulence anisotropy in a mixing digester, *Chemical Engineering Science*, 61(9), 2771–2779.
- Fairhurst, P.G., Barigou, M., Fryer, P.J., Pain, J-P., Parker, D.J. (2001). Using positron emission particle tracking (PEPT) to study nearly neutrally buoyant particles in high solid fraction pipe flow, *International Journal of Multiphase Flow*, 27, 1881–1901.
- Fangary, Y.S., Barigou, M., Seville, J.P.K., Parker, D.J. (2000). Fluid trajectories in a stirred vessel of non-Newtonian liquid using positron particle tracking, *Chemical Engineering Science*, 55, 5969–5979.
- Fawcett, N. J. S. (1989). The mean flow in the discharge of pitched blade turbines, FMP Interim Report 1046, October 1989.
- Fountain, G.O., Khakhar, D.V., Mezic, I., Ottino, J.M. (2000). Chaotic mixing in a bounded three-dimensional flow, *Journal of Fluid Mechanics*, 417, 265–301.
- Gabriele, A., Nienow, A.W., Simmons, M.J.H. (2009). Use of angle resolved PIV to estimate local specific energy dissipation rates for up- and down-pumping pitched blade agitators in a stirred digester, *Chemical Engineering Science*, 64(1), 126–143.
- Gaden D. (2013). Anaerobic Digestion Model with Multi-Dimensional Architecture (ADM-MDA), PhD Dissertation, Faculty of Mechanical Engineering, University of Manitoba, Winnipeg, Manitoba.
- Galletti, C., Paglianti, A., Yianneskis, M. (2005). Observations on the significance of instabilities turbulence and intermittent motions on the fluid mixing processes in stirred reactors, *Chemical Engineering Science*, 60, 2317–2331.
- Grady C. P. L., Daigger G. T. and Lim H. C. (1999). Biological Wastewater Treatment. 2nd Edition, Marcel Dekker Inc., New York.
- Grisky, R.G., Green, R.G. (1971). Flow of dilatant (shear thickening) fluids, *A.I.Ch.E. Journal*, 17(3), 725–728.
- Guha, D., Ramachandran, P.A., Dudukovic, M.P., Derksen, J.J. (2008). Evaluation of large eddy simulation and euler-euler CFD models for solids flow dynamics in a stirred digester reactor, *AICHE Journal*, 54(3), 766–778.

- Guida, A., Fan, X., Parker, D.J., Niewnow, A.W., Barigou, M. (2009). Positron emission particle tracking in a mechanically agitated solid-liquid suspension of coarse particles, *Chemical Engineering Research and Design*, 87, 421–429.
- Guillard, F., Trägårdh, C., Fuchs, L. (2000). A study of turbulent mixing in a turbine agitated digester using a fluorescence technique, *Experiments in Fluids*, 28, 225–235.
- Gujer W. and Zehnder A. J. B. (1983). Conversion processes in anaerobic digestion. *Water Science and Technology*, 15 (127–167).
- Gunkel, A.A., Weber, M.E. (1975). Flow phenomena in stirred digesters, Part I. The impeller stream, *A.I.Ch.E. Journal*, 21(5), 931–948.
- Hall, J.F., Barigou, M., Simmons, M.J.H., Stitt, E.H. (2005). Comparative study of different mixing strategies in small high throughput experimentation reactors, *Chemical Engineering Science*, 60, 2355–2368.
- Harper, J.C. and El Sahrighi, A.F. (1965). Viscometric behaviour of tomato concentrates. *J. Food Sci.* 30(3), 470.G.
- Hartmann, H., Derksen, J.J., Montavon, C., Pearson, J., Hamill, I.S., van den Akker, H.E.A. (2004(b)). Assessment of large eddy and RANS stirred simulations by means of LDA, *Chemical Engineering Science*, 59, 2419–2432.
- Hartmann, H., Derksen, J.J., van den Akker, H.E.A. (2004(a)). Macroinstability uncovered in a Rushton turbine stirred digester by means of LES, *A.I.Ch.E. Journal*, 50(10), 2383–2393.
- Harvey III, A.D., Lee, C.K., Rogers, S.E. (1995). Steady-state modeling and experimental measurement of a baffled impeller stirred digester, *A.I.Ch.E. Journal*, 41(10), 2178–2186.
- Harvey III, A.D., West, D.H., Tuffillaro, N.B. (2000). Evaluation of laminar mixing in stirred digesters using a discrete-time particle-mapping procedure, *Chemical Engineering Science*, 55, 667–684.
- Hashimoto, A.G. (1982). Effect of mixing duration and vacuum on methane production rate from beef cattle waste *Biotechnol. Bioeng.*, 24 , 9–23.
- Haynes J, Naidu R. (1998). Influence of lime, fertilizer and manure applications on soil organic matter content and soil physical conditions: a review, *Nutrient Cycling in Agroecosystems*, 51, 123–137.

- Havas, G., Sawinsky, J., Dedk, A., & Fekete, A. (1978 (b)). Investigation of the homogenization efficiency of various propeller agitators types, *Period. Polytech*, 22, 331 – 343.
- Hickman, A. D. (1985). Agitation, mixing and mass transfer in simulated high viscosity fermentation broths, PhD Thesis, University of Birmingham.
- Ho, C.C.; Tan, Y.K. (1985). Anaerobic treatment of palm oil mill effluent by digester digesters. *J. Chem. Tech. Biotechnol.* 35B, 155–164.
- Hobbs, D.M., Muzzio, F.J. (1997). The Kenics static mixer: a three-dimensional chaotic flow, *Chemical Engineering Journal*, 67, 153–166.
- Holden, P.J., Wang, M., Mann, R., Dickin, F.J., Edwards, R.B. (1998). Imaging stirred vessels macromixing using electrical resistance tomography, *A.I.Ch.E. Journal*, 44(4), 780-790.
- Holdsworth, S.D. (1993). Rheological models used for the prediction of the flow properties of food products: a literature review, *Trans IChemE*, 71, Part C, 139–179.
- Hoogendoorn, C. J. & Den Hartog, A. P. (1967). Model studies on mixers in the viscous flow region, *Chem. Eng. Sci.*, 22, 1689–1699,
- Hui, L.K., Bennington, C.P.J., Dumont, G.A. (2009). Cavern formation in pulp suspensions using side-entering axial-flow impellers, *Chemical Engineering Science*, 64, 509–519.
- Hutchings, B.J., Weetman, R.J., Patel, B.R. (1989). Computation of flow fields in mixing digesters with experimental verification, *A.S.M.E. Winter Annual Meeting*.
- IEA Bioenergy Task 37. (2011). Country Reports of Member Countries, Istanbul, April 2011. International Energy Agency. Accessed January 23, 2014.
- IEA Bioenergy. (2012). Biogas Production and Utilisation. International Energy Agency. May 2012. Accessed January 15, 2014.
- IPCC (2007a). Summary for Policymakers. Climate Change 2007: Mitigation. Fourth Assessment Report of the Intergovernmental Panel on Climate Change Panel Cambridge University Press, Cambridge, UK and New York, USA.
- IPCC (2007b). Changes in Atmospheric Constituents and in Radiative Forcing. In: Climate Change 2007: The Physical Science Basis. Contribution of Working Group I to the Fourth Assessment Report of the Intergovernmental Panel on Climate Change.

- IPCC (2007c). Summary for Policymakers. Climate Change 2007: The Physical Science Basis. Fourth Assessment Report of the Intergovernmental Panel on Climate Change. Cambridge University Press, Cambridge, UK and New York, USA.
- Ivanova, V. P. (2000). Theoretical and experimental study of protein-lipid interactions. PhD thesis. University of Göttingen, Göttingen, Germany.
- James, S.; Wiles, C.; Swartzbaugh, J.; Smith, R. (1980). Mixing in large-scale municipal solid waste-sewage sludge ADs. *Biotechnology and Bioengineering Symposium*, 10, 259–272.
- Jaworski, Z., Bujalski, W., Otomo, N., Nienow, A.W. (2000). CFD study of homogenization with dual Rushton turbines – Comparison with experimental results, Part I: Initial studies, *Chemical Engineering Research and Design*, 78(A), 327–333.
- Jaworski, Z., Wyszynski, M.L., Moore, I.P.T., Nienow, A.W. (1997). Sliding mesh computational fluid dynamics – a predictive tool in stirred digester design, *Proceedings Institution of Mechanical Engineers, Part E, Journal of Process Mechanical Engineering*, 211(3), 149–156.
- Jayanti, S. (2001). Hydrodynamics of jet mixing in vessels, *Chemical Engineering Science*, 56, 193–210.
- Jomha, A.I., Edwards, M.F., Woodcock, L.V. (1990). New method for predicting the power requirement for mixing shear thickening suspensions, *Chemical Engineering Science*, 45(2), 1389–1396.
- Jones, R.M., Harvey III, A.D., Acharya, S. (2001). Two-equation turbulence modeling for impeller stirred digesters, *Journal of Fluids Engineering*, 123(3), 640–648.
- Kaparaju P, Serrano M, Thomsen AB, Kongjan P, Angelidaki I. (2009). Bioethanol, biohydrogen and biogas production from wheat straw in a biorefinery concept. *Bioresource Technology* 100: 2562–2568
- Kelly, W., Gigas, B. (2003). Using CFD to predict the behaviour of power law fluids near axial-flow impellers operating in the transitional regime, *Chemical Engineering Science*, 58, 2151–2152.
- Khang, S. J. & Fitzgerald, T. J. (1975). A new probe and circuit for measuring electrolyte conductivity, *Ind. Eng. Chem. Fund.*, 14, 208 – 213.
- Khang, S. J. (1975). New scale-up and design criteria of stirrer agitated batch and flow mixing vessels, PhD Thesis, Oregon State University.

- Khopkar, A.R., Aubin, J., Xuereb, C., Le Sauze, N., Bertrand, J., Ranade, V.V. (2003). Gas-liquid flow generated by a pitched-blade turbine: Particle image velocimetry measurements and computational fluid dynamics simulations, *Industrial and Engineering Chemistry Research*, 42, 5318–5332.
- Kilander, J., Rasmuson, A. (2005). Energy dissipation and macro instabilities in a stirred square digester investigated using an LE PIV approach and LDA measurements, *Chemical Engineering Science*, 60(24), 6844–6856.
- Kovács, T., Troedson, M., Wormbs, G., Trägårdh, C., Östergren, K., Innings, F., Lingstrand, A., Strinning, O. (2003). Mixing of Newtonian and non-Newtonian fluids in static mixers under laminar flow conditions: Experiments and simulations, 11th Conference of Mixing, October 14-17, Bamberg, P21, 421–428.
- Kresta, S. M., and P. E. Wood (1991). “Prediction of the three-dimensional turbulent flow in stirred digesters,” *AIChE J.*, 37, 448.
- Kukura, J., Arratia, P.C., Szalai, E.S., Bittorf, K.J., Muzzio (2002). Understanding pharmaceutical flows, *Pharmaceutical Technology*, 48–72.
- Lafitte-Trouqué S, Forster CF. The use of ultrasound and γ -irradiation as pre-treatments for the anaerobic digestion of waste activated sludge at mesophilic and thermophilic temperatures. *Bioresource Technology* 2002, 84:113–118
- Lamberto, D.J., Alvarez, M.M., Muzzio, F.J. (1999). Experimental and computational investigation of the laminar flow structure in a stirred digester, *Chemical Engineering Science*, 54, 919–942.
- Lamberto, D.J., Alvarez, M.M., Muzzio, F.J. (2001). Computational analysis of regular and chaotic mixing in a stirred digester reactor, *Chemical Engineering Science*, 56, 4887–4899.
- Landau, J., Procházka, J., Václavík, V. & Fort, I. (1963). Studies on mixing XIV: homogenization of miscible liquid in the viscous region, *Coll. Czech Chem. Communication*, 28, 279–292.
- Lee C., Kim J., Hwang K., O’Flaherty V. and Hwang S. (2009). Quantitative analysis of methanogenic community dynamics in three anaerobic batch digesters treating different wastewaters, *Water Research*, 43 (1), 157–165.
- Lee, K.C., Yianneskis, M. (1994(a)). Mixing characteristics of a stirred reactor with an axial flow impeller, *I. Chem. E. Symposium Series*, 136.
- Lee, K.C., Yianneskis, M. (1994(b)). The extent of periodicity of the flow in vessels stirred by Rushton impellers, *Industrial Mixing Technology: Chemical and Biological Applications*.

- Lema J. M., Mendez R., Iza J., Garcia P. and Fernandez- Polanco F. (1991). Chemical reactor engineering concepts in design and operation of anaerobic treatment processes, *Water Sci. Technol.* 24(8), 79–86.
- Link, J.M., Deen, N.G., Kuipers, J.A.M., Fan, X., Ingram, A., Parker, D.J., Wood, J., Seville, J.P.K. (2008). PEPT and discrete particle simulation study of spout-fluid bed regimes, *AIChE Journal*, 54(5), 1189–1202.
- Liu, X., Bao, Y., Li, Z., Gao, Z., Smith, J.M. (2008). Particle image velocimetry study of turbulence characteristics in a vessel agitated by a dual Rushton impeller, *Chinese Journal of Chemical Engineering*, 16(5), 700–708.
- Lusk, P. (1998). Methane recovery from animal manures: a current opportunities casebook. 3rd Edition. NREL/SR–25145. Golden, CO: National Renewable Energy Laboratory. Work performed by Resource Development Associates, Washington, DC.
- Lyungqvist, M., Rasmuson, A. (2001). Numerical simulation of the two-phase flow in an axially stirred vessel, *Chemical Engineering Research and Design*, 79(A), 533–546.
- M'Manamey, W. J. (1980). A circulation model for batch mixing in agitated vessels, *Trans. I. Chem. E.*, 58, 271–276.
- Mackinnon, C. P. (1987). Research review: comparative mixing times, FMP Report 029, April 1987.
- Magnusson M, Alvfors P. (2012). Biogas from mechanical pulping industry: Potential improvement for increased biomass vehicle fuels. Proceedings of ECOS 2012: The 25th international conferences on efficiency, cost, optimization, simulation and environmental impact of energy systems.
- Mahmoudi, S.M.S., Yianneskis, M. (1991). The variation of flow pattern and mixing time with impeller spacing in stirred vessels with two Rushton impellers, 7th European Conference on Mixing. September 18-20, Brugge Belgium.
- Maingonnat, J.F., Muller, L., Leuliet, J.C. (2005). Modeling the build-up of a thixotropic fluid under viscosimetric and mixing conditions, *Journal of Food Engineering*, 3, 265–272.
- Mann, R., Pillai, S.K., El-Hamouz, A.M., Ying, P., Togatorop, A., Edwards, R.B. (1995). Computational fluid mixing for stirred vessels: Progress from seeing to believing, *The Chemical Engineering Journal*, 59, 39–50.
- Mavros, P., Mann, R., Vlaev, S.D., Bertrand, J. (2001). Experimental visualization and CFD simulations of flow patterns induced by a novel energy-saving dual-configuration impeller in stirred vessels, *Chemical Engineering Research and Design*, 79(A), 857–866.

- Mena, B., Manero, O. & Binding, D.M. (1979). Complex flow of viscoelastic fluids through oscillating pipes – Interesting effects and applications, *Journal of Non-Newtonian Fluid Mechanics*, 5, 427–448.
- Mersmann, A., Einkenel, W. D. & Käppel, M. (1976). Design and scale-up of mixing equipment, *Int. Chem. Eng.*, 16(4), 590–603.
- Meynell, P.J., (1976). Methane: Planning a Digester. Prism Press, London, 55–57.
- Micheletti, M., Baldi, S., Yeoh, S.L., Ducci, A., Papadakis, G., Lee, K.C., Yianneskis, M. (2004). On spatial and temporal variations and estimates of energy dissipation in stirred reactors, *Chemical Engineering Research and Design*, 82(A9), 1188–1198.
- Mills, P.J. (1979). Minimization of energy input requirements of an AD Agric. *Wastes*, 1, 57–59.
- Mishra V.P., Dyster K.N., Jaworski Z., Nienow A.W., Mckemmie J., 1998. A study of an up- and a down-pumping wide blade hydrofoil impeller: Part I. LAD measurements, *Can. J. Chem. Eng.*, 76, 577–588.
- Montante, G., Lee, K.C., Brucato, A., Yianneskis, M. (2001(a)). Numerical simulations of the dependency of flow pattern on impeller clearance in stirred vessels, *Chemical Engineering Science*, 56, 3751–3770.
- Montante, G., Lee, K.C., Brucato, A., Yianneskis, M. (2001(b)). Experiments and predictions of the transition of the flow pattern with impeller clearance in stirred digesters, *Computers and Chemical Engineering*, 25, 729–735.
- Montante, G., Magelli, F. (2004). Liquid homogenization characteristics in vessels stirred with multiple Rushton turbines mounted at different spacings, CFD study and comparison with experimental data, *Chemical Engineering Research and Design*, 82(A9), 1179–1187.
- Montante, G., Moštek, M., Jahoda, M., Magelli, F. (2005). CFD simulations and experimental validation of homogenisation curves and mixing time in stirred Newtonian and pseudoplastic liquids, *Chemical Engineering Science*, 60, 2427–2437.
- Narayan, K.S. and Ramasubramanian, V. (1982) Rheological properties of polysaccharide gums. *Indian J. Technol.*, 20, 333–333.
- Naude, I., Xuereb, C., Bertrand, J. (1998). Direct prediction of the flows induced by a propeller in an agitated vessel using and unstructured mesh, *The Canadian Journal of Chemical Engineering*, 76, 631–640.

- Nere, N.K., Patwardhan, A.W., Joshi, J.B. (2001). Prediction of flow pattern in stirred digesters: New constitutive equation for eddy viscosity, *Industrial and Engineering Chemistry Research*, 40, 1755–1772.
- Nienow, A.W. (1997). On impeller circulation and mixing effectiveness in the turbulent flow regime, *Chemical Engineering Science*, 52(15), 2557–2565.
- Nienow, A.W., Elson, T.P. (1988). Aspects of Mixing in Rheologically Complex Fluids, *Chemical Engineering Research and Design*, 66, 5–15.
- Nikiforaki, L., Montante, G., Lee, K.C., Yianneskis, M. (2003). On the origin, frequency and magnitude of macro-instabilities of the flows in stirred vessels, *Chemical Engineering Science*, 58, 2937–2949.
- Nishikawa, M., Okamoto, Y., Hashimoto, K., Nagata, S. (1976). Turbulence energy spectra in baffled mixing vessels, *Journal of Chemical Engineering of Japan*, 9(6), 489–493.
- Norwood, K.W., Metzner, A.B. (1960). Flow patterns and mixing rates in agitated vessels, *A.I.Ch.E. Journal*, 6(3), 432–437.
- Nouri, J.M., Whitelaw, J.H., Yianneskis, M. (1987). The scaling of the flow field with impeller size and rotational speed in a stirred reactor, 2nd International Conference on Laser Anemometry – Advances and Applications, 489–500.
- OMAF (Ontario Ministry of Agriculture and Food), (2000). Agricultural Pollution Control Manual, Ontario Government, Guelph, Ontario, March 2000.
- Osman, J.J., Varley, J. (1999). The use of computational fluid dynamics (CFD) to estimate mixing times in a stirred digester, *I.Chem.E. Symposium Series*, 146, 15–22.
- Pakzad, L., Ein-Mozaffari, F., Chan, P. (2008(a)). Using computational fluid dynamics modelling to study the mixing of pseudoplastic fluids with a Scaba 6SRGT impeller, *Chemical Engineering and Processing*, 47, 2218–2227.
- Pakzad, L., Ein-Mozaffari, F., Chan, P. (2008(b)). Using electrical resistance tomography and computational fluid dynamics modeling to study the formation of cavern in the mixing of pseudoplastic fluids possessing yield stress, *Chemical Engineering Science*, 63, 2508–2522.
- Parkin, G.F.; Owen, W.F. (1986). Fundamentals of anaerobic digestion of wastewater sludges, *J. Env. Engg.*, 112(5), 867–921.
- Parkin, S. P. (ed.) McGraw-Hill (1984). Dictionary of Scientific and Technical Terms, 3rd edition, McGraw-Hill Book Company, New York.

- Patwardhan, A.W. (2001). Prediction of residence time distribution of stirred reactors, *Industrial and Engineering Chemistry Research*, 40, 5686–5695.
- Pavlostathis S. G. and Giraldo-Gomez E. (1991). Kinetics of anaerobic treatment: a critical review, *Critical Reviews in Environmental Control*, 21 (5,6), 411–490.
- Pettersson, M., Rasmuson, A.C. (1998). Hydrodynamics of suspensions agitated by pitched-blade turbine, *A.I.Ch.E. Journal*, 44(3), 513–527.
- Pirog, Robert L. (2005). World oil demand and its effect on oil prices, *Congressional Research Service*, 9 June 2005.
- Procházka, J., Landau, J. (1961). Studies on mixing. XII. Homogenation of miscible liquids in the turbulent region, *Collection of Czechoslov Chemical Communications*, 26, 2961–2973.
- Raghav Rao, K.S.M.S., Joshi, J.B. (1988). Liquid phase mixing in mechanically agitated vessels, *Chemical Engineering Communications*, 74, 1–25.
- Rammohan, A.R., Kemoun, A., Al-Dahhan, M.H., Dudukovic, M.P. (2001). A lagrangian description of flows in stirred digesters via computer-automated radioactive particle tracking (CARPT), *Chemical Engineering Science*, 56, 2629–2639.
- Ranade, V.V. (1997). An efficient computational model for simulating flow in stirred vessels: a case of Rushton turbine, *Chemical Engineering Science*, 52(24), 4473–4484.
- Ranade, V.V., Bourne, J.R., Joshi, J.B. (1991). Fluid mechanics and blending in agitated digester, *Chemical Engineering Science*, 46(8), 1883–1893.
- Ranade, V.V., Dommeti, S.M.S. (1996). Computational snapshot of flow generated by axial impellers in baffled stirred vessels, *Chemical Engineering Research and Design*, 74(A), 476–484.
- Ranade, V.V., Joshi, J.B. (1989(a)). Flow Generated by pitched blade turbines I: Measurements using laser Doppler anemometer, *Chemical Engineering Communication*, 81, 197–224.
- Ranade, V.V., Joshi, J.B. (1989(b)). Flow Generated by pitched blade turbines II: Simulation using *k*-model, *Chemical Engineering Communication*, 81, 225–248.
- Rao, M.A. and Kenny, J.F. Flow properties of selected food gums (1975). *Can. Inst. Food Sci. Technol.* 8(3), 142–142.

- Reilly, C.D., Britter, R.E. (1985). Mixing times for passive tracers in stirred digesters, 5th *European Conference on Mixing*. Würzburg, Germany. BHRA Fluid Engineering Centre (Cranfield, Bedford), 365–375.
- Revstedt, J., Fuchs, L. (2002). Research news, large eddy simulation of flow in stirred vessels, *Chemical Engineering and Technology*, 25, 443–446.
- Revstedt, J., Fuchs, L., Kovács, T., Trägårdh, C. (2000). Influence of impeller type on the flow structure in a stirred reactor, *A.I.Ch.E. Journal*, 46(12), 2373–2382.
- Revstedt, J., Fuchs, L., Trägårdh, C. (1998). Large eddy simulations of the turbulent flow in a stirred reactor, *Chemical Engineering Science*, 53(24), 4041–4053.
- Rulkens, Wim H., Houten, van R.T., Futselaar H., Temmink H., Bruning, H., Grolle, K., Bisselink, R. and Brouwer H. (2005). Innovative Concept for Sustainable Treatment of Municipal Wastewater, Wastewater Reclamation and Reuse for Sustainability, Jeju Do, Korea.
- Rushton, J.H., Costich, E.W., Everett, H.J. (1950). Power characteristics of mixing impellers Part I and Part II, *Chemical Engineering Progress*, 46(8), 395–404.
- Ruszkowski, S. (1985(a)). The FMP method for measuring mixing times, FMP Report 008, February 1985 (a).
- Ruszkowski, S. (1985(b)). A comparison of mixing time and mixing efficiencies for a range of impellers in a 0.61 m diameter vessel, FMP Report 009, October 1985(b).
- Ruszkowski, S.W., Muskett, M.J. (1985). Comparative mixing times for stirred digester agitators, 5th *European Conference on Mixing*. Würzburg, Germany. BHRA Fluid Engineering Centre (Cranfield, Bedford), 89–103.
- Sahu, A.K., Joshi, J.B. (1995). Simulation of flow in stirred vessels with axial flow impellers: effects of various numerical schemes and turbulence model parameters, *Industrial and Engineering Chemistry Research*, 34, 626–639.
- Sahu, A.K., Kumar, P., Patwardhan, A.W., Joshi, J.B. (1999). CFD modelling and mixing in stirred digesters, *Chemical Engineering Science*, 54, 2285–2293.
- Sano, Y., Usui, H. (1985). Interrelations among mixing time, power number and discharge flow rate number in baffled mixing vessels, *Journal of Chemical Engineering of Japan*, 18(1), 47–52.
- Sawyer, C.N.; Grumbling, A.M. (1960). Fundamental consideration in high-rate digestion, *Inc. Sew. Eng. Div. ASCE*, 86–92.
- Schäfer, M., Yianneskis, M., Wächter, P., Durst, F. (1998). Trailing vortices around a 45° pitched-blade impeller, *A.I.Ch.E. Journal*, 44(6), 1233–1246.

- Schink B. (1997). Energetics of syntrophic cooperation in methanogenic degradation, *Microbiology and Molecular Biology Reviews*, 61 (2), 262–280.
- Schofield, D.F. (1994). An Application of CFD to inert and reactive tracer mixing in a batch stirred vessel, *A. I. Ch.E. Symposium Series*, 299, 19–32.
- Schwartzberg, H. G. & Treybal, R. E. (1968). Fluid and particle motion in turbulent stirred digesters: fluid motion, *Ind. Eng. Chem. Fund.*, 7(1), 1–6.
- Semmler, N. (2002). Modern Biogas Technology: Environmentally sound & energy efficient advanced technology for organic waste management, Renewable Energy Technologies Inc., Trenton, Ontario, Canada, March 17, 2002.
- Shamlou, P. A. & Edwards, M. F. (1985). Power consumption of helical ribbon mixers in viscous Newtonian and non-Newtonian fluids, *Chem. Eng. Sci.*, 40(9), 1773–1781.
- Sheng, J., Meng, H., Fox, R.O. (1998). Validation of CFD simulations of a stirred digester using particle image velocimetry data, *The Canadian Journal of Chemical*, 76(3), 611–625.
- Sheng, J., Meng, H., Fox., R.O. (2000). A large eddy PIV method for turbulence dissipation rate estimation, *Chemical Engineering Science*, 55, 4423–4434.
- Sherman, P. (1975). Factors influencing the instrumental and sensory evaluation of food emulsions. Theory, Determination and Control of Physical Properties of Food Materials, page 251, (Ed.) Rha, C.K. D. Reidel Publishing Co., Boston, MA.
- Shiue, S. J. & Wong, C. W. (1984). Studies in homogenization efficiency of various agitators in liquid blending, *Can. J. Chem. Eng.*, 62, 602–609.
- Shook, C.A. & Roco, M.C. (1991). Slurry flow: principles and practice. Butterworth-Heinemann.
- Smith, L.C.; Elliot, D.J.; James, A. (1996). Mixing in upflow anaerobic filters and its influence on performance and scale-up, *Water Research*, 30(12), 3061.
- Solomon, J. (1984). Mixing, aeration and rheology of highly viscous fluids, PhD Thesis, University College London.
- Solomon, J., Elson, T.P., Nienow, A.W. (1981). Cavern sizes in agitated fluids with a yield stress, *Chemical Engineering Communications*, 11, 143–164.
- Stenstrom M., Ng A., Bhunia P. and Abramson S. (1983). Anaerobic digestion of municipal solid waste, *J. Environ. Eng.* 109, 1148–1158.

- Stroot, P.G.; McMohan, K.D.; Mackie, R.I.; Raskin, L. (2001). Anaerobic codigestion of municipal solid waste and biosolids under various mixing conditions—I. Digester performance, *Water Res.* 67(3), 294–301.
- Sun, H., Wang, W., Mao, Z. (2002). Numerical simulation of the whole three dimensional flow in a stirred digester with anisotropic algebraic stress model, *Chinese Journal of Chemical Engineering*, 10(1), 15–24.
- Szalai, E.S., Arratia, P., Johnson, K., Muzzio, F.J. (2004). Mixing analysis in a digester stirred with Ekato Intermig® impellers, *Chemical Engineering Science*, 59, 3793–3805.
- The Agstar Program. (2010). U.S. Farm Anaerobic Digestion Systems: A 2010 Snapshot. U.S. EPA. U.S. EPA. Accessed June 2, 2013.
- Van 't Riet, K., Smith, J.M. (1975). The trailing vortex system produced by Rushton turbine agitators, *Chemical Engineering Science*, 30, 1093–1105.
- Van Die, P. (1987). An Assessment of Agriculture Canada's Anaerobic Digestion Program, Engineering and Statistical Research Branch, Agriculture Canada Research Branch, 1–933.
- Vavilin V.A., Lokshina L.Y., Rytov S.V., Kotsyurbenko O. R., Nozhevnikova A.N. and N.P.S. (1997). Modelling methanogenesis during anaerobic conversion of complex organic matter at low temperatures. *Water Science and Technology*, 36 (6-7), 531–538.
- Vavilin V. A., Rytov S. V. and Lokshina L. Y. (1996). A description of hydrolysis kinetics in anaerobic degradation of particulate organic matter. *Bioresource Technology*, 56(2-3), 229–237.
- Verzicco, R., Iaccarino, G., Fatica, M., Orlandi, P. (2000). Flow in an impeller stirred digester using an immersed boundary method, *Center for Turbulence Research. Annual Research Briefs*, 251–261.
- Weetman, R.J., Oldshue, J.Y. (1988). Power, flow and shear characteristics of mixing impellers, *6th European Conference on Mixing*. May 24-26. Pavia, Italy.
- Wenersson, E.S., Trägårdh, C. (1998). Scaling of turbulence characteristics in a turbine agitated digester in relation to agitation rate, *Chemical Engineering Journal*, 70, 37–45.
- Whitmore T. N., Lloyd D., Jones G. and Williams T. N. (1987). Hydrogen-dependent control of the continuous anaerobic digestion process, *Appl. Microbiol. Biotechnol.*, 26, 383–388.
- Wichterle, K., Zak, L. & Mitschka, P. (1985). Shear stresses on the walls of agitated vessels, *Chem. Eng. Commun.*, 32, 289–305.

- Wilkins, R.J., Miller, J.D., Plummer, J.R., Dietz, D.C., Myers, K.J. (2005). New techniques for measuring and modelling cavern dimensions in a Bingham plastic fluid, *Chemical Engineering Science*, 60, 5269–5275.
- Wilkie, A.C., *et al.* (1995). Anaerobic digestion for odor control. Nuisance Concerns in Animal Manure Management: Odors and Flies. H.H. Van Horn, ed. Gainesville, FL: Florida Cooperative Extension, University of Florida, 56–62.
- Wittmer, S., Falk, L., Pitiot, P., Vivier, H. (1998). Characterisation of stirred vessel hydrodynamics by three dimensional trajectography, *The Canadian Journal of Chemical Engineering*, 76, 600–609.
- Wong, C. W. & Huang, C. T. (1988). Flow characteristics and mechanical efficiency in baffled stirred digesters with turbine impellers, Proc. 6th Euro. Conf. on Mixing, 29–34, Pavia, Italy, BHRA, 24–26 May 1988.
- Wu, H., Patterson, G.K. (1989). Laser-doppler measurements of turbulent-flow parameters in a stirred mixer, *Chemical Engineering Science*, 44(10), 2207–2221.
- Xu, Y., McGrath, G. (1996). CFD predictions of stirred digester flows, *Chemical Engineering Research and Design*, 74(A), 471–475.
- Yeoh, S.L., Papadakis, G., Lee, K.C., Yianneskis, M. (2004(b)). Large eddy simulation of turbulent flow in a Rushton impeller stirred reactor with sliding-deforming mesh methodology, *Chemical Engineering and Technology*, 27(3), 257–263.
- Yeoh, S.L., Papadakis, G., Yianneskis, M. (2004(a)). Numerical simulation of turbulent flow characteristics in a stirred vessel using the LES and RANS approaches with the sliding/deforming mesh methodology, *Chemical Engineering Research and Design*, 82(A7), 834–848.
- Yeoh, S.L., Papadakis, G., Yianneskis, M. (2005). Determination of mixing time and degree of homogeneity in stirred vessels with large eddy simulation, *Chemical Engineering Science*, 60, 2293–2302.
- Yianneskis, M. (1991). The effect of flow rate and tracer insertion time on mixing times in jet-agitated vessels, *7th European Conference on Mixing*. September 18-20, Brugge Belgium.
- Yianneskis, M., Popiolek, Z., Whitelaw, J.H. (1987). An experimental study of the steady and unsteady flow characteristics of stirred reactors, *Journal of Fluid Mechanics*, 175, 537–555.
- Yianneskis, M., Whitelaw, J.H. (1993). On the structure of the trailing vortices around Rushton turbine blades, *Chemical Engineering Research and Design*, 71(A), 543–550.

- Yoon, H.S., Balachandar, S., Ha, M.Y., Kar. K. (2003). Large eddy simulation of flow in a stirred digester, *Transactions of the A.S.M.E.*, 125, 486–499.
- Yu L, Wensel P, Ma J, Chen S. (2013). Multiphase modeling of settling and suspension in anaerobic digester. *Journal of Bioremed Biodegradation* 111: 28–39.
- Zalc, J.M., Szalai, E.S., Alvarez, M.M., Muzzio, F.J. (2002). Using CFD to understand chaotic mixing in laminar stirred digesters, *A.I.Ch.E. Journal*, 48(10), 2124-2134.
- Zemg, L.C. and Deng, X.Y. (2000). Singular nonlinear boundary value problem arising in the theory of viscous fluids, *Acta Math. Sci.*, 20(S), 577–582.
- Zhou, G., Kresta, S. (1996(a)). Impact of digester geometry on the maximum turbulence energy dissipation rate for impellers, *A.I.Ch.E., Journal*, 42(9), 2476–2490.
- Zhou, G., Kresta, S. (1996(b)). Distribution of energy between convective and turbulent flow for three frequently used impellers, *Chemical Engineering Research and Design*, 74(A), 379–389.
- Zipp, R.P., Patterson, G.K. (1998). Experimental measurements and simulation of mixing and chemical reaction in a stirred digester, *Canadian Journal Chemical Engineering*, 76, 657–669.

Appendix A. Literature review on microbial aspects of anaerobic digestion process

Digestion of particulate composites goes through four phases, termed hydrolysis/liquefaction, acidogenesis, acetogenesis and methanogenesis. These phases are a series of interlinked reactions proceeding spatially as well as temporally in consecutive and parallel steps and hence, influence one another. Hydrolysis is a process where complex macromolecular organic matter comprising carbohydrates, proteins and fats go through enzymatic degradation and transform to monosaccharides, amino acids and long chain fatty acids (LCFA) (Batstone et al., 2002b). Further, anaerobic digestion leads from acidogenesis, acetogenesis and methanogenesis via intermediates and by-products to biogas production composed mainly of CH₄, and CO₂. Understanding each phase is required to elucidate the impact of improper mixing conditions on the performance of anaerobic digestion.

Hydrolysis

Microorganisms require complex organic polymeric materials that are broken down to soluble compounds. Anaerobic degradation starts with the hydrolysis stage where organic polymers solubilise into simpler and more soluble intermediates that can pass the cell membrane (Pavlostathis and Giraldo-Gomez, 1991). Once inside the cell, these simple molecules provide energy and synthesize cellular components. This phase is also termed as liquefaction since the degradation process involves the dissociation of water.

Extracellular enzymes secreted by bacteria allow anaerobes (Batstone et al., 2002b) propel hydrolytic reactions, which comprises of two phases. In the first phase, a bacterial

colonization takes place where the hydrolytic bacteria cover the surface of solids. Hydrolytic bacteria and other bacteria use monomers produced by the release of enzymes on the particle surface. In the second phase, bacteria degrade the particle surface at a constant depth per unit of time (Vavilin et al., 1996). Released enzymes such as cellulase, cellobiase, xylanase and amylase degrade carbohydrates into simple sugars (monosaccharides), protease degrades protein into amino acids and lipase degrades lipids into glycerol and LCFA (Pavlostathis and Giraldo- Gomez, 1991).

The overall hydrolysis rate depends on organic material size, shape, surface area, biomass concentration, enzyme production and adsorption (Parawira et al., 2005; Grady et al., 1999; Boe, 2006). Hydrolysis is the rate-limiting step for digestion when the substrate is in particulate form (e.g. swine waste, cattle manure and sewage sludge). In a digestion process using degradable substrate, methanogenesis is the rate-limiting step (Vavilin et al., 1997).

Acidogenesis

The step subsequent to hydrolysis is acidogenesis (also termed fermentation). It is an anaerobic acid-producing microbial process without an additional electron acceptor or donor (Gujer and Zehnder, 1983). Monosaccharides and amino acids from hydrolysis degrade to a number of simpler products such as volatile fatty acids (VFA) including propionic acid ($\text{CH}_3\text{CH}_2\text{COOH}$), butyric acid ($\text{CH}_3\text{CH}_2\text{CH}_2\text{COOH}$) and acetic acid (CH_3COOH). However, the organisms oxidizing LCFA require utilization of an external

electron acceptor such as hydrogen ions or CO₂ to produce H₂ or formate (Batstone et al., 2002a).

The degradation of monosaccharides (e.g. glucose) manifests in different pathways leading to the emergence of different products such as VFA, lactate, and ethanol with different yields of energy (Burke, 2001). The dominant pathway depends on several factors that include substrate concentration, pH and dissolved hydrogen concentrations. For example, under very high organic loads, lactic acid production becomes significant. At higher pH (> 5), the production of VFA increases, whereas at low pH (<5) ethanol production decreases. Further lowering of pH (< 4) causes all processes to cease.

However, Grady et al. (1999) reports that hydrogen partial pressure to have the most influence on the fermentation pathway. Low partial pressure of hydrogen favours the fermentation pathway to acetate and hydrogen rather than ethanol or butyrate formation (Parawira et al., 2005). Thus, in a system where the hydrogen-utilizing organisms (such as methanogens) maintain low partial pressure of hydrogen, the fermentation pathway to acetate and hydrogen contributes the main carbon flow from carbohydrates to methane formation. However, the degradation of lipids and amino acids produces continuously higher VFA and alcohols (Schink, 1997; Boe, 2006). These products degrade further in a subsequent process referred to as acetogenesis (Björnsson, 2000).

Acidogenesis is often the fastest step in an anaerobic conversion of complex organic matter in liquid phase digestions. The formation of various toxic or inhibitory

components leads to a halt of methane production and an accumulation of long and short chain fatty acids. Eventually, the influence on the methane production causes process failure in the anaerobic digestion of complex organic matter (Vavilin et al., 1996).

Acetogenesis

The degradation of higher organic acids formed in acidogenesis is an oxidation step with no internal electron acceptor. Thus, the oxidizing organisms (normally bacteria) require an additional electron acceptor such as hydrogen ions or CO₂ for the conversion to acetate, carbon dioxide and hydrogen (Batstone et al., 2002a). This intermediate conversion is crucial for the successful production of biogas, as methanogens do not directly utilize these compounds. Since acetogens are obligate hydrogen producers and at the same time depend on a low partial pressure of hydrogen, they maintain a syntrophic (mutually beneficial) relationship with hydrogen-consuming methanogenic archaea (Schink, 1997). Methanogens serve as hydrogen sink during interspecies hydrogen transfer allowing the fermentation reactions to proceed.

Figure A.1 shows that low H₂ partial pressure is essential for acetogenic reactions to be thermodynamically favorable ($\Delta G' < 0$), whereas hydrogen consuming methanogenesis becomes more favourable at higher pressures.

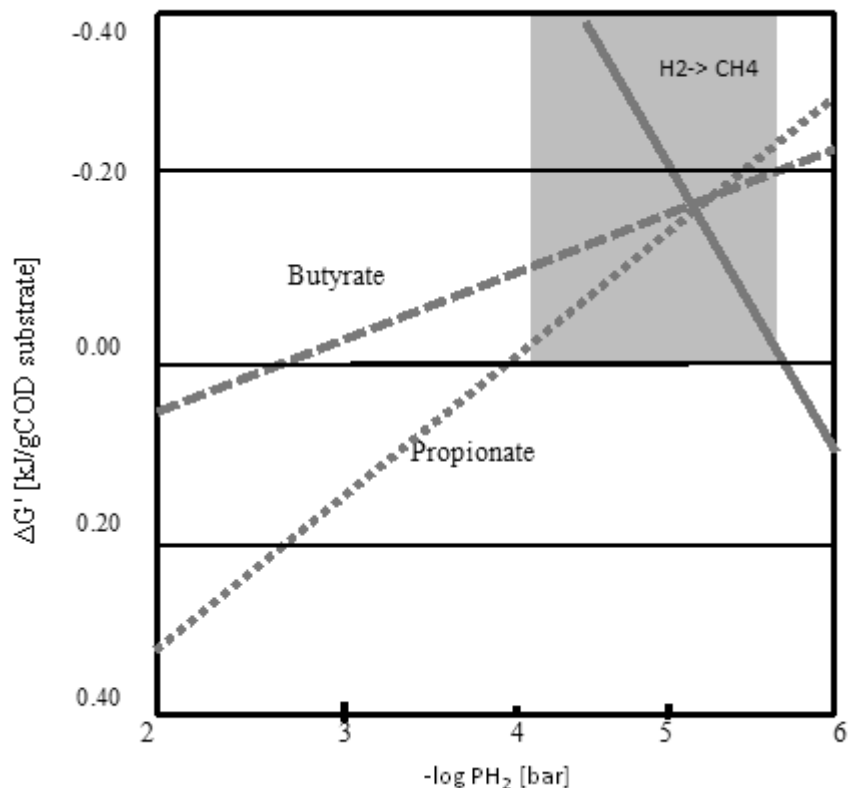


Figure A.1: Thermodynamic (Gibb's energy $\Delta G'$) dependence on H_2 partial pressure, calculations based on standard values of free energies at pH 7.0, 25°C (adapted from Batstone et al., 2002a)

Thus, these reactions can only occur simultaneously within a narrow range of very low PH (Conklin et. al, 2008). The shaded area shows the theoretical operating region for syntrophic acetogenesis from propionate.

Table A.1 shows an example of the free energy yield for the conversion of butyrate to acetate and methane. The fact that the degradation of butyrate to acetate is endergonic under standard conditions makes the reaction energetically unfeasible. Hence, it depends on co-culture with a hydrogen-scavenging partner organism (hydrogenotrophic methanogens) (Boe, 2006). The second reaction in Table A.1 provides a yield of energy, transferred partly by the methanogens back to the acetogens. Thus, the overall

syntrophic reaction is thermodynamically favourable with a small energy yield ($\Delta G' < 0$). The low energy yield makes the organisms very slow growing and sensitive to changes in organic load and flow rate. Acetogens are sensitive to environmental changes, and long periods are likely to be required for these bacteria to adjust to new environmental conditions (Björnsson, 2000).

Table A.1: Energetics of syntrophic degradation (Schink, 1997)

Reaction	$\Delta G^{\circ\prime}$ [KJ mol⁻¹]
Acetogenesis from butyric acid $2\text{CH}_3\text{CH}_2\text{CH}_2\text{COOH} + 4\text{H}_2\text{O} \rightarrow 4\text{CH}_3\text{COO}^- + 4\text{H}^+ + 4\text{H}_2$	96
Methanogenesis from hydrogen $4\text{H}_2 + \text{CO}_2 \rightarrow \text{CH}_4 + 2\text{H}_2\text{O}$	-131
Synthrophic reaction $2\text{CH}_3\text{CH}_2\text{CH}_2\text{COOH} + \text{CO}_2 + 2\text{H}_2\text{O} \rightarrow 4\text{CH}_3\text{COO}^- + 4\text{H}^+ + \text{CH}_4$	-35

Acetogenic bacteria profit not only from hydrogenotrophic methanogens, but also from acetoclastic methanogens. Acetate removal influences the energetics of VFA oxidizing reactions, especially the iso-valerate degradation that forms three molecules of acetate and only one molecule of H_2 (Schink, 1997). Moreover, acetate accumulation may have a biochemical inhibitory effect on acetogenesis (Boe, 2006).

Methanogenesis

During methanogenesis, methanogenic archaea converts the fermentation products such as acetate and H_2/CO_2 to CH_4 and CO_2 (Boe, 2006). Other methanogens are able to grow on one-carbon compounds such as formate, methanol and methylamine. Generally,

methanogens are specialists in substrate utilization, as some of them can use only one substrate.

There are two groups of archaea relevant for anaerobic digestion. One group, termed acetoclastic methanogens, split acetate into methane and carbon dioxide (Björnsson, 2000). The second group, termed hydrogenotrophic methanogens use hydrogen as the electron donor and CO₂ as the electron acceptor to produce methane (Björnsson, 2000). Nearly all known methanogenic species are able to produce methane from H₂/CO₂, whereas only a few species of methanogens are capable of utilizing acetate as a substrate.

However, estimation from stoichiometric relations shows that about 70% of the methane formed in anaerobic digesters derived via the acetate pathway (Schink, 1997). The hydrogen pathway is more energy yielding than the acetate pathway that normally not rate limiting (Klass, 1984). However, it is of fundamental importance due to its ability to keep the hydrogen pressure low in the system (Klass, 1984; Pavlostathis and Giraldo-Gomez, 1991; Björnsson, 2000).

Moreover, apart from methanogenic reactions, the inter-conversion between hydrogen and acetate also plays an important role in the methane formation pathway (Batstone et al., 2002a). Homoacetogens can either oxidize or synthesize acetate depending on the external hydrogen concentration. Table A.2 shows the H₂ consumption by hydrogenotrophic methanogenesis is thermodynamically more favourable than

homoacetogenesis ($\Delta G^{\circ} < 0$) (Giraldo-Gomez, 1991). Aceticlastic methanogenesis are also more favourable than acetate oxidation when it comes to acetate consumption. As already mentioned, hydrogenotrophic methanogenesis work better at high hydrogen partial pressure (Table A.2), while aceticlastic methanogenesis is independent from hydrogen partial pressure. At higher temperatures ($> 30^{\circ}\text{C}$), the acetate oxidation pathway becomes more favourable (Boe, 2006).

Hydrogenotrophic methanogenesis is the controlling process in the overall scheme of anaerobic digestion (Giraldo-Gomez, 1991). Its failure strongly affects the syntrophic acetogenic and causes accumulation of reduced fermentation products in anaerobic digester (Schink, 1997).

Table A.2: Reactions related to methanogenesis with standard temperatures (Boe, 2006)

Reaction		ΔG° [KJ mol ⁻¹]
Hydrogenotrophic methanogenesis	$4\text{H}_2 + \text{CO}_2 \rightarrow \text{CH}_4 + 2\text{H}_2\text{O}$	-135.0
Aceticlastic methanogenesis	$\text{CH}_3\text{COOH} \rightarrow \text{CH}_4 + \text{CO}_2$	-31.0
Acetate oxidation	$\text{CH}_3\text{COOH} + 2\text{H}_2\text{O} \rightarrow 4\text{H}_2 + 2\text{CO}_2$	+104.0
Homoacetogenesis	$4\text{H}_2 + \text{CO}_2 \rightarrow \text{CH}_3\text{COOH} + 2\text{H}_2\text{O}$	-104

For example, high organic load increases hydrogen and VFA production beyond the capacity of methanogens resulting in accumulation of VFA, or decrease in the capacity of methanogens due to inhibition by toxic compounds or pH drop (< 6) (Boe, 2006).

The hydrogen-consuming methanogens are among the fastest growing organisms in the anaerobic digestion process. They have a minimum doubling time estimated to six hours, compared with 2.6 days for the slow-growing acetoclastic methanogens (Schink, 1997). In addition, hydrogenotrophic methanogens are less sensitive to environmental changes than acetoclastic methanogens. Hence, methanogenesis from acetate are the rate limiting factors in the anaerobic treatment of easily hydrolysable substrates (Björnsson, 2000).

Appendix B. Literature review on non-Newtonian fluid

Rheology is a property of a fluid characterized by its flow curve that describes relationship between shear stress and shear rate. The ratio of shear stress to shear rate is the fluid apparent viscosity. Linear flow curve that passes through the origin characterizes a Newtonian fluid as shown in Figure B.1. The viscosity of such a fluid is therefore constant and independent of shear rate. Examples of Newtonian behaviour include water, milk, and sugar solutions (Holdsworth, 1993). On the other hand, a flow curve that is non-linear or/and does not pass through the origin represents non-Newtonian fluids. The apparent viscosity of such a fluid depends on the shear rate and is variable in shear flow. For some complex non-Newtonian fluids, the apparent viscosity depends also on the duration of shearing and the kinematic history of the fluid. Therefore, these complex fluids are time dependent.

The behaviour of a non-Newtonian fluid relates to the behaviour of a hypothetical Newtonian fluid where the concept of effective viscosity applied. Effective viscosity is the viscosity of a hypothetical Newtonian fluid that gives the same flow rate to pressure drop relationship as the non-Newtonian fluid.

Equation B.1 describes time-independent non-Newtonian fluids according to the following relationship:

$$\tau = \mu \dot{\gamma} \tag{B.1}$$

where τ is shear stress, $\dot{\gamma}$ is shear rate, and μ is the apparent viscosity function.

Thus:

$$\mu = \mu(\dot{\gamma}) \quad (\text{B.2})$$

Different forms of function in Equation B.2 yield different types of non-Newtonian fluids:

1. Shear thinning
2. Shear thickening
3. Viscoplastic (Bingham plastic and Herschel-Bulkley fluids)

Figure B.1 shows flow curves for these types of fluid rheological behaviour, along with a Newtonian flow curve.

Therefore, proper understanding of the effect of non-Newtonian fluids on the mixing of digesters and their impact on design is an important contribution to improve AD.

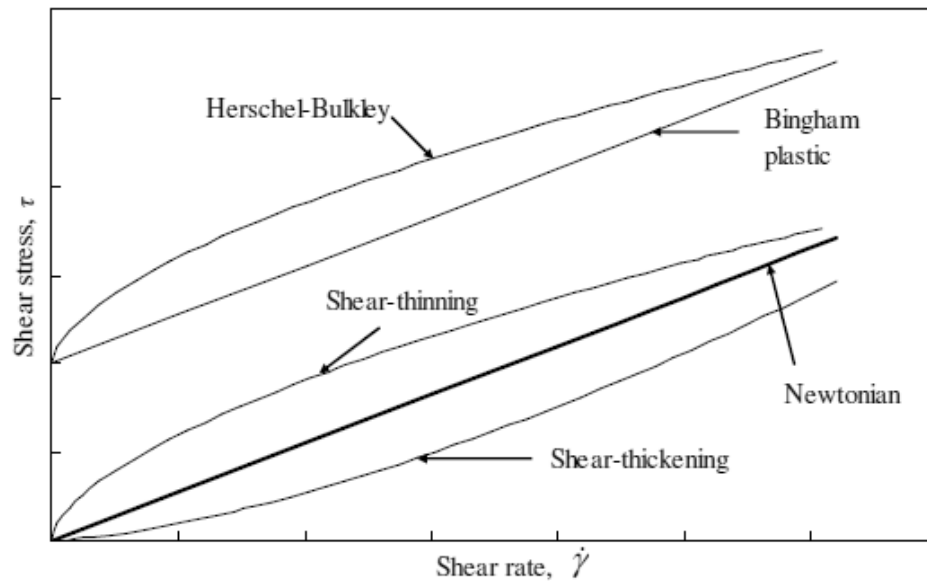


Figure B.1: Flow curves for Newtonian and non-Newtonian fluids.

B.1 Shear thinning fluids

Shear thinning fluids, also known as pseudoplastic fluids, are characterised by an apparent viscosity, which decreases with increasing shear rate. This behaviour is typical for polymer melts and solutions (e.g. aqueous polyacrylamide solutions), protein concentrates, and cream (Chhabra and Richardson, 1999; Holdsworth, 1993).

Most shear thinning fluids, however, exhibit a Newtonian behaviour at very low and very high shear rates. There are two limiting values of the apparent viscosity, a zero shear viscosity, μ_0 , and an infinite shear viscosity, μ_∞ , respectively. Figure B.2 shows a qualitative logarithmic plot of apparent viscosity as a function of shear rate for a shear thinning fluid based on the Carreau model (Carreau, 1972). The apparent viscosity is constant at both ends of very low and high shear rates indicating Newtonian behaviour in this region. The remaining region where viscosity decreases with increasing shear rate exhibits non-Newtonian regime behaviour. The rate of this decrease and the shear rate values marking the upper and lower limits of the non-Newtonian regime vary from one material to another.

Different mathematical models represent shear thinning behaviour as described below.

Power-law or Ostwald de Waele model:

This model describes the relationship between shear stress and shear rate using a power-law expression of the form:

$$\tau = k\dot{\gamma}^n \tag{B.3}$$

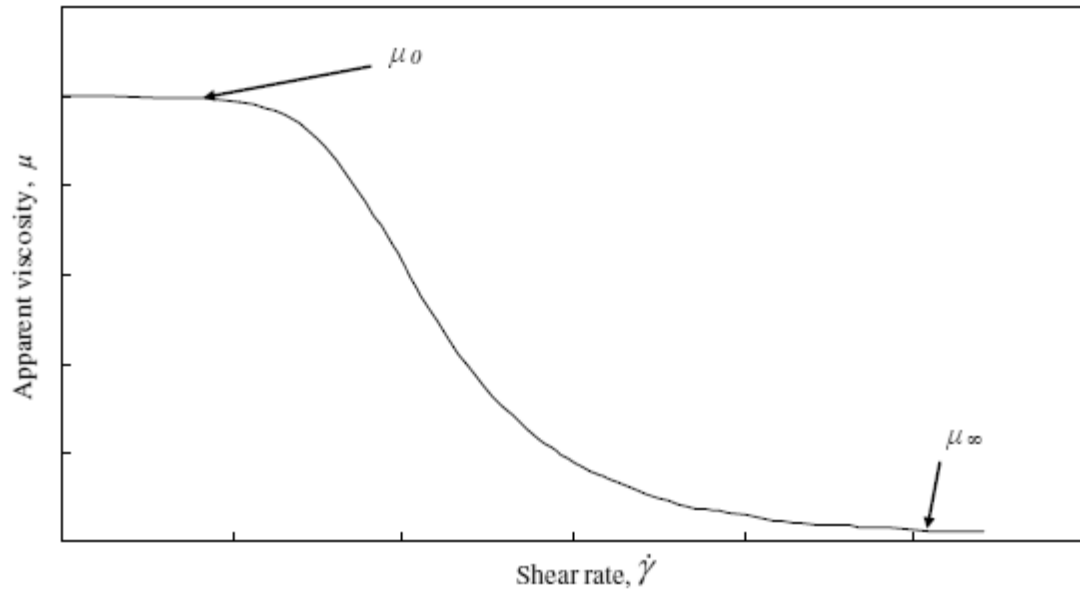


Figure B.2: Relationship between apparent viscosity and shear rate for a shear thinning fluid of the Carreau model

where the constants k and n are the flow consistency index and flow behaviour index, respectively.

Determination of these two parameters requires empirical curve fitting. The practical range of values the flow behaviour index, n , may take is 0-1 for shear thinning fluids. The smaller the value of n , the greater the degree of shear thinning and, thus, the more pronounced the non-Newtonian behaviour of the fluid. For n equals to one, the fluid reduces to a Newtonian case with a constant viscosity equal to k .

Derivation of an expression for the apparent viscosity of a shear thinning fluid requires combination of Equations B.1 and B.3, to give:

$$\mu = k \dot{\gamma}^{n-1} \tag{B.4}$$

One of the shortcomings of this model is that it describes only the shear-thinning regime of the flow curve without representation of zero and infinite shear viscosities at low and high shear rates. Furthermore, the empirically determined values of k and n depend on the range of shear rate considered (Chhabra and Richardson, 1999). Nevertheless, the power law model offers the simplest representation of shear thinning fluids. It is also most widely used because of its simplicity.

Carreau model:

When the fluid experiences very low and very high shear rates, deviations from the power law model becomes significant. The model proposed by Carreau (1972) takes account of the limiting values of viscosity at such extremes of shear rate, and given by:

$$\frac{\mu - \mu_{\infty}}{\mu_0 - \mu_{\infty}} = \left[1 + (\lambda \dot{\gamma})^2 \right]^{(n-1)/2} \quad (\text{B.5})$$

where λ is a curve-fitting parameter, given in time units.

Ellis model:

This model takes account of the zero shear viscosity only and is therefore appropriate when the deviations from the power law model are significant only at low shear rates. Unlike the power law and Carreau models, the Ellis model expresses apparent viscosity in terms of shear stress rather than shear rate, thus:

$$\mu = \frac{\mu_0}{1 + \left(\frac{\tau}{\tau_{1/2}} \right)^{\alpha-1}} \quad (\text{B.6})$$

where $\tau_{1/2}$ is the shear stress at which the apparent viscosity drops to $\mu_0/2$, and α is a measure of the extent of shear thinning.

B.2 Shear thickening fluids

In contrast with shear thinning fluids, shear-thickening fluids, also known as dilatant fluids have an apparent viscosity that increases with increasing shear rate. This type of fluid is most widely observed in concentrated solid-liquid suspensions, such as china clay and corn flour in water (Chhabra and Richardson, 1999). However, shear-thickening fluids are much less widespread in the chemical and processing industries than shear thinning fluids. Power-law describes mathematically shear-thickening behaviour with $n > 1$ (Equations B.3 and B.4).

B.3 Viscoplastic fluids

Viscoplastic fluids are fluids that do not flow or deform until the shear stress exceeds a certain value, known as the yield stress, γ_0 . Hence, the flow curve for such materials does not pass through the origin (Figure A.2). When the shear stress is below the yield stress value of the material, the material deforms elastically, i.e. like a rigid body. Once the applied shear stress exceeds the yield stress, the material begins to flow. At rest, the viscoplastic material has a rigid three-dimensional structure that resists external stresses below γ_0 . If the stress exceeds γ_0 , the material breaks down (Chhabra and Richardson, 1999; Holdsworth, 1993).

The apparent viscosity is effectively infinite at very low shear rates just before the viscoplastic material yields and begins to flow. This is somewhat similar to the behaviour of shear thinning fluids whose viscosity decreases with increasing shear. It is therefore possible to regard viscoplastic materials as possessing some kind of shear thinning behaviour instead of a true yield stress. Nonetheless, the concept of a yield

stress has proved to be a convenient approximation of the flow behaviour of some materials.

At shear stress values greater than the yield stress, the flow curve may be linear or non-linear. The Bingham plastic and Herschel-Bulkley models are two popular models that describe such flow behaviours.

Bingham plastic model

The model describes the behaviour of viscoplastic materials whose flow curve is linear (see Figure B.3), and given by (Boeghesani, 1988):

$$\begin{aligned} \tau &= \tau_0 + \mu_B \dot{\gamma}, & \text{for } \tau > \tau_0 \\ \dot{\gamma} &= 0, & \text{for } \tau \leq \tau_0 \end{aligned} \quad (\text{B.7})$$

where μ_B is the so-called plastic viscosity.

The apparent viscosity of a Bingham plastic fluid is (Mena and Binding, 1979):

$$\begin{aligned} \mu &= \mu_B + \frac{\tau_0}{\dot{\gamma}}, & \text{for } \tau \geq \tau_0 \\ \mu &\rightarrow \infty, & \text{for } \tau \leq \tau_0 \end{aligned} \quad (\text{B.8})$$

Herschel-Bulkley model

This model describes viscoplastic fluids with a non-linear flow curve (Figure B.2). The power-law represents this non-linearity, thus (Hodsworth, 1993):

$$\begin{aligned} \tau &= \tau_0 + k \dot{\gamma}^n, & \text{for } \tau > \tau_0 \\ \dot{\gamma} &= 0, & \text{for } \tau \leq \tau_0 \end{aligned} \quad (\text{B.9})$$

The apparent viscosity is:

$$\mu = k\dot{\gamma}^{n-1} + \frac{\tau_o}{\dot{\gamma}}, \text{ for } \tau \geq \tau_o; \text{ and} \quad (\text{B.10})$$

$$\mu \rightarrow \infty, \quad \text{for } \tau \leq \tau_o$$

B.4 Flow rate and velocity profile for non-Newtonian fluids

Consider a non-Newtonian fluid flowing in a pipe in a laminar flow regime. A constant pressure gradient, $\Delta p/L$ drives the steady volumetric flow rate, Q , of a Herschel-Bulkley fluid in laminar flow (Borghesani, 1988). Theoretically, Q is:

$$Q = \frac{\pi R^3 n}{\tau_w^3} \left(\frac{\tau_w - \tau_o}{k} \right)^{1/n} (\tau_w - \tau_o) \left[\frac{(\tau_w - \tau_o)^2}{3n+1} + \frac{2\tau_o(\tau_w - \tau_o)}{2n+1} + \frac{\tau_o^2}{n+1} \right] \quad (\text{B.11})$$

where R is the pipe radius, and τ_w is the wall shear stress, expressed as:

$$\tau_w = \frac{R\Delta p}{2L} \quad (\text{B.12})$$

For flow driven purely by gravity, the pressure gradient $\Delta p/L$ is equal to gL , where g is gravitational acceleration. For a power law fluid with $\tau_o = 0$, Equation B.11 reduces to the following expression:

$$Q = \frac{\pi R^3 n}{(3n+1)} \left(\frac{R}{2k} \frac{\Delta p}{L} \right)^{\frac{1}{n}} \quad (\text{B.13})$$

Equation B.13 reduces to the Buckingham-Reiner equation for a Bingham plastic fluid with $k = \mu_B$ and $n = 1$, thus:

$$Q = \frac{\pi R^3}{\tau_w^3} \left(\frac{\tau_w - \tau_0}{\mu_B} \right)^{1/n} (\tau_w - \tau_0) \left[\frac{(\tau_w - \tau_0)^2}{4} + \frac{2\tau_0(\tau_w - \tau_0)}{3} + \frac{\tau_0^2}{2} \right] \quad (\text{B.14})$$

In addition, it reduces to the Poiseuille equation for a Newtonian fluid with $\tau_0 = 0$, $k = \mu$, and $n = 1$, thus:

$$Q = \frac{\pi R^4}{8\mu} \frac{\Delta p}{L} \quad (\text{B.15})$$

The velocity distribution of a power law fluid in terms of radial position, r , is (Chhabra and Richardson, 1999):

$$u(r) = \left(\frac{\Delta p}{L} \right) \frac{(R^2 - r^2)}{4\mu_B} - \frac{\tau_0}{\mu_B} (R - r), \quad \text{for } r \geq R_p \quad (\text{B.16})$$

For a Bingham plastic fluid, Equation B.17 expresses the velocity profile as follows:

$$u(r) = \left(\frac{\Delta p}{2kL} \right)^{1/n} \left(\frac{n}{n+1} \right) \left[R^{(n+1)/n} - r^{(n+1)/n} \right] \quad (\text{B.17})$$

where R_p is the radius of the plug region and calculated from:

$$R_p = \frac{2L\tau_0}{\Delta p} \quad (\text{B.18})$$

The velocity of the plug region is:

$$u(r) = \left(\frac{\Delta p}{L} \right) \frac{R^2}{4\mu_B} \left(1 - \frac{R_p}{R} \right)^2 \quad (\text{B.19})$$

and for a Herschel-Bulkley fluid, the velocity profile is:

$$u(r) = \frac{nR}{n+1} \left(\frac{\tau_w}{k} \right)^{1/n} \left[(1-\phi)^{(n+1)/n} - \left(\frac{r}{R} - \phi \right)^{(n+1)/n} \right] \quad (\text{B.20})$$

where Φ is the ratio of yield stress to wall shear stress, i.e. τ_0/τ_w .

Defining the Reynolds number of a Newtonian fluid in terms of the effective viscosity of the fluid, μ_{eff} :

$$\text{Re} = \frac{\rho \bar{u} D}{\mu_{\text{eff}}} \quad (\text{B.21})$$

where u is the mean flow velocity, and D is the pipe diameter.

For a non-Newtonian fluid, the effective viscosity is (Chhabra and Richardson, 1999):

$$\mu_{\text{eff}} = m \left(\frac{8\bar{u}}{D} \right)^{n'-1} \quad (\text{B.22})$$

For a power law fluid,

$$m' = k \left(\frac{3n+1}{4n} \right)^n \quad \text{and} \quad n' = n \quad (\text{B.23})$$

For a Bingham plastic fluid,

$$n' = \frac{1 - \frac{4}{3}\phi + \frac{\phi^4}{3}}{1 - \phi^4} \quad (\text{B.24})$$

and

$$m' = \tau_w \left[\frac{\mu_B}{\tau_w \left(1 - \frac{4}{3}\phi + \frac{\phi^4}{3} \right)} \right]^{n'} \quad (\text{B.25})$$

Appendix C. Literature review on experimental studies on mixing

Power measurements

Power requirement of vessels is a commonly measured parameter due to its simplicity and important relationship to mixing performance. Excessive power draw requires a lot of energy to mix and thus costs more. Achieving the same level of mixing in anaerobic digester system at lower power consumption is desirable. Numerous factors such as fluid type, vessel geometry and choice of impeller affect the power draw. Generally, keeping the fluid type and vessel geometry the same while using variation of impeller types is a common practice. Measurement of the power requirement for a mixing digester requires measuring the torque M on the shaft of tank and converting it into power using equation:

$$P = 2\pi NM \quad (C.1)$$

Comparison between different digester geometries is possible using the dimensionless power number instead of power. Equation A.2 describes the Power number of a mixing vessel as:

$$P_o = \frac{P}{\rho N^3 D^5} \quad (C.2)$$

where ρ is the density of the fluid, N is the impeller speed and D is the impeller diameter.

For Newtonian fluids, Power numbers are proportional to the Reynolds number in the laminar regime and constant in the turbulent regime. There is a lack of understanding

about the transitional regime separating these two regimes. There are numerous empirical models proposed but there are no simple relationships available.

Various literatures are available on the measurement of power numbers and power consumption of mixing apparatus for various Newtonian fluids. Rushton *et al.* (1950) conducted an in depth study of the mixing of various Newtonian fluids in a stirred tank. The study investigates different impellers and extracts Power numbers over a large range of Reynolds numbers. Power number versus Reynolds number plot shows that in the laminar regime on a log-log scale, Power number decreases proportionally to an increase in Reynolds number. Power numbers are constant at high Reynolds numbers in the turbulent regime whereas the transitional regime between these two flow types shows a much more complex relationship. Other researchers studied about power consumption and power numbers as a function of impeller and tank dimensions, impeller choice and pumping directions (Tay and Tatterson (1985), Sano and Usui (1985), Bujalski *et al.* (1986 and 1987), Yianneskis *et al.* (1987), RaghavRao and Joshi (1988). They pointed out that larger diameter impellers provide more efficient power draw. Power number is also a function of disk thickness for a Rushton turbine and blade thickness for a pitch blade turbine. In addition, larger diameter impellers affect the Power number whereas clearance does not and down pumping pitched blade turbine is more efficient than up pumping.

There are very few studies on power numbers using non-Newtonian fluids. Edwards *et al.* (1976), considered a large range of rheologically different fluids to calculate the Metzner and Otto constants for various impellers. Nienow and Elson (1988) also

completed power measurements of yield stress and shear thickening materials. A much more recent work conducted by Ascanio *et al.* (2004) uses time periodic mixing of a shear thinning fluid to monitor power consumption. Use of intermittent mixing at lower impeller speeds helps lower energy consumption of the impeller. Jomha *et al.* (1990) completed power measurements of a shear thickening solid-liquid suspension. Predicted values agree quite well with results from existing equations.

Mixing times

Mixing time is defined as the time it takes for a volume of fluid to have the same concentration in all locations. A direct application of this definition leads to large times. Instead, application of a percentage of complete mixing such as 95% or 99% mixedness is appropriate.

Measurement of mixing times uses numerous experimental techniques such as acid base neutralization (Norwood and Metzner, 1960; Bujalski *et al.* 2002(b); Szalai *et al.*, 2004, Ascanio *et al.* 2004), decolourization techniques (Nienow and Elson, 1998) and injections of a tracer dye (Schofield, 1994; Mavros *et al.*, 2001; Kovács *et al.* 2003). A much more complicated technique called liquid crystal thermography LCT (Lee and Yianneskis, 1994(a); Lee and Yianneskis, 1997) uses liquid crystals and laser sheets. The crystals reflect light at different colors depending on the temperature. Thus, a uniform temperature yields a uniform color scattered by the liquid crystals. Electrical resistance tomography ERT (Holden *et al.*, 1998; Kovács *et al.* 2003) works by using multiple

probes to measure a resistance map of the vessel. An equal resistance implies a well-mixed system.

A much newer technique called Planar Laser Induced Fluorescence (PLIF) (Szalai *et al.*, 2004) uses a laser sheet passing through the vessel and a fluorescent tracer injected into the vessel. The tracer interacts with the laser sheet and CCD camera at right angle to the laser sheet captures the fluorescing light. The light fluoresced spreads evenly over the whole laser sheet indicating a complete mixing.

The effect of tank geometry, fluorescent intensity, and impeller geometry and type on mixing time using Newtonian fluids is the focus of many studies in the past. However, little work is available on non-Newtonian fluids. For Newtonian fluids, literature results indicate that mixing times are independent of the Reynolds number in the turbulent regime (Sano and Usui, 1985). Impeller types of relative size are equally effective since the Power number and energy dissipation are constant (Nienow, 1997). In case of highly viscous materials, even after hours of mixing, homogeneity is not attained (Szalai *et al.*, 2004).

Kovács *et al.* (2003) proved that mixing times are different for the same mixing geometry and power input for a shear thinning fluid compared with a Newtonian fluid. The rheology and polymeric structure of the non-Newtonian fluid is the contributing factor for the difference. The mixing times for the shear thinning fluids are much larger than the Newtonian fluid mixing times at the same conditions (Montante *et al.*, 2005).

Therefore, the viscosity of manure depending on the shear-rate or shear stresses causes considerable differences in viscosities. This makes mixing time a very useful quantity, which helps to estimate the efficiency of the manure homogenization in mixed anaerobic digesters.

Flow patterns

The study of flow patterns is common practice to understand mixing since flow patterns dictate how the system is mixed. The formation, shape and velocities of these flow patterns are of vital importance to understanding all manner of mixing configurations for all fluids. In the past, most work done are on Newtonian fluids since non-Newtonian fluids are mostly opaque and many of the flow measurement techniques are optical that require transparent materials. In addition, non-Newtonian materials have complex rheologies making them very difficult to work with (Maingonnat *et al.*, 2005). There are limited studies on shear thickening materials compared to other non-Newtonian fluids. These fluids are very rare and extremely difficult to work with. However, Grisky and Green (1971) used these fluids in the laminar regime but only measured friction coefficients in a conduit. The following section provides description of techniques available for the experiments and review of experimental works performed using them.

Flow followers:

One of the simplest techniques to understand flow patterns is by using a flow follower. A particle of neutral buoyancy is inserted into the flow and is followed either by eye or

camera techniques. Sano and Usui (1985) measured the discharge flow in a stirred tank for water using the flow follower technique. The technique involves counting the number of times the particle passes through the impeller region for a given time. Yianneskis (1991) used the technique much further to obtain flow patterns in a jet-agitated vessel using many acrylic particles with a light sheet illuminating the flow. Mahmoudi and Yianneskis (1991) measured flow patterns in stirred tank using flow followers with a laser sheet selecting the plane studied. The test identified three stable and four unstable flow patterns for different impeller spacing of two Rushton turbines. Solomon, *et al.*, 1981, used flow followers to measure flow inside a Carbopol solution using a vertical light beam. The results show a well-agitated flow inside the cavern formed around the impeller.

Use of flow follower technique is limited to only transparent materials since the camera needs to see the particle in the fluid. In addition, the particle moving in multiple dimensions requires more than one camera to get an idea of the full flow pattern. Due to the necessity of the particle observation, a large size is used. The large particle used for the observation is unable to follow any of the small structures such as Kolmogorov scale of turbulence and the boundary layer flow near the cavern boundary (Usui 1985). It is impossible to follow a smaller particle size corresponding to these structures but the technique gives an overall good estimation of the flow pattern.

Multiple camera techniques:

Multiple camera techniques can be used to track the three dimensional motion of a particle by using three monochrome cameras. Two cameras focus at each side of the tank and the third one at the bottom, thus aiming at all three axis of the tank. All three cameras start recording seeded particles in the tank. This enables the derivation of the 3D motion of the particle and allows the determination of the velocity distribution (Wittmer *et al.*, 1998; Barrue *et al.*, 1999). The technique requires a lot of data manipulation to link all three images to provide the flow fields. In addition, it requires a transparent fluid.

Hot wire anemometry:

Hot wire anemometry is a probe technique using two separate wires. The voltage recorded as the flow passes the wires translates into a velocity. Gunkel and Weber (1975) used this technique to measure the flow of air in a baffled tank and succeeded to measure the pumping capacity of the six bladed disc turbine quite reliably. The hot wire probe technique is quite intrusive because disrupts the measured flow resulting in readings that are less accurate. In addition, it only measures one direction and location of flow at a time. As result, the full flow field measurement using this technique takes a very long time.

Planar laser induced fluorescence:

Planar laser induced fluorescence (PLIF) is another optical technique for measuring flow patterns. Concentration maps before the dye is fully mixed show the flow patterns of the

system, including dead zones (Kukura *et al.*, 2002). Bakker and van den Akker (1996(a)) used this technique to measure the yield of a reactor system in turbulent flow.

Guillard *et al.* (2000) studied the turbulent flow in a stirred tank with a Rushton turbine and PLIF. The results show the presence of coherent mixing structures in the upper part of the tank and strong tangential flow in the impeller stream. Fountain *et al.* (2000) used PLIF to measure the flow structure of a stirred tank with a disc impeller. Zalc *et al.* (2002) reported that flow of a Rushton turbine is partially chaotic and contains large areas of poor mixing in the laminar regime. Increasing the Reynolds number did not yield more efficient mixing. Alvarez-Hernández *et al.* (2002) and Szalai *et al.* (2004) used PLIF to study the flow patterns in the laminar regime for a variety of impellers. Hall *et al.* (2005) investigated an eccentric agitation in a small un-baffled tank using PLIF. Results indicate that eccentric mixing in an un-baffled vessel provides improved mixing over a baffled system with centrally fixed impeller at small scale. PLIF is good at obtaining flow pattern data but is unable to measure velocities.

Laser Doppler velocimetry/anemometry:

Laser Doppler Velocimetry (LDV) or Laser Doppler Anemometry (LDA) is an optical technique for measuring fluid velocity and flow patterns. It uses two argon-ion laser beams pinpointing on a location in the tank. The crossing of the two laser beams forms a small volume where small reflective particles of neutral buoyancy used for seeding. These particles pass through the small volume, and scatter the laser light. Calculation of

velocity at the specific location uses detected scatters. Performing similar procedure in multiple locations allows the overall flow field extraction.

Rushton *et al.* (1950) and Yianneskis *et al.* (1987) measured the flow fields generated in a stirred tank mixed by a six-blade disc turbine. Both conclude that the impeller diameter affects more than the off-bottom clearance. Nouri *et al.* (1987) found that the impeller diameter did not affect the normalized velocities near the impeller in a stirred tank. Weetman and Oldshue (1988) studied the flow fields formed by different impellers. Wu and Patterson (1989) reported the normalized velocities are function of location and not impeller speed for Rushton turbine.

Ranade and Joshi (1989(a)) found that the angle of the pitched blade turbine affects the flow fields whereas blade width changes the flow slightly. In addition, using a larger diameter impeller produces more radial flow. Hutchings *et al.* (1989) and Ranade *et al.* (1991) measured flow fields in a stirred tank with various impellers. Yianneskis and Whitelaw (1993) and Lee and Yianneskis (1994b) studied the trailing vortices generated by the impeller blades. Harvey III *et al.* (1995) and Xu and McGrath (1996) measured flow fields induced by a pitched blade turbine. Rutherford *et al.*, 1996, found that thinner blade impellers produce higher mean velocities, power numbers and flow numbers for a Rushton turbine. Armenante and Chou (1996) showed that a second impeller changes the flow pattern completely, giving strong vertical circulation between the impellers.

Bakker and van den Akker (1996) investigated the yield of a reactor system in turbulent conditions. Bakker *et al.* (1996) showed that a pitched blade turbine in the laminar regime pumps radially with the flow confined to the impeller with dominant tangential velocities. Schäfer *et al.* (1998), Naude *et al.* (1998) and Sahu *et al.* (1999) obtained flow field data for a variety of different impeller types. Bittorf and Kresta (2000) used LDV. The results show that an active volume during mixing with an axial impeller is two thirds of the tank height. The size of active volume is independent of impeller diameter, impeller speed and off bottom clearance. However, for a pitched blade turbine, the location of active volume is dependent on the impeller off bottom clearance. Bittorf and Kresta (2001) showed that the flow at the wall generated by an axial impeller forms a 3D wall jet consistent with jet theory. Patwardhan (2001) measured the residence time distribution of a down pumping pitched blade turbine.

Montante *et al.* (2001(a)) noticed that change of impeller off bottom clearance for a Rushton turbine forced the flow pattern from a DL to a SL. Jones *et al.* (2001), Nikiforaki *et al.* (2003), Micheletti (2004), and Hartmann *et al.* (2004(b)) also measured flow patterns for various tank configurations and impeller types. Galletti *et al.* (2005) aimed to measure the instabilities of the flow in stirred vessels and found that they vary greatly from one region to another.

LDV is an accurate technique for measuring flow patterns and velocities. However, the data acquisition takes long time and requires individual measurement at each position. In addition, LDV is another optical technique used only for transparent materials.

Particle image velocimetry:

Particle Image Velocimetry (PIV) is another optical technique that requires transparent materials similar to LDV for measuring fluid velocity and flow patterns. The method uses a laser sheet projected into the vessel. A fast CCD camera at right angles to the laser sheet captures many images of small tracer particles ($\sim 60\mu\text{m}$) over an interval of time in the mixing fluid passing through the laser sheet. The result of these interactions gives 2D velocity fields (Kukura *et al.*, 2002). La Fontaine and Shepherd (1996) measured flow fields in a stirred tank and identified stagnant flow regions, circulation loops and turbulent flow. Bakker *et al.* (1996) and Sheng *et al.* (1998) measured the flow fields generated in a stirred tank with a pitched blade turbine and an axial impeller respectively.

Lamberto *et al.* (1999) found that after 2 hours 15% of the tank still not mixed due to segregated zones in an un-baffled tank with a radial impeller. Fountain *et al.* (2000) measured the flow fields on a disc impeller and Ranade *et al.* (2001) looked at the trailing vortices formed with a Rushton turbine. Bugay *et al.* (2002) and Escudié and Liné (2003) measured the flow patterns formed with a Lightnin A310 axial impeller and Rushton turbine respectively. Khopkar *et al.* (2003) confirmed that trailing vortices are present for a down pumping pitched blade turbine in an aerated and non-aerated vessel. Escudié *et al.* (2004) located the trailing vortices of a Rushton turbine and their sizes.

Szalai *et al.* (2004) and Micheletti (2004) measured flow patterns and mixing performance of four Ekato Intermig impellers and a Rushton turbine respectively. Hall *et al.* (2005) found that an eccentrically agitated un-baffled vessel provided better mixing than a baffled system with a centrally placed impeller in a small-scale vessel.

Couerbe *et al.* (2008) measured flow patterns of a non-Newtonian fluid exhibiting thixotropic shear thinning behaviour with a yield stress that uses an axial impeller. The results show an outward pumping at high impeller speeds and formation of cavern at lower speeds. Measurement of the lower flow loop is difficult because of the tank conical bottom causes parallel effects.

PIV is a more rapid technique than LDV that allows measurement of instantaneous velocity fields within a given measurement plane. However, the recorded velocity values are less accurate than LDV obtained values.

3D Phase Doppler Anemometry:

3D Phase-Doppler Anemometry (PDA) is a similar technique to LDV with difference on the number of lasers used. PDA uses six lasers instead of two that allows the measurement of all 3-velocity components at once. Pettersson and Rasmuson (1998) used this technique to measure flow patterns and local fluid velocity vectors in a stirred tank. The measurement of the extra velocity component takes longer computation time than the LDV technique. Once again, the technique requires transparent material.

Two components Phase Doppler Anemometry

Two component PDA is similar to LDV but uses two different size tracers instead of one. The technique distinguishes between the two particle sizes and uses to measure the flow field of two different phases at the same time such as flow field of a solid-liquid suspension (Lyungqvist and Rasmuson, 2001). Measuring the fluid flow field uses the very small particle while the solid flow field measurement uses a larger particle similar to the solid fraction. However, as mentioned previously the smaller particle used to measure the fluid flow fields are not small enough to measure Kolmogorov eddies. This technique is again an optical and applicable only to transparent materials.

Ultrasonic Doppler Velocimetry

Ultrasonic Doppler Velocimetry (UDV) is an unobtrusive probe technique to measure flow fields in opaque materials by using ultrasonic signals. It uses a probe to transmit and receive ultrasonic signals reflected back by the structure of the fluid. Determination of velocity uses the difference in the transmitted and received signal in multiple locations. The outcome gives an idea of the overall flow pattern of the system. Ein-Mozaffari *et al.* (2007) measured the flow field at critical locations inside a rectangular tank for a paper pulp suspension where the suspended fibers reflect the ultrasonic signals back to the probe. The results show dead zones at the corners of the rectangular tank and grew in size with the yield stress of the paper pulp suspension. Pakzad *et al.* (2008) used this technique to measure the flow field in an opaque solution of Xanthan gum that is pseudoplastic with an apparent yield stress. Measurement of velocity of the flow inside opaque materials is possible with UDV technique.

Computer automated radioactive particle tracking:

Computer-automated radioactive particle tracking (CARPT) uses a radioactive tracer that is neutrally buoyant in the studied liquid. The tracer emits radiation via β -decay. This means an atom inside the tracer particle emits either an electron or a positron. This can cause a nearby nucleus to become excited reducing to its ground state via emitting one or more γ -rays. In addition, the emitted positrons immediately annihilate with any electron giving off back-to-back γ -rays (Chaouki *et al.*, 1997). Many scintillation detectors placed all around the sides of the tank detects the γ -rays. The intensity of the radiation measured decreases with increased distance from the detector requiring calibration for each particle used. Measuring multiple detections along with the corresponding intensity at a short interval of time allows the determination of the particles' 3D location. The obtained locations yield the trajectory of the particle and make it possible to obtain velocity flow fields, dead zones and eyes of circulation (Rammohan *et al.*, 2001; Guha *et al.*, 2008). This technique is much quicker at obtaining results than the laser-based techniques. It is also non-invasive and applicable for opaque materials and equipments.

Positron emission particle tracking:

Positron emission particle tracking (PEPT) is a radioactive tracer technique similar to CARPT that can be used to measure flow fields unobtrusively in both transparent and opaque fluids and equipment (Barigou, 2004). The technique is able to track the position over time of a positron-emitting particle accurately and non-invasively inside an opaque vessel or material.

Fangary *et al.* (2000) measured flow fields of both water and a shear thinning CMC solution in a stirred tank. Results identified zones of effective fluid agitation and stagnation and concluded that axial flow impellers become more axial the more viscous the fluid. Guida *et al.* (2009) measured the flow fields of a solid-liquid suspension of glass particles in water stirred by a pitched blade turbine. This is still a new technique so little work is available on the mixing of opaque fluids using PEPT. Similar to CARPT, PEPT is non-invasive technique that works well with opaque materials and gives the overall flow pattern much quicker than optical techniques. However, PEPT does not need calibration before the start of the experiment in order to locate the particle inside the tank.

Turbulent measurements

Turbulence occurs at high Reynolds numbers. The fluid contains random flow structures compared to the simple streamlines of laminar flow. Velocity values are not constant and fluctuate around a mean value. Larger fluctuations correspond to more turbulent flow. Turbulence is extremely complex described by certain parameters rather than the continually changing flow patterns. Turbulent kinetic energy and energy dissipation are the most common parameters that describe turbulent mixing. There are number of works involved on measuring the turbulence parameters of Newtonian fluids using techniques such as hot film anemometry. Anandha Rao and Brodkey (1972); Nishikawa *et al.* (1976) inserted probe into the flow and recorded voltages. Calibration of recoded voltages to specific velocities gives a measure of the turbulence.

Constant temperature anemometry, CTA (Wernersson and Trägårdh, 1998) measures turbulent parameters. The probe measures velocities in two directions simultaneously at a single location. Escudié and Liné (2006); Chung *et al.* (2007); Liu *et al.* (2008); Gabriele *et al.* (2009) used PIV whereas Pettersson and Rasmuson (1998) used 3D phase-Doppler anemometry to measure turbulence. A much more simplistic method to observe turbulence structures are Photographic velocity measurements (Van'tRiet and Smith, 1975). This technique uses seeded particles in the flow with successive photographs taken to observe the particles motion.

Van'tRiet and Smith, 1975 reported the presence of turbulence in a Newtonian fluids at Reynolds numbers as low as 300. Tank geometry, especially impeller clearance and diameter has a large effect on energy dissipation with the number of baffles having no real effect (Zhou and Kresta, 1996a). In addition, different flow impellers have very different dominant characteristics of energy dissipation (Zhou and Kresta, 1996b).

Cavern data

Cavern data are the experimentally determined shape and size of caverns or pseudocaverns formed when mixing yield stress or shear thinning materials. Lack of fixed cavern boundary makes things complicated in obtaining pseudo-cavern data. Therefore, past studies focus on cavern data obtained from yield stress materials.

Solomon, *et al.* (1981) used hot film anemometry to determine the cavern boundary of Xanthan gum, an opaque yield stress material. Measurement of caverns sizes under aerated conditions is difficult due to interaction of the gas with the probes causing false readings. Solomon, *et al.* (1981) also used the flow follower to measure the size and shape of caverns. Results from the study indicates growth in size of carven with an increase in impeller speed when a stagnant fluid observed from outside.

Elson and Cheesman (1986) used an X-ray technique to visualize caverns in opaque yields stress fluids. The X-ray technique requires the injection of X-ray opaque fluid such as a Barium solution into the impeller region. The solution fills the cavern so that the shape of the carven is X-rayed (Nienow and Elson, 1988). Elson (1990) monitored the motion of the tank walls, bottom and free surface by observing the motion and thus the cavern boundary as the impeller speed increased for an opaque Xanthan gum solution. Values from the experiment are very close to predictions from the Elson and Cheesman (1986) model where the cavern touched the tank wall. Baffles have negative effect on cavern growth both vertically and horizontally. Hence, obtaining a complete motion of the tank for baffled tank requires higher impeller speeds.

Amanullah *et al.* (1997) measured caverns formed by a shear thinning Herschel-Bulkley Carbopol solution equipped with down pumping axial impeller. Injection of violet crystal near the impeller allows the measurement of the carven. Higher impeller clearance resulted in detection of larger caverns for the same power input. Comparison of the size of carven generated by axial impeller and Rushton turbine shows axial

impellers with larger cavens. Cavern height to diameter ratio remained constant with increase in impeller speed until the cavern touched the tank wall.

Wilkens *et al.* (2005) used a novel technique to measure caverns formed in ketchup using pitched blade turbine and a radial impeller. Assortment of very small (roughly 1-mm²) pieces of copolymer plastics injected in the impeller region during mixing and allowed to freeze with the ketchup in a freezer. Dissecting the frozen ketchup yields the cavern shape by the location of the pieces of copolymer plastics. Both impeller types form an elliptical torus caverns but, the taller caverns corresponds to a pitched blade turbine.

Pakzad *et al.* (2008(b)) used electrical resistance tomography to study the formation of caverns during the mixing of pseudoplastic fluids possessing yield stress (Xanthan gum). Results show that a significant cavern growth during the transitional regime.

Ein-Mozaffari *et al.* (2007) and Hui *et al.* (2009) used ultrasonic Doppler Velocimetry (UDV) to measure cavern sizes in a pulp suspension. UDV uses a single probe to transmit and receive ultrasonic signals reflected back by the fibres. From these reflections, the velocity of the fibre at different positions can be determined. The cavern boundary corresponds to a zero velocity value recorded.

Hui *et al.* (2009) compared UDV to ERT and found that the accuracy of results from ERT measurement improved at the expense of longer processing time. The cavern

volume obtained from UDV is larger than carven volume from UDV under predicting the location of the cavern boundary with 10% differences in volumes. Elson and Cheesman (1986) used a cylindrical model under predicting the cavern volumes because the model does not contain an axial force component. The large discrepancy between the cavern prediction models and the experimental techniques found to be due to the cavern interaction with the walls of the tank.

Appendix D. Literature review on CFD studies on mixing

Computational Fluid Dynamics (CFD) is a powerful tool for exploring mixing systems since the simulation requires less work than required by experiment (Mann *et al.*, 1995; Kukura *et al.*, 2002). Again, most CFD simulations done in the past use Newtonian fluids since the viscosity of these fluids is constant and solving the Navier Stokes equation is easier.

Newtonian simulations

Ranade and Joshi (1989b) used a technique called FIAT (which uses SIMPLE, semi-implicit algorithm pressure linked equation) to simulate the flow patterns generated by a pitched blade turbine. This model agrees reasonably well with experimental data, but the axial velocities below the impeller remained over predicted. Hutchings *et al.* (1989) used FLUENT to model the 2D flow field of a Rushton turbine and axial impeller using the $k-\epsilon$ turbulence model. The model uses an experimental data from LDV as boundary conditions for the impeller region, excluding this region from the simulation. Results show good comparison with the overall flow patterns obtained from the experimental data.

Ranade *et al.* (1991) also used the $k-\epsilon$ turbulence model to measure the flow of a down pumping pitched blade turbine. The simulations show good comparison with the experimental data. Bakker and van den Akker (1994) modeled the micromixing of a Rushton turbine to predict the yield of a chemical reactor, but all the micromixing models over predicted the yield. Bakker and Fasano (1994) measured the mixing times and chemical distributions in a vessel stirred by a Rushton turbine predicting well both

factors. Schofield (1994) used another CFD program called PHOENICS to simulate the transient tracer dye diffusion in a stirred tank with a Rushton turbine. The model uses the k- ϵ turbulence model and the results from simulations agree well with experimental visualizations.

Sahu and Joshi (1995) used SIMPLE and the k- ϵ turbulence model to simulate an axial impeller in a stirred tank. Predicted values are in good qualitative agreement with the experimental results predicting most of the flow patterns. Harvey III et al. (1995) used another technique called multi-block incompressible Navier-Stokes solver to measure the flow field induced by a pitched blade turbine. The radial and axial components are in good agreement at low Reynolds number ($Re < 21$) with a 25% difference on the tangential velocities near the impeller. Ranade and Dommeti (1996) used FLUENT to simulate the mixing of a pitched blade turbine without using any experimental data as boundary conditions near the impeller. Results agree both qualitatively and quantitatively with experimental data and show correctly the flow characteristics in the impeller swept volume.

Eggels (1996) is the first to use large eddy simulations (LES) to study the turbulent flow generated by a Rushton turbine. LES simulations provide more detailed data than the standard CFD simulations that use Reynolds Averaged Navier Stokes (RANS). LES simulations use finer grid to resolve turbulent flow structures and instantaneous flow characteristics. However, it is computationally expensive. Both the mean flow and turbulence intensities agree with known experimental data. Ciofalo et al. (1996) used the

k- ϵ turbulence model to measure the flow and free surface of an un-baffled tank with a radial impeller. Predictions from using the k- ϵ turbulence model are poor compared with experimentally measured value.

Armenante and Chou (1996) used FLUENT with experimental data in the impeller region and two different turbulence models to predict the flow generated by single and double pitched blade turbines. The algebraic stress model shows better agreement with experimental results than the k- ϵ turbulence model. Bakker and van den Akker (1996a) used a new lagrangian CFD model to measure the yield of a reactor in turbulent conditions. The result shows that when the feed simulated far away from the impeller, the predictions of the yield are very good. Bakker et al. (1996b) used CFM (computational fluid mixing) software to measure the flow patterns in the laminar and turbulent regimes using a pitched blade turbine. Laminar predictions are very good using correct velocities as the boundary conditions surrounding the impeller. The turbulent simulations however only predicted some of the flow structures with a significantly under predicted turbulence.

Ranade (1997) used FLUENT to simulate the laminar and turbulent flow generated by a Rushton turbine without using any experimental data as boundary conditions. The simulations show good agreement with experimental data for a wide range of Reynolds numbers. It also captures the flow in the impeller region.

Jaworski et al. (1997) used a sliding grid to simulate the laminar flow of a Rushton turbine. A sliding grid is where the tank split into two regions, with one remaining

stationary while the other rotates mimicking the rotation of the impeller. Flow patterns and power numbers obtained show good agreement with experimental data without the need for experimental data input. Hobbs and Muzzio (1997) used FLUENT to measure the flow at low Reynolds in a tank equipped with static mixer. The model uses particle tracking to predict the residence time distribution. The mixing characteristics simulated show good agreement with reported experimental data.

Revstedt et al. (1998) also used LES to simulate flow fields generated by a Rushton turbine and obtained results that are in good agreement with experimental data. There are some discrepancies however in the impeller region caused by an inadequate description of the impeller. Brucato et al. (1998) used the inner-outer approach to simulate the flow field of a single and dual Rushton turbine and an axial impeller. The inner-outer method gives quite good results for flow and turbulence. Models using the inner-outer method give a more accurate presentation of flow and turbulence than models using the impeller boundary conditions technique. However, they are computationally demanding. The inner-outer method uses two overlapping regions in the simulations. These are regions containing the impeller and the tank wall and baffles. The two regions exchange an overlapping data during simulation process. The sliding grid agrees best concerning flow patterns but under predicts the turbulence. This method however is the most computationally demanding that is applicable to transient simulations.

Zipp and Patterson (1998) simulated the conversion rate of a chemical reaction with a Rushton turbine with results that agree well with the experimental data. Sheng et al. (1998) used RANS to simulate the flow of an axial impeller using two turbulence models with experimental boundary conditions on the impeller. Flow fields are very similar for both the $k-\epsilon$ RNG and the Reynolds stress models. However, the turbulence values differ widely for the two models. Naude et al. (1998) used MFR model with an unstructured mesh to simulate the flow of a complex impeller type in turbulent flow. MFR uses the sliding grid technique but the rotating grid does not move. Instead, each element has a tangential velocity allowing fast steady state simulations. Pumping and power numbers obtained agree well with experimental data.

Wechsler et al. (1999) used RANS with the $k-\epsilon$ turbulence model to compute steady and unsteady simulations of a pitched blade turbine. There is a good agreement between the steady and unsteady simulations even though the steady state simulations only require a fraction of the time and computational expense. Ducoste and Clark (1999) used a new CFD technique called FIDAP (fluid dynamics International, Evanston, IL) to simulate flocculator fluid mechanics with a Rushton turbine and A310 foil impellers. The obtained result agrees reasonably with experimental data for both impellers. Derksen and van den Akker (1999) used LES to simulate the flow of a Rushton turbine. The prediction of turbulent kinetic energy agrees well but the impeller outflow predictions are not good.

Osman and Varley (1999) used FLUENT in conjunction with pre-processing software MIXIM to perform a finite volume simulation of the flow generated by a Rushton turbine. The report states the mixing times are twice that of the experimental data, but the tracer movement simulated well. Barrue et al. (1999) used FLUENT to simulate the particle trajectory in a stirred tank with a Rushton turbine in turbulent flow. The particles lagrangian trajectory matches well with experimental results. Sahu et al. (1999) simulated five different axial impellers using a technique called zonal modeling with k- ϵ turbulence model. Lamberto et al. (1999) used FLUENT to simulate the laminar flow in an un-baffled tank with a radial impeller. Both validated the models with experimental data.

Aubin et al. (2000) also used FLUENT software in conjunction with SIMPLE to simulate the laminar flow of viscous glucose stirred by a helical screw with and without a draft tube. The use of the draft tube shows circulation that is more efficient. Verzicco et al. (2000) used direct numerical simulations (DNS) to measure the flow induced by an 8 bladed paddle impeller. DNS is the most computationally demanding CFD technique because uses an extremely fine grid to complete the simulations. However, results from DNS are much better than both LES and RANS.

Harvey III et al. (2000) simulated the mixing times and isolated mixing regions by allowing 104 passive particles to move through one period of flow. This technique gives very accurate results when compared with direct particle integration at a fraction of the computational cost. Brucato et al. (2000) simulated a mixing sensitive parallel reaction

in stirred tank with a Rushton turbine. The results show good agreement with experimental results at low impeller speeds including the prediction of selectivity in reaction. Revstedt et al. (2000) used LES to measure the flow generated by two types of dual radial impellers. Data is similar for both types of impellers at the same power input, but at equal impeller speed, the Rushton turbine produces higher velocities and volumetric flow.

Jaworski et al. (2000) used FLUENT to understand the degree of homogenization for a dual Rushton turbine stirred tank. The model uses the sliding grid technique along with two different turbulence models. The k - ϵ turbulence model results are the most accurate simulations but the predicted mixing times are two to three times longer than experimental values. Fountain et al. (2000) simulated the flow fields in a stirred tank caused by a disc turbine using FLUENT. Nere et al. (2001) used the impeller boundary condition approach in the turbulent regime to simulate the flow fields generated by multiple impellers. The developed models predict the eddy viscosity and improve the predictions for all three-velocity components.

Montante et al. (2001a, 2001b) simulated the flow generated by a Rushton turbine using both the sliding grid technique and the inner-outer method. The prediction of flow patterns is good, especially at high impeller clearances and at low clearances. The flow in the upper part of the tank agrees well with experiments. The change of flow pattern because of clearance variations happens at the same locations as the experiments.

Lamberto et al. (2001) used FLUENT to simulate Lagrangian particle tracking in an unbaffled tank with a radial flow impeller. Particles show the poorly mixed regions identified in experiments. Once a particle entered one of these poorly mixed zones, it remains there indefinitely. The values for the prediction of mean velocities are good but less accurate when only a single loop is present. In addition, the model over predicts the discharge angle for these cases.

Jayanti (2001) simulated jet mixing in cylindrical vessel and found that having a conical bottom reduces and removes some of the dead zones, and thus reducing the mixing time. Derksen (2001) performed LES with a pitched blade turbine in the turbulent regime and found that simulation with a mesh of size 3603 agrees best with the experimental data. Ranade et al. (2001) used FLUENT to measure the trailing vortices of a Rushton turbine using two different turbulence models. The result satisfactorily agrees with experimental data. The $k-\epsilon$ turbulence model predicted the turbulence much better than $k-\epsilon$ RNG turbulence model.

Patwardhan (2001) found that the simulated residence time distribution of a down pumping pitched blade turbine obtaining result that matches the experimental results. Lyungqvist and Rasmuson (2001) used another commercial CFD package called CFX4 to model the two-phase flow fields in an axially stirred vessel. The results agree well indicating the axial slip velocities and turbulent kinetic energy differences between each phase. However, the model under predicts the radial and tangential velocities while the overall flow fields show good comparison with experimental data.

Jones et al. (2001) tested six different two-equation turbulence models on flow in an unbaffled tank with paddle impeller. All models over predict the radial velocities in the impeller discharge stream while tangential velocities are predicted well except near the shaft. The low Reynolds k - ϵ turbulence model is the only one to predict the kinetic energy well in the discharge stream, but all models qualitatively predicted the circulation patterns well. Sun et al. (2002) simulated the flow created by a Rushton turbine using the inner-outer technique with the anisotropic algebraic stress model to handle the turbulence. This new turbulence model gave better predictions than the standard k - ϵ turbulence model, showing good turbulent flow field comparisons with experimental data. Revstedt and Fuchs (2002) used LES to simulate the flow in a stirred tank using single and multiple impellers of various types. The simulation results agree well with experimental data.

Murthy Shekhar and Jayanti (2002) simulated the flow field of an eight bladed paddle impeller in the laminar, transitional and turbulent flow regimes using the sliding mesh approach. The k - ϵ turbulence model predicted flow and turbulence near the impeller well. However, the results from the low Reynolds k - ϵ turbulence model predicted the flow better away from the impeller, meaning that the flow in the vessel is not fully turbulent. Power numbers measured in the laminar regime matched well with experimental data but the mixing times did not. Overall, the low Reynolds k - ϵ turbulence model allowed better results that compares to experimental results.

Bartels et al. (2002) compared DNS simulations and RANS simulations of flow in a stirred vessel using a Rushton turbine. The simulations using DNS show much closer results to experiment values but the computational power and time are extremely large. The RANS simulations still gave relatively accurate predictions despite the much simpler and less time-consuming model. Bhattacharya and Kresta (2002) used the MFR technique alongside the k- ϵ turbulence model to simulate the flow at the wall when using a pitched blade turbine. Circulation patterns and velocity profiles of the jets matched well with experimental results. Zalc et al. (2002) simulated the flow patterns generated by the three Rushton turbines and found results that are in agreement with experimental data when using particle-tracking methods. The observed flow is partially chaotic and contains large areas of poor mixing where increasing the Reynolds number does not yield more efficient mixing.

Bujalski et al. (2002a) used FLUENT to simulate the flow of a dual Rushton turbine in the turbulent regime. The test includes the sliding grid method along with MFR and two turbulence models. The power number predictions improved when results compared to earlier attempts. Bujalski et al. (2002b) used FLUENT to measure the mixing times of a Rushton turbine. The model uses the sliding grid with the k- ϵ RANS turbulence model. Position of feed point of tracer is of high importance for simulations particularly in the proximity to the sliding mesh boundary. Some of the simulations predicted well the mixing times obtained from experiments. Kovács et al. (2003) used FLUENT to simulate the mixing of a viscous Newtonian fluid in a Lightnin 45 static mixer by performing particle tracking simulations to measure the degree of mixing.

Campolo et al. (2003) used the RANS approach with the k - ϵ turbulence model to simulate the flow of a Rushton turbine in a stirred tank by simulating a dispersion of fluid particles. Flow fields from the simulations are in agreement with experimental data. The fluid particles showed that mixing proceeds differently in the lower and upper parts of the tank. Khopkar et al. (2003) aimed to simulate with FLUENT the gas-liquid flow in a stirred vessel with a down pumping pitched blade turbine and the k - ϵ turbulence model. The prediction of flow patterns is very similar to experimental results pointing out the decrease in pumping efficiency with aeration. However, the model over predicted the axial velocities and turbulent kinetic energy near the impeller.

Yeoh et al. (2004a) used both LES and RANS to simulate the flow of a Rushton turbine in turbulent flow using a sliding and deforming mesh. The method uses a similar approach to the sliding grid, except the mesh at the interface deforms during rotation. Once deformation exceeds a limit, the mesh resets and then deforms again.

Shear-thinning simulations

There are some CFD studies performed on shear thinning non-Newtonian fluids. In these fluids, shear rate increases with decrease in viscosity. Aubin et al. (2000) used the FLUENT software and SIMPLE to study the laminar flow of two shear-thinning fluids. Carbopol and Natrosol used as working fluids and stirred by a helical screw impeller with and without a draft tube. The draft tube provided better circulation and the axial velocities are less significant for these shear-thinning fluids when compared to the mixing of a Newtonian fluid. Kelly and Gigas (2003) also used FLUENT in the laminar regime to model the mixing of a shear thinning Carbopol solution stirred by an axial

impeller. The prediction of power numbers is 5% of the experimental values and function of Reynolds number and flow behaviour index. The simulation obtained discharge angle from the impeller compares well with experimental flow patterns.

Kovács et al. (2003) used FLUENT to study the mixing of a shear thinning fluid flowing through a Lightnin 45 type static mixer. The model simulates also the particle tracking to measure the degree of mixedness of the static mixer. No difference observed after four elements of the static mixer when compared with Newtonian fluid data for Reynolds below 10. However, at a Reynolds of 100 the shear thinning fluid generated secondary motion creating better mixing. Montante et al. (2005) simulated the mixing of a shear thinning fluid with multiple pitched blade turbines. The model uses passive tracer to estimate mixing times and the values obtained match well with experimental results.

Yield stress simulations

Very few CFD simulations using yield stress fluids are available in the literature. Yield stress fluids flow once the shear stress is above the yield stress of the material. Balhoff and Thompson (2004) simulated the flow of a yield stress fluid in a packed bed using a network model. Comparison with experimental data shows good agreement with Bingham plastic fluids but not Herschel-Bulkley materials. Couerbe et al. (2008) simulated the mixing of a thixotropic shear thinning fluid with a yield stress in a tank stirred with an axial impeller using the commercial CFD code CFX. The model uses two shear dependent laws, one for high shear rates and one for low shear rates to simulate the viscosity. Good quantitative comparison of results with experiment achieved. However, the prediction became quite poor near the impeller at low speeds.

Pakzad et al. (2008a) simulated the Xanthan gum mixed by a Scaba 6SRGT impeller in the laminar regime using FLUENT and MFR model. The velocity profiles obtained from the simulation agree well with UDV experimental data. The simulated cavern data also agree well with Elson and Cheesman (1986) cylindrical cavern model. Pakzad et al. (2008b) studied the cavern formation of a shear thinning fluid possessing a yield stress for a radial flow Scaba 6SRGT impeller using FLUENT. Simulations agree well with experimental data and theory based data. Results also show a significant cavern growth in the transitional regime. In addition, the simulations suggest for a given material, the use of laminar model for Reynolds numbers up to 200 is reasonable.

Appendix E. Literature review on AD modeling

The first dynamic model developed is by Andrews (1971). The model consisted of a single substrate (un-ionized acetic acid) and single biomass (acetate utilizing methanogens) with the assumption of constant pH. Nevertheless, it is the first model to incorporate the inhibitory effect of high un-ionized volatile acid concentration on the growth of methanogens. The general Monod type kinetic equation expresses the growth of methanogens with modification to include the inhibition function.

Hill and Barth (1977) enhanced Andrews's model by adding the second bacterial group for acid formation and incorporated hydrolysis. They also added the carbonate equilibrium, nitrogen balance, cation exchange and inhibition of the methane formation by ammonia and volatile fatty acids (VFA). Their model considers three substrates and two kinds of microorganisms (acid formers and methanogens). The model includes the inhibitory effect of high concentration of volatile acids on both acid formers and methanogens, the inhibitory effect of high ammonia levels on the growth of methanogens, and decay of biomass.

Eastman and Ferguson (1981) developed a model for sludge digestion, which considered the hydrolysis of particulate substrate rather than methanogenesis as the rate-controlling step. The system considered in their study is a continuous stirred tank reactor (CSTR) using primary sewage sludge as substrate. The acidogenic phase in the model includes both the hydrolysis and digestion stages. The hydrolysis of biodegradable solids to smaller soluble molecules followed by the conversion of the soluble molecules to

digested products by the acid-forming bacteria defines the substrate pathway. The main assumptions in this model are: (1) cell decay contributes to the pool of digested products; (2) nitrate, and sulfate concentrations are negligible; and (3) electron acceptors consist solely of organics and carbon dioxide. The mass balance calculations express the substrate as chemical oxygen demand, COD. The first-order equation with respect to the particulate biodegradable COD defines the hydrolysis kinetics under constant pH and temperature. They found that the hydrolysis constant to be 3 h^{-1} , growth yield coefficient to be $0.48 \text{ g COD of VSS/g COD}$, and decay coefficient to be 0.018 h^{-1} .

Mosey (1983) developed an AD model with four different bacterial groups and included the hydrogen gas in the digestion of acetic, butyric and propionic acids in addition to the conversion of propionic and butyric acids to acetic acid (2000). This model is the first one that incorporates the dissolved hydrogen gas. Rozzi *et al.* (1985) modified Mosey's model by using hydrogen partial pressure instead of the dissolved hydrogen gas equations introduced by Mosey. Due to the complexity of the numerical integration problem, Rozzi *et al.* (1985) kept pH constant in the course of their simulation. Both Mosey's and Rozzi's models are applied only to glucose as a soluble substrate.

Bryers (1985) developed an anaerobic model that considers only one kind of methanogenic biomass but used two kinetic expressions for converting acetic acid and hydrogen respectively to methane. This model did consider the role of propionic acid utilizing bacteria by individually specifying the bacterial concentration, as the acid is an important intermediate and has a significant effect on the stability of that system.

Pavostanthis and Gossett (1986) proposed a model where sludge composition is more detailed than the one illustrated by Eastman and Ferguson (1981). This model assumes that the biodegradable fractions of the activated sludge are all viable organisms. This biochemical oxygen demand, BOD fraction is of two kinds soluble and particulate. Upon microbial death immediate release of the intracellular soluble BOD will occur. At the same time, the extracellular hydrolysis induced by the active biomass in the digester solubilizes the dead cell particulate BOD. The result is an increase in the soluble BOD for subsequent utilization by the acid-forming bacteria. The model takes into account the classical two-stage anaerobic pathway constituted by acidogenesis and methanogenesis. The proposed model is rather complex due to the assessment of large number of parameters. One other issue in this model is that the two processes of biomass death and lysis are theoretically different in terms of final products. The authors reported unsuccessful attempts of measuring cell lysis rates, thus leading to combine of the two processes into a single death/lysis step and no lag phase between death and lysis on one hand and release of all intercellular on the other hand. The hydrolysis process of the biodegradable particulate BOD uses the first-order empirical equation. Cell decay constant obtained is 2 d^{-1} , while the hydrolysis constant is 0.15 d^{-1} .

Shimizu *et al.* (1993) proposed a model that considered the hydrolysis of intracellular biopolymers as the rate-limiting step in the AD process. This model assumes that as hydrolysis of the cell walls and membrane proceeded, there is a release of intracellular high biopolymers in the bulk phase. Extracellular enzymes hydrolyze these compounds

to volatile organic acids (acetic, propionic, butyric, valeric and caproic acids) and the B-oxidation process converts higher fatty acids to acetic acid. In the final stage of the digestion process, the conversion of acetic acid, hydrogen and carbon dioxide to methane occurs. In order to reduce model complexity, the aforementioned authors used the first-order kinetics for all reactions i.e., sludge solubilisation, hydrolysis of intracellular polymers, conversion of higher fatty acids to acetic acid and H₂, and methanogenesis.

Angelidaki *et al.* (1999) developed a model where the substrate composition is defined by its organic (carbohydrates, lipids, and proteins), inorganic components (ammonium, phosphate, cations, and anions), and their degradation intermediates (volatile fatty acids). Carbohydrates are included in the model as particulate, soluble, and inert fractions. The particulate hydrolyses to soluble carbohydrates, which then converts to volatile fatty acids by acidogenic bacteria. Glycerol trioleate that converts to long chain fatty acids by acidogenic bacteria expresses the lipids. The long chain fatty acids degrade to acetate and H₂ by acetogenic biomass. The authors modeled proteins as gelatin composed of particulate, soluble, and inert fractions. The particulate components hydrolyze to amino acids that convert in the subsequent degradation step to acetate, propionate, butyrate, and valerate. The authors used the first-order to model the hydrolysis step since past studies (Noike, *et al.*, 1985, Pavlostathis *et al.*, 1988) demonstrated that first-order kinetic model is the best for describing the complex chemical-biological interactions of the AD system. The modeling of the biomass decay also uses the first-order equation. Monod equation, including a limiting term for

ammonia nitrogen as nutrient for biomass growth represents kinetically the biological processes (uptake and substrate degradation). The process kinetics accounts for the effects of pH and temperature.

Vanviline *et al.* (2001) developed a multi-component, multi-species model called “METHANE” that takes the processes of hydrolysis, acidogenesis, acetogenesis and methanogenesis conducted by various groups of microorganisms as well as the gaseous phase into account. The model uses a system of differential equations for three groups of variables as suspended organic matter, soluble components and gaseous phase components. It also considers the four basic stages of the AD i.e. hydrolysis, acidogenesis, acetogenesis and methanogenesis together with lysis and hydrolysis of cell biomass. Additionally, the model takes in to account the substrate limitation and inhibition functions.

Siegrist *et al.* (1993, 2002) developed a model for mesophilic and thermophilic digestion of sewage sludge based on the reaction proposed by Gujer and Zehnder (1983). The model considers the CSTR reactor and takes into account the variation in digested sludge and biogas composition. In addition to the biogas and hydrolysis of the particulate COD, the model considers six substrate processes namely: amino acid digestion, sugar digestion, LCFA, intermediates (propionic), acetotrophic methanogenesis, and hydrogenotrophic methanogenesis. The model also includes six processes of cell decay for the microbial groups catalyzing the bioconversion processes. Chemical equilibrium for the dissociation of bicarbonate, ammonium, acetic and propionic acids accounted in

evaluating pH. Siegrist *et al.* (2002) used the first-order equations for hydrolysis kinetics of particulate organic material and the biomass decay process. The expression of other kinetics uses Monod type equation modified to consider the inhibition.

Batstone *et al.* (2002) introduced the Anaerobic Digestion Model Number 1 (ADM1). The aim of the model is to provide a tool that overcomes the limitation of the models developed over the last few decades characterized by their specificity. Due to this focus, some peculiar and specific aspects are not included in order to obtain an easy-to-use model. This model therefore can serve as a platform for applications to specific processes (Yasui *et al.*, 2006). This model classifies the complex system of the anaerobic conversion process into two main groups:

(i) Intracellular or extracellular enzymes that act on the organic substances govern the biochemical reactions. The disintegration of the particulate compounds, and their hydrolysis, which produces soluble monomers, are extracellular reactions. The degradation of the soluble substances is instead a process that occurs inside the bacterial cells and results in biomass growth, and

(ii) Chemical-physical reactions are not biologically catalyzed and include the processes of ionic association/dissociation, and gas-liquid mass transfer. Biochemical reactions are irreversible processes, while physical-chemical reactions are reversible systems.

Biochemical equations are the heart of the model that represents the biological system. Physical-chemical reactions describe the effect of the state variables such as pH and gases concentration on the anaerobic process. The complex substances initially

disintegrate to obtain particulate carbohydrates, lipids, proteins, and inert material. The model assumes inactive biomass derived from the cellular decay process increases the fraction of particulate composite substances. In the following hydrolysis stage, the particulate carbohydrates, lipids, and proteins convert into their soluble forms of monosaccharides, long chain fatty acids and amino acids, respectively. The acidogenic bacteria metabolize them and convert to organic acids (propionate, valerate, butyrate and acetate) and hydrogen. The acetogenic bacteria will then metabolize the organic acids and convert them to acetic acid and hydrogen. Methanogenic bacteria further transform the latter to methane and carbon dioxide.

The ADM1 model assumes all extracellular processes follow the first-order kinetics. The first-order kinetics equations that are dependent on the microbial concentration describe cellular decay processes. Monod type kinetics expresses the substrate utilization in terms of substrate consumption and not microbial growth, with the aim of simplifying the implementation of the inhibition functions. In addition to pH inhibition for all the bacterial groups, hydrogen inhibition for the acetogenic bacteria and free ammonia inhibition for the acetoclastic methanogens are also included in the model. The chemical-physical processes are important in modeling the anaerobic systems as they express the inhibiting factors for the biological reactions and quantify some variable parameters such as gas flow rate, alkalinity, and pH. The gas phase in this model contains carbon dioxide, methane, and hydrogen. Henry's law describes the gas-liquid equilibrium for the diluted liquid phase. Carbon dioxide and ammonia are acids and bases present in the free form.